University College Cork, Ireland
Coláiste na hOllscoile Corcaigh

Nanomaterial Design and Fabrication for Energy Storage

Volume 1 of 1

Thesis presented by

Tomás Clancy, B.Sc (Hons.)

for the degree of

Doctor of Philosophy

University College Cork,

Tyndall National Institute,

Electrochemical Materials & Energy

Supervisor: Dr. James Rohan

Head of Department: Dr. Fatima Gunning

2019

Contents

Declaration

I, Tomás Clancy, certify that the work I am submitting is my own and has not been submitted for another degree, either at University College Cork or elsewhere. All external references and sources are clearly acknowledged and identified within the contents. I have read and understood the regulations of University College Cork concerning plagiarism

_____

Tomás Clancy

Acknowledgments

You are holding the fruits of years of work and research, and although there is only one author written below the title, a number of people deserve credit for the completion of this body of work.

Foremost, my supervisor, Dr James Rohan, whose support and encouragement were crucial for completion of this thesis. James's knowledge and guidance helped me in all the time of research and writing of this thesis. I could not have imagined having a better advisor and mentor for my Ph.D study.

I would like to thank all the people I met and helped me over the years and a special thank you to the Electrochemical Materials & Energy group: Declan Casey, Lorraine Nagle, Brian Shanahan, Michael Moore, Ian Seymour, Louise McGrath, Fiona Barry, Ricky Anthony and Richard Doyle.

Thanks to all my friends in Tyndall with a special mention to the "Tea Group".

I would like to thank my parents, Tom and Jean, and two brothers, Eoin and Padraig for their support and quiet encouragement.

I also want to express my appreciation and thanks to my girlfriend Sinéad who stuck with me during the long months of writing and re-writing even when I retreated to long days with my computer.

Cork, August 20th, 2018

Abbreviations

1,3-propane sulfone	PS
3D ultrathin graphite foam	UGF
Alternating current	AC
Anodic aluminium oxide	AAO
Aqueous rechargeable lithium battery	ARLB
Atomic force microscopy	AFM
Atomic layer deposition	ALD
Ball milling	BM
Cathode electrolyte interface	CEI
Chemical vapour deposition	CVD
Chronoamperometry	CA
Chronopotentiometry	CP
Cyclic voltammetry	CV
Density Functional Theory	DFT
Diethyl Carbonate	DEC
Dimethyl Carbonate	DMC
Dioxolane	$C_3H_6O_2$
Direct current	DC
Disodium propane-1,3-disulfonate	PDSS
Double-walled Si-SiO$_x$ nanotubes	DWSiNTs
Electric vehicles	EV
Electrochemical impedance spectroscopy	EIS
Electrolytic manganese dioxide	EMD
Electron diffraction pattern	EDP
Energy dispersive X-ray spectrometry	EDX
Ethylene carbonate	EC
Ethylmethyl carbonate	EMC
Field emission scanning electron microscope	FESEM
Finite element analysis	FEA
Fluorinated ethylene carbonate	FEC
Full width half maximum	FWHM
Galvanostatic intermittent titration technique	GITT
Highly fluorinated ether	HFE
Infrared	IR
Internet of things	IoT
Layered transition metal oxides	Li_xMO_2
$Li(CN)_2C_3N_2CF_3$	LiTDI
$LiAl_{0.1}Mn_{1.9}O_4$	LAMO
$LiB(C_2O_4)_2$	LiBOB

$LiCoO_2$	LCO
$LiFePO_4$	LFP
$LiMn_2O_4$	LMO
$LiN(SO_2CF_2CF_3)_2$	LiBETI
$LiN(SO_2CF_3)_2$	LiTFSI
$LiN(SO_2F)_2$	LiFSI
$LiNi_{0.5}Mn_{1.5}O_4$	LNMO
$LiNi_{0.5}Mn_{1.5-x}Ti_xO_4$	LNMTO
$LiNi_{1-x-y}Co_xAl_yO_2$	NCA
$LiNi_xMn_yCo_zO_2$	NMC
$LiPF_3(CF_2CF_3)_3$	LiFAP
$LiSO_3CF_3$	LiOTf
Lithium aluminium	LiAl
Lithium ethylene dicarbonate	LEDC
Lithium ion	Li-ion
Lithium perchlorate	$LiClO_4$
Lithium phosphorous oxy-nitride	LiPON
Lithium propylene dicarbonate	LPDC
Lithium titanate ($Li_4Ti_5O_{12}$)	LTO
LIthium super ionic conductor	LiSICON
Magnesiothermic reduction	MR
Metal phosphate coatings	MPO_4
Metal-assisted chemical etching	MACE
Nickel-metal hydride	Ni-MH
Olivine phosphates	$LiMPO_4$
Open-circuit voltage	OCV
Physical vapour deposition	PVD
Plastic lithium ion	PLiON
Poly(3,4-ethylenedioxythiophene)	PEDOT
Poly(ethylene oxide)	PEO
Polyaniline	PAN
Polymer gel electrolyte	PGE
Polypyrrole	Ppy
Potentiostatic intermittent titration technique	PITT
Propylene carbonate	PC
Radio frequency	RF
Rapid thermal annealing	RTA
Saturated calomel electrode	SCE
Scanning electron microscopy	SEM
Solid electrolyte interface	SEI
Stainless steel	SS

Abstract

The 'Internet of Things' scenario envisions billions of wireless sensors acting as the environmental interface to provide data that will, amongst other benefits reduce analysis costs, improve safety and predict future trends. Non-rechargeable batteries are the predominant energy source for today's commercial wireless sensors and both the energy and power demands dramatically reduce the lifetime of the primary batteries. The value of the useful data gathered is offset by the frequent battery replacement necessitated by their short lifetimes. The ultimate challenge facing the mass distribution of wireless sensors is meeting the energy and power requirements to match the lifetime of the microdevices.

Hybrid systems comprising a significantly smaller and rechargeable energy storage elements coupled to energy harvesters are of interest to enable wireless operation over the lifetime of the device. Li-ion rechargeable batteries provides the highest energy density (~270 Wh/kg) but the limitations of a typical organic solvent–based Li-ion batteries include a modest cycle life (<1,000) and low power density (<1,000 W/kg) which can hamper device operation particularly during the energy intensive periods of sensor measurement and wireless communication.

Microbatteries, such as solid-state Li-ion batteries have a larger potential energy density due to the removal of inactive binder and conductive additive materials in the electrodes. They also offer the potential for Li metal anodes and a cycle life ($\geq$ 5,000). The drawbacks which have limited their use in commercial systems include the need to maintain thin electrodes (at the micron level) particularly for the low electronic conductivity oxide cathodes typically utilised. Based on the time (τ) it takes to diffuse in a material of dimension L ($\tau = L^2/D$), where D is the diffusion coefficient, it can be estimated that the time taken for Li^+ to diffuse in typical battery materials of micron dimension will be two to three orders of magnitude slower with a corresponding lower power capability than for a nanoscale ($\leq$ 100 nm) material. A cathode with limited thickness and conductivity in combination with a low ionic conductivity solid-state electrolyte results in poor power capabilities and a significant potential drop can occur during high current operation. A small form factor capable of high current operation is critical in the development of the next-generation hybrid systems. Changing the geometry, size and thickness of the electrodes will have a direct effect on the battery capabilities.

In this work, we focused on electrode design, electrode nanoscale electrochemical properties, fabrication of new materials and substrates. We have optimised the 3D structuring, the fabrication of 3D nanoarchitectures, the electrochemical performance of advanced electrode materials and nanoscale thin-films. COMSOL Multiphysics simulations demonstrated the advantages of 3D and 3D core-shell nanoarchitectures when used with the appropriate electrolyte characteristics. It is shown that the planar thin-film architecture gave better cell performance when used with the solid-state electrolyte. The 3D and 3D core-shell nanoarchitectures show better battery performance for the polymer electrolyte than the planar thin film, with 3D being the best. The 3D core-shell nanoarchitecture shows a significant improvement in performance by comparison with the thin-film and 3D nanoarchitecture when a polymer-gel or a liquid electrolyte are used. The 3D nanoarchitecture shows a slight decline in performance when going from a polymer-gel electrolyte to a liquid electrolyte with faster Li-ion transport. The 3D core-shell shows improved cell performance with faster Li-ion transport. The adoption of nanoarchitectures with suitable electrolytes can have a significant improvement in battery areal energy and power performance.

A 3D core-shell nanoarchitecture electrode with Cu nanotubes as current collector with a Ge thin-film, achieved a capacity increase of 153 % in comparison to a planar Ge electrode. The 3D core-shell nanoarchitecture gave mechanical stability to the active Ge electrode as it underwent volume expansion during lithiation which enhanced cycle life and allowed overlithiation of the crystalline $Li_{15}Ge_4$ phase to increase the capacity capabilities of the active Ge.

The utilisation of DC sputtering for the deposition of $LiCoO_2$ and the optimisation of rapid thermal annealing as an annealing technique is described. The electrochemical performance of a nanoscale thin-film of $LiCoO_2$ was studied and revealed a hybrid Li^+ ion storage system of intercalation and intercalation pseudocapacitance in an aqueous system. At extremely high scan rates and galvanostatic current densities of up to 100 mV/s and 200 C respectively, a capacity retention equivalent to 97 mAh/g (4.8 $\mu Ah/cm^2$, 48.3 $\mu Ah/cm^2\mu m$) is obtained. A significant contribution of non-diffusion controlled kinetics (intercalation pseudocapacitance) at high scan rates is shown.

Electrodeposited thin-film V_2O_5 exhibited high power capabilities due to intercalation pseudocapacitance electrochemical kinetics when used in an aqueous electrolyte. However, V_2O_5 suffers from dissolution in aqueous electrolytes which results in severe capacity fade

and ultimately a loss of capacity after 100 cycles. A TiO_2 coating and a vinylene carbonate electrolyte additive were used to enhance cycle stability and improve electrochemical kinetics. Capacity retention was increased to 59 % after 200 cycles for V_2O_5 in aqueous electrolyte with 10 wt. % vinylene carbonate additive and a 100 nm TiO_2 coated V_2O_5 in aqueous electrolyte with 5 wt. % vinylene carbonate additive.

Chapter 1 General Introduction, Objectives & Overview

General introduction:

The Paris Agreement in 2016 signified a decisive moment in the ongoing battle against climate change. For the first time in history, World leaders unified to legally approve action against pollution through the United Nations Framework Convention[1]. The lowering of emissions and the long term goal of keeping the increase in global average temperature to below 2°C above pre-industrial levels, is what this international network of government bodies has dedicated itself to achieve. Only Syria and Nicaragua did not initially sign up, but have since in October and November 2017, respectively[2].

Greenhouse gases act like a blanket and trap the heat within our atmosphere which results in an increase in global temperature that has a knock on harmful effect of increasing sea levels, increased frequency of droughts and storms that all accumulate to put a massive strain on food production, clean water sources and energy production. The most prevalent greenhouse gas is CO_2 and is produced from the burning of fossil fuels like coal, oil and natural gas. The air and water pollution caused by the burning of coal and oil are linked to a number of health problems such as cancer and heart attacks[3]. Electricity, heating, transport and communication are heavily dependent on the burning of these fossil fuels. The replacement of fossil fuels with renewable sources of energy, which produce little to no emissions, is the core strategy in tackling climate change.

Strong winds, sunny skies, heat from the earth and fast running water can provide a large renewable energy source through wind, solar, geothermal and hydroelectric energy, respectively, as seen in Figure 1.1. The innovation in utilising these energy sources through design, manufacturing process and R&D while energy management systems are needed to only use energy when required has been and will continue to be critical, in order to reach the goal set out in the Paris Agreement. Wind and solar energy sources are the most popular sources that are used globally are they can be distributed over a large geographical area and are modular systems resulting in their being less prone to large scale failure[4]. The big issue with such renewable energy sources are their unpredictability and intermittence; however

1

modern grid technologies such as advanced batteries to store unused energy until required and smart systems that only use energy when needed are instrumental in the deployment of these energy sources[5].
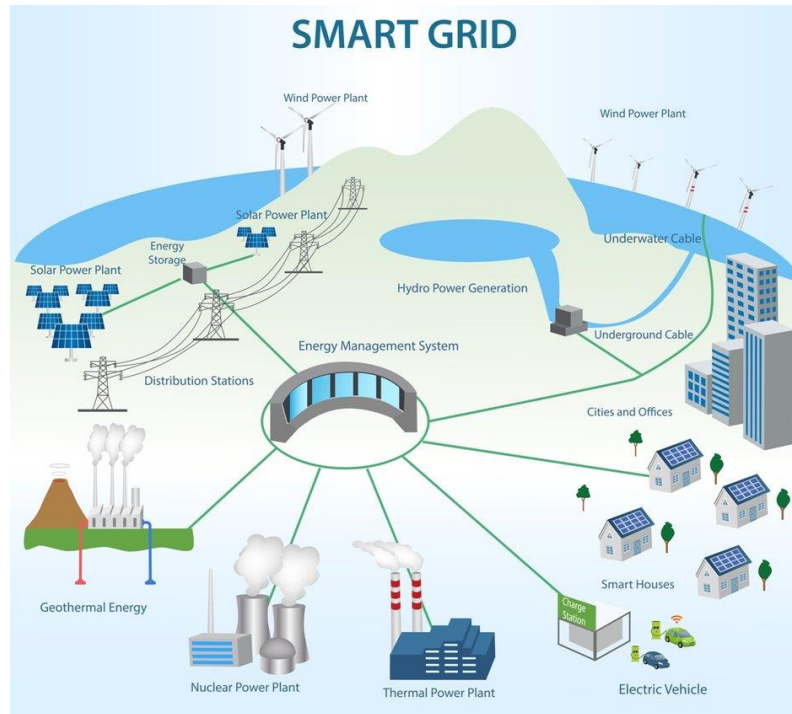
Some of the advanced batteries used in grid control are lithium ion batteries like those that have been used to power laptops and smartphones but are now being utilised with power management systems in both large plant and small domestic scale units to utilise the energy from either a wind/solar farm or rooftop solar panels. Tesla's Hornsdale 100-megawatt battery in Australia has been a revolution during the summer months, where energy usage is high due to the increased use in air conditioning units, as it reacts faster than the inefficient peaker power plants that only run in times of high demand[7]. In some locations a wall mounted domestic 14 kWh lithium ion battery to store the energy from solar panels can cover around 75% of the yearly energy requirements of a 3 bedroom house[8]. These lithium ion batteries are similar to those developed for electric vehicles (EV's) though typically larger, 40 and 50 kWh batteries are used in EV's such as the New Nissan Leaf and Tesla Model 3, respectively[9].

This can lead to a potential scenario where on a warm sunny day when everyone is outside enjoying the sun the energy from the solar panels is stored in the battery rather than being

wasted and can be used in the evening when people have gone inside after their day in the sun and any excess energy can be used to charge their EV, Figure 1.2. Imagine if every house in an estate had solar cells on their roof. The estate could be classed as a solar farm and if a small battery was added to each house it would maximise the efficiency of this "solar farm". The creation of this self-sustaining energy cycle eco system on a domestic level is a practical reality and one that countries are succeeding at implementing[10]. The main constraint to implement such a scenario is the capital cost associated with installing and purchasing solar panels and battery systems for the homeowner. The slow uptake of electric vehicles is due to the initial costs, vehicle range per charge, charging infrastructure and battery lifetime. Three out of these four technical issues are dependent on the battery technology. The cost of manufacturing batteries of the size required for both domestic units and EV's are significant.
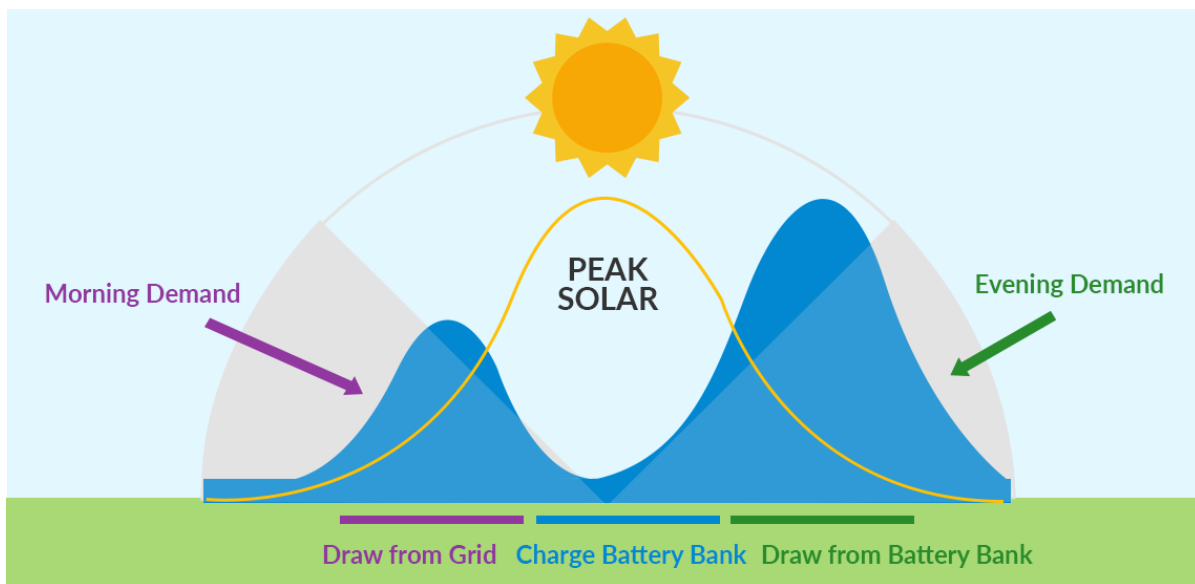
Figure 1.2: Schematic of how the electricity generated from PV solar cells at times where supply is greater than demand (noon) can be stored in a battery and be used at times of when demand is higher than supply (morning/evening). Reproduced[11]

Advances have been made in the development of lithium ion batteries such as the integration of the abundant energy dense material silicon with the graphite anode and the reduction in the amount of cobalt used in the transition metal oxide cathode leading to cheaper and more energy dense batteries[12]. However more advances are needed in order to reduce the cost and increase the energy density of the battery in order to make it more attractive practically (EV's) and financially (EV's & domestic energy storage).

Smart systems are critical for energy usage to be efficient. The "smart" in the system is a sensor that can measure a variable which will then tell the system to react accordingly. A real world example is air conditioning in buildings; generally the air conditioning is turned on for a set period throughout the building e.g. 8 o'clock to 6 o'clock, which means the energy usage is fixed no matter how many people are in the building. A smart air conditioning system uses CO_2 sensors to determine the room occupancy which can then tell the air conditioning system to turn on to an appropriate level and if required turn off if the room is unoccupied, thus only using the energy that is actually required rather than having it constantly powered on. An issue with these autonomous sensors is the associated maintenance. They are powered by non-rechargeable batteries with a 5 year lifetime; however, in practice these batteries may only last a few months due to sensors of this type having very demanding energy and power requirements. This results in larger maintenance costs associated with battery replacement, while also potentially having health risks during sensor downtime[13]. A rechargeable battery integrated into a hybrid system with an energy harvester can meet the energy and power demands of the sensor. The energy harvester is there to recharge the battery daily meaning that rather than sourcing batteries with a 5 year initial capacity a much smaller battery capacity can be utilised. This hybrid system of a rechargeable battery and energy harvester could result in a sensor that would last up to 20 years and cut maintenance costs by 50. Even by sourcing a battery of smaller capacity, the size of the battery generally still dictates the size of the sensor while additional components need to be added to the device in order to meet the power demands of the sensor which is not ideal for these autonomous wireless sensors to be seamlessly integrated into society.

Smart systems are dependent on the technology advancements of the energy harvester, battery, power management system and sensor with the battery being the most critical component in order to create a self-sustaining energy cycle ecosystem that at least lasts the lifetime of the wireless sensor. Typical rechargeable batteries under development for such applications are solid state batteries based on lithium battery technology due to their ease of implementation into device with a small form factor in comparison to Li-ion batteries. Solid state batteries are fabricated using mature semiconductor manufacturing processes that can easily produce batteries of sub-mm dimensions[14]. The difference between solid state and Li-ion batteries is that a solid electrolyte is used instead of liquid organic electrolyte, the electrodes are free of inactive additives (binders and conductive particles). Since space is at a premium for these applications, solid-state batteries are utilised as the solid-state electrolyte

is significantly thinner and inactive materials in the electrode material are removed to allow for more active material. Since solid state electrolytes typically have an ionic conductivity in the order of 10^{-6} S/cm, in comparison to 10^{-3} S/cm for liquid electrolytes, its thickness is typically 1 μm in order to shorten the diffusion length[15]. This compensates for its low ionic conductivity rather than the liquid filled porous membrane that is 25 μm thick and separates the two electrodes. The solid state electrolyte means Li metal can be used as the anode since the solid state electrolyte prevents dendrite formation which results in short circuiting when used with liquid electrolytes[16]. Li metal acts as an infinite Li source, is more energy dense than graphite while the solid state electrolyte means the battery is non-flammable, tolerant at high temperatures and stable for thousands of cycles in contrast to the flammable liquid electrolyte[17].

Physical vapour deposition is a line of sight deposition technique used to deposit solid state battery components that limits deposition onto planar substrates. The only method to improve energy density is by increasing the thickness of the cathode electrode, however cathodes thicker than 5-10 μm suffer from stress in the film that cause delamination and cracking[18]. Even if the issues associated with stresses in the film were resolved all of the theoretical capacity of the cathode could not be delivered at practical rates due to the increase in the diffusion length[19]. The thickness of the electrode has a quadratic relationship to the time is takes for the Li^+ ions to diffuse all the way into the electrode, Figure 1.3. This has resulted in solid state batteries with a limited energy density and low power capabilities.
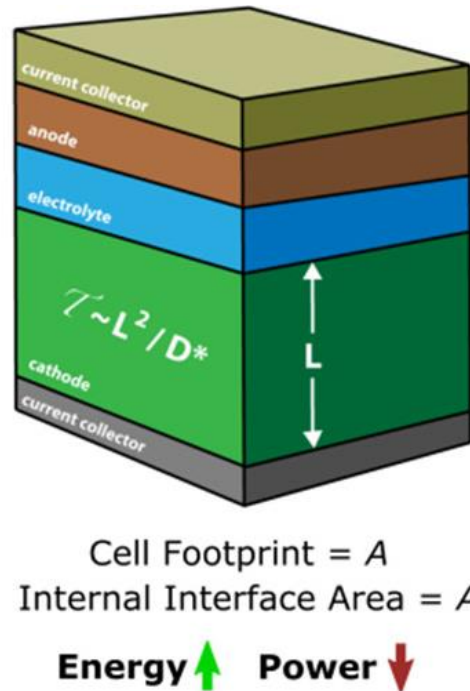
Figure 1.3: Schematic of mathematical relationship of increasing electrode thickness with diffusion time. Reproduced[20]

Solid state battery performance can be improved by developing new electrolytes that have a higher ionic conductivity and new electrodes that are composed of materials that have a higher capacities and voltage. The easiest way to obtain incremental improvements in the energy density and power capabilities of a solid state battery is by fabricating batteries on 3D substrates. The areal capacity can be improved while maintaining electrode thicknesses that meet the power demands as shown in **Figure 1.4**. 3D solid state batteries were first proposed by Long et al. in 2004 and there have been numerous reports that have outlined the benefits, proposed architectures and assembled half cells and full cells[17, 19, 21]. The realisation of fabricating these 3D solid state batteries has proven difficult mainly due to the use of physical vapour deposition technique since this is a line of sight deposition the required film uniformity on justifiable aspect ratios has proven challenging. Deposition techniques such as chemical vapour deposition and atomic layer deposition have been shown capable of depositing electrodes and electrolyte of acceptable uniformity into high aspect ratios, however such techniques are costly which currently makes these processes uneconomical for industry[22]. Fabrication and deposition techniques of 3D solid state batteries need to be improved while the cost has to be decreased also. Improvement in the electrolyte characteristic and properties can also play a major role in meeting the power demands of wireless sensors and improving cycle life.

Cell Footprint = A
Internal Interface Area $> A$
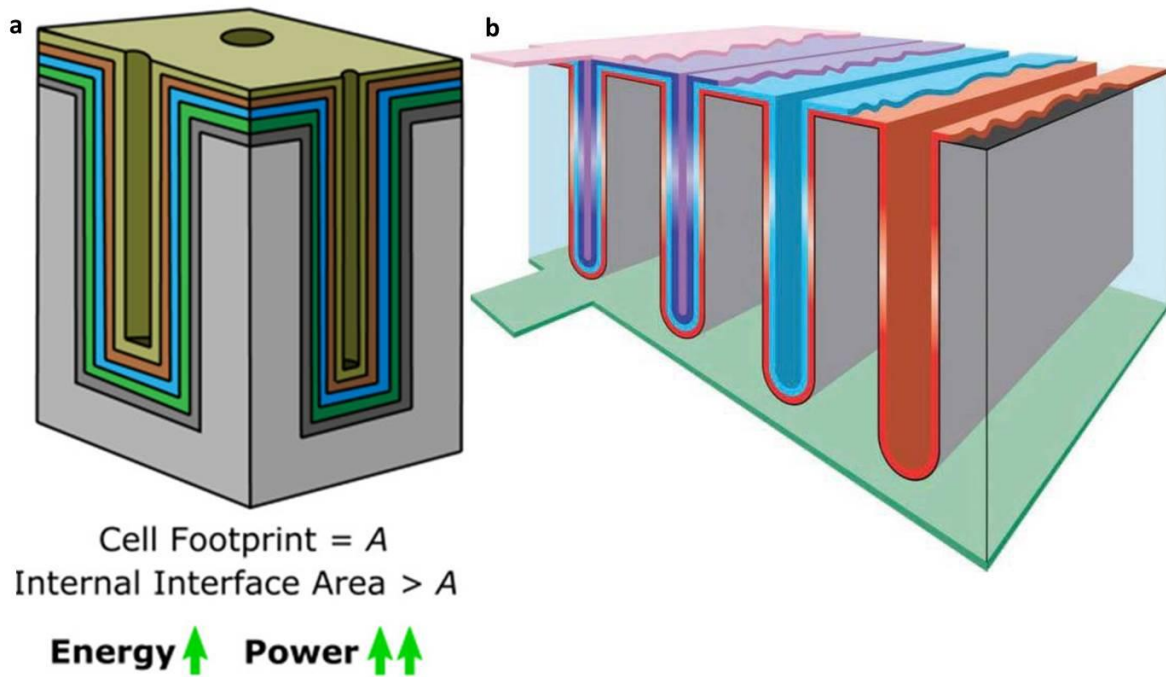
Energy ⬆ **Power** ⬆⬆

Figure 1.4: Schematic of a, energy and power relationship with increasing aspect ratio of 3D structure. b, conformal fabrication of a battery in a 3D structure. Reproduced[17, 20]

The critical improvements needed with both solid state and Li-ion batteries that will have the largest impact are:

- Design of electrodes in appropriate electrolytes
- Utilisation of energy dense anode electrodes
- Fabrication of high aspect 3D architectures
- Utilisation of unique nanoscale electrodes
- Cost effective deposition techniques of electrode materials.

Objectives:

The objective of the project is to use state-of-the-art microfabrication techniques to fabricate a high energy- and power-density 3D Li-ion battery for various applications e.g., miniature transmitters, remote sensors, smart cards and MEMS devices. The goal is to enable increased lifetime and functionality of portable systems with specific Li-ion batteries power capabilities and capacities adapted to the specific applications by varying the electrode architecture and electrolyte. An improved method of fabrication of 3D nanowire and nanotube current-collector pads with high aspect ratio and deposition of active electrode materials upon them is

described. The proposed 3D architecture would overcome the energy-density and power-density deficiency of the conventional planar battery by incorporation of sufficient electrode materials onto nano-features that are micron sized in height which can be created by simply electrodepositing the current collector metal into a nano porous anodic aluminium oxide (AAO) template.

In this study, we report on advanced multiphysics simulations in the design of nanoarchitecture to optimisation their electrochemical performances. Li-ion battery materials that are compatible with 3D structuring using the developed fabrication route were analysed. The Ge based anodes demonstrate improved capacity and cycle life through the deposition upon 3D nanoarchitectures. Direct current (DC) sputter deposition was utilised to deposit thin-films of $LiCoO_2$ at a higher rate and shorter process time than the typically used radio frequency (RF) sputter process. We investigated the electrochemical properties of a nanoscale thin film in an electrolyte with a high ionic conductivity at room temperature so the electrochemical performance is primarily dependent on the rate of lithium transport in the electrode rather than Li^+ ion transport in the electrolyte. Also, the electrodeposition of nanoscale thin-films of V_2O_5 electrode are reported and analysed in the highly conductive electrolyte. The highly conductive electrolyte was aqueous based which can have complicated side reactions like organic based electrolytes. V_2O_5 is slightly soluble in water (4 mM) which is a significant amount when considering the amount of V_2O_5 in a nanoscale thin-film. The effect of vinylene carbonate (VC), a typical organic additive, and a TiO_2 coating were investigated both separately and in combination in the aqueous electrolyte in order to minimise the dissolution of V_2O_5 and extend cycle life.

The objectives of this work are listed below:

- The demonstration of the effect of nano-architecture electrodes in various electrolytes using COMSOL Multiphysics® simulation.
- The demonstration of a fabrication route for high aspect ratio 3D nano architecture current collectors that can be used to mechanically support energy dense anode materials thereby increasing the capacity and cycle life.
- The demonstration of high electrochemical performance and properties of nanoscale anode and cathode materials.

- The demonstration of lower cost plating techniques electrode material and increasing its cycle life in an aqueous electrolyte by using a protective coating and/or an organic additive.

Overview:

The chapter 2 introduces the general literature review of a battery, its history, the evolution of the lithium batteries and their basic working principles. In the review, the state-of-the-art electrode materials and 3D architectures for Li-ion batteries are reviewed. Finally, the effect of the electrolyte composition on the performance of lithium batteries with regards to the lithium salt and solvent (organic mixture or aqueous) are discussed. Chapter 3 discusses the fundamental principles of the electrochemical and characterisation techniques used in this study.

COMSOL Multiphysics was used to compare the effect that electrode architecture coupled with various electrolyte conductivities have on the battery performance in chapter 4. The battery performance of a typical all solid-state microbattery was used as a standard. The effects of improved electrolyte characteristics on the battery performance were investigated in the standard thin-film microbattery, 3D and 3D core-shell nanoarchitectures. We show that both nanoarchitectures have inferior performance to the standard all solid-state microbattery, due to the additional area 3D architecture and core current collector, however we show that with improved electrolyte characteristics both nanoarchitectures have superior battery performance with the core-shell nanowire being the best.

Starting with anode materials for high capacity and long cycle life, 3D Cu nanotubes were investigated as a current collector for Ge thin films in order to act as mechanical support and increase the amount of Ge per area is presented in chapter 5. A scanning electron microscopy (SEM) was used to investigate the coverage of the Ge deposit upon the Cu nanotubes. The electrochemical performance is studied with the cyclic voltammetry and chronopotentiometry techniques.

Chapter 6 then investigates the electrochemical properties of nanoscale films of $LiCoO_2$. In order to ensure the cell performance is solely dependent on the electrochemical performance of the nanoscale $LiCoO_2$ and not the ion transport in the electrolyte analysis was performed in

an aqueous electrolyte. The effect the substrate and the rapid thermal annealing (RTA) conditions have on the crystalline structure of nanoscale $LiCoO_2$ were also investigated.

Chapter 7 discuss the use of V_2O_5 as an electrode in aqueous environment and its electrochemical properties. TiO_2 protective coatings and various concentrations of VC electrolyte additive were investigated in order to improve cycle life as V_2O_5 is slightly soluble in an aqueous environment.

Chapter 8 draws conclusion from the conducted work, summarises the achievements and presents an outlook for future work.

References:

[1]   United Nations, United Nations Treaty Collection Chapter XXVII environment, 7. d Paris agreement, Paris, 12 December 2015 (CN 92.201), **2016**

[2]   *United Nations Paris Agreement*. 2016. http://treaties.un.org/Pages/ViewDetails.aspx?src=TREATY&mtdsg_no=XXVII-7-d&chapter=27&clang=_en

[3]   M. Kampa, E. Castanas, *Environ. Pollut.* **2008**, *151*, 362-367.

[4]   *Europe keeps setting clean-energy records*. 2018. http://qz.com/1328344/renewable-energy-europe-keeps-setting-new-records-and-killing-off-coal/

[5]   *How Energy Storage Works*. 2013. http://www.ucsusa.org/clean-energy/how-energy-storage-works#bf-toc-0

[6]   *How Secure Is Our Smart Grid?* 2017. http://www.govtech.com/blogs/lohrmann-on-cybersecurity/how-secure-is-our-smart-grid.html

[7]   *Hornsdale Power Reserve*. 2017. http://hornsdalepowerreserve.com.au/

[8]   *Join the Solar Revolution*. 2016. http://www.solarelectric.ie/sonnen/

[9]   a) *New Nissan Leaf*. 2018. http://www.nissan.ie/vehicles/new-vehicles/leaf-40kwh.html; b) *Tesla Model 3 battery packs*. 2017. http://electrek.co/2017/08/08/tesla-model-3-battery-packs-50-kwh-75-kwh-elon-musk/

[10]   *Germany produces enough renewable energy in six months to power country's households for an entire year*. 2018. http://www.independent.co.uk/environment/renewable-energy-germany-six-months-year-solar-power-wind-farms-a8427356.html

[11]   *What Is a Solar Battery? How To Back Up or Completely Power Your Home Energy System*. 2018. http://www.letsgosolar.com/faq/what-is-a-solar-battery/

[12]   *The Future of Battery Technology*. 2016. http://www.visualcapitalist.com/future-battery-technology/

[13]   C. Ó. Mathúna, T. O'Donnell, R. V. Martinez-Catala, J. Rohan, B. O'Flynn, *Talanta* **2008**, *75*, 613-623.

[14]   a) F. L. Cras, B. Pecquenard, V. Dubois, V.-P. Phan, D. Guy-Bouyssou, *Advanced Energy Materials* **2015**, *5*, 1501061; b) K. Kushida, K. Kuriyama, T. Nozaki, *Appl. Phys. Lett.* **2002**, *81*, 5066-5068.

[15]   a) J. B. Bates, N. J. Dudney, B. Neudecker, A. Ueda, C. D. Evans, *Solid State Ionics* **2000**, *135*, 33-45; b) M. Marcinek, J. Syzdek, M. Marczewski, M. Piszcz, L. Niedzicki, M. Kalita, A. Plewa-Marczewska, A. Bitner, P. Wieczorek, T. Trzeciak, M. Kasprzyk, P.Łężak, Z. Zukowska, A. Zalewska, W. Wieczorek, *Solid State Ionics* **2015**, *276*, 107-126; c) Y. R. Su, J. C. Falgenhauer, C. Lupo, B. K. Meyer, D. Schlettwein, A. Polity, J. Janek, *Meeting Abstracts* **2015**, *MA2015-01*, 103; d) L. Long, S. Wang, M. Xiao, Y. Meng, *J. Mater. Chem. A* **2016**, *4*, 10038-10069.

[16]   B. J. Neudecker, N. J. Dudney, J. B. Bates, *J. Electrochem. Soc.* **2000**, *147*, 517-523.

[17]   J. F. M. Oudenhoven, L. Baggetto, P. H. L. Notten, *Advanced Energy Materials* **2011**, *1*, 10-33.

[18]   N. J. Dudney, *Materials Science and Engineering: B* **2005**, *116*, 245-249.

[19]   J. W. Long, B. Dunn, D. R. Rolison, H. S. White, *Chem. Rev.* **2004**, *104*, 4463-4492.

[20]   A. Pearse, T. Schmitt, E. Sahadeo, D. M. Stewart, A. Kozen, K. Gerasopoulos, A. A. Talin, S. B. Lee, G. W. Rubloff, K. E. Gregorczyk, *ACS Nano* **2018**, *12*, 4286-4294.

[21]   a) P. H. L. Notten, F. Roozeboom, R. A. H. Niessen, L. Baggetto, *Adv. Mater.* **2007**, *19*, 4564-4567; b) L. Baggetto, R. A. H. Niessen, F. Roozeboom, P. H. L. Notten, *Adv. Funct. Mater.* **2008**, *18*, 1057-1066; c) M. Roberts, P. Johns, J. Owen, D. Brandell, K. Edstrom, G. El Enany, C. Guery, D. Golodnitsky, M. Lacey, C. Lecoeur, H. Mazor, E. Peled, E. Perre, M. M. Shaijumon, P. Simon, P.-L. Taberna, *J. Mater. Chem.* **2011**, *21*, 9876-9890.

[22]   a) S. M. George, *Chem. Rev.* **2010**, *110*, 111-131; b) X. Meng, X.-Q. Yang, X. Sun, *Adv. Mater.* **2012**, *24*, 3589-3615; c) A. J. Pearse, T. E. Schmitt, E. J. Fuller, F. El-Gabaly, C.-F. Lin, K. Gerasopoulos, A. C. Kozen, A. A. Talin, G. Rubloff, K. E. Gregorczyk, *Chem. Mater.* **2017**, *29*, 3740-3753; d) L. Ma, R. B. Nuwayhid, T. Wu, Y. Lei, K. Amine, J. Lu, *Advanced Materials Interfaces* **2016**, *3*, 1600564; e) M. Létiche, E. Eustache, J. Freixas, A. Demortière, V. De Andrade, L. Morgenroth, P. Tilmant, F. Vaurette, D. Troadec, P. Roussel, T. Brousse, C. Lethien, *Advanced Energy Materials* **2017**, *7*, 1601402.

Chapter 2 Literature Review

History:

A battery is an electrochemical cell that stores energy in the form of chemical energy and releases it in electrical form. The electrical energy from the battery is used to power an electrical load in an electric circuit to do work. Other forms of chemical energy storage are the products of electrolysers and their use in fuel cells which, like batteries, are electrochemical energy-conversion devices.

Alessandro Volta, a Professor of Natural Philosophy (physics) at the University of Pavia in Italy invented the first battery in 1799 which has been referred to as the Voltaic pile which consisted of a pile of alternating copper and zinc metal discs separated by a cloth saturated in salt water. One end of the pile finished with silver and the other end finished with zinc, a continuous current of electricity was produced once the ends were connected by a wire. The French word for battery 'la pile' is derived directly from the Voltaic pile.

In 1836, the next significant step in the development of batteries, the Daniell Cell, was invented by the Professor of Chemistry at King's College, London, John Daniell. He took a copper container and filled it with copper sulfate solution, he then placed an ox's gullet filled with sulfuric acid into the container. A vertical zinc rod was placed inside the ox's gullet and electrical connections were made to the copper container and zinc rod. Discharge of the electrochemical cell caused the zinc rod to dissolve and copper to plate on the inside of the copper container. The battery had a potential of 1.1 V and gave a continuous current from a device and thus had practical applications. Commercial telegraphic systems used Daniell cells, with a porous pot instead of an ox gullet, in the early 1850s following the swift deployment of the telegraphic technology and resulting services.

Following on from the headway made by Daniell on the advancement of batteries, Georges Leclanché, a French chemist, developed a battery that could only be discharged once, known as a primary battery, with a cell potential of 1.5 V in 1866. The battery consisted of a glass jar filled with a solution of ammonium chloride with a carbon rod uncased in a porous ceramic pot packed with manganese dioxide and carbon powder as the positive electrode and a zinc rod as the negative electrode. The Leclanché cell was further developed when a zinc can

replaced the glass jar and zinc rod as the can could act as both a container and negative electrode. This major development was patented and the technology made available for everyday use.

Prior to batteries, the only available electricity was static electricity from such as we observe during thunderstorms or produced by friction between dissimilar materials. The availability of continuous current from a portable electrochemical cell caused a revolution in technology resulting in the advancement and discovery of new technologies. The alkali metals calcium, potassium and sodium were for the first time extracted using electrolysis due to the enabling battery technology.

Another French chemist, Gaston Planté, in 1859 was the first to present a feasible battery that could be discharged and then recharged for reuse. This type of battery is known as a secondary or rechargeable battery. In order for the battery to be recharged the chemical reaction in the battery needs to be reversible so that chemicals are reverted back to their original form. The lead-acid (Pb-acid) battery he developed consists of dilute sulfuric acid (H_2SO_4) in a glass container with a stack of two lead sheets separated by porous cloth in a spiral shape. The lead-acid battery gave a cell potential of 2 V, however the initial current was very small due to the small surface area of the fresh lead sheets. After numerous discharge and charge cycles the current improved, due to the chemical reaction tacking place on the electrode surface. The reaction involved the conversion of the cathode to lead oxide (PbO_2) the active material and the anode into porous Pb with a significantly increased surface area. This cycling became known as the formation process. However, the formation process could take months which increased the cost of manufacturing and made them impracticable. French chemical engineer Camille Fauré in 1881 made a significant advancement and reduced the formation process from months to hours. His progression involved coating the lead plates with a paste of pre-oxidised, PbO_2 and H_2SO_4. Thanks to the innovation and contribution of both Planté and Fauré the Pb-acid battery, now in use for over 150 years, is still very much a significant player in the secondary battery market, as a low cost and reliable energy source for golf carts, wheelchairs and as SLI (starting lighting and ignition) batteries in the majority of automobiles.

In the 19th century the first batteries with an alkaline solution were reported and developed. Competition arose between Waldemar Jungner and Thomas Edison as both inventors patented very similar alkaline batteries with a cell potential of 1.2 V. Jungner's alkaline nickel-cadmium (Ni-Cd) battery had a nickel hydroxide (Ni(OOH)) positive electrode and a

mixture of cadmium and iron powders as the negative electrode. Edison's alkaline battery used similar materials. It also had a nickel hydroxide positive electrode but differed in the use of an all iron negative electrode and was called the nickel-iron (Ni-Fe) battery. The alkaline electrolyte used in both batteries was potassium hydroxide. Both batteries had to deal with the possibility of H_2 gas evolution on overcharging or over-discharging. This gas evolution would lead to an increase in internal pressure and rupture or explode the cell. The Ni-Cd battery won out despite its higher cost due to its higher efficiency when charging and improved safety as less H_2 gas is formed when discharging. Ni-Cd was one of the most popular rechargeable batteries in the world due to its higher energy density and discharge current capabilities[1]. Developments and advances in the Ni-Cd fabrication process significantly reduced the manufacturing costs and it achieved a sizable portion of the rechargeable market.

In the 20th century the nickel-metal hydride (Ni-MH) battery was developed which gave almost 300% more capacity than its cousin the nickel-cadmium. The nickel-metal hydride comprised of a nickel hydroxide positive electrode and a metal alloy, including rare-earth metals as the negative electrode. The nickel-metal hydride battery was discovered in 1967 at the Battelle-Geneva Research Centre, which was heavily funded by Daimler-Benz and Volkswagen, and took 20 years to make the first commercial product and bring to market in 1989. In the mid 2000's the nickel metal-hydride powered more than 2 million hybrid cars worldwide and almost half of all portable electronics in Japan[2]. Ni-MH batteries were classed as a high-energy green battery. La- and Zr- based Ni metal alloys were typical anode materials used in the Ni-MH batteries. These metal alloys tolerate large concentrations of H^+ ions in the crystalline lattice resulting in the formation of a metal hydride as the product after charging. H^+ ions are formed from the splitting of water in the electrolyte. This is a solid-state reaction mechanism as the charging and discharging processes depend on the proton transfer between the cathode and anode. The homogeneous solid-state reaction removed problems associated with mechanical stability of the electrodes, low electrical conductivity of the oxidised anode and morphology changes at the electrode surfaces seen in Ni-Cd batteries which require a precipitation and dissolution reaction mechanism.
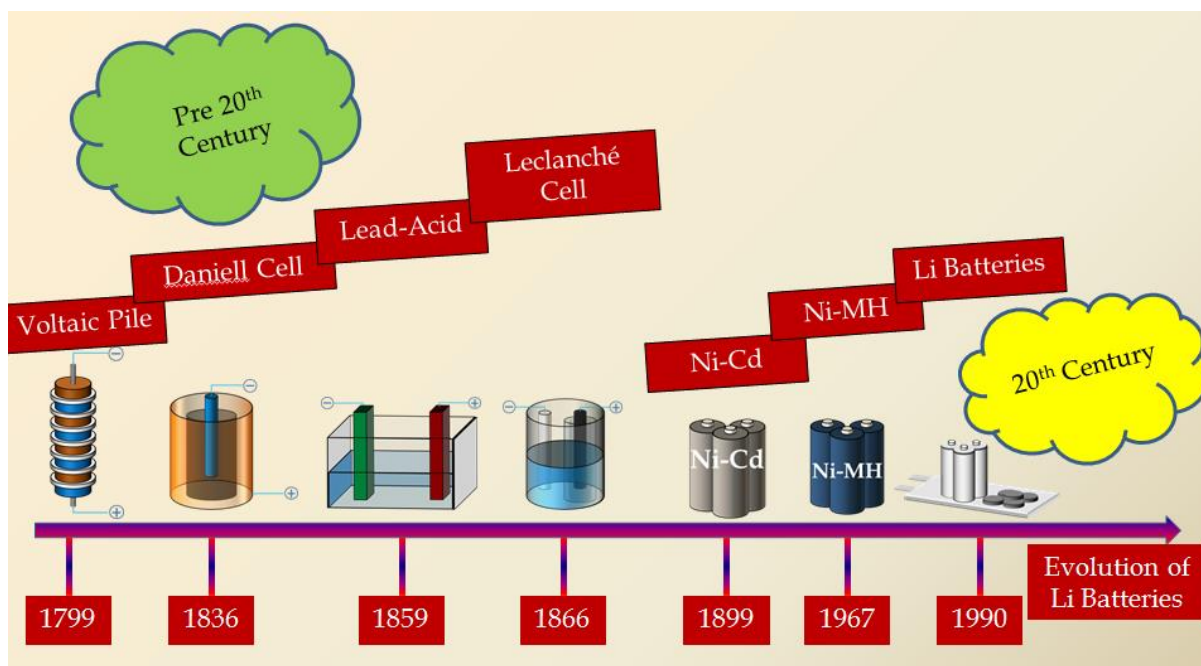
Figure 2.1: History of the battery timeline.

Evolution of Lithium Batteries:

Lithium batteries were proposed in the 1970s by M. Stanley Whittingham while working in Exxon. The battery comprised a titanium(IV) sulphide (TiS_2) cathode material, which could host Li^+ ions in its lattice, in a process termed intercalation, due to its layered-type structure. Lithium metal was the proposed anode material. Lithium perchlorate ($LiClO_4$) in dioxolane ($C_3H_6O_2$) was used as the electrolyte. Lithium metal was first investigated as an anode material due to it having the largest electrochemical potential (-3.04 V vs SHE) and the largest gravimetric energy density (3860 mAh/g). TiS_2 is a difficult material to work with since it reacts in air to form hydrogen sulphide compounds, which are toxic to most animals and give an unpleasant odour. His research proved the concept behind intercalating cathode materials; however it also highlighted a problem with lithium metal as the anode material. Lithium metal is used in primary batteries to power electronic devices, such as watches and medical implants with high reliability and capacity densities, and was not foreseen to be an inhibitor in the rechargeable battery[3]. The problem arose at the electrode/electrolyte interface at the lithium metal anode. During cycling of the lithium metal, redeposition of lithium was non-uniform and resulted in the growth of lithium dendrites upon cycling that could penetrate the separator and make contact with the cathode resulting in a short circuit,

15

unwanted reactions, pressure build-up and eventually risk of explosion on exposure to the atmosphere, Figure 2.2[4].
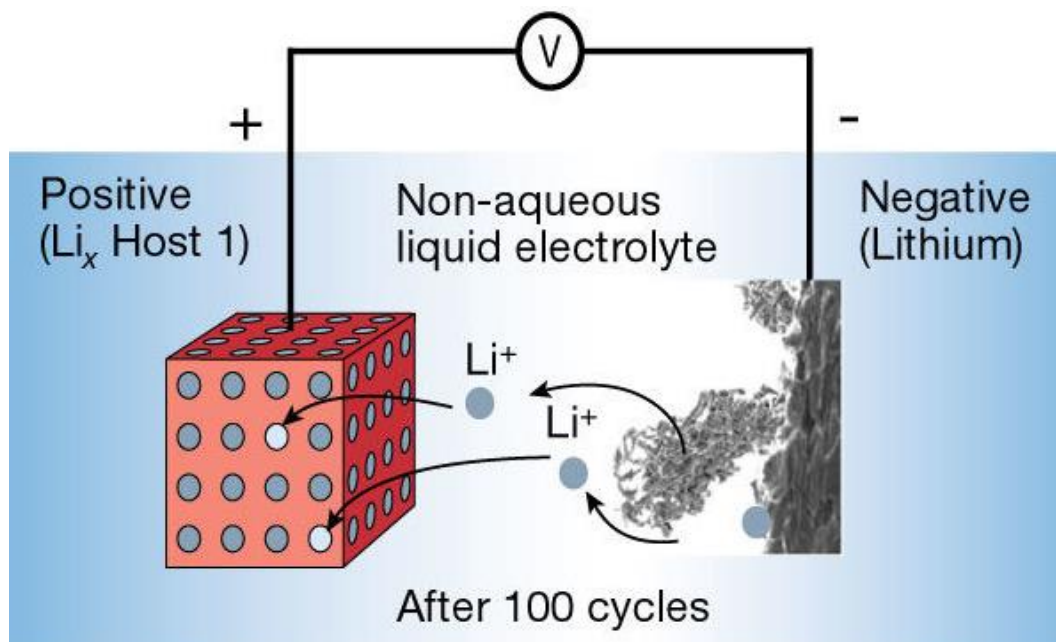
Figure 2.2: Rechargeable Li-metal battery. (Reproduced)[5]

Bell labs demonstrated that layered transition metal oxides were a viable candidate as a cathode material to replace the TiS_2 due to their higher capacities and redox potentials[6]. Goodenough et al. proposed a number of layered transition metal oxides such as Li_xMO_2 (M = Co, Mn or Ni)[7]. Goodenough and Mizushima developed the first usable rechargeable lithium battery with a cell potential of 4 V in 1979. However the issues associated with the use of a lithium metal anode persisted.

To overcome the safety issue associated with lithium metal anodes and the organic electrolyte interface alternative approaches were investigated. The main focus of the early research on lithium batteries was on the electrode materials. Murphy et al. and Scrosati et al. proposed the complete replacement of lithium metal from the anode with an insertion electrode, in the early 1980s, which lead to the lithium ion (Li-ion) battery concept, Figure 2.3[8]. This meant that lithium was in ionic rather than metallic form which had significant safety benefits such as the removal of highly reactive lithium metal. The Li_xMO_2 cathodes proposed by Goodenough et al. have a high redox potential to compensate for the replacement of lithium metal with a less energy dense anode that operated at a higher redox potential. The first materials that showed promising characteristics for replacing lithium metal were metals that

would alloy or intercalate with Li. These metals solved the dendritic growth issue as Li ions either alloyed (bonded) or sat between the metal layer rather than growing upon the surface. Cycle life was very short due to the volume expansion when alloying/dealloying with Li resulting in mechanical instability and delamination from the current collector. Lithium aluminium (LiAl) alloy with a 1:1 composition was one of the first materials to be investigated as a possible replacement but the volume expansion of 200% resulted in rapid capacity fade[9].
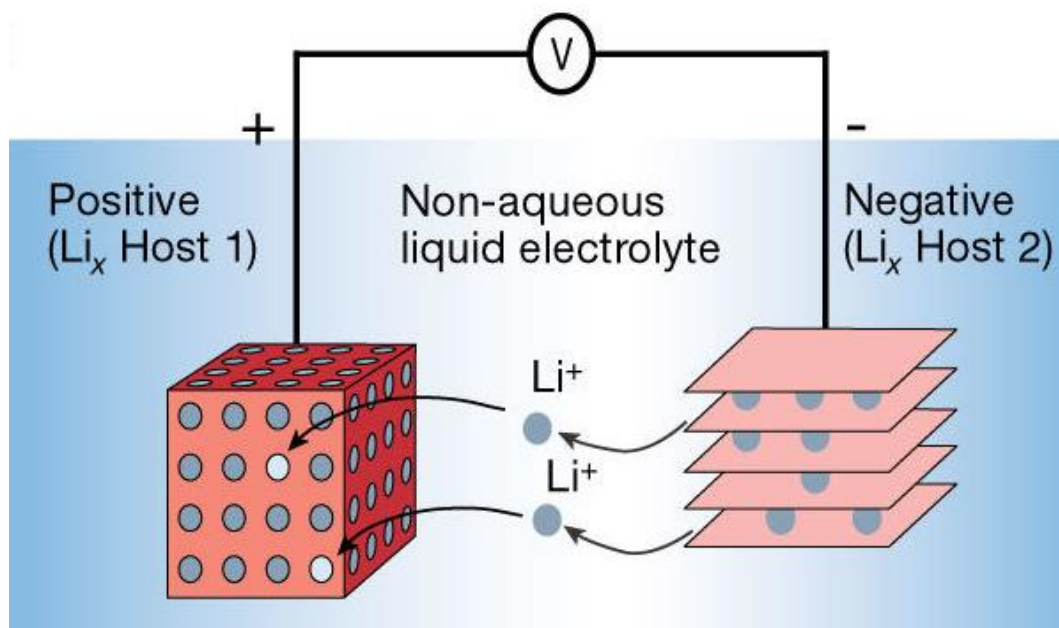
Figure 2.3: Rechargeable Li-ion battery. (Reproduced)[5]

Rachid Yazami in 1980 showed that a graphite electrode can accept lithium ions close to the potential of lithium metal using a solid polymer electrolyte since the liquid organic electrolytes at the time decomposed above the potential at which the lithium ions could be stored[10]. Polymer based electrolytes were looked at as a possible solution to dendrite formation on the lithium metal anode by replacing the liquid electrolyte with a solid polymer[11]. The solid polymer restricted ion movement (had low ionic conductivity) at room temperature which is the essential operating temperature for the majority of electronic devices. A viable liquid electrolyte and anode combination proved more difficult to demonstrate and it took almost 10 years for the discovery of the appropriate carbonaceous materials with a low redox potential (0.3 V vs Li/Li$^+$) close to that of lithium and with high reversibility in an organic liquid electrolyte[12].

The combination of the layered transition metal oxide cathode, carbonaceous anode and organic electrolyte resulted in the first commercial Li-ion battery in 1991 from Sony Corporation with a cell potential of 3.7 V and an energy density of 180 Wh/kg[13]. The soaking/mixing of the solid polymer with liquid electrolyte resulting in polymer gel electrolytes with a practical ionic conductivity at ambient room temperature[14]. Bellcore researchers used the polymer gel electrolyte to make batteries, called plastic Li-ion (PLiON), that are thin, light and flexible and are in most smart phone devices today[14].

Today in standard Li-ion batteries, C_6 is the anode material and $LiCoO_2$ is the cathode material. These materials are not without their problems and additives, such as carbon black, are needed to improve their electrical conductivity. They also have higher manufacturing costs due to the materials air sensitivity requiring the usage of specialised assembly conditions and equipment. The electrolyte is ionically conductive for Li^+ ions and provides the environment for the charge transfer between the anode and cathode. This reaction can be extended depending on the stability window of the electrolyte and with the electrode interface. Organic electrolytes are generally used in Li-ion batteries but even they have a stability window of $\leq$ 4.2 V which is the theoretical potential for the $LiCoO_2$ reaction. The organic electrolyte decomposes on the C_6 anode forming a resistive film generally referred to as a solid electrolyte interface (SEI). Slow electrochemical kinetics at the electrolyte/electrode interface results in large internal resistance at increased charge and discharge rates. These issues are not completely resolved yet but their impact has been reduced resulting in gradually improved battery performance through the years. Substantial improvements are still required to facilitate more efficient use of renewable energy sources through grid-scale storage, EVs and at a smaller scale to enable the technology advancements for the developing internet of things (IoT) devices. To summarise, the following are some of the advantages and disadvantages of the current state-of-the-art commercial lithium ion batteries;

Advantages:

- High energy density 270 Wh/kg.
- High operating voltage 3.7 V, due to organic electrolyte
- Available in a wide range of sizes and energy densities due to the materials being scalable and lighter.
- No memory effect and low self-discharge, 0.1% per month.

Disadvantages:

- Large internal resistance resulting in large voltage drops at higher discharge rates.
- Restricted cycle life, typically <1,000 cycles.
- Higher cost.
- Safety concerns due to the use of flammable organic electrolytes.

How Batteries Operate:

A battery operates on the principle of converting chemical energy to electrical energy through an electrochemical oxidation-reduction (redox) reaction. A battery is made up of a cathode (positive) electrode and an anode (negative) electrode, separated by an electrolyte that conducts ions between the electrodes while being electrically insulating, Figure 2.4. If the electrolyte was electrically conducting the battery could not hold charge as it would self-discharge and ultimately, short circuit. The majority of lithium battery electrolytes are organic salt solutions, polymers, ceramics, fused salts and aqueous solutions of acids, bases, or salts. In low ionic conducting electrolytes such as organic salt solutions, polymers and ceramics the cathode and anode are placed as close as possible to minimise the internal resistance.
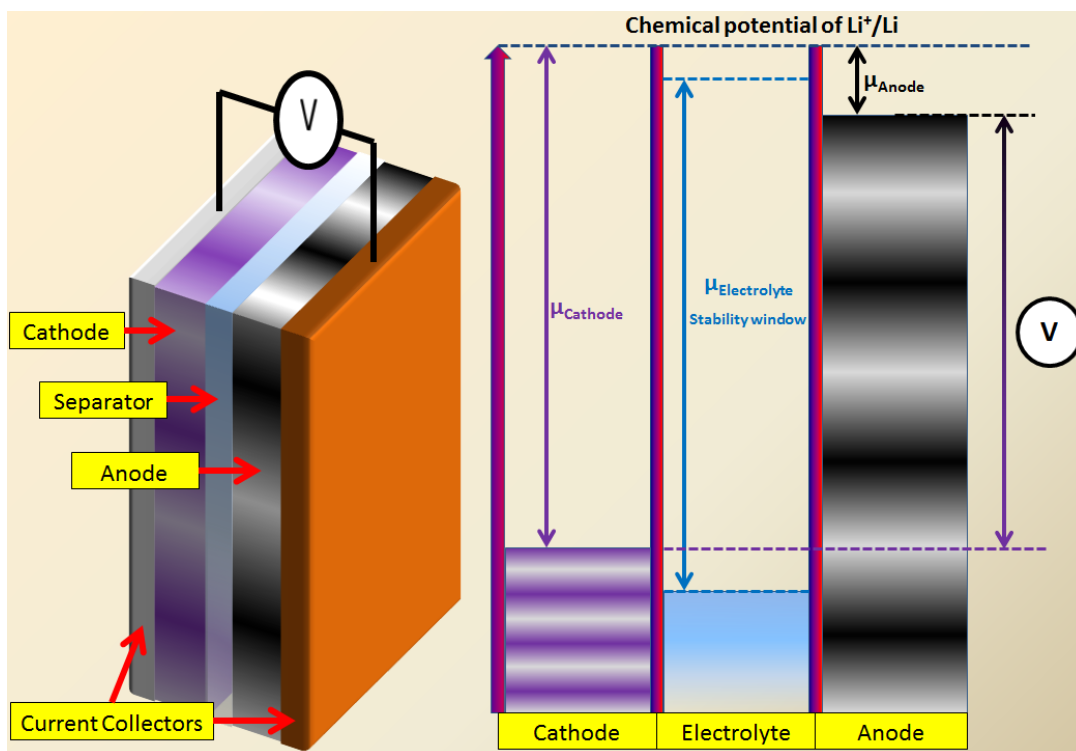
Figure 2.4: Schematics of typical battery cell and example of energy levels involved.

An internal resistance of milliohms (mΩ) is acceptable to minimise voltage drop at large currents. This low resistance is possible when the separation is at most 1 mm[15] but more typically less than 200 microns. In liquid organic salt electrolytes, the electrodes are prevented from contacting each other and short circuiting through the use of micron scale separators of electrically insulating, porous material. The pores of the separator fill with electrolyte and the ionic current is conveyed through these pores.

Both electrodes undergo a half-cell chemical reaction. During discharge the anode reaction is an oxidation as it gives up its electrons to the external circuit to do work and transfer to the cathode. The cathode undergoes a reduction reaction as it gains electrons from the external circuit. The positive ions (cations) in the electrolyte move in the towards the cathode during the discharge of a battery. The driving force for the external current supplied from the chemical reaction is the difference in the electrode potentials of the two electrodes.

Strengths of oxidizing and reducing agents are indicated by their standard electrode potentials. Materials with a positive electrode potential are used as anodes and materials with negative potential are used as cathode materials. The greater the difference between the electrode potentials, the larger the cell potential and the energy of the reactions. The most common batteries use zinc (Zn), lead (Pb) and lithium (Li) as the anode active material and a

metal oxide such as manganese (MnO_2), cobalt (CoO_2), nickel (NiOOH), or lead (PbO_2) in a higher valence state or metal halide as the active cathode material.

Cathode materials in different cell chemistries typically comprise oxides or sulphides, due to their high valence states and thus larger cell potential. The trade-off is that these materials characteristically have a low electrical conductivity meaning that the internal resistance increases with increasing load due to the restricted flow in electrons through the electrodes. The active electrode material can be mixed with conductive additives such as carbon black, to improve the pathway for the electrons but the pastes also contain an electronically insulating polymer binder. This paste is then placed on a high conductivity metal current collector such as copper, aluminium or nickel to complete the electrical connection.

OCV, Potential & Cell discharge

The difference between the potentials of the cathode and anode when there is no net current flow (equilibrium) is called the open-circuit voltage (OCV). When power is drawn from the battery it is no longer in equilibrium and the potential drops from the OCV. This drop is due to electrode overpotential and internal resistance in the cell. Electrode overpotential is made up of two parts:

1. Activation overpotential
   - The kinetic limitation of the charge transfer reaction at the electrode i.e. the activation energy that has to be reached before the redox reaction can occur.
2. Concentration overpotential
   - The differences in concentration between reactants and products at the electrode surface and bulk solution. Slow mass transfer results in the depletion of the reactants at the electrode interface due to slow diffusion from either the bulk solution, the electrode or both.

The result of the electrode overpotential is a loss in the form of heat referred to as a polarization loss. Calculating the activation and concentration overpotentials is possible when measuring the mass transfer and electrochemical kinetic data. This analysis is hindered by the addition of inactive electrochemical materials, such as binders and conductive additives, and complex electrode architectures that also vary in thickness and porosity. Internal resistance from current collectors, electrolyte and active materials results in a potential drop during operation that influences current drain and battery performance.

Internal resistance is also known as ohmic polarisation and is directly proportional to the energy drawn by the external circuit. These losses are taken into account when calculating the operational potential E.

$$E = E_o - [(\eta_{ct})_a + (\eta_c)_a] - [(\eta_{ct})_c + (\eta_c)_c] - iR_i = iR \qquad 2.1$$

The operational potential is a difference between the OCV (E_o) and the sum of the influential losses of electrode polarisation and Ohmic resistance, Figure 2.5. The electrode polarisation is made up of the charge-transfer overpotential at the anode and cathode $[(\eta_{ct})_a$ and $(\eta_{ct})_c]$ and concentration polarisation at the anode and cathode $[(\eta_c)_a$ and $(\eta_c)_c]$. The Ohmic resistance is made up of the load current (i) and the internal call resistance (R_i). Equation 2.1 can be simplified if the current is small as the drop from the OCV to the operational voltage is insignificant due to small electrode polarization losses and the majority of the available energy is accessed.

$$E = E_o - iR_i = iR \qquad 2.2$$

Reversible electrochemical reactions take place at the electrodes of a rechargeable battery. During the discharge reaction the thermodynamics at the cathode can be expressed by the following equation:

$$aA + ne \rightarrow cC \qquad 2.3$$
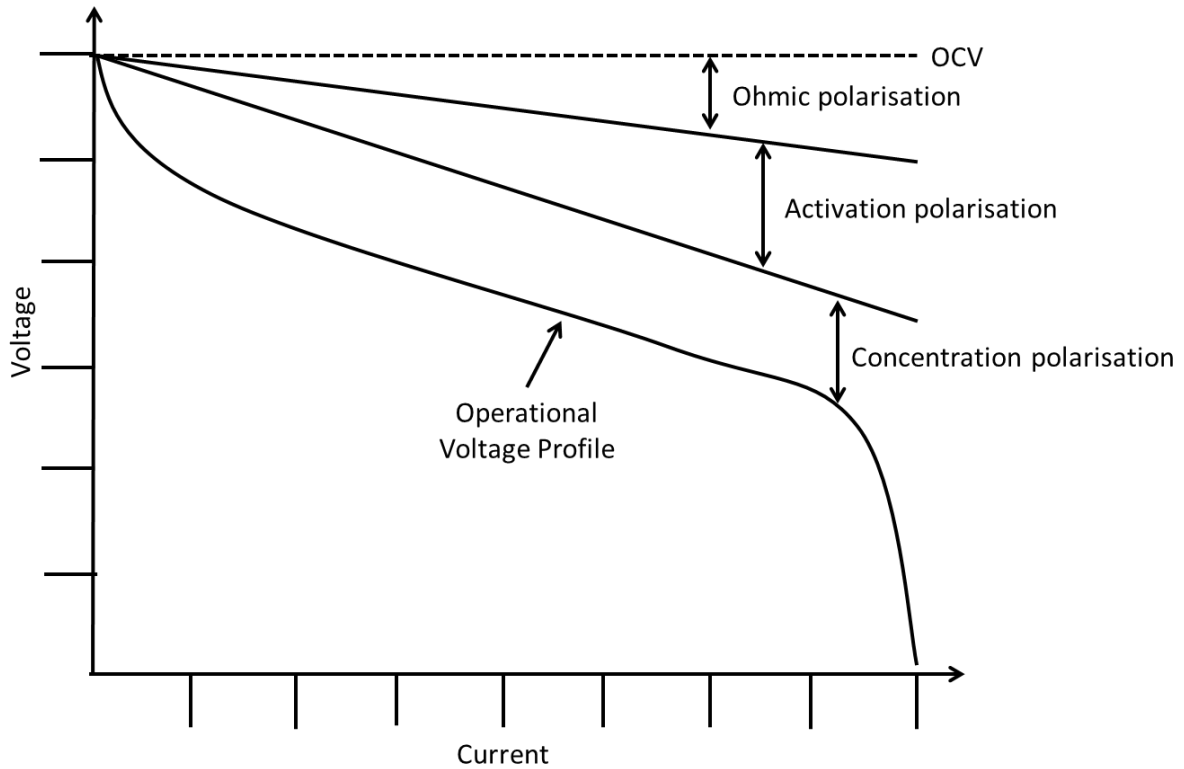
Figure 2.5: Polarisation curve.

This reaction proceeds with *a* number of *A* molecules consume *n* number of *e* electrons to reduce to form *c* number of *C* molecules.

The opposite reaction takes place at the anode:

$$bB - ne \rightarrow dD \qquad\qquad 2.4$$

b number of *B* molecules release *n* number of *e* electrons to oxidise to *d* number of *D* molecules.

The overall reaction is the combination of the two half-cell reactions that take place at both the cathode and anode.

$$aA + bB \rightarrow cC + dD \qquad\qquad 2.5$$

The half-cell reaction that takes place in lithium cobalt oxide (LiCoO$_2$), a typical Li-ion battery electrode, is shown in Equation 2.6:

$$LiCoO_2 \leftrightarrow Li_{1-x}CoO_2 + xLi^+ + xe^- \qquad (0 \leq x < 0.5) \qquad\qquad 2.6$$

For this reaction to take place, $Li_{1-x}CoO_2$ solid particles must interact with the Li-ions in the electrolyte and an electron from the current collector. The lithiation of the $Li_{1-x}CoO_2$ particles will happen first at the electrode/electrolyte interface. Diffusion of an electron and Li-ion through a $LiCoO_2$ particle will result in further discharge of the electrode and battery. Low discharging currents give more time for diffusion to take place and the battery to reach equilibrium resulting in lower concentration gradients and uniform distribution of lithiated particles within the electrode. As seen in Equation 2.1 and 2.2 the ohmic resistance plays an important role in the operational voltage as it is directly proportional to the current load. At increasing current the ohmic term becomes larger resulting in a greater deviation in voltage away from the OCV.

The driving force of a battery is the change in standard free energy (ΔG^0) in the reaction at the electrodes given by:

$$\Delta G^0 = -nFE^0 \qquad\qquad 2.7$$

F is the Faraday constant and E^0 is the standard potential. The Nernst equation is used to describe the potential E of the electrode when it undergoes a non-equilibrium reaction:

$$E = E^0 - \frac{RT}{nF} \ln \frac{a_C^c a_D^d}{a_A^a a_B^b} \qquad\qquad 2.8$$

R is the gas constant, T is the absolute temperature and a_i is the activity of the electrode species. The amount of electrical energy a battery can produce per mass or volume depends on the conversion of chemical energy stored in the electrode:

$$\Delta G^0 = -xnFE \qquad\qquad 2.9$$

Where x is the molar quantity of the active materials involved in the reaction.

The storage capacity is measured as the amount of current drawn/acquired timed by the number of hours it can deliver/receive until a chosen cut-off voltage. The SI unit for battery capacity is ampere-hour (Ah) and 1 Ah is 3600 coulombs. Since capacity is dependent on the voltage cut-off point the discharge/charge rate has a critical role in its value. The potential losses due to electrode and ohmic polarisation result in a voltage drop and are also dependent on discharge/charge rates, Figure 2.6. As a result, less current can be drawn/acquired which leads to a smaller capacity or energy available. The SI unit for energy joules (J) which is

24

equivalent to 1 watt per second. The energy in a battery is described using the units of watt-hour (Wh) (3.6 kJ), or operational voltage times the capacity (Wh = V x Ah).
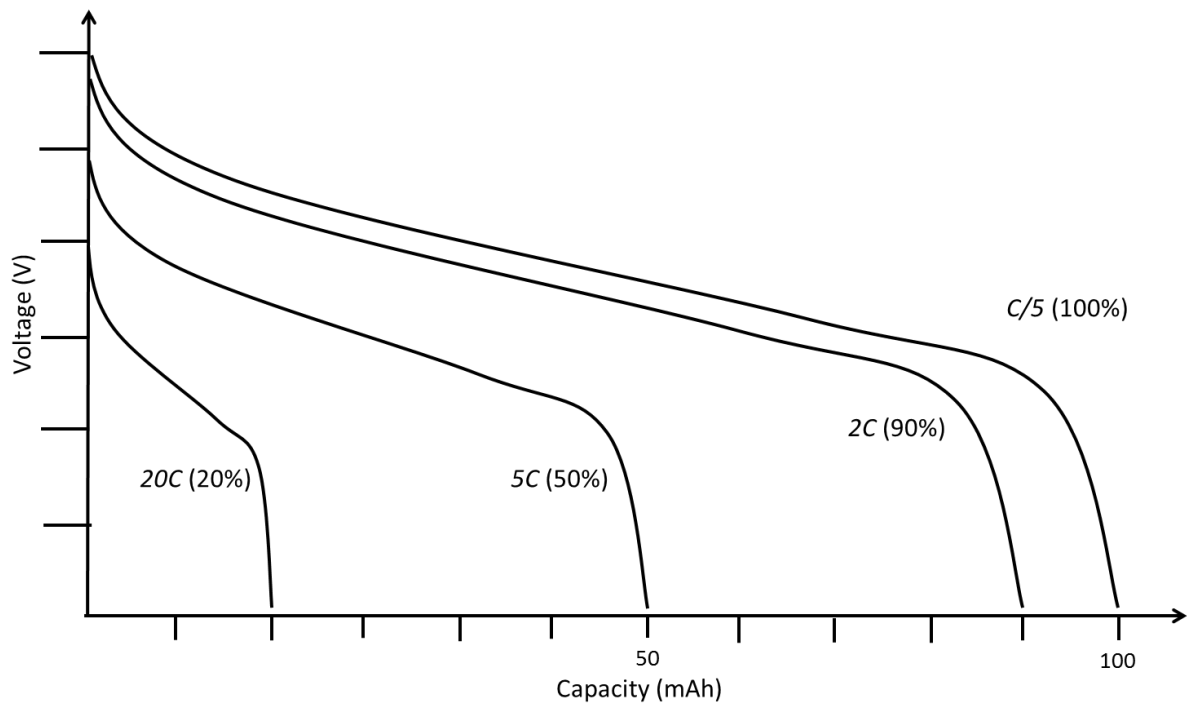

Figure 2.6: Typical effect of C-Rate on discharge curve and capacity.

Discharge/charge rates are determined from the specific capacity of the battery. For a battery with a specific capacity of 100 mAh, a 5 hour discharge/charge rate or current would be 20 mA. To simplify the expression of discharge/charge rates a C-rate is defined (C/t), as the discharge/charge time in hours. For the above example the discharge/charge rate would be $C/5$ for a 5 hour rate. For the same battery a 30 minute discharge/charge would be *2 C* rate meaning a *200* mA current. In practice a discharge/charge rate of *2 C* would typically result in a shorter discharge/charge time than 30 minutes due to the losses incurred at higher discharge/charge currents.

C-rates are also used when considering individual electrode reactions. The theoretical capacity of the electrode materials are used to determine the discharge/charge rates. Using Faraday's constant F, theoretically one molar mass of active material per electron transfer in the redox reaction produces 96,485 Coulombs C or 26.8 Ah.

The overall reaction in a typical Li-ion battery of $LiCoO_2$ and graphite (C_6) is given below:

$$Li_xC_6 + Li_{1-x}CoO_2 \rightarrow LiCoO_2 + C_6 \qquad (0 \leq x < 0.5) \qquad 2.10$$

25

To calculate the theoretical capacity and energy of the full battery the capacity of the individual electrode must first be known:

$Li_{1-x}CoO_2$ (assuming x = 0.5)

$$Molecular\ weight\ (Mw): 97.87\ g/mol$$

$$Molar\ mass: \frac{Mw}{(1-x)} = \frac{97.87\ g/mol}{0.5} = 195.74\ g/mol$$

$$Theoretical\ Capacity: \frac{nF}{Molar\ Mass} = \frac{(1)(96485\ C/mol)}{195.74\ g/mol} = 492.92\ C/g$$

$$Ah = \frac{C}{3600} \therefore \frac{492.92\ C/g}{3600} = 0.13692\ Ah/g = 136.92\ mAh/g$$

C_6

$$Molecular\ weight\ (Mw): 72.06\ g/mol$$

$$Theoretical\ Capacity: \frac{nF}{Molar\ Mass} = \frac{(1)(96485\ C/mol)}{72.06\ g/mol} = 1338.95\ C/g$$

$$Ah = \frac{C}{3600} \therefore \frac{1338.95\ C/g}{3600} = 0.37193\ Ah/g = 371.93\ mAh/g$$

$LiCoO_2$ is the rate limiting electrode with 136.92 mAh/g

$$Minimum\ amount\ of\ C_6\ per\ LiCoO_2: \frac{136.92}{371.93} = 0.36\ g$$

$$Theoretical\ Capacity\ of\ Full\ Battery: \frac{136.92}{1+0.36} = 100.10\ mAh/g$$

$$Theoretical\ Energy\ of\ Full\ Battery\ 3.7\ V: 100.10\ x\ 3.7 = 370.38\ mWh/g$$

The chemistry of the total battery system determines the amount of energy that can be utilised. Once electrode materials are chosen that can theoretically provide the required energy other factors that must be considered include the reaction kinetics, diffusion rate and quantity of energy accessed, electrode architecture, cell design, electrolyte stability, electrolyte conductivity, separator and current collector stability.

Current distribution can have a significant influence on the performance of the battery. Primary current distribution is the simplest condition in which it only depends on the geometry of the electrochemical system and the current does not substantially affect the voltage. The voltage at a particular current depends only on the ohmic drop or the conductivity of the electrolyte and the distance between the cathode and anode. If the electrolyte has a high ionic conductivity the distance between the electrodes has little or no effect and uniform current distribution is achieved with an insignificant ohmic drop.

At low ionic conductivities, secondary current distribution is observed and the distance between the electrodes becomes an influential factor resulting in overpotentials within the electrolyte and at the electrode/electrolyte interface. Primary and secondary current distributions are identical for a high ionic conductive electrolyte. The overpotentials to be considered at the electrode/electrolyte interface are charge transfer, diffusion and crystallisation. Charge transfer overpotential can occur during the transfer of electrons from the electrode to the ions in the electrolyte, whereas diffusional overpotential depends on the ionic coordination in the electrolyte supplying the ions to the electrode. Crystallisation overpotential depends on the crystallisation energy required to nucleate a new material on the electrode.

Significant changes in the electrolyte composition and ionic strength over the course of the electrochemical reaction have a direct impact on ionic supply. These changes are taken into account in tertiary current distributions as well as the ohmic drop in the electrolyte and the overpotentials at the electrode/electrolyte interface. The Nernst-Planck equation is solved for each of the chemical species that undergo diffusion, migration and convection (mass transport) in the electrolyte. Electroneutrality is approximated for each of the species concentrations. All ions and electroactive species are accounted for in tertiary current distributions as the kinetic expressions for the electrochemical reactions account for both the activation and concentration overpotential. This means that the rate of reactant consumption at the electrode/electrolyte interface results in the transport of reactions to the interface being a rate limiting factor for the electrolysis reaction. Unlike primary and secondary current distributions the electrolyte current density is not assumed to follow Ohm's law, which results in concentration variations in the electrolyte no longer being neglected. The current density at the electrode/electrolyte interface is expressed as a function of the overpotentials and the concentration of the electroactive species at the interface.

Anode materials

Intercalation

Carbon

Carbon is the most common anode used in Li-ion batteries today. Carbon can be found in a number of different structures in nature. The carbon type of interest for Li-ion batteries is graphite, which has an ABAB layered structure as seen in Figure 2.7, and coke, which is an amorphous carbon with a high surface area. Lithium ions are able to intercalate between the carbon planes in graphite which involves a transformation to a AAAA structure over a number of phase changes giving a unique voltage profile[16]. Lithiated graphite has a composition of LiC_6 with a capacity of 372 mAh/g and has been well studied[17]. Coke is amorphous and as such has fewer ABAB layers present than graphite but this is offset somewhat by the occurrence of lithiation also between the crystalline particles. Overall the composition of lithiated coke is half that of graphite, $Li_{0.5}C_6$. Carbonaceous anodes have lithiation potential close to that of lithium metal (0.3 V vs Li/Li^+) which allows for a large battery voltage however this also means there is a greater chance of lithium metal plating in the event of cell overcharge and the safety implications associated with lithium metal plating mentioned previously.
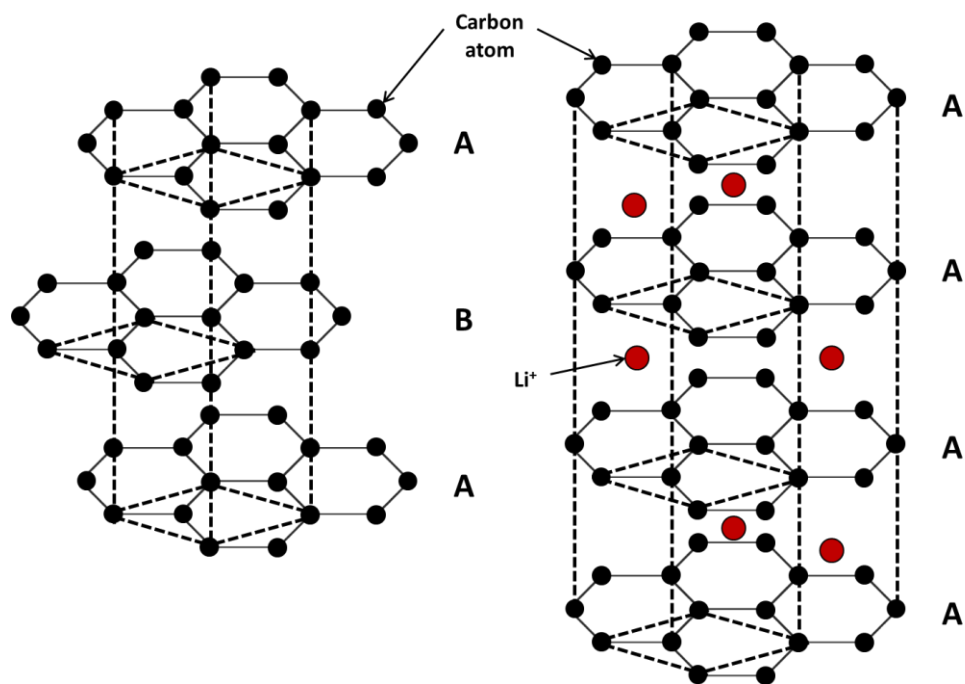

Figure 2.7: Graphite misaligned ABA layered structure and aligned AAAA lithiated layered graphite structure.

28

In the first cycle of graphite lithiation the capacity value measured is larger than the theoretical capacity of LiC_6. This extra capacity in the first cycle can be assigned to the partial electrolyte decomposition to form a passivation layer on the graphite surface as seen in Figure 2.8. The passivation layer inhibits further electrolyte decomposition but also increases the resistance of the electrode, restricts Li^+ ion movement and consumes lithium meaning less electrochemical active lithium all of which results in poorer cell performance. The passivation layer is commonly referred to as a solid electrolyte interphase (SEI).
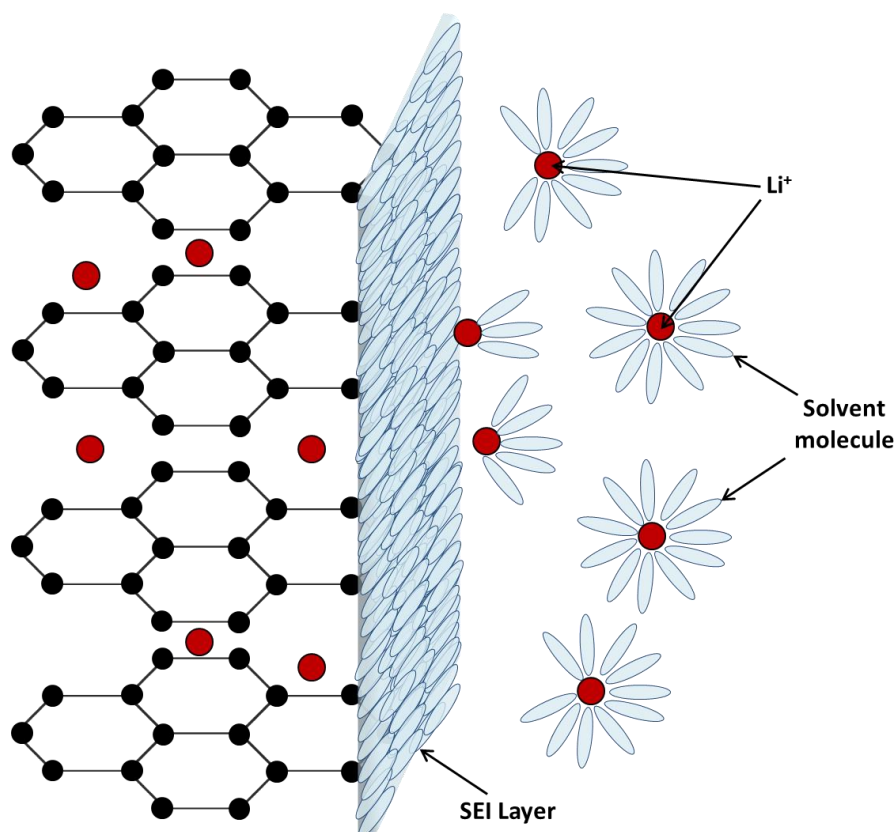
Figure 2.8: SEI formation on graphite is made up of decomposed electrolyte solvent and salts.

The irreversible capacity used in the formation of the SEI layer is proportional to the specific surface area[18]. The surface area should be minimised to prevent excessive irreversible capacity, however, large particles are kinetically undesirable. Spherical shaped graphite particles are used in commercial graphite anodes in a trade-off between surface area and the diffusion path for the Li^+ ions.

Commercial graphite producers have recently published information on the use of a carbon coating on the graphite to inhibit exfoliation and minimise surface area[19]. Metal coatings of the graphite active anode material have also been investigated and shown to improve cycle stability and capacity[20]. The improved performance is ascribed to the SEI layer forming on

the metal coating surface and a decrease in the SEI layer formed on the graphite resulting in an increase in Li^+ ion reaction rate.

Lithium titanate
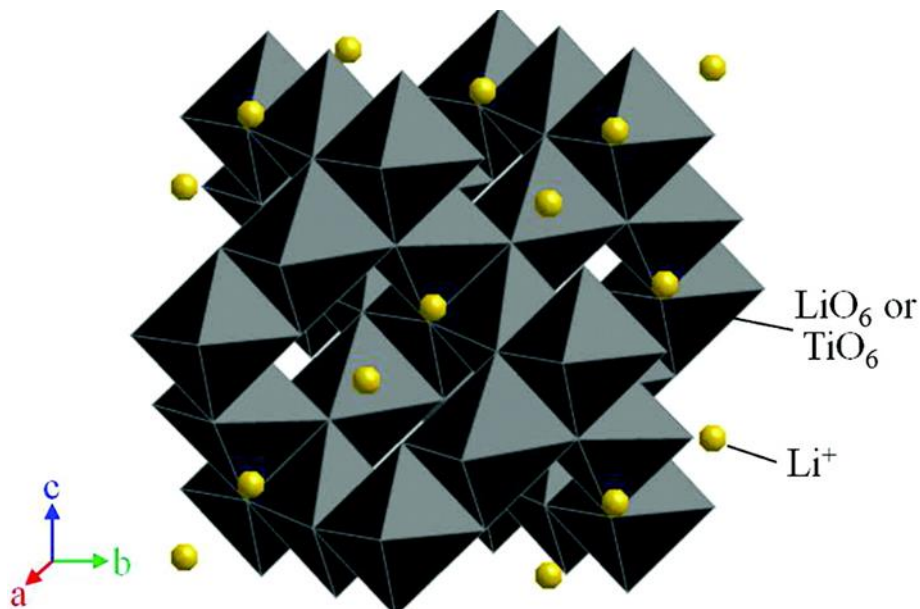
Figure 2.9: Schematic representation of the crystal structure of spinel-typed $Li_4Ti_5O_{12}$. (Reproduced)[21]

Lithium titanate ($Li_4Ti_5O_{12}$) (LTO) is an alternative to graphite as an anode material for Li-ion batteries[21]. The advantages that LTO has over graphite are an extremely long cycle life and significantly better safety properties. The improved safety properties come as a trade-off in battery voltage as lithiation of LTO occurs at a much higher redox potential (1.55 V vs Li/Li^+). The operational capacity of LTO is almost half that of graphite (175 mAh/g) and together with the higher redox potential results in Li-ion batteries with lower energy density by comparison with its graphite anode counter-parts. LTO has a spinel structure like the cathode material lithium manganese oxide ($LiMn_2O_4$) but with lithium ions occupying only some of 16d sites. The first studies of LTO where carried out by Murphy et al., Dahn et al. and Ohzuku and showed during cycling there is a coexistence of two phases, LTO is the starting material and $Li_7Ti_5O_{12}$ being the fully lithiated phase[8a, 22]. Their coexistence is believed to be the reason why LTO has extremely long cycle life as both phase have the same lattice constant and no volume change resulting in a zero-strain lithiation process.

Alloying

Metals that can alloy with lithium and have superior capacity over the standard graphite anode, were first applied by Matsushita in the 1980s[23]. Metals such as Bi, Pb, Sn, and Cd were used in commercial cells but their poor cycle life due to volume expansion during charging/discharging caused mechanical instability which led to delamination, cracking and pulverisation of the active material and delamination from the current collector and conductive binder[24]. To combat such problems the most frequently used remedies are to permit the materials to "breath" by providing space around the active material to expand and making protective conductive coatings to ensure a good electrical contact with the current collector even after multiple cycles in which volume expansion occurs[25]. Silicon (Si), germanium (Ge) and tin (Sn) have theoretical gravimetric capacities of 4200, 1624 and 993 mAh/g and volumetric capacity of 9783, 8645 and 7272 mAh/cm^3, respectively[26]. These advantages have the potential to significantly impact the next generation of lithium batteries, Figure 2.10.
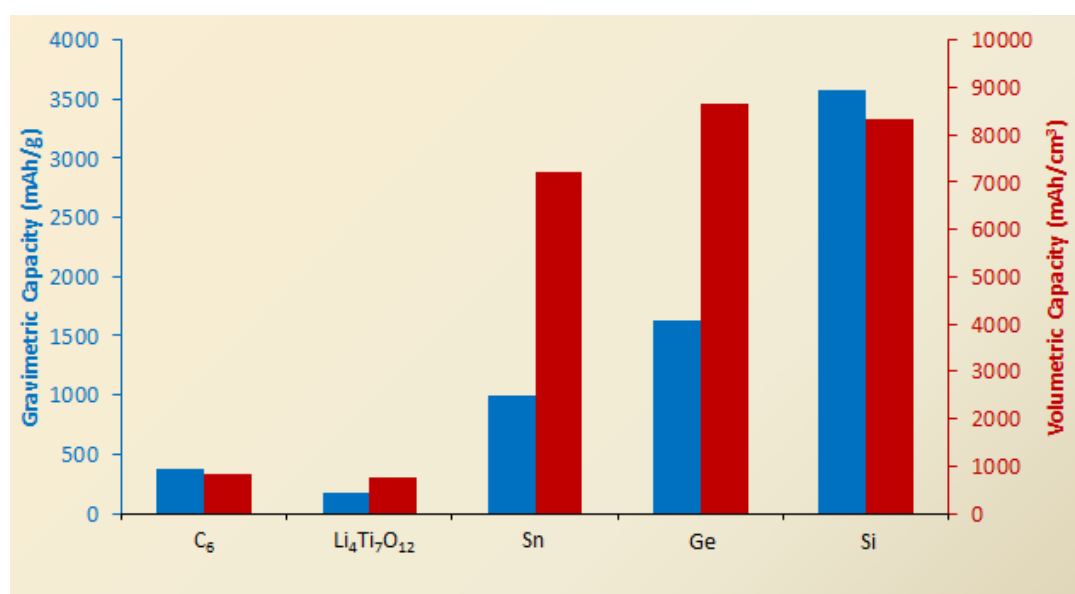
Figure 2.10: Theoretical capacity of anode materials[18, 23, 27].

Silicon

Si is the most attractive material to replace graphite not only because it has 11 times the gravimetric and volumetric capacity of graphite but also because it is the second most abundant material on earth[27]. The amount of Li that can alloy with Si is based on the final lithiated product of $Li_{22}Si_5$ following a range of intermediates during lithiation, specifically $LiSi$, $Li_{12}Si_7$ and $Li_{13}Si_4$[28]. The electrochemical lithiation process of an Si anode at room

temperature undergoes a solid state reaction with a smooth phase transition from crystalline to amorphous, as revealed from the galvanostatic profile which is dissimilar to the step profile seen in heat formed Li_xSi, Figure 2.11[29]. The Gibbs free energy needed to form the crystalline and amorphous Li_xSi is calculated using density functional theory (DFT) and gives an explanation for the difference seen between the heat formed and electrochemically formed Li_xSi[30]. It is more favourable to form an amorphous Li_xSi (a-Li_xSi) during electrochemical lithiation at room temperature in comparison to the lithiation process of crystalline Li_xSi which is kinetically unfavourable at room temperature. The phase transformation of Si during the electrochemical lithiation showed that the final lithiated Si composition is $Li_{15}Si_4$ (3575 mAh/g and 8338 mAh/cm^3) and not the $Li_{22}Si_5$ composition as first thought[31].
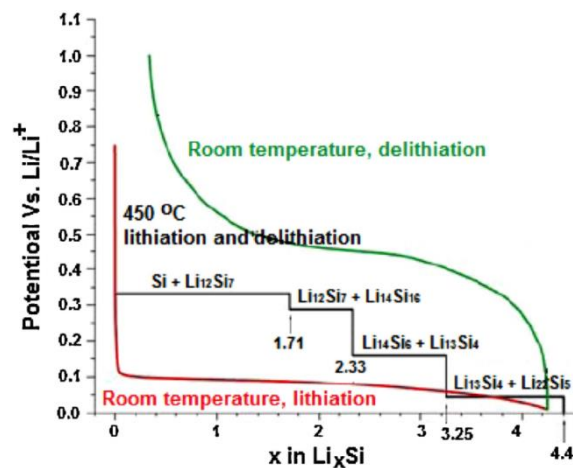
Figure 2.11: Si electrochemical lithiation and delithiation curves at room and higher temperature. Black line: theoretical voltage curve at 450°C. Red and green line: lithiation and delithiation of crystalline Si at room temperature, respectively. (Reproduced)[29]

Ongoing research has contributed significantly to the ability to design and fabricate nanomaterials for battery applications. Nanoarchitectures such as nanowires and core-shell nanotubes have been shown capable of alleviating the volume expansion of 300% for $Li_{3.75}Si$[32]. Si nanoarchitectures and nanoparticles are now better understood with respect to the lithiation process and the mechanical stress in the Si nanoarchitectures and nanoparticles resulting in key design criteria. Liu et al. assessed the effect that nanoparticle size has on the cycle life using in-situ transmission electron microscope (TEM) analysis[33]. The critical diameter was found to be 150 nm for crystalline Si meaning that diameters below this parameter would undergo volume expansion without cracking and pulverisation, Figure 2.12. The prevention of cracking and pulverisation results in a reduction in the amount of freshly

exposed Si and an increase in cycle life which is attributed to less SEI layer formation reactions. Electrolyte consumption is slowed down however the SEI layer continues to increase which increases Li diffusion length and resistance, all of which are detrimental and limit the cycle life of the Si electrode[34].

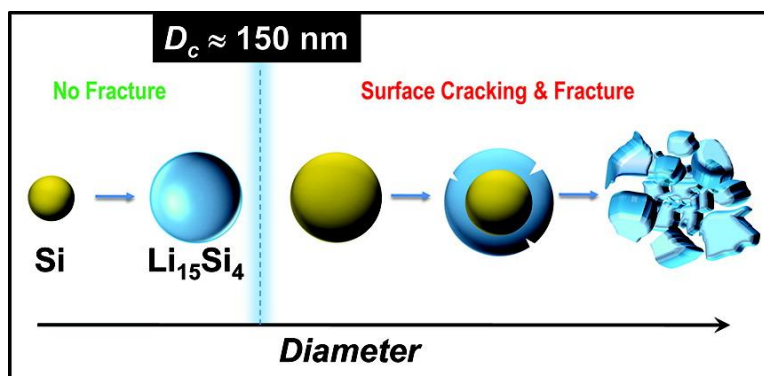**Figure 2.12:** Critical diameter for Si nanoparticles. (Reproduced)[33]

Typically Si nanowires and nanotubes fabricated are crystalline Si (c-Si). The lithiation of c-Si anode starting material results in a natural core-shell structure due to the formation of a-Li_xSi as shell and c-Si as the core. The difference in structures due to lithiation forms a stress-induced interface between the a-Li_xSi and c-Si that can lead to fracture of the nanowires[35]. c-Si nanowires prefer to undergo volume expansion in the <110> direction when being lithiated as that plane is desirable for Li^+ ion diffusion due to lower surface energies[36]. If a c-Si nanowire is not in the preferred <110> orientation during lithiation, it can result in mechanical instability and cleavage of the nanowire e.g. <112> c-Si nanowire[37]. The fabrication of vertically aligned Si nanowires was published by Chan et al. in 2008 with the use of chemical vapour deposition (CVD)[32]. The one-dimensional (1D) nanowires were fabricated using a vapour-liquid-solid (VLS) mechanism from CVD, where Si nanowires where grown template-free directly onto stainless steel using a gold (Au) catalyst, Figure 2.13. They demonstrated a capacity of 4,277 mAh/g at *C/20*. The electrode performance is attributed to the excellent adhesion to the stainless steel current collector due to the fabrication process and the substantial porosity of the Si nanowire allowing for mechanical stability. The process used by Chan et al. is not ideal as the Au catalyst is expensive, a poor electrochemical active material and large density with an unfavourable impact on the overall Si-Au electrode capacity however it provided a proof of concept and is the foundation behind the use of a tin catalyst to fabricate nanowires using high boiling point solvent syntheses[38].
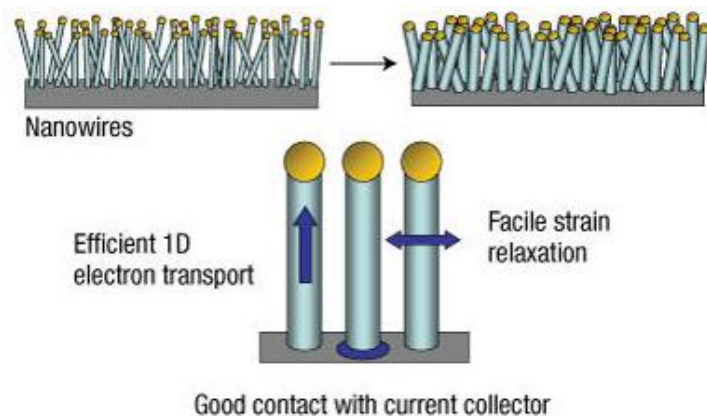
Figure 2.13: Schematic of morphological changes that occur in Si nanowires during electrochemical cycling. (Reproduced)[32]

Critical material parameters such as electrical conductivity and ion diffusion need to be considered when designing and fabricating electrodes. Si has a relatively low electronic conductivity and ion diffusion coefficient of $\sim 10^{-3}$ S/cm and $\sim 10^{-12}$ cm^2/s respectively[39]. These parameters have a significant effect on the transfer kinetics and not all of the Si active material is utilised at high charge/discharge rates. Nanoarchitectures and nanoparticles can accommodate these relatively low values and utilise more of Si material at high charge/discharge rates in comparison to a bulk Si electrode. The effect of Li$^+$ ion diffusion can be described by the following equation[40]:

$$\tau \sim \frac{L_{ion}^{2}}{D_{ion}} \qquad\qquad 2.11$$

where τ is the time it takes for Li$^+$ ion to diffuse into the active material, L_{ion} is the diffusion length of the active material and D_{ion} is the Li$^+$ ion diffusion coefficient of the active material. Equation 2.11 shows that nanosized materials significantly reduce the diffusion time of materials with a low diffusion coefficient being proportional to the square of the diffusion length of the active material.

Novel work by Wu et al. has addressed many of the problems that are typical of Si anodes[41]. The use of an inactive coating on the outer layer of the Si nanotubes acts as a mechanical support to the nanotube structure while also allowing Li$^+$ ions to pass through. The inactive SiO$_x$ layer protects the electrolyte from having direct contact with the active Si layers. This means that a stable SEI with little or no cracking and non-continuous growth is formed on the SiO$_x$ outer layer unlike a typical SEI layer formed on Si. The use of a nanotube design also gives space for the Si to expand inwards and "breath" during lithiation as the SiO$_x$ restricts

expansion outwards and provides mechanical support. This design is called the double-walled Si-SiO$_x$ nanotubes (DWSiNTs). They showed in Figure 2.14 that cycling DWSiNTs at *C/5* rate for 900 cycles had a specific reversible capacity of 1780 mAh/g with capacity retention at 94% after 500 cycles and 76% after 900 cycles. A higher charge/discharge rate of *12 C* was used for ultra-long cycling of 6,000 cycles revealing capacity retention of 93% and 88% after 4,000 and 6,000 cycles, respectively.
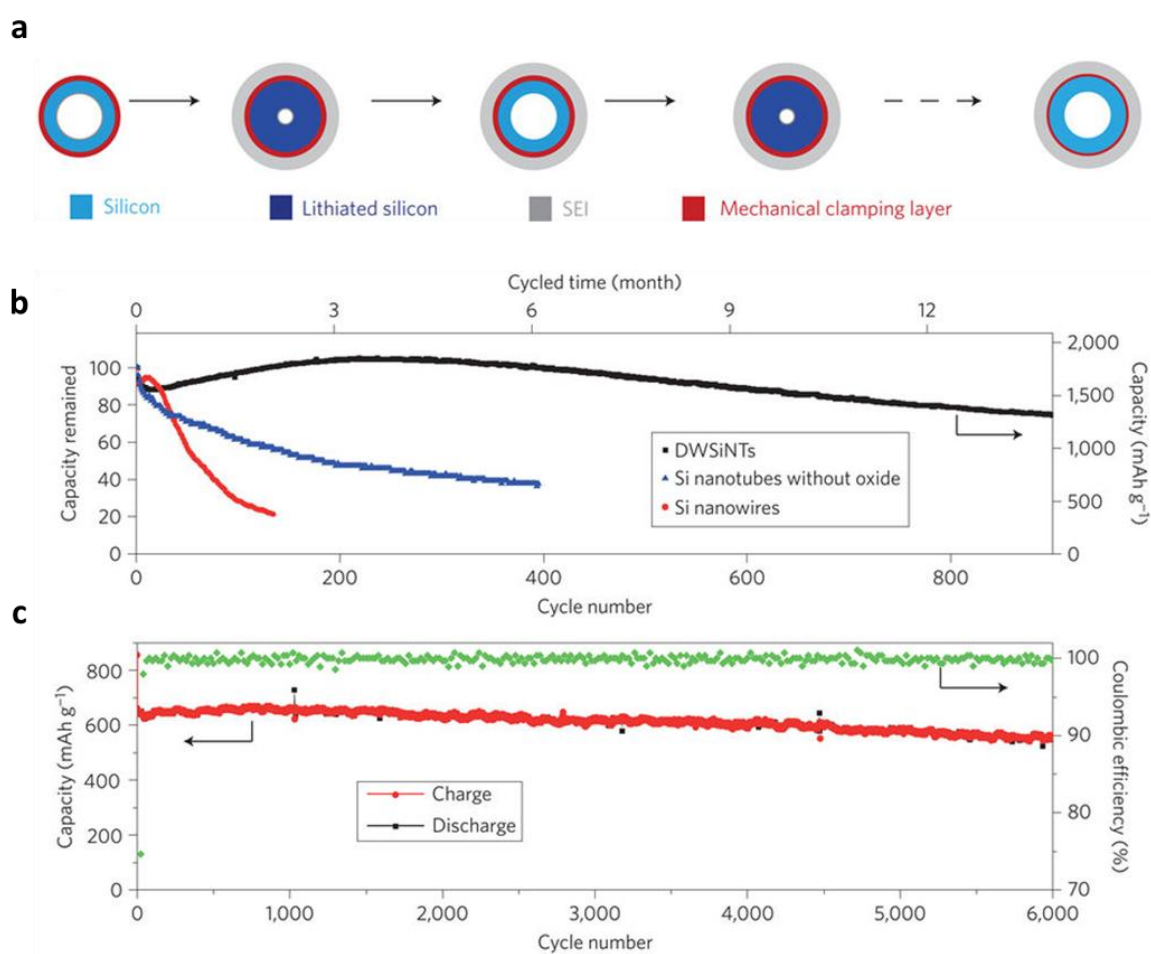
Figure 2.14: a, Designing a mechanical constraining layer on the hollow silicon nanotubes can prevent silicon from expanding outside towards the electrolyte during lithiation. As a result, a thin and stable SEI can be built. **B,** Capacity retention of different silicon nanostructures cycled at the same charge/discharge rate of *C/5*. **C,** Lithiation/delithiation capacity and columbic efficiency of DWSiNTs cycled at *12 C* for 6,000 cycles. (Reproduced)[41]

For the future development and the eventual commercialisation of Si based anodes there needs to be a balance between the ultra-long cycle life, scalability, cost of manufacturing and practical volumetric energy densities. The DWSiNTs design has proven a lot of concepts and solutions to problems associated with Si anode materials however the low loading of 0.02 –

0.1 mg/cm^2 and CVD fabrication process present their own challenges. Although nanoparticles and nanoarchitected Si anodes fabricated from CVD have impressive electrochemical performance, the CVD fabrication process suffers from the requirement for expensive gaseous precursors such as silane (SiH$_4$) and disilane (Si$_2$H$_6$) with a low product yield. These limitations have hampered the production of such Si anodes. A recent review paper by Xu et al. with a particular focus on the fabrication process on Si anodes using CVD, ball milling (BM), metal-assisted chemical etching (MACE) and magnesiothermic reduction (MR) explains the fabrication process and the effect the process has on the electrochemical performance[42]. It is worth noting that MR shows the most potential due to its low processing cost and raw materials, easy scalability and the ability to produce a range of Si anode nanoarchitectures on a large and sustainable scale. Both BM and MACE are scalable processes however they are limited to nanoparticle preparation and are not considered environmentally friendly processes.

A typical lithium battery composite electrode uses particles of active materials mixed with a conductive carbon material and polymer binder. Si carbon composites have been extensively studied and acknowledged as a potential strategy to control volume expansion and form a stable SEI layer[43]. Carbon is a ductile, elastic and conductive material which allows for the Si active material to expand without fracture, preserve mechanical integrity and maintain a robust conductive contact. Carbon also forms a stable SEI layer in standard organic electrolytes resulting in minimal electrolyte consumption. Cycling of 3D silicon porous materials mixed in a carbon and polymer matrix has been shown to provide an improved electrochemical performance. The major issue with this approach is the low rate capabilities due to the thick carbonaceous matrix. Impressive work has been performed by Li et al. who fabricated a porous Si microparticle with a thin carbon coat and no carbon coating within the pores, Figure 2.15[44]. The resulting design showed better performance than if the microparticle was coated in the pores or not coating at all. The non-filled porous micro Si particles allowed for the Si to undergo volume expansion within the pores with the carbon coating giving structural stability and restricting SEI formation to its outer surface. A low current density of *C/20* (*1 C* = 4,200 mA/g) was applied for the first 4 cycles to form a stable SEI layer with an initial cycle capacity 1798 mAh/g. A current density of *C/4* was applied from the 4th to the 1,000th cycle to give a stable capacity of 1,490 mAh/g.
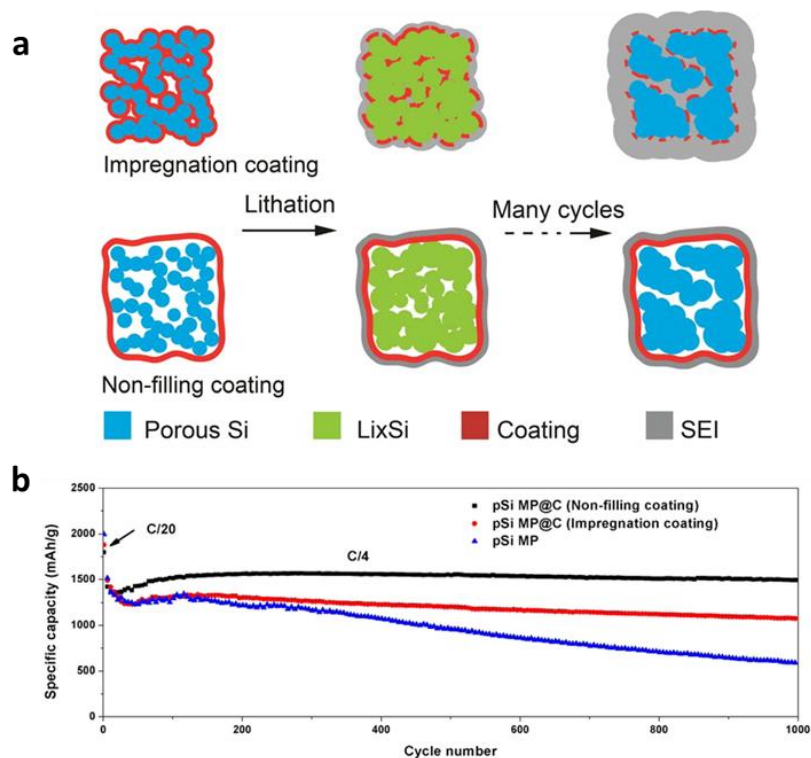
Figure 2.15: a, Schematic of coating design on mesoporous Si microparticles (pSiMPs) and their structural evolution during cycling. **b,** Reversible delithiation capacity for the first 1000 galvanostatic cycles of the pSiMPs with different coating. The active material loading was around 0.5 mg/cm^2. (Reproduced)[44]

A summary of the key design criteria required for Si anodes are:

1. Critical dimension of the Si nanoparticles below which cycling is stabilised.
2. Porous materials increase the rate capabilities due to an increase in surface area and cycle life as the pores allow the nanoarchitectures to maintain their structural integrity.
3. The formation of a stable SEI layer is critical to the cycle life. This can be done by using electrolyte additives, inactive coatings or conductive coatings.

More research is needed to understand the process of lithiating Si, volume expansion, how the electrolyte and electrolyte additives react in forming the SEI layer on the surface and how surface coatings react with the electrolyte to form an SEI layer to improve mechanical stability. However, the shorter diffusion lengths and increase in surface area of nanoparticles and nanoarchitectures have enabled the advancement and commercialisation of Si as an anode material is closer to reality.

Germanium

Ge has similar physical and chemical properties to Si which is attributed to the four valance electrons that result in the formation of the same crystal structure. Ge is a face centred cubic crystal (FCC) and has lattice parameters of a = b = c = 565.75 pm, $\alpha = \beta = \gamma = 90^o$. Ge suffers from the same mechanical instability during lithiation as Si due to large volume expansion ($\sim$300%)[26b, 32]. The mechanical instability not only results in delamination from the current collector but also cracking of the SEI which results in the formation of more SEI layers on freshly exposed anode material and consumption of electrolyte[45]. Ge is more expensive than Si and has a lower theoretical gravimetric capacity of 1,624 mAh/g but a similar volumetric capacity of 8,645 mAh/cm^3. However, Ge has some very attractive materials properties that make it an ideal candidate for a high capacity, high power anode material especially if volume is at a premium. Ge has an electronic conductivity 10,000 times greater than Si due to its smaller band gap of 0.66 eV versus 1.12 eV at 300 K and has a Li$^+$ ion diffusion coefficient that is 400 times faster than Si[46]. The superior transport properties of Ge over Si and graphite allow for fast transport of both electrons and Li$^+$ ions to realise high charge/discharge rates and efficient charge transport[47]. There has been a significant increase in the number of papers published on the use of Ge based materials for lithium ion battery application. With the improvements in production technology for Ge and its widespread developing usage in solar cells, polymerization catalysts, phosphors, metallurgy and chemotherapy it is expected that the cost will drop in the future[48].

Understanding the lithiation process of Ge is critical in designing nanoarchitectures to solve and inhibit the problems caused by volume expansion and unstable SEI layers. Graetz et al. were among the first to investigate the lithiation process by depositing a nanosize thin film of 60 nm amorphous Ge using e-beam evaporation, Figure 2.16[49]. Ex-situ XRD was used to examine the lithiated Ge at 0 V (vs Li/Li$^+$) and after delithiation at 1.5 V. The amorphous Ge transformed to crystalline Li$_{22}$Ge$_5$ when lithiated to 0 V and showed a mixture of crystalline and amorphous phases upon delithiation to 1.5 V. The differential capacity plots show multiple peaks which indicate multiple phases of Li$_x$Ge are formed during lithiation. A stable capacity of 1,700 mAh/g was obtained at a *C/4* charge/discharge for 60 cycles. The rate capabilities were also tested with a lithiation rate of *C/2* and a discharge rate of *1,000 C* for 35 cycles. The charge and discharge capacity had good overlap indicating good cycle efficiency with an initial discharge capacity of 800 mAh/g and the 30th cycle giving a capacity of 500 mAh/g or a 35% capacity fade that is thought to be due to the extreme cycling

conditions. Even though the capacity fade is large, the fact that 800 mAh/g capacity is obtained at a *1,000 C* discharge rate (~3.6 sec) shows the potential of Ge as a high power anode material.
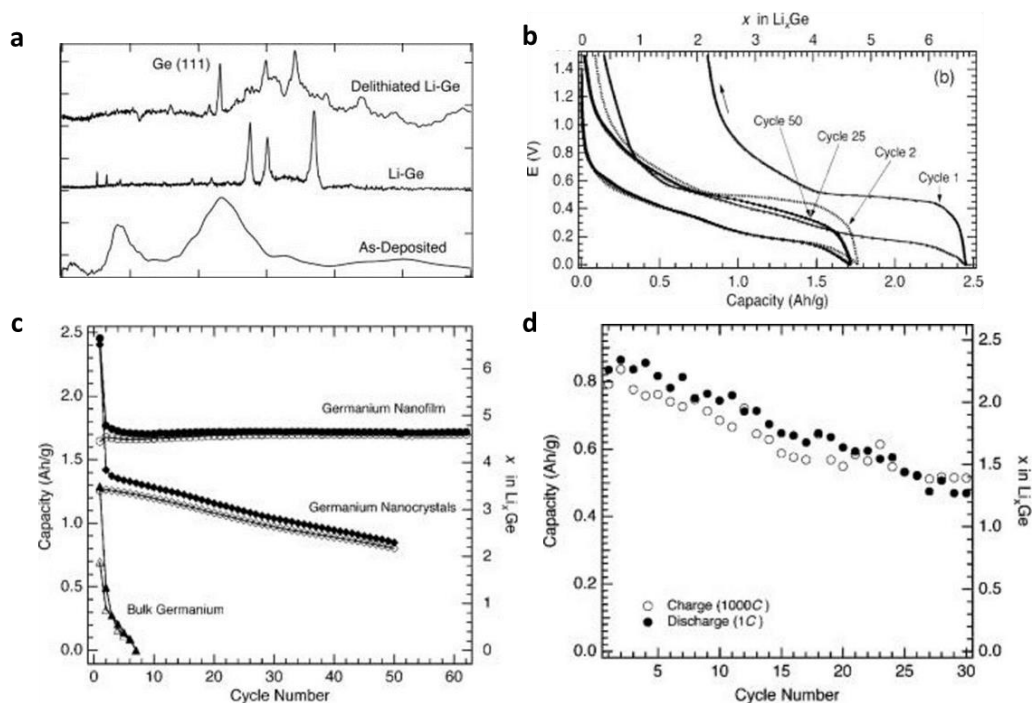
Figure 2.16: a, XRD patterns of the as-deposited, electrochemically lithiated, and electrochemically delithiated electrodes. **b,** Voltage profiles cycled at a rate of *C/4*. **c,** Cycle life of nanofilm, nanocrystals and bulk crystalline germanium. **d,** Cycle life of nanofilm germanium at a lithiation rate of *1 C* and a delithiation rate of *1000 C*. (Reproduced)[49]

Laforge et al. performed extensive electrochemical analysis on rf sputtered Ge with a variety of thicknesses and compared the effect of doping on electrochemical performance, Figure 2.17[50]. They showed that either p or n-doped Ge had improved electrochemical performance with n-doping showing the best result indicating a direct correlation between increased conductivity and cycle life. During CV profiling of a 200 nm amorphous Ge film a broad delithiation peak at 0.4 V seen in the initial cycles was replaced with a sharp peak at 0.6 V after 5 cycles. That sharp peak appears sooner with decreasing Ge film thickness, Figure 2.17a, which is attributed to a compression stress level decrease with decreasing film thickness. A peak at 0.6 V only appears during the first cycle during lithiation because of the formation of a stable SEI layer. An initial capacity value of 1660 mAh/g was achieved for the first cycle with a $Li_{22}Ge_5$ phase and stabilised at 1470 mAh/g for the remaining cycles with capacity dropping after 100 cycles due to extensive cracking and delamination of the Ge from the current collector.

Figure 2.17: a, CV achieved from the third cycle on Ge for several thicknesses. **b,** Cycling life of Ge coatings for several thicknesse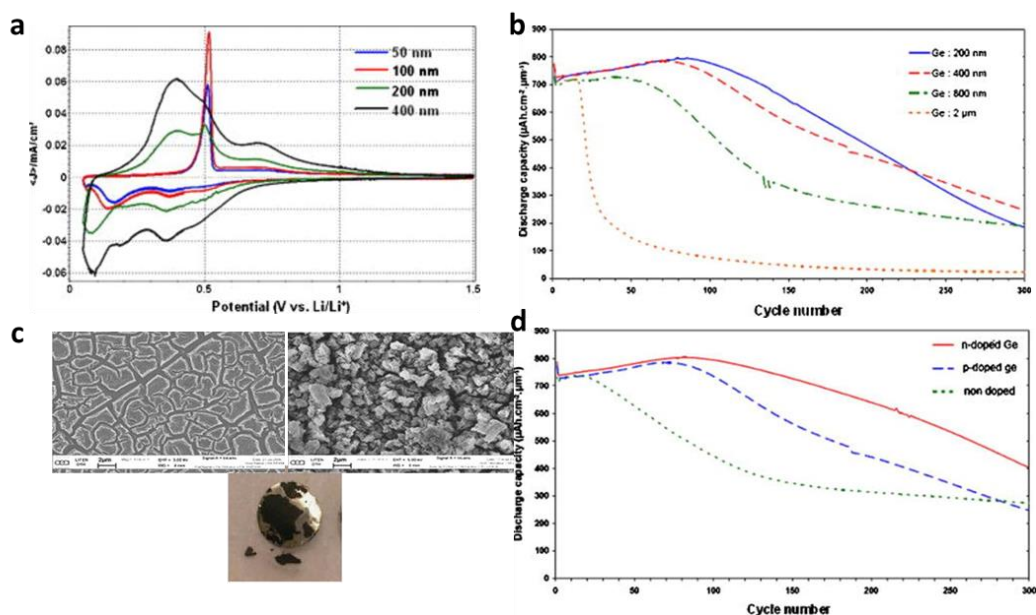s. **c,** SEM of germanium films after 10 and 110 discharge/charge cycles and optical image of the sample after 300 cycles. **d,** Influence of the doping on the cycling life of a 400 nm Ge. (Reproduced)[50]

A similar sample of 200 nm and 50 nm amorphous Ge (a-Ge) deposited by both evaporation and sputtering, was studied by Baggetto et al. using in-situ XRD and electrochemical analysis, Figure 2.18[51]. Various cut-off potentials were used, 505, 420, 250, 100 and 0 mV during CV analysis. This allows for the lithiation peaks to be assigned to their corresponding delithiation peaks removing any ambiguity. A sharp lithiation peak at 150 mV is coupled with a broad delithiation peak at 450 mV while a small sharp lithiation peak at 50 mV results in the replacement of the broad delithiation peak at 450 mV with a sharp doublet of peaks at 485 mV and 525 mV. In-situ XRD was performed during the galvanostatic cycling with different cut-off potentials of 130 mV and 20 mV. No crystalline phase was seen with a cut-off potential of 130 mV, while a 20 mV cut-off potential shows an XRD pattern of cubic $Li_{15}Ge_4$. Crystalline $Li_{15}Ge_4$ (c-$Li_{15}Ge_4$) transforms back to a-Ge during delithiation. The in-situ XRD explains the disappearance of the board peak at 450 mV seen in the CV profile when a cut-off voltage is decreased from 100 mV to 0 mV and the appearance of a set of sharp peaks at 485 mV and 525 mV. In-situ XRD reveals that c-$Li_{15}Ge_4$ is not formed until cycling goes below 130 mV indicating that the broad delithiation peak at 450 mV is associated to the delithiation of a-Li_xGe and the intense sharp peak at 525 mV is associated with the delithiation of c-$Li_{15}Ge_4$. The gravimetric and volumetric capacity of lithiated Ge at room temperature is 1385 mAh/g and 7366 mAh/cm^3 respectively contrary to the ex-situ

XRD analysis done by Graetz et al. who obtained capacity values consistent with the $Li_{22}Ge_5$. The XRD analysis of Graetz et al. indicates, however, that only small quantities of the $Li_{22}Ge_5$ are present with $Li_{15}Ge_4$ having a larger presence[49]. Both Al-Obeidi et al. and Nadimpalli et al. did in-situ stress analysis and found that $Li_{15}Ge_4$ is the final lithiated phase[52]. Al-Obeidi suggest that overlithiation of the c-$Li_{15}Ge_4$ phase happens when cycled below 65 mV which would explain the results of capacity and crystalline phase obtained by Graetz et al.
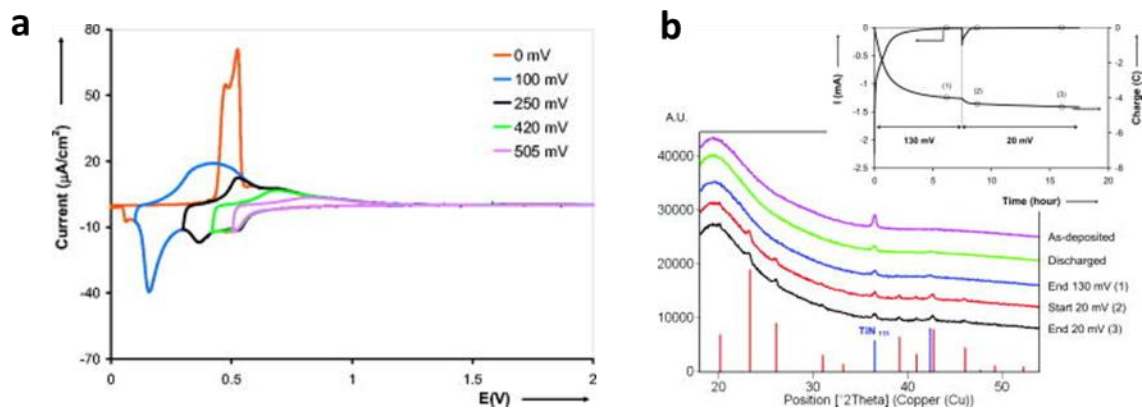
Figure 2.18: a, CV of a 50 nm evaporated Ge film at various cut-off potentials at a scan rate of 0.05 mV/s. **b,** XRD patterns measured during the potentiostatic insertion of a cycled Ge in two successive steps at 130 and 20 mV. The inset shows the current and charge evolution as a function of time during the potentiostatic steps. (Reproduced)[51]

In-situ TEM is a valuable method for analysing electrochemical anode materials having the ability to capture structural, phase and chemical changes in real time down to the atomic scale[53]. Liu et al. used this technique to investigate the lithiation process of Ge and found that c-Ge nanowires underwent a 2-step phase transformation, Figure 2.19[54]. The electrochemical lithiation process drives the solid-state amorphisation of Ge similar to the Si lithiation process[31a]. The in-situ TEM images clearly show a natural occurring core-shell structure with a c-Ge core and an a-Li_xGe shell with a Li_2O coating due to the native oxide layer that forms on the Ge being lithiated with the electron diffraction pattern (EDP) confirming the 2-step phase transformation seen. The phase transformations of a-Li_xGe indicated from the CV analysis do not show a phase boundary which is attributed to the rapid kinetics.

$$cGe \rightarrow a\, Li_x Ge \rightarrow c\, Li_{15}Ge_4 \qquad\qquad 2.12$$
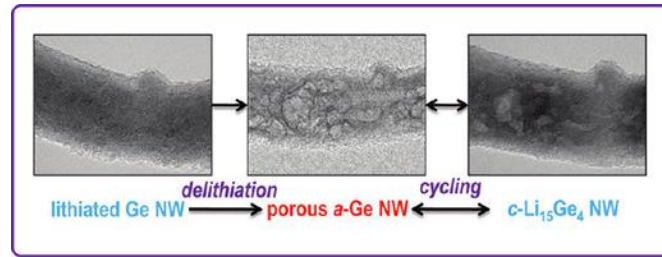
Figure 2.19: TEM image of microstructure evolution of a Ge Nanowire during cycling. (Reproduced)[54]

Upon delithiation of the nanowire from c-$Li_{15}Ge_4$ a nanoporous a-Ge structure is formed. The nanoporous structure is formed after cycling due to the fast kinetics of Li^+ in Ge which produces vacancies that form pores. The formation of nanopores in thin-film Ge are not typically seen due to crack formation and Ge delamination. However nanopores were reported in a thin-film Ge after cracking and is thought to be due to an improved adhesion with the current collector caused by interdiffusion and the formation of a non-uniform intermetallic layer[55]. These nanopores allow volume expansion to occur internally, i.e., inside the pores, while the outer diameter of the nanowire undergoes a smaller diameter increase during lithiation which reduces the damage to the SEI layer and prolongs electrode life. The formation of the nanopores in Ge nanowires has another beneficial feature called pore memory effect, in which the pores retain their shape and size and reappear at the same locations. This results in a reduction in freshly exposed Ge that normally appears due to cracking caused by volume expansion and this leads to a reduction in SEI formation.

The lithiation of c-Si is highly anisotropic meaning expansion along the <110> and <111> directions being the largest and smallest respectively. Li^+ ions find it difficult to lithiate into the close packed <111> planes, however lithiation occurs by a ledge flow process where the Li^+ ions peel off the atomic scale <111> facets to lithiate other crystal planes[56]. That reaction by comparison with lithiation along the <110> is significantly slower resulting in expansion along the <111> plane which causes a stress build up and an increased likelihood of cracking and pulverisation. The lithiation process of c-Ge is isotropic as seen by the radius increasing and the elongation of the nanowire in comparison to the anisotropic expansion of c-Si nanowire with insignificant elongation[37]. Further evidence of the different expansion mechanisms between Si and Ge using first-principles calculation, CV and Raman spectroscopy has been reported in which the lithiation voltages of the (110), (111) and (100) planes are close together for Ge while the voltages for Si are separated as the (110) plane has a higher potential than the (111) and (100)[57]. The interface between the core c-Si and a-

Li$_x$Si shell and the strain caused due to the anisotropic expansion are the reasons the build-up of strain during lithiation causes cracking and pulverisation of Si. Ge nanoarchitectures by comparison with their Si counterparts, are more resilient even though there is a sharp interface between c-Ge and a-Li$_x$Ge which is believed to be due to a lack of obvious peeling at the (111) plane and isotropic lithiation, Figure 2.20[58].
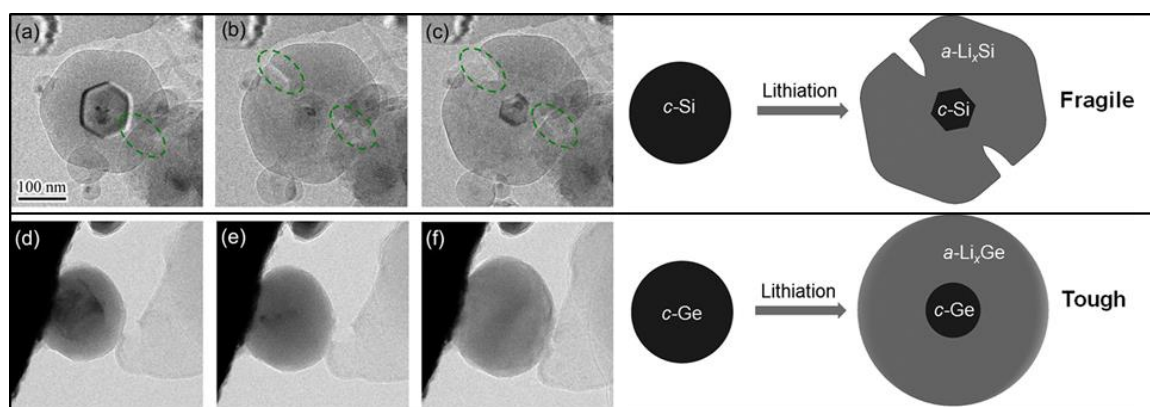
Figure 2.20: TEM **a-c,** Lithiation-induced anisotropic swelling and fracture in a c-SiNP. **d-f,** The isotropic swelling without fracture in a c-GeNP. (Reproduced)[58]

As with Si fabrication, VLS was used to generate Ge nanowires using a Au catalyst which gave a capacity of 850 mAh/g at a *C/20* charge/discharge rate. At a charge/discharge rate of *2 C* a 600 mAh/g capacity was obtained. However the presence and effect of the Au catalyst, as used to grow Si nanowires described in the previous section had the same detrimental effect[59]. The replacement of the Au catalyst with a Sn catalyst was used by Kennedy et al. on stainless steel current collector at 430ºC for 10 min[60]. The nanowire had an average thickness of between 1.5-2.0 µm and was made up of (111) c-Ge with a diameter of 73 nm and a Sn head with a diameter of 126 nm. The material loading was 0.22 mg/cm^2 with a mass ratio of 1:5 of Sn:Ge. This mass ratio gives a theoretical capacity of 1320 mAh/g as the Sn is also a lithium anode active material. A reported stable capacity of 900 mAh/g over 1,100 cycles at *C/2* charge/discharge rate was achieved, Figure 2.21. SEM and TEM analysis revealed the fusion between the nanowires due to what they described as lithiation assisted electrochemical welding after the first cycle and the formation of nanopores after 10 cycles. The nanowire structure is completely gone by the 100th cycle and is replaced by a porous structure. The rate capabilities of this nanostructure were tested and gave very impressive results such as a discharge rate of *20 C* (~3 min) and *100 C* (~36 sec) for 80 cycles with a charge rate of *2 C* (~30 min) giving capacities of 610 mAh/g and 372 mAh/g, respectively.
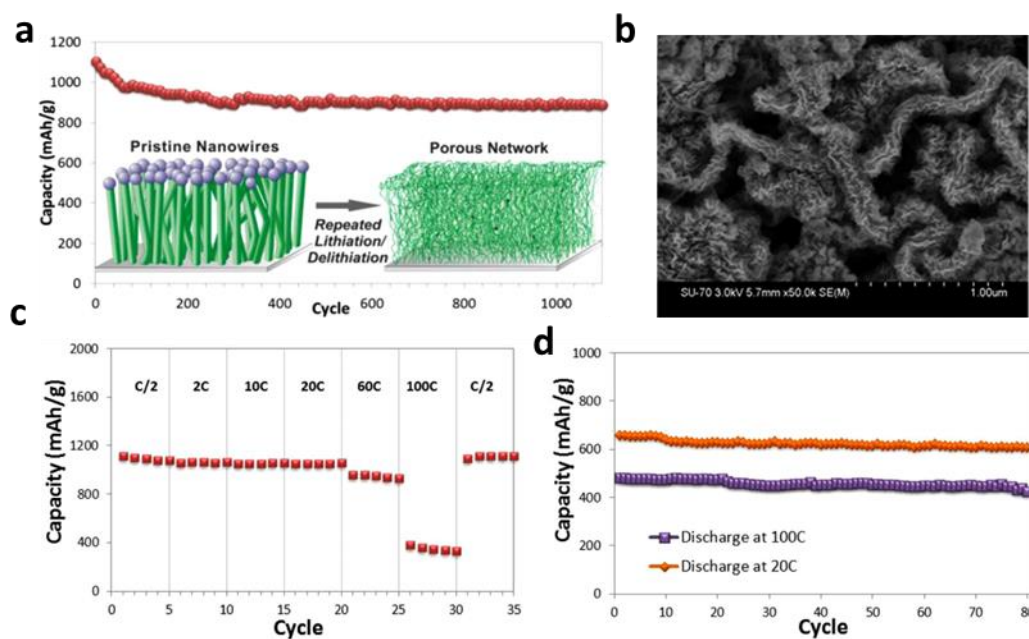
Figure 2.21: a, Discharge capacities of Sn seeded Ge Nanowire over 1100 cycles at *C/2* rate. **b,** SEM images after 10 cycles. **c,** Discharge capacities measured for 5 cycles at 6 different discharge rates with a constant *C/2* charge rate. **d,** Discharge capacities at *20* and *100 C* discharge rates with a constant *C/2* charge rate. (Reproduced)[60]

Electrochemical analysis using the galvanostatic profiles to extrapolate differential capacity plots show similar phase transformations at specific potentials as discussed in the previous section. During lithiation the nanowire undergoes lithiation of c-Li_xGe with a sharp peak at 370 mV, the broad peak at 190 mV is the transformation to a-$Li_{15}Ge_4$ and the sharp peak at 110 mV is formation of c-$Li_{15}Ge_4$. On the reverse cycle the broad peak at 240 mV is the delithiation of a-$Li_{15}Ge_4$ and the sharp peak at 460 mV is the delithiation of c-$Li_{15}Ge_4$. It is worth noting that excellent performance of the initial Ge nanowire was dependent upon the addition of vinylene carbonate (VC) (3 wt.%) to the electrolyte. VC is known to help form a stable SEI layer and was critical in the formation of the nanoporous network in this study.

Ge nanotubes for Li-ion battery applications are fabricated using the Kirkendall effect[61]. The Kirkendall effect exploits different material diffusion rates. The voids form at elevated temperatures when the outward diffusion of a material is much faster than the diffusion speed of a material inwards[62]. Ge nanowires were coated with antimony (Sb) acetate and polyvinyl pyrrolidone and annealed at 700°C for 5 hours under a Ar/H_2 environment. The extensive annealing results in the Ge atoms diffusing outwards much faster than Sb atom diffuse inwards resulting in the formation of Ge nanotubes with a low Sb concentration. The nanotube structure allows volume expansion both inwards and outwards during lithiation

44

resulting in excellent electrode performance of 900 mAh/g and 600 mAh/g capacities at *C/5* and *20 C* charge/discharge rates after 50 and 25 cycles respectively.

Another technique to increase the capacity of nanowires is by depositing small nanowire branches onto the nanowire stem which is called a nanowire heterostructure[63]. This nanowire structure was used to make Ge nanowires with Si nanowire branches, which formed a vine like shell, using a VLS mechanism with Cu_3Ge and Sn nanoparticles as catalyst for Ge and Si nanowire growth, respectively. Mass ratios of Si:Ge (branches:stems) used where 1:2, 1:3 and 1:4 resulting in mass loading and theoretical capacities of 0.285, 0.253, 0.238 mg/cm^2 and 2155, 1933, 1823 mAh/g, respectively. The capacity increased during the early cycling due to the slow transport kinetics of Si. The three mass ratios were cycled for 100 cycles at *C/5* charge/discharge rate giving a capacities of 1612 (1:2), 1459 (1:3) and 1256 (1:4) mAh/g.

Core-shell nanoarchitectures have also been achieved using a simple fabrication process where the current collector is a Cu nanowire, acting as the core, and an ultra-thin film of Ge anode material as the shell, Figure 2.22[64]. The nanowire current collector was fabricated using an anodized aluminium oxide (AAO) template that had pore diameters of 40-50 nm and a density of 10^{11} $pores/cm^2$ with a Cu backing. The vertically aligned Cu nanowires of 1-2 µm in length were grown by electrodepositing Cu into the pores of the Cu backing AAO template. The AAO templates was then dissolved leaving free standing Cu nanowires. Ge was then coated onto the Cu nanowires by rf sputtering. TEM analysis showed uniform coating of Ge with a thickness of ~50 nm which is believed to be because the nanowire had a smaller diameter than typical electrodeposited nanowire (200 - 250 nm). The core-shell nanowire structure can buffer the volume changes during lithiation while also maintaining an excellent electrical contact between the core Cu nanowire current collector and the Ge anode shell allowing for advanced rate capabilities. The ultra-thin film of Ge shortens the Li^+ ion diffusion length resulting in the ability of the electrode to operate at *40 C* (90 sec) and *60 C* (60 sec) for 80 cycles giving capacities of 850 and 734 mAh/g respectively.
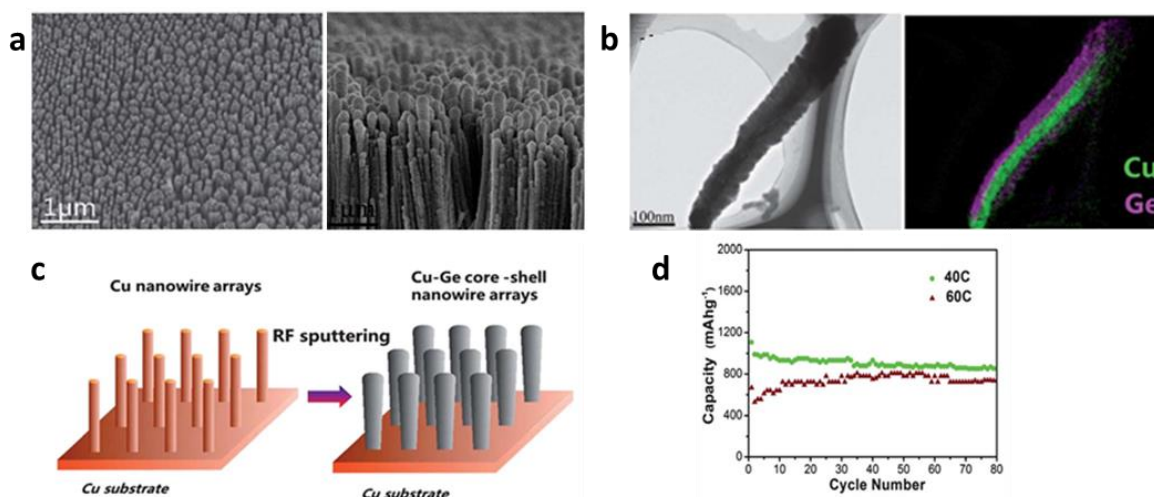
Figure 2.22: a, SEM images of the Cu nanowires and Cross-section of the Cu–Ge core-shell nanowires. **b,** TEM images of the Cu–Ge core–shell nanowire and corresponding EELS elemental mapping. **c,** Schematic illustration for synthesis of the Cu–Ge core-shell. **d,** Discharge and Charge capacities for the Cu–Ge core-shell nanowires at a rate of *40 C* and *60 C*, respectively. (Reproduced)[64]

Tin

Sn is seen as a very attractive alternative to graphite as it can hold up to 4.4 Li per Sn atom meaning it has a high theoretical capacity of 993 mAh/g and volumetric capacity of 7217 mAh/cm^3. Sn has superior lithium diffusion coefficient (6×10^{-7} – 8×10^{-8} cm^2/s) and electronic conductivity (9.17×10^4 S/cm) than the other alloying electrodes of Si and Ge[66]. The operational potential of Sn is in the range of 0.3 – 1.0 V during lithiation to form Li-rich alloy phases while also undergoing large volume changes (250%), Figure 2.23[65].
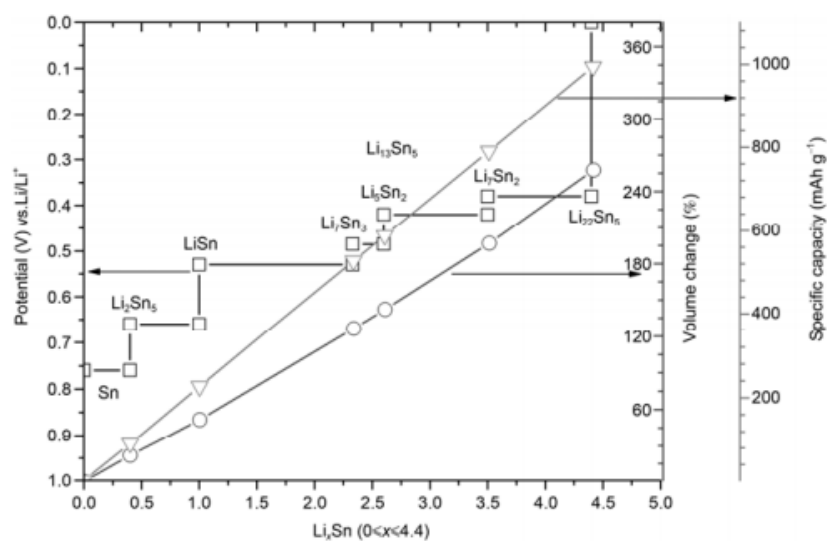
Figure 2.23: The theoretical formation potentials, specific capacities, and volume changes of Li$_x$Sn phases. (Reproduced)[65]

The cycling of Sn resulted in a large irreversible capacity in the initial cycle and rapid capacity fade for subsequent cycles, Figure 2.24. In-situ AFM was used to investigate the morphology changes that occurred during lithiation/delithiation and unveiled that significant surface roughening occurred during the first two cycles of an electroplated Sn electrode[67a]. The surface roughening/pulverisation of the Sn electrode cause the destruction of the SEI layer and expose fresh Sn to the electrolyte to form an SEI layer on its surface which accounts for the large irreversible capacity seen in the initial cycles. The continued decomposition of electrolyte to form an SEI layer on fresh Sn leads to the consumption of the electrolyte and eventual cell failure. The pulverisation of the Sn electrode during cycling is caused by the lithiation/delithiation process as the presence of multiple lithiated Sn phases causes inhomogeneous volume expansion coupled with the size of volume expansion[68]. The first two lithiated phases of Sn, Li_2Sn_5 and $LiSn$, have a similar density and lattice constant but the remaining Li_xSn phases are very different and cause mechanical stresses due to the lattice mismatch and eventual pulverisation[69].
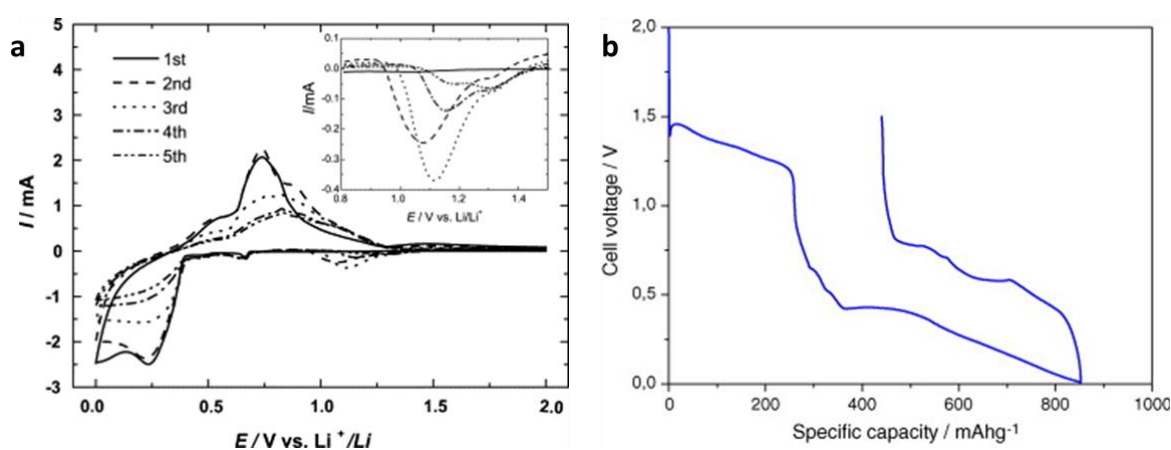
Figure 2.24: a, CV's of electrodeposited Sn thin film in 1M $LiClO_4$/PC at a scan rate of 0.5 mV/s. **b,** Galvanostatic profile of first cycle of Sn in 1M $LiPF_6$ EC:DMC 1:1 electrolyte at a *C/10* rate in the range 0.01–1.5 V. (Reproduced)[67]

The formation of an SEI layer in an organic electrolyte is due to the Sn surface catalysing electrolyte decomposition. The SEI layer is dependent on the cycle rate and can be limited by cycling at high rates[67b]. An amorphous Sn thin-film that was rf sputtered and contained nanosized particles was able to form a relatively thick SEI layer during cycling which resulted in the Sn electrode not being pulverised and improved cycle life[70]. Large Sn crystals that were pulse electrodeposited gave an initial coulombic efficiency of 93%. This indicates that the pulverisation and exposure of fresh Sn is limited due to the larger Sn crystals having a smaller electrode/electrolyte interface.

A Sn film covered by a SnO_2 layer shows that an SEI layer was not formed and that the cycle performance was improved. The basic reaction of SnO_2 with Li shows that the lithium bonds to the oxygen in the SnO_2 and forms a Li_2O framework with nanosized $Sn^{[26d]}$. The inactive Li_2O acts as a buffer for the volume expansion during the lithiation of Sn and results in improved cycle performance. There is a large irreversible capacity in the initial cycle due to the formation of the inactive Li_2O phase and the theoretical capacity is slightly smaller than that of pure Sn (SnO_2 = 782 mAh/g) however the enhanced cycle life is an acceptable compromise for this small drop in capacity. The CV analysis of an electrostatically sprayed (ESD) SnO_2 film shows a peak at 0.85 V (A) in the initial cycle indicating the formation of the Li_2O buffer and the peaks at b and c are assigned to the lithiation of the nanosized Sn, Figure 2.25[71]. Peak A is replaced after the initial cycle by reversible peaks labelled a_1 and a_2. The cut-off potential limit has also been shown to have an effect on the cycle performance as cycling above 1.5 V corrodes the Li_2O buffer framework that is holding and connecting the nanosized Sn to the current collector.
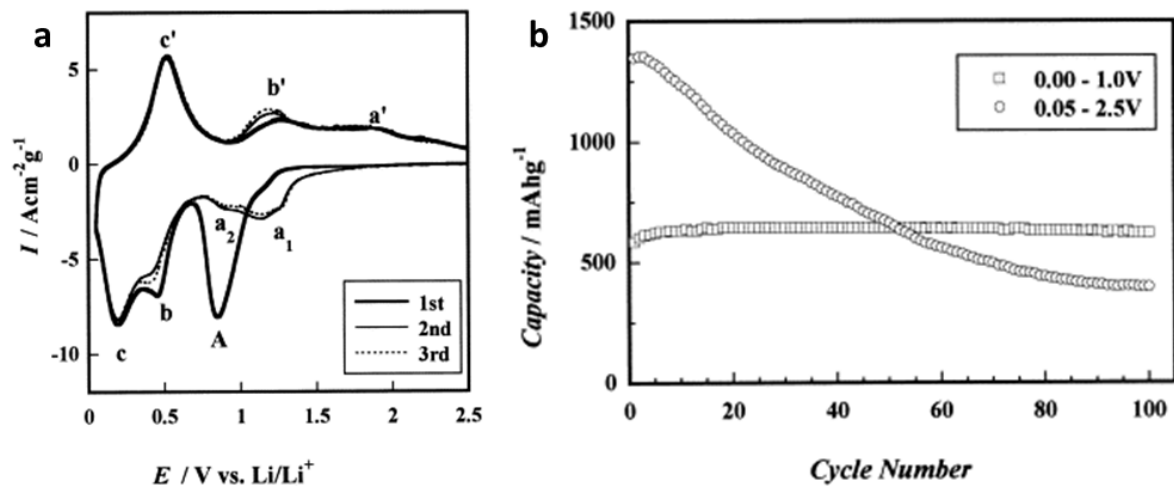
Figure 2.25: a, CV cycles of the SnO_2 film in the range of 0.05 - 2.5 V at a scan rate of 0.2 mV/s in 1 M $LiClO_4$/PC:EC. **b,** Cycle performance of SnO_2 at a range of 0.00 – 1.00 V and 0.05 – 2.5 V at a current density of 0.20 mA/cm^2. (Reproduced)[71]

The research into Sn based alloys has been extensive as inactive metals can act as a buffer to the volume expansion such as Sn-Co[72], Sn-Fe[73] and Sn-Ni[74] etc. Intermetallic alloys that react during lithiation/de-lithiation topotactically, such as Sn-Cu[75], provide a stable framework as they expand isotropically due to their cubic symmetry. An inactive phase was introduced as a buffer for the volume expansion while also maintaining an electrical path to the current collector to overcome the issues associated with these alloying metals[66b]. This

concept of metals in inactive buffer matrix has been shown to improve cycle life however mechanical instability in the form of cracking and delamination still remains an issue for such materials. Sn-Co-C has been used by Sony as their anode in the Nexelion cell[76]. This utilised nanosized metal alloy (Sn-Co) in a carbon composite anode. Sony never published the electrochemical characteristic in half cell or composition of the composite electrode material. Investigation into the preparation of such a material and the effect it has on performance was performed by Todd et al[77]. Their work shows that $Sn_{30}Co_{30}C_{40}$ prepared by magnetron sputtering or mechanical attrition has a similar nanostructure to Sn-Co-C used by Sony and had varying performance depending on material preparation. Magnetron sputtering shows the best performance with a capacity close to the theoretical of 700 mAh/g. Mechanical attrition using $CoSn_2$, Co and C as starting materials gave a capacity of 450 mAh/g while using CoSn and C as starting materials gave a capacity of 300 mAh/g. Replacement of almost 50% of Co with Fe reduced the cost of the anode, with a relatively small impact on performance was shown by Ferguson et al[78]. Reverse engineering and analysis of a Nexelion cell implies that Sony also made this change to more recent versions of the Nexelion cells[79].

Nanocomposites of these metal alloys showed a significant increase in cycle life however new issues arose from the aggregation of the nanoparticles, the trapping of Li^+ in the inactive metal host and electrolyte decomposition on the inactive components resulting in an unstable SEI layer.

Cathode materials

Cathode materials with the highest potential are generally intercalation electrodes that have a crystalline structure that allows for Li^+ ions to be stored in interstitial sites of the crystalline lattice. These electrodes are generally made up of transition metal oxides or phosphate oxides that have layered, spinel, olivine and multi-phase layered crystalline structures as shown in Figure 2.26.
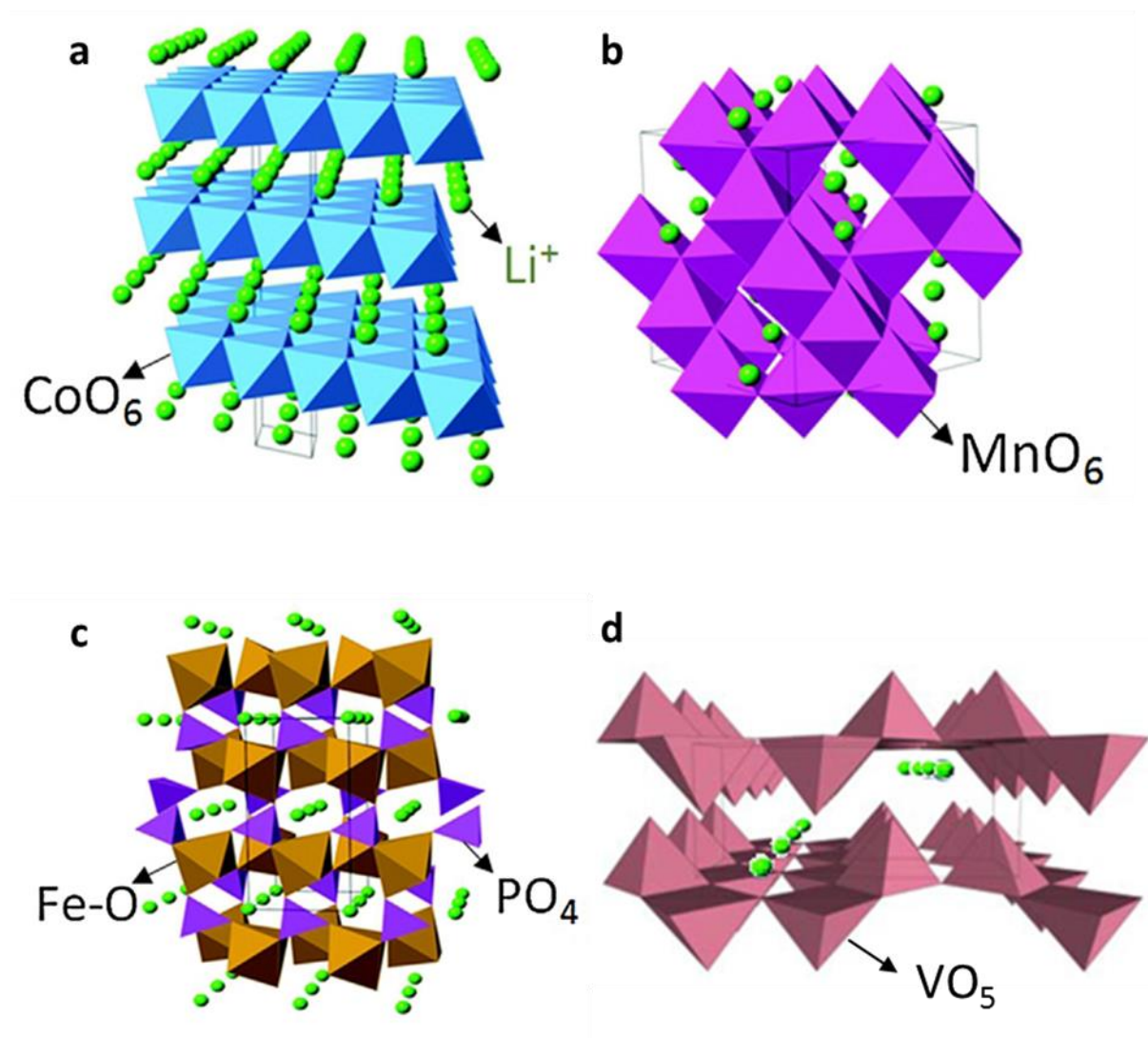

Figure 2.26: Crystal structures of cathode materials for lithium-ion batteries: **a,** layered a-LiCoO$_2$; **b,** spinel LiMn$_2$O$_4$; **c,** olivine LiFePO$_4$; **d,** multi-phase layered LiV$_2$O$_5$. (Reproduced)[80]

Lithiated Layered Oxide

Layered oxide materials have attracted a lot of interest over the years due to their ability to adapt their geometry to hold Li^+ ions by increasing their interlayer separation[81]. Lithiated transition metal oxides $LiMO_2$ (Co, Mn and Ni) are an important cathode material for lithium ion batteries and have been extensively used in commercial batteries for many years. Their ability to operate at high potentials (3.0 - 4.2 V vs Li/Li^+) and cycling stability has made them a standard cathode material in lithium ion batteries. These compounds have a $\alpha NaFeO_2$-type structure with a disordered rock-salt superstructure[82]. This is a layered structure consisting of lithium and transition metal atoms occupying the octahedral sites between alternating layers of MO_2. The layered structure is made up of strong interlayer covalent bonding and weak interlayer bonding to ions in octahedral sites. These weak interlayer bonds are maintained by van der Waals forces and electrostatic attraction. The complete delithiation of layered structure results in the formation of an unstable $CdCl_2$-type structure and as a result delithiation is limited to maintain structural stability and cycle life. Typically delithiation of Li_xMO_2 is limited to $x \geq 0.5$ as M-O bonds have high ionic characteristics due to the high electronegativity of oxygen. Li_xMO_2 develops a negative charge in the MO_2 layers that is off-set by the positively charged Li^+ ions still present rather than repulsed by the parallel layers[83]. Electrolyte decomposition of standard organic electrolytes happens at ≥ 4.3 V and cathode corrosion due to the presences of HF in the electrolyte is well known and causes a decrease in cycle life. Surface coatings are a popular approach used to protect the cathode material by attracting and neutralising the HF molecules[84]. The surface coating also prevents direct contact between the electrolyte and cathode material and acts as a physical barrier. Lithium rich layered transition metal oxides, described as $xLi_2MnO_3.(1-x)LiMO_2$, have been shown to improve the thermal stability and electrode performance[85]. This structure was proposed by Thackeray et al, where Li_2MnO_3 and $LiMO_2$ structures are integrated together which can allow for a higher operation voltage of ≥ 4.5 V. The extra lithium phase of Li_2MnO_3 only becomes active at voltages ≥ 4.5 V meaning the oxygen loss from the $LiMO_2$ balances the local charge[86].

$LiCoO_2$ was the cathode material used in the first commercial lithium ion battery by Sony. Delithiation is limited to $x \geq 0.5$ in Li_xCoO_2 resulting in a specific capacity of 136 mAh/g when operating in an optimum voltage range of 4.2 V to 3.0 V[87]. The phase transformation of $LiCoO_2$ during delithiation was investigated by Reiners et al. using in-situ XRD and produced a phased diagram for the delithiation process, Figure 2.27[88]. The rhombohedral

structure of LiCoO$_2$ has a hexagonal lattice in the c-axis direction. There is a mixture of the 1st and 2nd hexagonal phases after delithiation to Li$_{0.93}$CoO$_2$, at delithiation to Li$_{0.75}$CoO$_2$ it is fully converted to the 2nd hexagonal phase. Close to the optimum Li$_{0.5}$CoO$_2$ delithiation limit a monoclinic phase is present. LiCoO$_2$ electrodes that have undergone extensive cycling, have via TEM analysis been shown to form a less active spinel LiCo$_2$O$_4$ phase on the surface of the electrode and this is thought to be partially responsible for the capacity loss during extensive cycling[89]. A characteristic of LiCoO$_2$ is the significant difference in electrical conductivity depending on lithium composition. LiCoO$_2$ acts like a semiconductor and Li$_{\leq 0.6}$CoO$_2$ behaves like a metal at ambient temperatures[90].
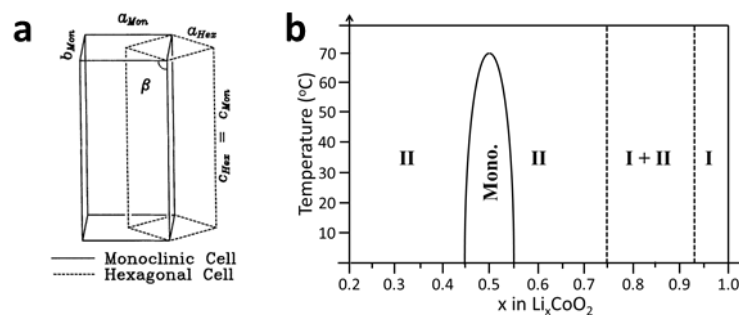
Figure 2.27: a, Monoclinic (solid) and hexagonal (dashed) unit cells. **b,** Phase diagram for Li$_x$CoO$_2$. (Reproduced)[88]

LiCoO$_2$ is easily produced by a variety of methods. One of the simplest methods of making LiCoO$_2$ particles is by mixing cobalt oxide and lithium hydroxide in a Li:Co ratio of (1.05:1) and sintering in air at 700 - 1,000 °C for as little as 1 hr[91]. The synthesis temperature has significant effect on the structure of LiCoO$_2$. High temperature synthesis, classified as temperatures $\geq$ 400 °C gives the desirable hexagonal layered structure for lithiation, while low temperature synthesis ($\leq$ 400 °C) results in a cubic spinel structure[92]. Binder-free and uniform thin-films of LiCoO$_2$ have also been deposited using pulse laser (PLD) and rf sputtering for micro power applications.

Early work by Bates et al. shows that the orientation of the high temperature synthesised rf sputtered LiCoO$_2$ is dependent on the thin-film thickness[93]. The dominant crystal orientations present in typical thin-films of LiCoO$_2$ are (003), (101) and (104). The ideal orientations for Li to intercalate/de-intercalate at LiCoO$_2$ are the (101) and (104) planes as they are almost parallel to the substrate, at 35° and 10° respectively, Figure 2.28[94]. The (003) orientation results in lithiation/delithiation being dependent on cracks and grain boundaries as the hexagonal layered structure is at 90° to the substrate. A number of other factors can have

a significant effect on the performance of thin-film $LiCoO_2$ depending on the deposition technique such as substrate material, gas pressure, gas composition, applied bias, substrate temperature, annealing technique, annealing temperature and annealing gas composition. The atomic ratio of Li/Co can be influenced by the deposition condition during sputtering. $LiCoO_2$ is an unstable molecule during sputtering as the low atomic weight Li atoms can be removed from the sputtered film resulting in the formation of inactive Co_3O_4[95]. During sputtering a working gas composition that has O_2 present results in a O_2 plasma that contains negative oxygen ions that re-sputter and stabilise the $LiCoO_2$ thin film[96].
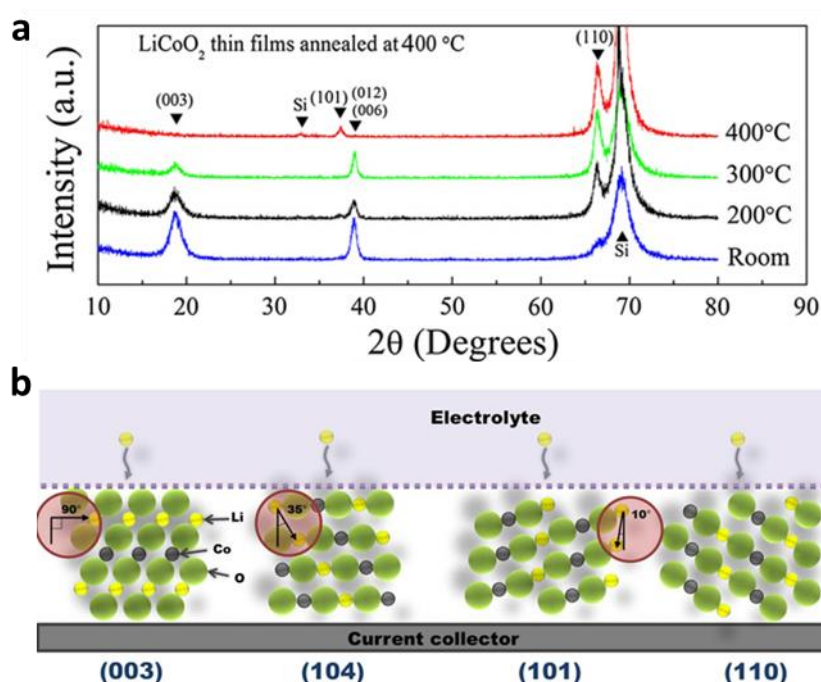
Figure 2.28: a, X-ray diffraction patterns of the annealed $LiCoO_2$. **b,** Lithium-ion diffusion and intercalation pathway in $LiCoO_2$ thin film layers oriented to various lattice planes. (Reproduced)[94]

Reports of cathode materials with nanoarchitecture geometries have been minimal because of the difficultly in synthesising 3D electrode arrays of transition metal oxide materials[97]. Xia et al published work on the synthesis of $LiCoO_2$ nanowires using a two-step hydrothermal method, Figure 2.29[98]. The first step involved the hydrothermal growth of Co_3O_4 nanowires on Ti/Au substrate. The second low temperature (LT) hydrothermal step resulted in the lithiation of the Co_3O_4 nanowires by placing the electrode in an autoclave with 2 M LiOH solution at 240 °C for 48 h. The LT-$LiCoO_2$ nanowires were annealed for 2 h in air at a high temperature (HT) of 750 °C to give the desired hexagonal layered structure, HT-$LiCoO_2$. The hydrothermal lithiation process results in the formation of $\leq$ 50 nm nanoporous LT-$LiCoO_2$

nanowires that are then annealed and transformed to HT-LiCoO$_2$ nanowires. The nanowires had a chain-like structure with grains connected by ends that are 100 - 200 nm in length. A CV profile of HT-LiCoO$_2$ nanowires gave the typical CV profile with very little peak separation for the major delithiation/lithiation peaks at 3.93 V and 3.89 V, respectively. The cycle performance showed that after 50 cycles 90% of the initial capacity (0.27 mAh/cm^2) at *0.1 C* rate was retained. One of the main benefits of nanoarchitectures is highlighted by the rate performance at *10 C* (6 min) charge/discharge with a capacity of 103 mAh/g. Earlier work done by Shaijumon et al. used electrodeposited Al nanowires fabricated using an Al ionic liquid bath and AAO template as the current collector. LiCoO$_2$ was deposited on the Al nanowires by a sol-gel spin coating process. 3 spin coated layers resulted in a ~30 nm thick LiCoO$_2$ on the 8 μm height Al nanowires with a capacity retention of 70% of the initial capacity (0.125 mAh/cm^2) at an *8 C* (7.5 min) rate[99].
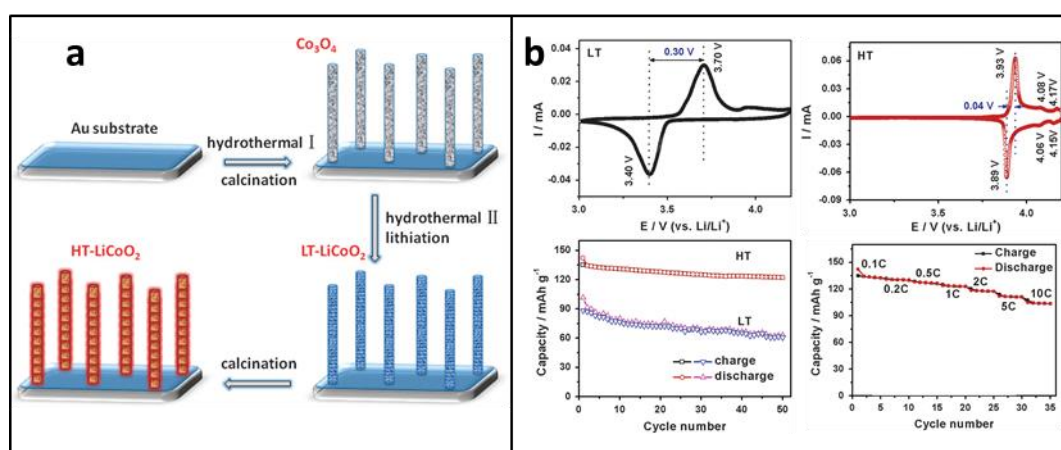
Figure 2.29: a, Illustration of a facile two-step hydrothermal method for preparation of LT- and HT-LiCoO$_2$ nanowire arrays on metal substrates. **b,** The typical CV curves for the LT-LiCoO$_2$ and the HT-LiCoO$_2$ nanowire arrays respectively between 3 and 4.2 V at a scan rate of 0.1 mV/s, comparison of cycle performance between the LT-LiCoO$_2$ and HT-LiCoO$_2$ nanowire arrays and the rate performance of the HT-LiCoO$_2$ nanowire arrays. (Reproduced)[98]

As mentioned in the previous section surface coatings have been shown to thwart some of the interactions between the electrode and electrolyte that negatively affect the electrodes surface and degrade the electrolyte. Atomic layer deposition (ALD) was used to deposit a thin film of Al$_2$O$_3$, around 1.1 – 2.2 Å thick, onto the LiCoO$_2$ nanoparticles that gave an increase in the operational potential range to 4.5 – 3.3 V that resulted in improved gravimetric capacity and energy density[100]. Excellent rate capabilities were also observed, displaying a capacity of 133 mAh/g at a *7 C* charge/discharge rate, Figure 2.30. ALD of greater than 2 cycles resulted in a negative impact on performance due to the low conductivity of Al$_2$O$_3$ having greater

influence. TiO_2 was also looked at as a coating material for $LiCoO_2$ by Cheng et al.[101] It was discovered that TiO_2 deposited using ALD showed an inferior performance in comparison to bare $LiCoO_2$ particles due to the consumption of TiO_2 in the formation of $LiTi_yCo_{1-y}O_{2+0.5y}$ as a result of Ti^{4+} inserting into $LiCoO_2$. A thorough investigation on the effect of metal phosphate coatings (MPO_4) on nanoparticle $LiCoO_2$ was performed by Kim et al.[102] Their investigation found that the particle size of the coating material had a direct effect on the coating coverage. Nanoparticles of $AlPO_4$ and $FePO_4$ that had particles sizes ≤20 nm fully encapsulated the $LiCoO_2$ particles while large nanoparticles of $CePO_4$ and $SrHPO_4$ resulted in an incomplete coverage. The fully encapsulated $LiCoO_2$ particles with $AlPO_4$ showed the best capacity retention, an initial capacity of 230 mAh/g at a c-rate of *C/10* and an extended voltage window of 4.8 V vs Li/Li$^+$. ZnO has also been utilised as a coating to extend cycle life by decreasing the degradation of $LiCoO_2$ which reduces the amount of Co dissolved and the prevention of a LiF film forming on the electrode surface[103]. ZnO coating is a more resistant material than $LiCoO_2$ however the coating increases the charge-transfer rate compared to an uncoated $LiCoO_2$ electrode.
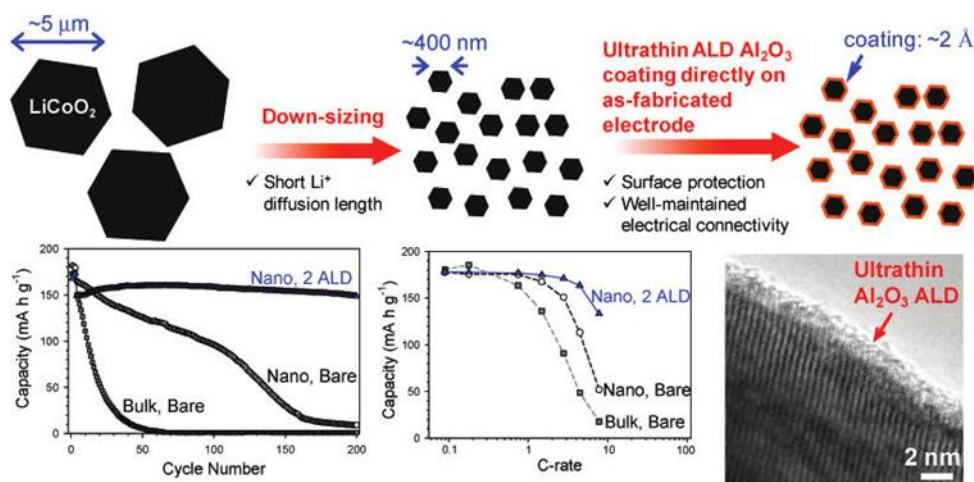
Figure 2.30: Schematic of fabrication process of nanosized $LiCoO_2$ with an ultrathin ALD Al_2O_3, comparison of cycling performance of the electrodes at *2.8 C*, comparison of rate performance of electrodes and TEM of 6 ALD cycles of Al_2O_3 on nanosized $LiCoO_2$ respectively. (Reproduced)[100]

$LiCoO_2$ is more expensive than other $LiMO_2$ materials based on the cost of cobalt. The Democratic Republic of Congo control almost 50% of the world's share of cobalt[104]. The price of cobalt has increased dramatically in the last year with a price of $32,782 per tonne in December 2016 to now trading at $68,143 per tonne in December 2017, Figure 2.31 [105]. The price issue associated with the cost of cobalt as a raw material for synthesising $LiCoO_2$ and

also the relatively small capacity of $LiCoO_2$ has led to the development of cathode materials that either have reduced cobalt content or are entirely cobalt free.
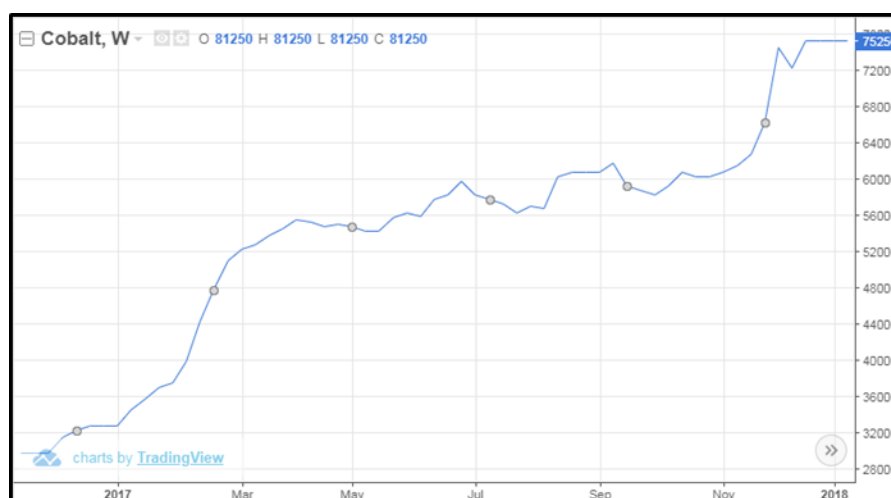
Figure 2.31: Stock price of Cobalt from 2017-2018 according to Trading Economics. (Reproduced)[105]

The replacement of cobalt with a relatively abundant nickel in the transition metal oxide would dramatically reduce the cost of the cathode material. The reversible capacity of $LiNiO_2$ is higher than $LiCoO_2$ as the stoichiometric amount of lithium that can be extracted during charging is more with 0.55 for $LiNiO_2$ and 0.5 for $LiCoO_2$[106]. Computational modelling has shown that the low valence Ni^{+2} cations provide high-rate pathways which are a desirable property for achieving high rate performance[107]. The preparation of $LiNiO_2$ is significantly more complicated than $LiCoO_2$ even though both have the same structure due to the difficulty in minimising excess nickel in the structure during synthesis[108]. The excess nickel atoms take up the lithium sites resulting in composition of $Li_{1-y}Ni_{1+y}O_2$ which is not the desired composition[109]. This structure results in the NiO_2 layers being pinned together and as a consequence a reduction in the lithium diffusion coefficient. The structure with this abnormal composition and low lithium concentration is unstable due to a high equilibrium O_2 partial pressure that makes the electrode degrade when cycling and in contact with organic solvents. The formation of irreversible phases during cycling has resulted in an extremely low cycle life of 98 when the capacity was restricted to 130 mAh/g, the same as $LiCoO_2$[109b, 110]. The thermal stability of $LiNiO_2$ is also a problem as Ni metal dissolves in the electrolyte and NiO forms on the surface of the electrode at temperatures as low as 60 °C[111].

The combination of Ni and Co into the $LiMO_2$ structure was a proposed strategy to overcome the stability issues associated with the $LiNiO_2$ and the capacity shortcomings of $LiCoO_2$. The $LiNi_{1-x}Co_xO_2$ ($0 < x \leq 0.4$) structure was found to be more stable than the $LiNiO_2$ counterpart; however the stability was still inadequate for practical applications[113]. The addition of an inactive di-, tri- or tetravalent cation (Al, Ga, Mg or Ti) with the Ni and Co components in the layered structure was investigated as a stabilising component for the molecule[114]. The idea behind the use of inactive components is that it would prevent the Li removal and as a result maintain the O_2 partial pressure at a level that preserves the structural integrity. $LiNi_{1-x-y}Co_xAl_yO_2$ (NCA) showed promise as an advanced cathode material as initial reports showed improved capacity and stability properties in comparison to the $LiCoO_2$ and $LiNi_{1-x}Co_xO_2$ cathodes respectively[115]. Continued research and development of NCA cathode material has resulted in its use in commercial applications, for example, the 18650 Panasonic cell is used in the Tesla Model S electric vehicle, Figure 2.32.
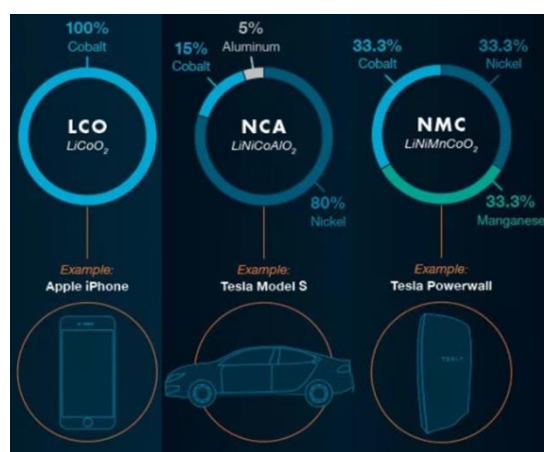
Figure 2.32: Chemistry of cathode materials used in commercial applications. (Reproduced)[112]

The addition of Mn into the $LiNi_{1-x}Co_xO_2$ has also been shown to be an effective approach to further stabilise the structure. The Mn^{4+} in $LiNi_xMn_yCo_zO_2$ (NMC) does not change its oxidation state during cycling and is able to stabilise the redox Ni^{2+} and Ni^{4+} states[109b, 116]. The NMC cathode is preferred over the NCA cathode in certain applications, such as the Tesla Powerwall where stability is more important than capacity. The composition of NMC has allowed for the development of novel electrodes with a core-shell type structure, Figure 2.33. The core layer is made of a higher capacity/power nickel rich NMC, $LiNi_{0.8}Mn_{0.1}Co_{0.1}O_2$, and the shell is made up of a more balanced NMC composition, $LiNi_{0.46}Mn_{0.31}Co_{0.23}O_2$ stabilises the interactions at the electrode/electrolyte interface and

allows for a practical cycle life[117]. The average composition of the core-shell type structure is $LiNi_{0.68}Mn_{0.18}Co_{0.18}O_2$.
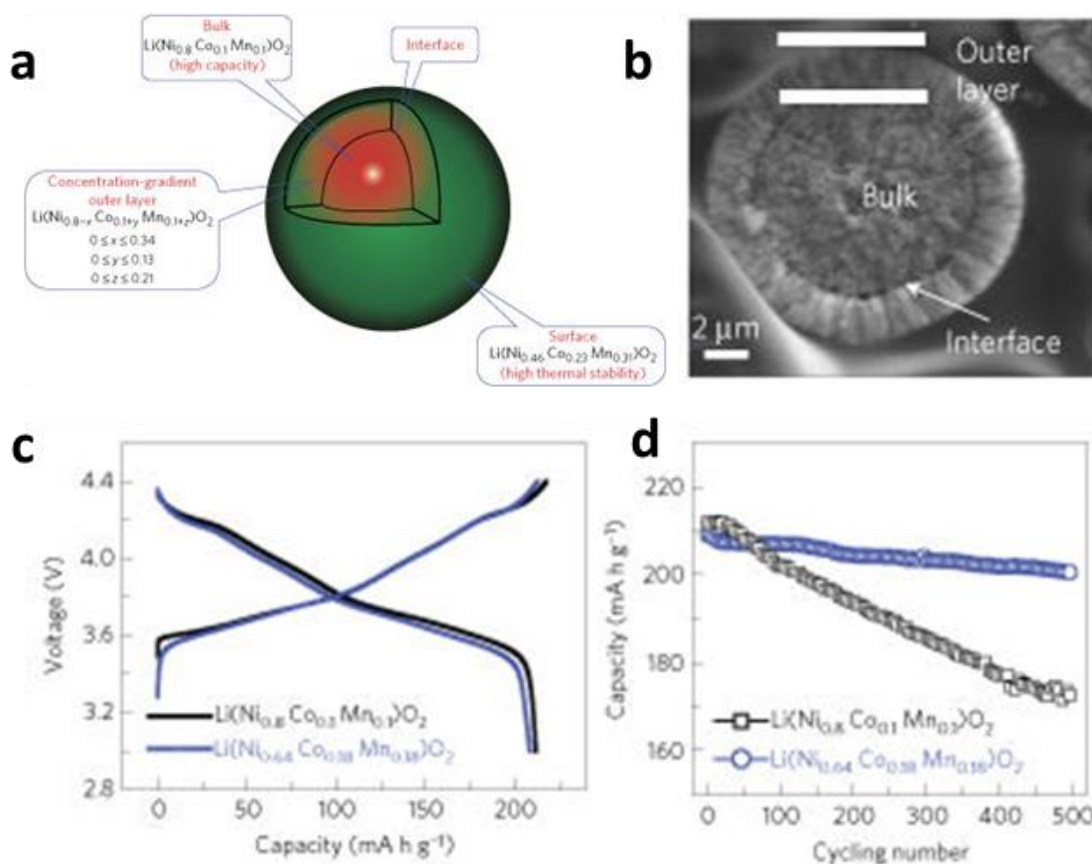
Figure 2.33: a, Schematic diagram of NMC particle with Ni-rich core and concentration gradient shell. **b,** SEM of core-shell NMC. **c,** Galvanostatic profile of initial charge/discharge cycles for NMC and core-shell NMC at *C/2* rate at 55°C. **d,** Cycle performance of NMC and core-shell NMC at *1 C*. (Reproduced)[117]

Spinel Oxide

The term spinel comes from the description of the $MgAl_2O_4$ structure. The spinel $LiMn_2O_4$ (LMO) structure has Li in the tetrahedral 8a sites and the Mn in the octahedral 16d sites with a ccp array of oxygen anions[80a, 118]. This 3D structure allows for Li^+ ions to diffuse through the unoccupied tetrahedral and octahedral interstitial sites. LMO has a theoretical capacity of 142 mAh/g and high potential of 4.0 V. These characteristics in combination with the relative abundance and low cost of Mn have prompted the use of LMO in commercial applications such as the Nissan Leaf. The lithiation process on LMO involves a two-step process with the formation of an intermediate phase, Figure 2.34. The CV profile of LMO shows two

symmetrical redox peaks at 4.0 V and 4.1 V for the delithiation cycle. The peaks are equal in magnitude which suggests that the intermediate phase holds half of the lithium available ($Li_{0.5}Mn_2O_4$) before being delithiated to the final phase of λ-MnO_2[119].
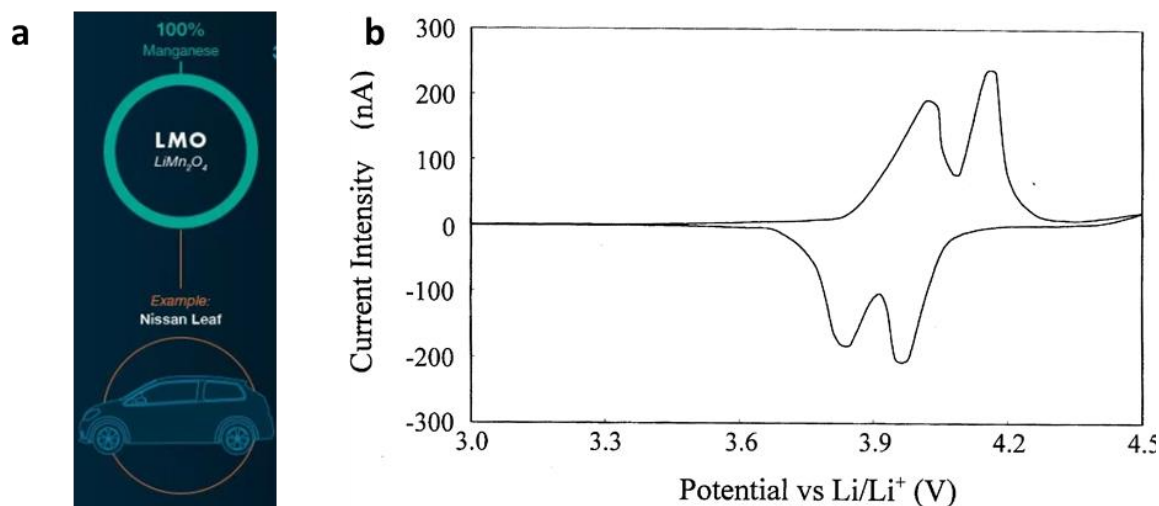
Figure 2.34: a, Commercial application of LMO cathode. **b,** CV of LMO at a scan rate of 0.02 mV/s. (Reproduced)[112, 120]

An issue associated with LMO cathode is the poor cycle life and stability at elevated temperatures. This issue is caused by the irreversible side reactions with an organic electrolyte that form HF species which catalyse the dissolution of Mn^{3+}[121].

$$2Mn^{3+} \rightarrow Mn^{2+} + Mn^{4+} \tag{1}$$

The dissolution of Mn^{3+} not only leads to structural instability of the LMO cathode but the Mn^{2+} ions dissolved in the organic electrolyte can plate on the anode, at the reduction potential of Mn^{2+} (1.8 V), and results in a negative impact on the cell performance[122]. A large capacity loss is generally seen in the first cycle, this is attributed to the loss of oxygen during cycling and the already oxygen deficient LMO, formed in a typical synthesis, leads to micro fractures and structural collapse along the (111) planes[123].

The use of nanoarchitectures improves the rate performance due to reduced diffusion lengths but has also been shown to aggravate the dissolution of Mn by increasing the area of the electrode/electrolyte interface. An effective solution to improve LMO performance is by doping the electrode with a lower valence state element[124]. An easy way of doping LMO is with excess lithiation where the stoichiometry is $Li_xMn_2O_4$, $1 < x < 2$[125]. Okubo et al, showed that excess lithium can be intercalated into LMO if the particles size is below the critical diameter[126]. The work reported that nanoparticles with a 15 nm average diameter

could accommodate close to the stoichiometric amount of $Li_2Mn_2O_4$ by a solid-state process that involved a boundary free mechanism allowing for capacities of 160 mAh/g at a *10 C* rate. The critical diameter discovery ($\leq$ 43 nm) explains the superior performances of nanoarchitectures reported for LMO cathodes, Figure 2.35[127]. Excess lithiation of nanoarchitectured LMO with a diameter below the critical diameter is enabled as these dimensions can accommodate the structural transition from the cubic spinel phase to a tetrahedral phase where the expansion in unit cell allows for more lithium intercalation[7b]. Lee et al. reported the synthesis of LMO nanowires with a < 10 nm diameter by reacting α-MnO_2 with LiOH at a reduced pressure[128]. The high aspect ratio of 7 μm in length nanowires gave capacity values of 105 mAh/g and 75 mAh/g for *60 C* and *150 C* respectively.
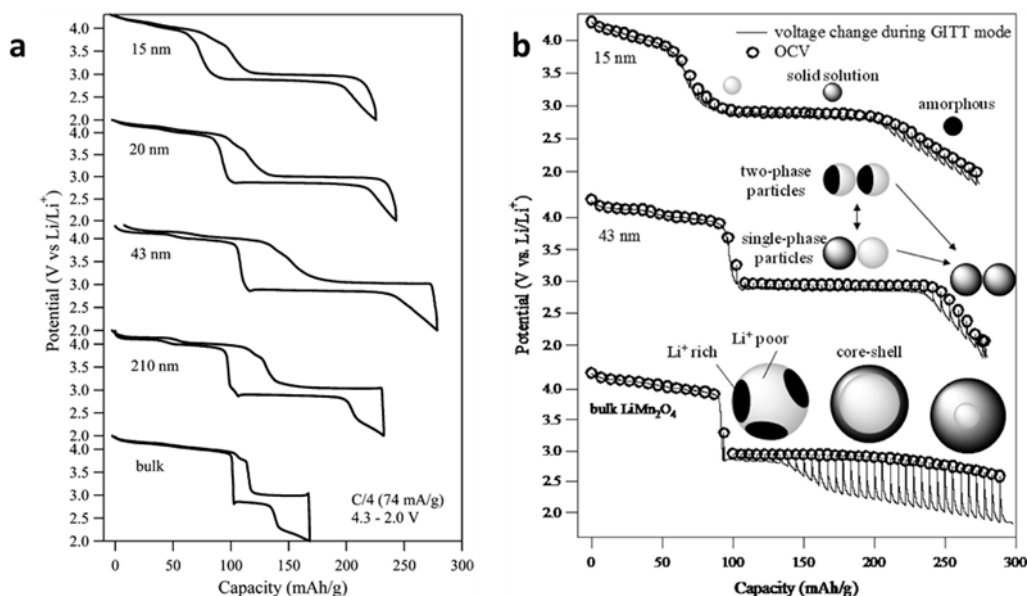
Figure 2.35: a, Galvanostatic profiles of various sized LMO particles at *C/4*. **b,** GITT profiles of bulk, 43 nm and 15 nm LMO sized particles with illustrations of lithiation process. (Reproduced)[126]

The partial substitution of Al into the spinel structure is another strategy that has been used to restrict the dissolution of the Mn^{3+} species. Ohzuku et al, showed that $LiAl_{0.1}Mn_{1.9}O_4$ (LAMO) can be prepared by mixing electrolytic manganese dioxide (EMD), Li_2CO_3, $Al(OH)_3$ and H_3BO_3 in water and sintering at 900 °C for 12 h and 650 °C for 24 h[129]. The LAMO showed superior performance over LMO with little or no decrease in capacity during cycling, Figure 2.36. The galvanostatic profile only shows one distinct plateau in comparison to the three seen when cycling between 3 - 5 V. Both differential chronopotentiogram profiles, extracted from the galvanostatic data, showed the characteristic redox peaks at 4 V and 4.15 V indicating that the addition of Al into the spinel structure did not affect the

lithiation process. The most significant difference is the absence of the redox peaks at 4.5 V and 3.3 V, which are an indication of the structural change from spinel to double-hexagonal phase, for the LAMO cathode. This absence means that there is little or no damage done to the spinel structure of the LAMO cathode unlike the LMO cathode. Nanorod LAMO and LMO cathodes analysed after immersion for different times in organic electrolyte again highlighted the superior stability of LAMO[130].
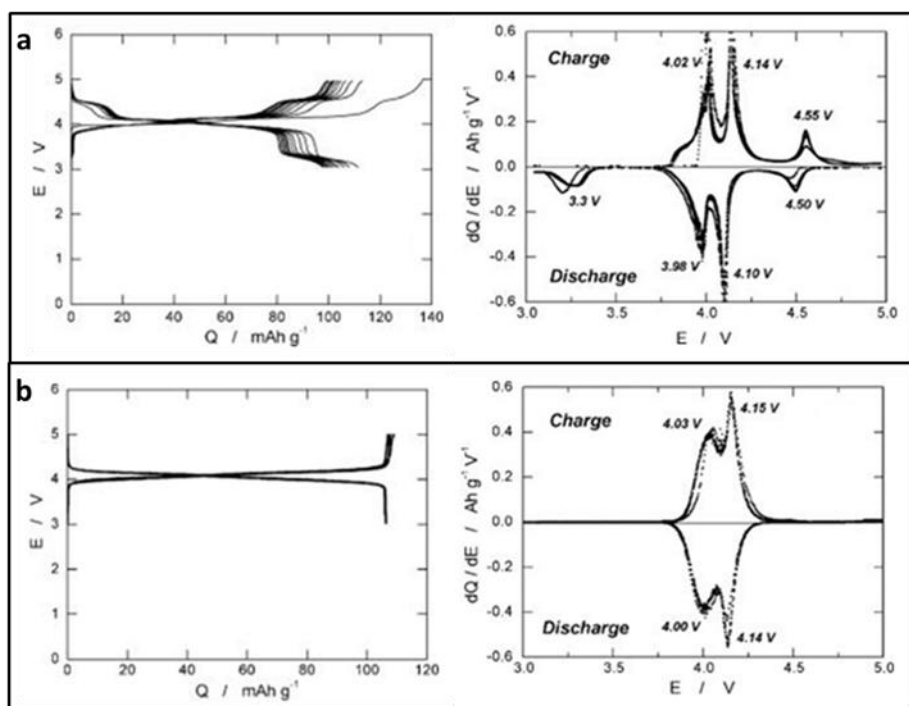
Figure 2.36: a, Galvanostatic (0.17 mA/cm^2) and differential chronopotentiograms profile of LMO respectively. **b,** Galvanostatic (0.20 mA/cm^2) and differential chronopotentiograms profile of LAMO respectively. (Reproduced)[129]

Transition metals have also been added to LMO to improve the cell performance. The addition of Fe results in the presence of an additional plateau at high voltages during discharge[131]. The addition of Co has also been proven to stabilise the spinel structure, improve cycle life and the overall cell performance[132]. The addition of Co increases the cost and has decreased investigations using Co as an additive in the LMO structure. Ni addition to the LMO structure is the most common transition metal used for spinel type cathodes. Capacity increases with increasing Mn content and the most popular composition is LiNi$_{0.5}$Mn$_{1.5}$O$_4$ (LNMO) with a capacity of 147 mAh/g. LNMO has very good cycle stability and just one dominant plateau at 4.7 V by comparison with the two of typical spinel cathodes. The reason for the high potential and single plateau is the Ni^{3+}/Ni^{4+} redox couple being pinned at the top of the O-2p bands respectively[133]. CV analysis of LNMO shows the typical

profile of 2 peaks that are close together at 4.6 V and 4.75 V due to the redox couples of Ni^{2+}/Ni^{3+} and Ni^{3+}/Ni^{4+} respectively. The unique feature of LNMO in comparison to standard spinel cathodes is that all the redox activity takes place on Ni rather than Mn as it remains in the +4 state.

LNMO has 2 different structures depending on the fabrication process, an ordered structure ($LiNi_{0.5}Mn_{1.5}O_4$) has a $P4_332$ space group that only has Mn^{4+} ions present and a disordered structure ($LiNi_{0.5}Mn_{1.5}O_{4-\delta}$) has a Fd3m space group that is mainly made up of Mn^{4+} ions but has some Mn^{3+} ions present[135]. The ordered LNMO has a simple primitive cubic structure with Li, Ni, Mn and O_2 occupying the 4a, 12d, 4c and 8c, 24e sites respectively. The disordered state has a face-centred cubic spinel structure with the Li and O_2 atoms in the 8a and 32e sites respectively and the Ni and Mn atoms randomly dispersed in the 16d octahedral sites[134]. The disordered state has an electrical conductivity 2 orders of magnitude greater than the ordered structure resulting in superior electrochemical performance with 80% capacity retention at *6 C*, Figure 2.37[135]. Ceder et al have investigated and reported on the diffusion pathway of lithium in the disordered structure[136].
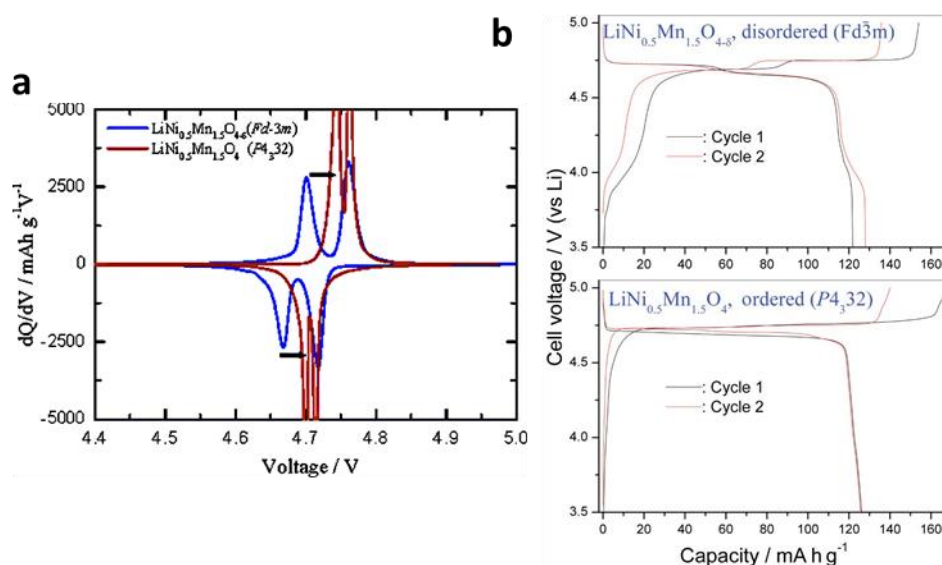
Figure 2.37: a, Differential chronopotentiogram profiles of ordered and disordered LNMO. **b,** Galvanostatic profiles of ordered and disordered LNMO at 75 mA/g at 30°C. (Reproduced)[134]

LNMO is not without its drawbacks like most electrode materials, the preparation of pure LNMO proves difficult due to the formation of $Li_xNi_{1-x}O$ impurity during synthesis which has a negative effect on electrochemical performance[137]. Another issue with the use of LNMO is that most of the standard organic electrolytes used in Li-ion batteries start to

decompose around the redox potential of Ni^{3+}/Ni^{4+} of 4.6 V which is the thermodynamic stability limit of carbonate solvents[138]. Partial substitution of either Mn or Ni in the LNMO electrode has been used by different research groups in order to improve the electrochemical performance. Titanium (Ti) has been substituted into the LNMO structure with improved performance[139]. $LiNi_{0.5}Mn_{1.5-x}Ti_xO_4$ (LNMTO) improves the disorder of the structure to Fd3m which displays faster lithium diffusion, improved rate capabilities and a high operational potential in comparison to standard LNMO. Too much Ti substitution (x > 0.3) reduces the capacity as the Ti atoms block the migration pathway of electrons to the octahedral sites[140]. Fe has also been used to stabilise the LNMO structure for extensive cycling by taking up the tetrahedral sites[141]. The use of both Ti and Fe has also been investigated and it has been revealed that a composition of $LiNi_{0.45}Mn_{1.35}Ti_{0.10}Fe_{0.10}O_4$ shows the best capacity retention due to the single phase mechanism and structural stability, Figure 2.38[142].
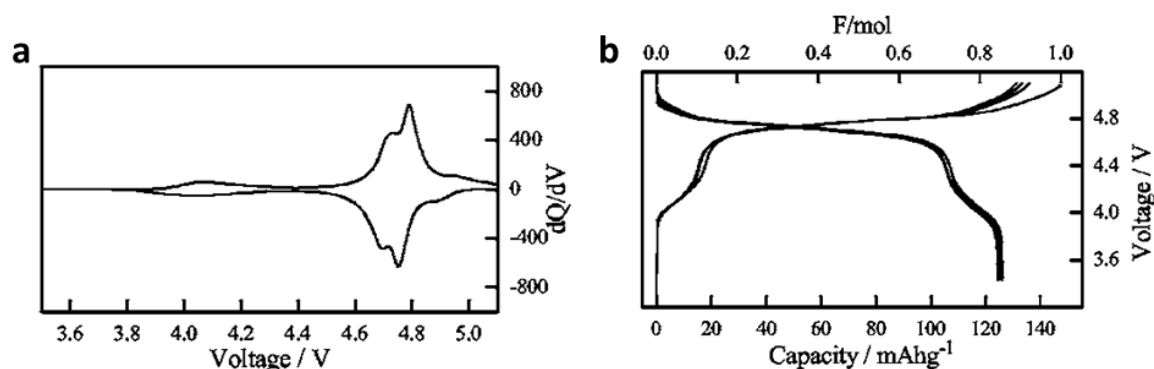
Figure 2.38: a, Differential chronopotentiogram profile and **b,** galvanostatic profile (cycles 1-10) of $LiNi_{0.45}Mn_{1.35}Ti_{0.10}Fe_{0.10}O_4$. (Reproduced)[142]

Other elements have been used for partial substitution, such as Ru, Mg, Cr and F, in LNMO[143]. Raman analysis by Oh et al. demonstrates that Zr and Al partial substitution into LNMO tends to result in an ordered spinel structure while Cr substitution exhibits a disordered structure[144]. The disordered structure is believed to be the reason why Cr partial substitution electrodes have exemplary electrochemical performance due to the higher conductivity, structural and chemical stability properties associated such structures.

Coating the LNMO electrode has also been investigated as a possible strategy to improve the electrochemical performance. The coating material protects the LNMO from degrading when reacting with the electrolyte and prevents side reactions from occurring. ZnO has been used as a protective coating that represses the dissolution of Mn and gathers fluoride anions that

are generated from the decomposition of $LiPF_6$ salt based electrolytes by converting HF to ZnF_2[145]. Such a coating gives a capacity of 137 mAh/g without any loss for 50 cycles in a 55 $^\circ$C environment, Figure 2.39[146]. The thermal stability enhancement is also seen with a ZrO_2 coating at the same temperature of 55 $^\circ$C as the resistance at the electrode/electrolyte interface is decreased. The capacity retention and rate capabilities are drastically increased with a BiOF coating on LNMO as again the coating attracts the HF present in the electrolyte and neutralises it. SnO_2, Au and Ag have also been investigated as coating materials for LNMO, Au is shown to prevent HF from dissolving Mn and improves performance unlike an Ag coating[147]. Li_3PO_4 has also shown to be effective as it prevents the degradation of a solid polymer electrolyte[148].
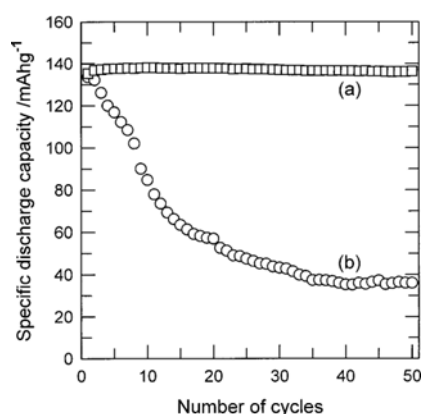
Figure 2.39: Cycle performance of **a,** ZnO coated LNMO and **b,** LNMO at 55 $^\circ$C at 0.4 mA/cm^2. (Reproduced)[146]

Olivine Phosphate

Olivine phosphates ($LiMPO_4$) are a promising cathode material due to their Pnma structure. The phosphorous occupies the tetrahedral sites, with a small disordered hexagonal cubic-packed oxygen array, the transition metal and lithium atoms occupy the octahedral sites and is stored in the [010] direction forming a 1D channel parallel to the b-axis. The transition metal atoms are stored in the b c plane in the [110] direction also forming a chain with the chains bridged together by the phosphate forming a 3D structure[149].

$LiFePO_4$ (LFP) is the most commonly used olivine phosphate cathode to date due to its capacity of 170 mAh/g, low cost, non-toxicity, thermal and cycle stability (small volume change 6.8%)[150]. Delithiation of LFP to $FePO_4$ results in the oxidation of Fe^{+2} to Fe^{+3} with the olivine framework being stabilised by the PO_4^{-3} anions electron withdrawing nature. The 3D structure has lattice parameters of a = 10.33 Å, b = 6.01 Å, c = 4.69 Å[151]. The strength of the P-O covalent bond reduces the interaction to the neighbouring Fe and as a result a stable

operational voltage at 3.5 V is obtained due to the lowering of the redox couple energy[152]. Electrical conductivity of LFP is low by comparison with other cathode materials (10^{-9} S/cm) as the electron transport mechanism occurs via small polaron hopping[153]. The diffusion coefficient is also low for lithium ions (10^{-14} cm^2/s) due to the formation of the LFP/FePO$_4$ interface during delithiation[154].

The mechanism of lithium ion de-intercalation in LFP has been the topic of extensive research. The formation of 2 phases during de-intercalation rather than an unbroken change in lithium content results in a constant voltage during cycling due to the evolution of a fixed activity[155]. Lithium ion diffusion slows down moderately during de-intercalation, at a certain current density, as the surface area of the interface decreases. This results in a concentration polarization increase and eventually the reaction ceases without utilisation of all of the active material leaving a non-utilised core (LFP) and an utilised shell (FePO$_4$) structure, Figure 2.40. Upon discharging, the applied current density which typically does not take into account the loss of active material from the initial charge, results in an eventual over polarization and reaction termination. This leaves a structure with the core LFP from the initial charging with a remnant layer of FePO$_4$ from the subsequent discharge. This core structure of LFP/FePO$_4$ is a dead zone that severely reduces cycle life and contributes to capacity decay at high current densities.
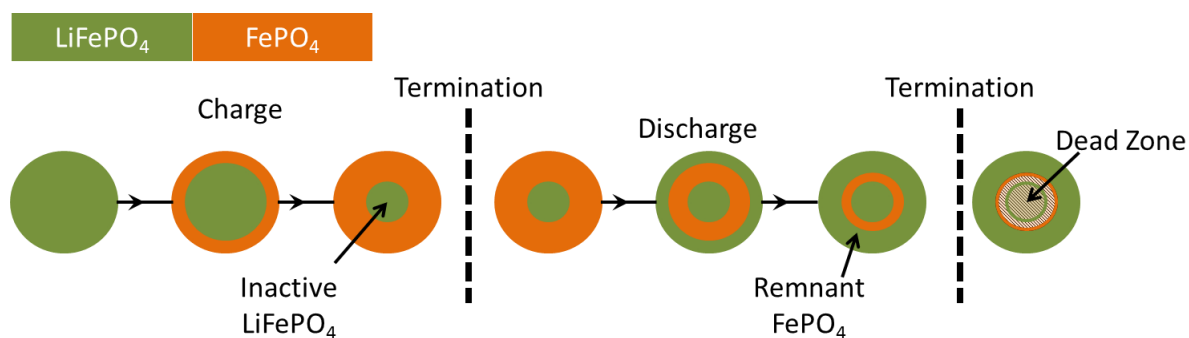
Figure 2.40: Schematic illustration of the "radial model" from the cross section of LFP.

The limitations associated with the 2 phase de/intercalation mechanism are shown to be overcome with the use of nanoparticles as the process undergoes a single phase mechanism[156]. Nano architectures also reduce the lithium ion diffusion length and blockages in the Li 1D channel along the b-axis. Blockages along the 1D channel are normally due to defects such as Fe^{+2} atoms occupying the Li atom sites (d^{Fe}). In a typical hydrothermal fabrication process of bulk LFP ~8% is made up of d^{Fe}. In nanoparticles the number of

defects per particle is substantially smaller leading to a minimal number of blockages by comparison[157]. It is also worth noting that the defect of Li$^+$ atoms occupying the Fe atoms sites (d^{Li}) makes it possible for lithium ions to change diffusion channels and negate the effects from the more prevalent d$^{Fe[158]}$.

The fabrication of one of the first single-crystalline LFP nanowires with a uniform carbon coating of 2 - 5 nm was reported by Zhu et al[159]. The 100 nm diameter LFP nanowires were fabricated from an aqueous solution of Fe(NO$_3$)$_3$, LiH$_2$PO$_4$ and poly(ethylene oxide) (PEO) by electrospinning at an accelerating voltage of 15 kV on stainless steel and thermal annealing at 700 °C in an nitrogen environment. The carbon coating increased the electrical conductivity while also protecting the active material from side reactions that occur with typical organic electrolytes and minimising aggregation of LFP. After 25 cycles TEM analysis displayed structural stability of the LFP nanowires, Figure 2.41. Excellent electrochemical performance was recorded with an initial capacity of 169 mAh/g that stabilised to 146 mAh/g over 100 cycles at a *1 C* rate. A high charge/discharge rate of *10 C* was able to give an unexpectedly high capacity of 93 mAh/g, when considering the rate capabilities issues associated with LFP.
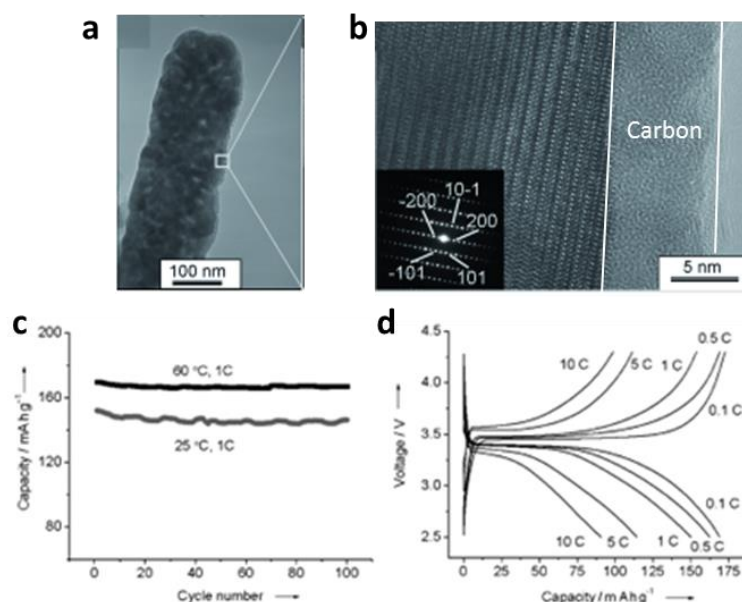
Figure 2.41: a, TEM of single-crystalline LFP nanowire after 25 charge–discharge cycles. **b,** Corresponding HRTEM from the marked region showing that the single-crystalline structure is maintained. Inset: SAED pattern, region of 500 nm in diameter. **c,** Cycling stability at *1 C* rate at room temperature and at 60 °C. **d,** Galvanostatic profiles of LFP at different C-rates. (Reproduced)[159]

The three most frequent strategies used to improve the rate capabilities of LFP caused by its insulating nature and lethargic diffusivity are conductive coatings, nanosizing and metal doping. These strategies are often combined and result in dramatically improved performance as seen in the previous example of nanowires with a carbon coating. Carbon coating is one of the easiest strategies to integrate into the fabrication processes used for LFP. Ball milling is one of the most common synthesis processes for nanoparticle electrode materials and a carbon coated LFP can be easily synthesised with the simple addition of acetone[160]. $FeC_2O_4.H_2O$ reacts with acetone to form a carbon coating on the LFP particles due to the oxygen deficiency in the precursor and reduces the grain size of the LFP when forming the crystalline phase. An initial capacity of 149 mAh/g was obtained which is in agreement with other carbon coated LFP particles. LFP particles synthesised without any acetone showed almost no capacity at *5 C* while the LFP wet milled in acetone gave a capacity of 75 mAh/g at *5 C*. The synthesis process has a significant effect on the properties and composition of the electrode material. Depending on the synthesis process metallic iron phosphate (Fe_2P) can form on the LFP surface which is due to the reduction of LFP to Fe_2P[161]. The Fe_2P increase the conductivity of the LFP cathode and results in exceptional performance. However careful control over Fe_2P formation is needed as large amounts can block the lithium ion diffusion channels[162].

The effect of an additional coating on top of the carbon coating has also been investigated[163]. A simple electroless bath is used to deposit the Sn coating and it is shown to protect the LFP from undergoing chemical corrosive side reactions with the electrolyte and suppress the dissolution of Fe from LFP. Kang et al. coated 50 nm LFP nanoparticles with 5 nm of amorphous lithium phosphate ($Li_4P_2O_7$) to help promote lithium diffusion[164]. The thinking behind such an idea is that LFP undergoes lithiation/delithiation in the [010] direction and the amorphous $Li_4P_2O_7$ would promote de/intercalation in this direction. A composite electrode was made with a 15 wt. % conductive carbon back and 5 wt.% polyethylenetetrafluoride binder. A capacity utilisation of 166 mAh/g was obtained at *2 C* and capacity retention of 80% at a *50 C* rate, Figure 2.42. The cycle stability and rate capabilities showed extremely impressive characteristics with a stable capacity of 140 and 100 mAh/g at *20 C* and *60 C* respectively over 50 cycles. As a proof of concept the conductive carbon black percentage was increased to 60 wt. % to investigate how much the rate performance can improve with the $Li_4P_2O_7$ coating. The 60 wt. % carbon black electrode was cycled 100 times at *197 C* (~18 s) and *397 C* (~9 s) giving capacities of 100 and 60

mAh/g respectively. If a double coating was applied with a metallic conductive layer (e.g. Sn coating) on top of the Li^+ ion enhancer layer of $Li_4P_2O_7$ then that could potentially reduce the extremely high carbon black wt. % needed to achieve idealistic C-rates.
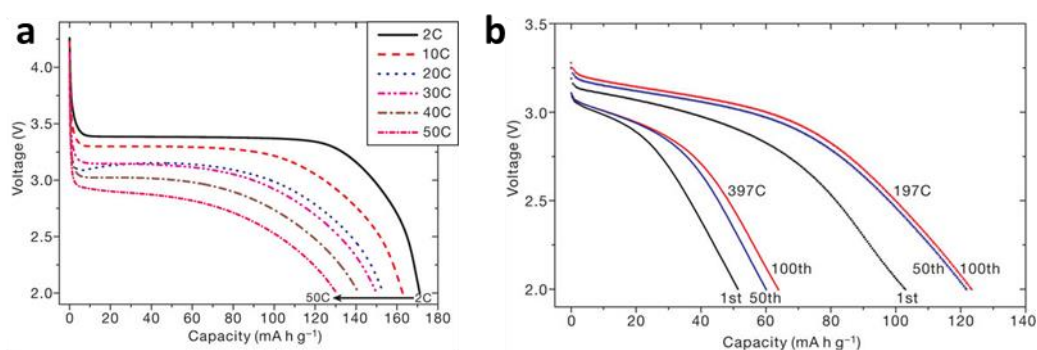
Figure 2.42: a, Discharge profiles of fully charged LFP with $Li_4P_2O_7$ coating at various C-rates. **b,** Discharge profiles of the 1st, 50th and 100th cycles at C-rates of *197 C* and *397 C*. (Reproduced)[164]

Vanadium substitution for Fe in LFP has been shown to increase the initial capacity and stabilise cycle life[165]. V-ion doped LFP with a carbon coating has been synthesised by carbothermal reduction with a V to Fe ion ratio of 0, 1, 2, 3 and 4 at.%[166]. The doping has no effect on the crystalline structure but does decrease the lattice parameters with increasing V-ion content due to the ionic radius of V^{5+} being 0.059 nm which is smaller than both Li^+ and Fe^{+2} whose ionic radii are 0.076 and 0.078 nm respectively. The electrochemical analysis found that the V-ion doping does not have an effect on the electrochemical reaction but does on the ion conductivity, Figure 2.43. The diffusion coefficient increased with increasing V-ion concentration and peaked at 3 at. %. In non-doped carbon coated LFP the ionic conductivity is much smaller than the electronic meaning more energy is required to slow down the electrons and speed up the lithium ions to maintain electro neutrality in the crystal lattice via an internal electric field. The V-ion doped carbon coated LFP reduces the energy required as the lithium difference between the electronic and ionic conductivities is smaller and the energy for nucleation of LFP in the 2 phase region is decreased resulting in better rate capabilities and cycle stability[167]. A long cycle life was reported for the 3 at. % V-ion doping with 98% capacity retention after 250 cycles and no significant fade thereafter for 500 cycles with an initial capacity of 140 mAh/g at *1 C*. The rate capabilities were investigated at *1, 3, 5, 8, 1* and *5 C* for 20 cycles each and the capacity was fully recaptured for the later *1* and *5 C* rates.
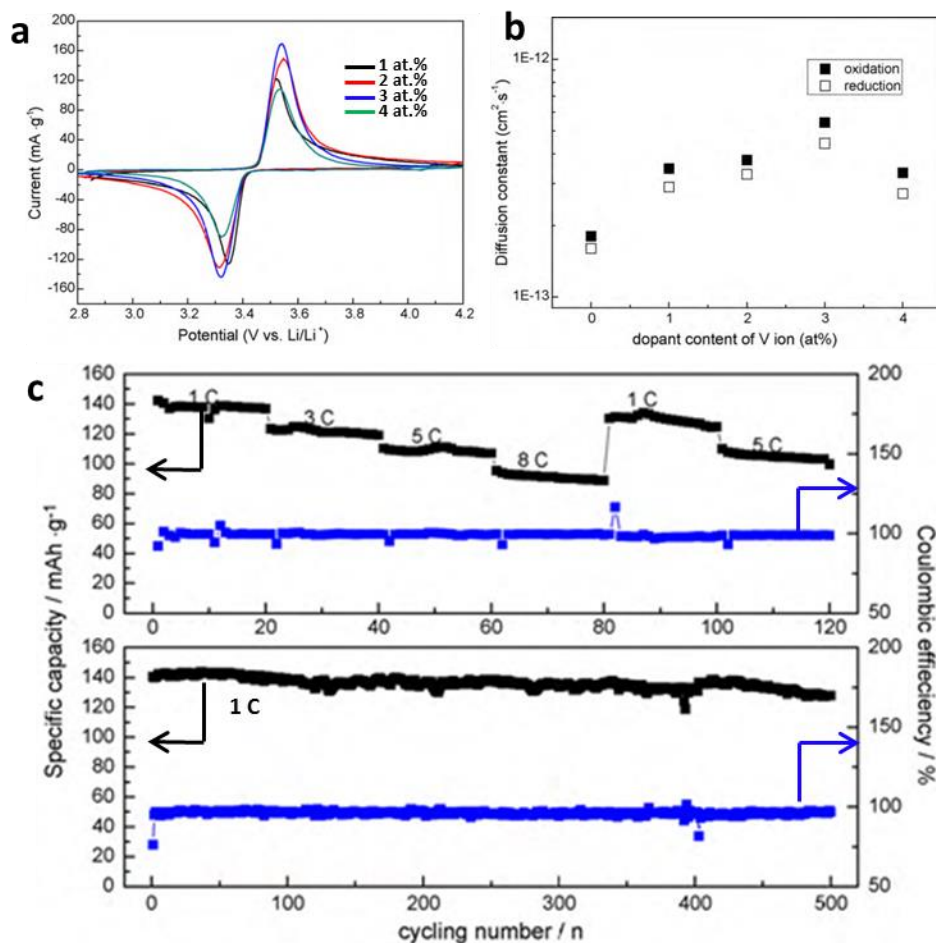
Figure 2.43: a, CVs of various V-ion content with a scan rate of 0.05 mV/s. **b,** Diffusion constant vs. V-ion content of samples. **c,** Rate performance and cycling performance of V-doped sample with 3 at.%. (Reproduced)[166]

Other phosphates such as $LiCoPO_4$, $LiMnPO_4$ and $LiNiPO_4$ have been investigated due to their higher potentials of 4.8, 4.1 and 5.1 V, respectively, however due to their much lower electrical conductivity and diffusion coefficient they have limited capacity at practical rates[168]. The delithiation products of $LiCoPO_4$ and $LiMnPO_4$ are $Co_2P_4O_7$ and $Mn_2P_4O_7$, respectively, which degrade the lifetime and are a safety concern due to oxygen evolution.

Multi-phase Layered Oxide

Vanadium has multiple valence states with oxidation states from 2 to 5, meaning a range of oxide materials can be formed. Vanadium pentoxide (V_2O_5) is a mixed valence material with vanadium in the V^{4+} and V^{5+} states and also has a rich crystalline structure. Orthorhombic V_2O_5 is made-up of layers of VO_5 square pyramids that consist of 6 oxygen atoms, 5 oxygens from VO_5 and 1 oxygen from neighbouring VO_5 pyramid, around a vanadium atom. The core VO_5 square pyramids are connected by sharing corners and edges in the x and z-directions

and the sixth V-O bond is a weak van der Waals force in the y-direction from a neighbouring VO_5 square pyramid that results in a distorted trigonal bipyramid around the V atom.

V_2O_5 as a reversible cathode material for lithium ion batteries was first published by Whittingham et al[170]. The work published showed that lithiation of V_2O_5 via perovskite-like vacancies produced $Li_xV_2O_5$[169a, 170-171]. The multi valence state of V_2O_5 means that multiple phases are formed during lithiation. Small amounts of lithiation (x < 0.13) did not affect the crystalline structure but as lithiation continued the V^{5+} is reduced to V^{4+} resulting in a distorted structure due to bond breaking during phase changes, Figure 2.44. Delmas et al. investigated and published the different phases that were formed during lithiation of V_2O_5[169b]. The lithiation process underwent by V_2O_5 involves 5 phases: α, ε, δ, γ and ω with every Li intercalated equivalent to a capacity of 142 mAh/g.
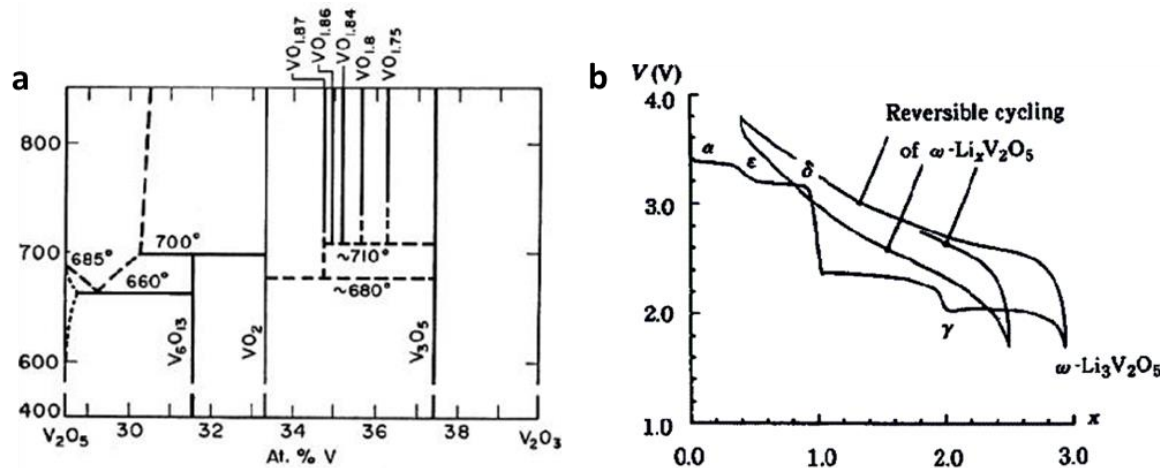
Figure 2.44: a, Partial phase diagram of the vanadium-oxygen binary. **b,** Evolution of $Li_xV_2O_5$ phases with degree of lithium intercalation into V_2O_5 and the cycling of the ω-phase. (Reproduced)[169]

The α and ε-phases appears when x < 0.1 and 0.35 < x < 0.7 respectively. The α-phase has minimal effect on the V_2O_5 structure while the ε-phase involves some buckling of layers. The δ-phase is present when 1.00 < x < 1.8 and involves an increase in the number of layers that have buckled and also an increase in interlayer spacing all while maintaining V_2O_5 fundamental structure. The octahedra VO_6 present in the δ-phase all have one long V-O bond as the V^{5+} is uprooted towards one of the tips of an octahedron oxygen making a coordinated pyramidal that is bonded to other pyramids by weak V-O bonds[172]. At higher concentrations of lithium in the δ-phase the weak V-O bonds are broken and neighbouring oxide layers move and collapse to accommodate the Li^+ ions. In a galvanostatic profile the presence of a δ-phase is indicated with a sudden drop in potential at ~ 3 V to ~2.4 V which is followed by a

plateau during lithiation. Cocciantelli et al. suggested that the α, ε and δ-phases coexist as some particles begin different stages of the lithiation process depending on particle distribution on the current collector and particle size[173].

The γ-phase is formed at $1.9 < x < 2.8$ and corresponds to a small drop in potential at 2.3 V to 2 V in the galvanostatic lithiation profile. More work published by Cocciantelli et al. on V_2O_5 with a particular focus on γ-$Li_xV_2O_5$ shows that structural changes occur during the phase transformation from the δ-phase, Figure 2.45[174]. Galvanostatic cycling was performed with an electrode potential limit at 2 V. The first lithiation profile shows the characteristic plateaus at 3.4 V and 3.2 V followed by a potential drop to 2.3 V and plateau for $\alpha \rightarrow \varepsilon$ and $\varepsilon \rightarrow \delta$ respectively. After the plateau at 2.3 V there is a small potential drop to the electrode cut-off point indicating $\delta \rightarrow \gamma$. The delithiation profile shows a shortening of the $\varepsilon \rightarrow \alpha$ and $\delta \rightarrow \varepsilon$ plateaus and an addition plateau at 3.6 V. The subsequent lithiation cycles show a drop in potential at $\varepsilon \rightarrow \delta$ that is not as severe with a small shoulder appearing at 2.7 V followed by 2 quasi plateaux during the initial lithiation of the δ-phase. The change in galvanostatic profile after the 1st cycle indicates a structural change when cycled to the γ-phase at 2 V.
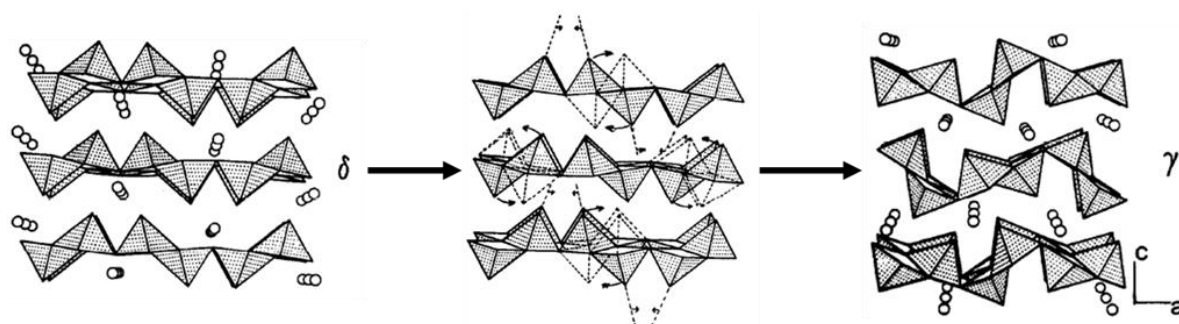
Figure 2.45: Structural relationship between δ- and γ-phases, showing the possible shift of apical oxygen atoms and the consecutive rearrangement of the VO_5 pyramids. (Reproduced)[173]

Saturation of the γ-phase with lithium results in the formation of the ω-phase (x = 3.0). The ω-phase has a cubic rock salt structure and is formed when cycled below 1.9 V[169b]. The ω-phase formation and electrochemical performance was extensively studied by Leger et al. after initial work done by Delmas et al who suggested that the ω-phase would also be suitable as a cathode material[175]. The ω-phase is an irreversible structure because during the 1st lithiation cycle the α, ε, δ and γ phases can all be seen from the galvanostatic profile and on the subsequent delithiation profile no plateau is obvious just a smooth sloped profile. The ensuing cycles all have the same smooth sloped profile indicating a single ω-phase. During

the 1st delithiation of the ω-phase only 2.6 Li are removed meaning that 0.4 Li is trapped during the formation of the phase. The 2nd lithiation profile indicates that $Li_{0.4}V_2O_5$ is only lithiated to $Li_{2.65}V_2O_5$ with good cycle overlap in the ensuing cycles and the reversible theoretical capacity of lithiation formed ω-phase V_2O_5 is 320 mAh/g.

The potential window of 3.8 – 1.5 V was used during galvanostatic cycling at both *C/20* and *C/5* rates, Figure 2.46. The 1st lithiation cycle V_2O_5 is the formation cycle of ω-phase $Li_3V_2O_5$ giving a specific capacity of 450 mAh/g and from the 2nd lithiation/delithiation cycle on the capacity is 335 mAh/g and 320 mAh/g for the 1st and 30th reversible cycles respectively at the *C/20* rate. The *C/5* rate underwent a larger capacity drop from the 1st reversible cycle of 300 mAh/g to 250 mAh/g at the 50th cycle which is expected due to the more intense current density. Leger et al. concluded that the ω-$Li_xV_2O_5$ shows better electrochemical performance in comparison to δ-$Li_xV_2O_5$ and γ- $Li_xV_2O_5$ due to the formation of a very stable tetragonal symmetry in ω-$Li_xV_2O_5$ and not a cubic symmetry as previously reported.
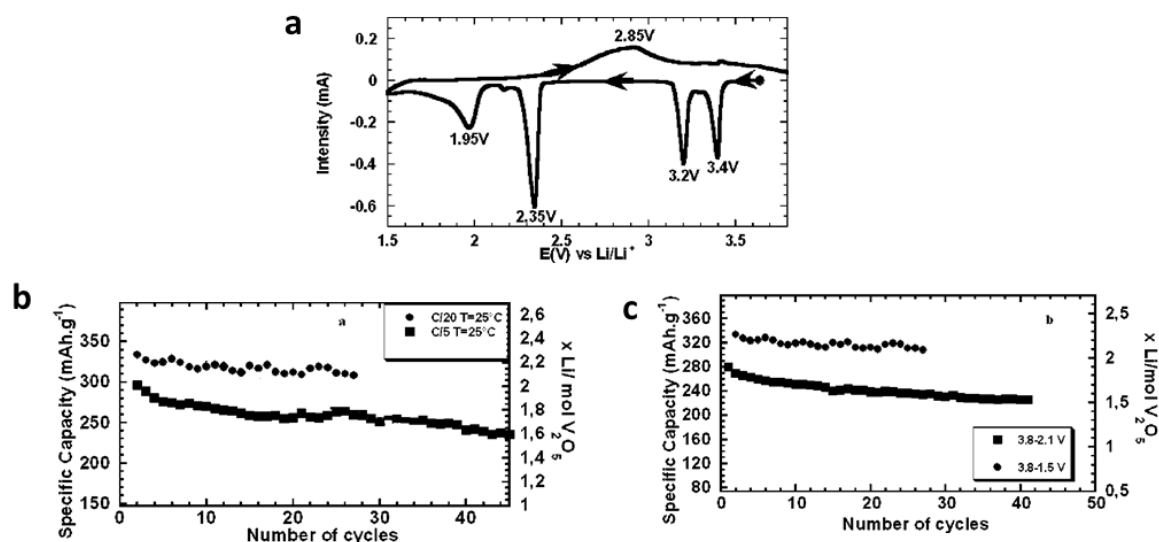
Figure 2.46: a, CV of $Li_xV_2O_5$ to ω-phase at a scan rate of 0.01 mV/s. **b,** Cycle performance at *C/20* and *C/5* rates. **c,** Cycle performance at 2.1 V and 1.5 V cut-off potentials. (Reproduced)[176]

The most common strategies implemented to overcome the poor cycle life and rate capabilities of V_2O_5, due to its low diffusion coefficient (10^{-12} cm²/s) and low electrical conductivity (10^{-5} S/cm), are nanoarchitectures, conductive coating and doping[169a, 176]. As seen with the other electrode materials previously discussed, these strategies are often combined with desirable outcomes. One of the most impressive reports from such a strategy

is by Chao et al[177]. CVD is used to fabricate 3D ultrathin graphite foam (UGF) current collector. V_2O_5 was deposited onto the 3D UGF using a solvothermal synthesis technique which resulted in the nanosized V_2O_5 deposit, with a 0.7 mg/cm^2 loading, having an arrow-tail like hierarchal structure. A 15 nm conductive poly(3,4-ethylenedioxythiophene) (PEDOT) shell was electrodeposited onto the UGF/V_2O_5 to preserve the structure and improve the electron transfer and decrease electrode polarization, Figure 2.47.
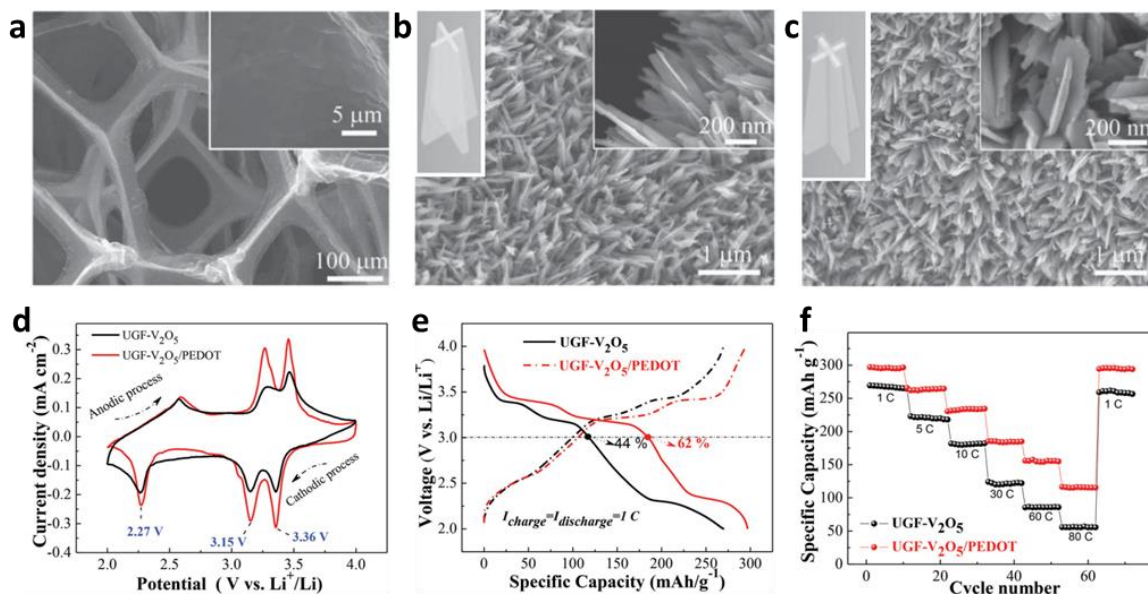
Figure 2.47: SEM images of **a,** UGF; **b,** UGF/ V_2O_5; and **c,** UGF/ V_2O_5 with PEDOT coating. UGF/V_2O_5 and UGF/V_2O_5-PEDOT comparison **d,** CV curves at a scan rate of 0.02 mV/s; **e,** galvanostatic profiles at *1C*; and **f,** rate performance at various C-rates. (Reproduced)[177]

CV analysis and galvanostatic cycling in the 4.0 – 2.0 V potential window meant that V_2O_5 was cycled to γ-Li$_2$V$_2$O$_5$ with a theoretical capacity of 284 mAh/g. The peaks present in the CV are consistent with the galvanostatic profile and correspond to the $\alpha \rightarrow \varepsilon$, $\varepsilon \rightarrow \delta$ and $\delta \rightarrow \gamma$ reductions at 3.36, 3.15 and 2.27 V respectively. The electrochemical performance of the core-shell UGF/V_2O_5-PEDOT cathode was compared to the uncoated UGF/V_2O_5 cathode, which revealed that 62% of the 297 mAh/g capacity accessed at a *1 C* rate was obtained over 3 V meaning that a higher energy density was achieved for the core-shell cathode in comparison to the uncoated cathode that acquired 44% of the 264 mAh/g at *1 C*. The rate capabilities of the core-shell cathode were rigorously tested up as high as *80 C* (45 s) with a very stable capacity of 115 mAh/g. The cycle life was stable and capacities of 265 mAh/g and 163 mAh/g at *5 C* (500 cycles) and *60 C* (1,000 cycles), respectively, were achieved.

Doping of V_2O_5 is another strategy that has been extensively researched and has shown promise when cations such as Ni, Cu, Ag, Mn and Sn used as dopants. The substitution of the vanadium ion with the cations has a direct effect on the electronic structure and the crystalline lattice which in turn affects the electrochemical performance. The replacement of the vanadium ion with Ni^{2+} ions results in an increase in the lattice constant and a stabilisation of the structure that relates to an electrochemical performance of 262 mAh/g at *1 C* and a 0.2% capacity fade per cycle[178]. Mn ion substitution results in oxygen vacancies that increase Li^+ ion diffusion and electronic conductivity while the use of metallic ions such at Cu and Ag results in similar improvements in material properties[179]. Sn doping has also been shown to stabilise cycling at 500 mA/g (*1.76 C*) for 50 cycles to give a capacity of 334 mAh/g[180]. This is believed to be due to the expansion of the crystalline lattice and an increase in the amount of V^{4+} ions, needed to balance the net charge, which gives rise to more oxygen vacancies which increases the Li^+ diffusion and electronic conductivity.

A more detailed study on the effect of Sn doping concentration (0%, 2%, 4% and 8%) on the formation of V^{4+} and oxygen vacancies was carried out by Li et al[181]. The XRD, FESEM and XPS analysis were carried out to determine the doping effect on the crystalline lattice, morphology and oxidation states. The lattice increased along the x, y and z directions with increase Sn^{4+} concentrations as expected due to the Sn^{4+} ion having a larger ionic radius than V^{5+}. The size of the $Sn_xC_2H_4O_3V$ precursor particles decreased from 8 μm to 3.5 μm and the porosity of $Sn_xV_{2-x}O_{5-y}$ increased with increasing Sn content. The ratio of V^{4+}:V^{5+} increases with Sn concentration as Sn^{4+} ions occupy the V^{5+} sites and as a result oxygen vacancies are produced which are considered fast channels for Li^+ diffusion and electron transport. The 4% Sn doping, $Sn_{0.04}V_{1.96}O_{5-y}$, showed the best electrochemical performance in the 4.0 – 2.0 V potential window where the cathode was cycled to the $γ$-$Li_2Sn_{0.04}V_{1.96}O_{5-y}$ phase as verified by the CV peaks and galvanostatic plateaux, Figure 2.48. The rate capabilities were investigated at 50 (C/5.68), 100 (C/2.84), 200 (C/1.42), 500 (*1.76 C*), 1,000 (*3.52 C*) and 2,000 mA/g (*7.04 C*) currents and gave stable capacities of 277, 272, 251, 220 and 190 mAh/g respectively (*1 C* equal to 284 mAh/g ($γ$-$Li_2V_2O_5$)). The cycle stability at 200 mA/g current showed a capacity fade of 0.36% per cycle and a capacity of 212 mAh/g after 50 cycles.
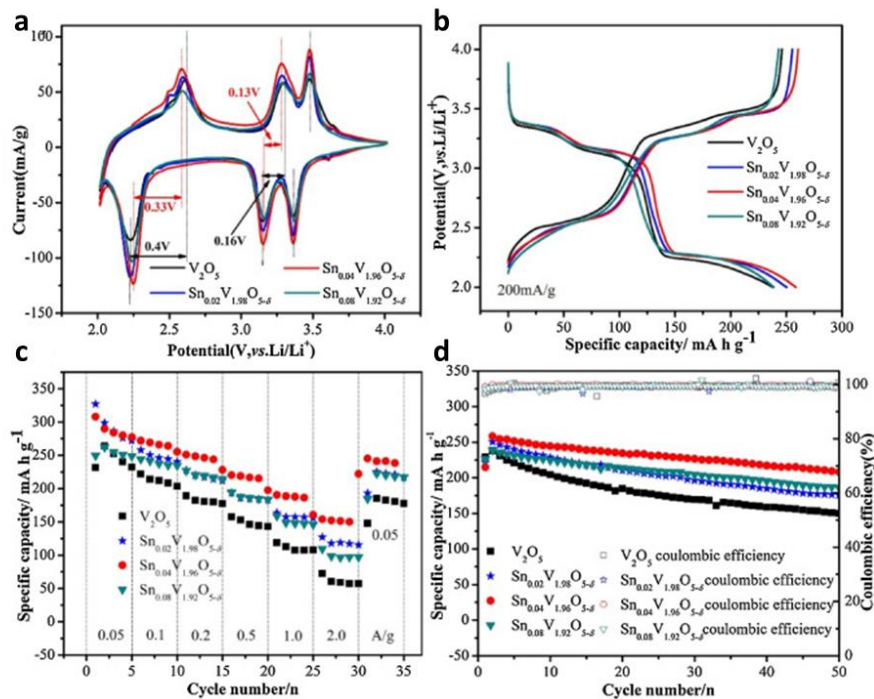
Figure 2.48: Electrochemical performance of all V_2O_5 electrodes with various Sn content. **a,** CV's at a scan rate of 0.1 mV/s. **b,** Galvanostatic profile at 200 mA/g. **c,** Rate performance at various current densities. **d,** Cycle performance at 200 mA/g. (Reproduced)[181]

Electrolyte

An ideal electrolyte could be considered an inert component of a battery as it facilitates the transport of ions between electrodes without contributing to the net energy storage and Faradaic processes that occur inside the electrode. The criteria for an ideal electrolyte are:

1. Good ionic conductors that enable fast Li^+ ion transport and a good electronic insulator for minimal self-discharge.
2. Good solvation of Li^+ ions.
3. Wide electrochemical window to ensure no electrolyte degradation at the working potentials of the cathode and anode i.e. larger electrochemical window electrodes with a larger difference in potential can be used to maximise cell voltage.
4. Chemically inert to cell components such as electrodes, current collectors, electrode additives, separator and cell packaging.
5. Thermally stable in the operating environment.
6. Nontoxic and environmentally friendly.
7. Form a stable electrolyte interface layer.

Electrolytes can be classified as follows:

1. Organic Electrolyte
   - Liquid
     - Lithium salts dissolved in an organic solvent or solvent mixture.
   - Polymer
     - Lithium salts dissolved in an organic solvent in a polymer network that is either in solid or gel form.
2. Aqueous Electrolyte
   - Lithium salts dissolved in water.
3. Inorganic Solid Electrolyte
   - Lithium based glass and glass-ceramic materials.
4. Ionic liquid Electrolyte
   - Lithium salts dissolved in ionic liquid.

The focus of this review will be on liquid organic and aqueous electrolytes.

Organic Electrolyte

Organic electrolytes have been the electrolyte of choice since the first commercial Li-ion battery was introduced by Sony. The choice of lithium salt has a significant effect on the properties of the electrolyte and therefore the electrochemical performance, Table 2.1. To allow the transport of Li$^+$ ions in the electrolyte the salt needs to completely dissolve and dissociate throughout the electrolyte. To ensure suitable dissolution the lithium salt is made up of a complex stabilising anion. The anion needs to be chemically and thermally stable, inert during the electrochemical redox reaction of the battery and resistant to hydrolysis. The dissolution of the lithium salt heightens the complexity of the electrolyte system which can cause changes to the physico- and electro-chemical properties of the solvent through intermolecular forces and solvent reactivity[182].

Aluminium is typically used as the current collector for the cathode material because of its high electrical conductivity, low cost and low weight. Aluminium and its native oxide layer have a rather low oxidation potential and can undergo anodic aluminium dissolution at potentials > 3.8 V which would typically rule out its use in lithium ion batteries due the disintegration of the electrical aluminium current collector connection. The use of aluminium as a cathode current collector is enabled by a passivation layer that is formed by a chemical or electrochemical reaction with the electrolyte[183]. The passivation layer that is typically formed with aluminium is aluminium oxy-fluoride due to the lithium salt anion containing fluorine[184]. The anion of the lithium salt is critical not just for the formation of a passivation layer on the aluminium current collector but also on the composition of the SEI layer formed on the anode material.

Lithium hexafluorophosphate (LiPF$_6$) is one of the most common salts used in commercial ion batteries[185]. LiPF$_6$ is used as a salt for lithium ion batteries because of its high ionic conductivity in organic solvents in comparison to other salts and the ability to prevent aluminium corrosion by forming a passivation layer on the aluminium cathode current collector[186]. LiPF$_6$ electrolytes also have some drawbacks such as low thermal stability and it is not suitable for operation in environments where the temperature is > 50 $^{\circ}$C, as LiPF$_6$ will decompose and result in rapid capacity fade and potential thermal runaway[187]. A fire as a result of thermal runaway would also result in toxic by-products. LiPF$_6$ is in equilibrium with its decomposition products and favours the decomposition products at elevated temperatures.

$$LiPF_6 \leftrightarrow PF_5 + LiF \qquad\qquad (2)$$

PF_5 is a strong Lewis acid and has been reported by Sloop et al. to help ring opening of cyclic carbonates, used as solvents, leading to further degradation of electrolyte[188]. The decomposition temperature of solid $LiPF_6$ is about 100 °C. The reason for the drop in decomposition temperature of $LiPF_6$ when dissolved in solvent is due to the intermolecular interactions and the formation of insoluble LiF which enhances salt degradation[189].

$$PF_5 + H_2O \rightarrow 2HF + POF_3 \qquad\qquad (3)$$

$LiPF_6$ also reacts readily with trace amounts (ppm) of water[190]. The PF_5 attacks the lone pair of electrons in the oxygen in the water molecule and decomposes to form hydrofluoric acid (HF) that can attack and rapidly corrode all components of the battery cell. A cascade reaction can happen and result in HF reacting with the organic solvent to form a highly toxic fluoro-organic and other toxic species.
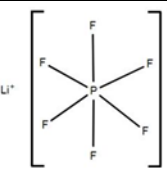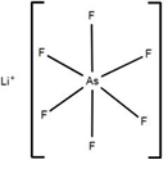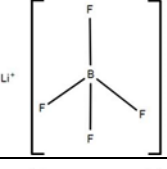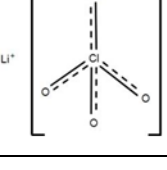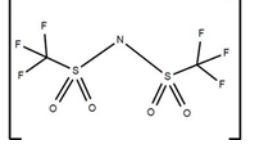
A number of lithium salts were looked at for their use in the first generation of lithium ion batteries. Lithium hexafluoroarsenate ($LiAsF_6$) has some advantageous properties in comparison to $LiPF_6$ as it is has a larger thermal stability window, due to the strong As-F bond there is a large electrochemical window and resistant to hydrolysis[191]. $LiAsF_6$ has a slightly larger ionic conductivity and better cycle performance. The major drawback and prevention of $LiAsF_6$ use as a lithium salt in electrolytes is due to the potential formation of a highly toxic AsF_3 molecule[192].

Lithium tetrafluoroborate ($LiBF_4$) has better thermal stability, reduced activity towards hydrolysis, improved passivation layer on Al cathode current collector and a larger electrochemical window[193]. Its low ionic conductivity due to a low dissociation in organic solvents and the formation of a SEI layer that is 2 times more resistant, but reduces with decreasing temperature, has blocked its deployment in electrolytes[194].

Lithium perchlorate ($LiClO_4$) has numerous favourable characteristics such as stability against hydrolysis, high ionic conductivity, good thermal stability, passivation of Al current collector and is fluorine free which prevents the formation of toxic decomposition products[195]. However, $LiClO_4$ is banned in the use of lithium-ion batteries as the very strong oxidizing ability of the ClO_4^- anion and its interaction with organic solvents leads to a high risk of explosion[196].

Lithium bis(trifluoromethanesulfonyl)imide LiN(SO$_2$CF$_3$)$_2$ (LiTFSI) has was first synthesised in the 1980s before commercial lithium ion batteries[197]. The main features of LiTFSI include very stable against hydrolysis, high solubility in organic solvents, high thermal stability, large electrochemical window and comparable ionic conductivity with LiPF$_6$[198]. The critical flaw is its inability to form a passivation layer on Al. It has been hypothesised that a passivation layer is not formed due to the anion being too stable and not donating a fluoride ion to form aluminium (oxy-) fluoride passivation layer or that the initial Al(TFSI)$_3$ complex formed is dissolved into the electrolyte[193b, 199]. Recent studies have shown that increasing the concentration > 1.8 M results in the formation of a stable passivation layer of LiF on Al[200]. The use of a fluorine base electrolyte additive to a LiTFSI electrolyte has also resulted in the passivation of the Al current collector[201].

Table 2.1: Properties of 1st generation Li salts in organic electrolytes for Li-ion battery systems.

Li Salt	Structure	M$_w$ g	σ (1M EC/DMC 25ºC) mS/cm	E$_{ox}$ V	Al passivation	Stable against Hydrolysis	T$_{decomp}$ ºC	Reference
LiPF$_6$		151.9	10.7	4.2-4.5	Yes	Unstable	80	[202]
LiAsF$_6$		195.9	11.1	5.1	Yes	Stable (In nonaqueous electrolyte)	240	[202]
LiBF$_4$		93.9	4.9	5.2	Yes	Unstable	132	[202]
LiClO$_4$		106.4	8.4	4.6	Yes	Stable	> 236	[202]
LiTFSI		287.1	9.0	5.3	No	Stable	360	[186]

The anion is the only degree of freedom in the lithium salt. Modifying the chemical structure on the anion of the 1st generation lithium salts can help improve some of their performance limiting properties. $LiPF_6$ has been successfully employed as the lithium salt of choice even with the compromised associated with it.

In the second-generation wave of Li ion salts, Table 2.2, efforts have been made to modify the anion by adding organic ligands to some of the fluorine atoms for stabilisation. Lithium tris(pentafluoroethyl)-trifluorophosphate $LiPF_3(CF_2CF_3)_3$ (LiFAP) is a commercially available derivative of $LiPF_6$. The perfluoroalkyl substitutes have strong electron withdrawing property that results in a small drop in ionic conductivity while maintaining a high solubility that is characteristic of $LiPF_6$[203]. The bulky perfluoroalkyl substitute suppresses the anion propensity to hydrolysis. The SEI layer formed on graphite anodes has the same composition as $LiPF_6$ salt; however the SEI layer is completely formed after 1 cycle ensuring minimal exposure of the electrolyte with the graphite surface and extending cycle life as a result[204]. LiFAP improves some of the issues that are associated with $LiPF_6$ however the viability of its use is hindered by its cost and high molecular weight where almost 3 times the mass of $LiPF_6$ is needed to make a 1 M solution of LiFAP.

A lot of attention has been given to the development lithium borate salts in recent years due to the opinion that the limitations of the 1st generation $LiBF_4$ salt can be overcome[205]. Lithium bis(oxalate)borate $LiB(C_2O_4)_2$ (LiBOB) as a electrolyte salt for Li-ion batteries was filed and published as a patent in 1999 and 2003 respectively[206]. LiBOB is susceptible to hydrolysis however since there is no fluoride present in the anion the products do not contain HF and are not very chemically active. The electrochemical window limit is narrower (4.5 – 4.2 V) than $LiBF_4$ but is within the acceptable range for standard cathodes. A high stability potential of 6.0 V is recorded for an Al current collector in LiBOB salt electrolytes. The native oxide layer, Al_2O_3, on the Al is not dissolved by the electrolyte and an additional layer of $AlBO_3$ is formed on top of on the native oxide[207]. A unique property of organic electrolytes containing LiBOB salts is that there are 2 distinct stages for the formation of the SEI layer[208]. The 1st stage starts at 1.8 – 1.6 V, the oxalate ligands are reduced to a protective layer on the anode. The 2nd stage, the organic solvent is reduced at 0.8- 0.7 V and forms on top of initial layer. This means that the anode is protected before solvent reduction. As a result propylene carbonate (PC) solvent can be used in an electrolyte with LiBOB salts without the risk of exfoliation of a typical graphite anode. The solubility of LiBOB is lower than $LiBF_4$ with a solubility of 0.362 M in PC but has an ionic conductivity of 6.76 x 10^{-3}

S/cm which is close to that of 1 M LiPF$_6$[209]. The concentration of the LiBOB salt can be increased to 1 M in ethylene carbonate (EC) mixtures with linear carbonates. The thermal stability of LiBOB salt electrolytes has an increased thermal stability of around 170 °C[194b]. It is worth noting that there has been evidence to suggest that LiBOB is incompatible with cobalt concentrated based cathodes[210]. It is thought that cobalt can catalyses the decomposition of the BOB$^-$ anion during anodisation and is the reason why LiNi$_{0.85}$Co$_{0.10}$Al$_{0.05}$O$_2$, LFP and LMO perform so well at elevated temperatures.

The major drawback of the 1st generation lithium imide salt, LiTFSI, was its inability to form a passivation layer with Al at cathode working potentials. Modification of the anion has resulted in the commercialisation of two new lithium imide salts, lithium bis(perfluoroethylsulfonyl)imide LiN(SO$_2$CF$_2$CF$_3$)$_2$ (LiBETI) and lithium bis(fluorosulfonyl)-imide LiN(SO$_2$F)$_2$ (LiFSI)[199c, 211]. The solubility of all imide salts in organic solvents is high in comparison to other salts due to the imides containing numerous heteroatoms and electro-withdrawing terminal –CF$_3$ groups that are able to delocalise the charge on the imide[198b, 212]. Both salts are resistive against hydrolysis and have remarkable ionic conductivity at temperatures below 0 °C due to their higher lithium-ion transference number[213]. The ionic conductivities of the salts at a room temperature are comparable to that of LiPF$_6$ in the same organic solvent. LiFSI has better thermal stability than LiPF$_6$ with decomposition beginning at > 180 °C however there are no safety benefits with its use in an electrolyte as its combustion performance is the same as LiPF$_6$ based organic electrolytes. The SEI layer formation on graphite for LiFSI begins at the same potential as LiTFSI and the commercial standard, LiPF$_6$, at 0.8 - 0.7 V which is the organic solvent reduction potential[194b]. LiBETI begins to form an SEI layer at 1.0 - 0.9 V which means the graphite anode is protected before the reduction of the organic solvent which helps to reduce or prevent exfoliation[214]. LiBETI undergoes Al dissolution at ≥ 4.5 - 4.6 V which is acceptable for the majority of cathode materials[184, 215]. The potential for the beginning of Al dissolution using LiFSI varied between 3.3 - 3.7 V, which is believed to be due to impurities in the salt and if the concentration of LiCl is lowered to < 50 ppm the Al corrosion potential can be increase to 4.0 – 4.2 V[211, 213].

The use of computational chemistry based on quantum chemistry to tailor lithium salts exclusively for lithium ion battery applications has resulted in the synthesis of imidazolide lithium salts from low cost precursors[216]. These salts are very stable due to the heterocyclic anion containing bonds that are all covalent and multiple bonds being conjugated which is
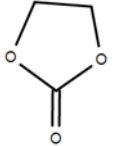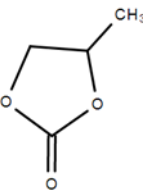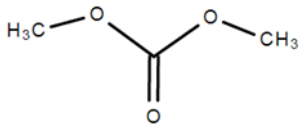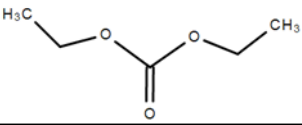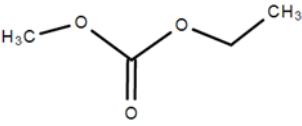
similar to imides without delocalised bonds and conjugation. A commercially available imadazolide lithium salt is 4,5-dicyano-2-(trifluoromethyl)-imidazolide $Li(CN)_2C_3N_2CF_3$ (LiTDI). The thermal stability of LiTDI is up to > 250 °C and has Al corrosion resistant up to 4.75 V, due to the native oxide not being removed, which is more than acceptable for lithium ion battery systems[186, 217]. The SEI layer formation begins < 1.0 V, similar to LiBETI and exfoliation of the graphite anode is greatly reduced as the anode is protected prior to solvent reduction at 0.8 - 0.7 V[218]. The most interesting property of this lithium salt is that its peak ionic conductivity is at a low salt concentration (0.5 - 0.7 M) when compared to 1 M for the conventional $LiPF_6$ salt. LiTDI also has a high transference number of $0.5 – 0.6$ meaning that when the peak ionic concentration is combined with a typical organic solvent solution it has a higher ionic conductivity than $LiPF_6$ due to $LiPF_6$ having a lower transference number of 0.3 - 0.4[185, 219].

Table 2.2: Properties of 2nd generation Li salts in organic electrolytes for Li-ion battery systems.

Li Salt	Structure	M_w	σ (1M EC/DMC 25°C)	E_{ox}	Al passivation	Stable against Hydrolysis	T_{decomp}	Reference
		g	mS/cm	V			°C	
LiFAP		452.0	8.2	4.5-4.5	Yes	Stable	180	[203]
LiBOB		193.8	7.5	4.3-4.5	Yes	Unstable	290	[220]
LiBETI		387.1	5 (EC/DMC/EMC)	>5.5	No (Al dissolution ≥ 4.5-4.6 V)	Stable	350	[221]
LiFSI		187.1	12 (0.85 M)	5.6	No (Al dissolution 4.0-4.2 V)	Stable	>200	[222]
LiTDI		192.0	6.7	4.8	Yes	Stable	>250	[186]

Another critical part of the electrolyte solution is the choice of solvent. Organic solvents used almost exclusively for lithium ion batteries are aliphatic carbonates. Aliphatic carbonates are dipolar aprotic solvents that generally have a high dielectric constant and low viscosity[183, 185, 223]. These solvents can be separated into 2 groups based on these properties, Table 2.3. Cyclic carbonates have a high dielectric constant that allows for high lithium salt dissociation but have a low viscosity. Linear carbonates have low viscosities that allows for fast Li$^+$ ion transport and good wetting for impregnation of the electrode material. Ethylene carbonate (EC) and propylene carbonate (PC) are the main cyclic carbonates that have been investigated as a solvent of lithium salts[223a, 223d]. EC is solid at room temperature and has a melting point of 36 ^{o}C, however as mentioned above the dissolution of lithium salts in solvents can change the physico- and electro- chemical properties through intermolecular forces and solvent reactivity[224]. 1 M LiPF$_6$ in EC is liquid at room temperature however the viscosity of the electrolyte solution is too high and results in an electrolyte with too low an ionic conductivity. Linear carbonates such as diethyl carbonate (DEC), dimethyl carbonate (DMC) and ethylmethyl carbonate (EMC) have low viscosities and low dielectric constants meaning they only meet half the properties need for an organic electrolyte. Mixing the cyclic and linear carbonates results in solvent that can dissolve an appropriate amount of lithium salt and have a practical ionic conductivity[202].

Table 2.3: Properties of cyclic and linear solvents used in Li-ion battery systems.

Solvent	Structure	T_{mp}	T_{bp}	Dielectric constant / ε (25°C)	Dipole moment	Density (25°C)	Molar Volume (25°C)	Reference
		°C	°C		μ/D	g/cm³	dm³/mol	
Ethylene Carbonate (EC)		36	248	89.8 (40 °C)	4.9	1.32 (40 °C)	62	[225]
Propylene Carbonate (PC)		-49	242	64.9	4.94	1.20	84	[225]
Dimethyl Carbonate (DMC)		5	91	3.1	0.88	1.06	84	[225]
Diethyl Carbonate (DEC)		-53	126	2.8	0.94	0.97	122	[225]
Ethylmethyl Carbonate (EMC)		-74	110	3.0	0.89	1.01	104	[225-226]

Aliphatic carbonates have a large oxidation potential in comparison to esters and ethers and are stable up to 4.5 V due to the passivation of the Al current collector. The passivation of the Al current collector is critical for the operation of the cathode as highlighted earlier. No passivation layer is formed on noble metals, such as Au and Pt, and they undergo anodic reactions at potentials below 4 V making them unsuitable as current collectors in organic electrolytes, Figure 2.49[227]. The high oxidation state of the aliphatic carbonates means high reactivity at potentials below 1.5 V on the anodes surface. The reduction of the electrolyte onto the surface of the anode is the SEI layer and acts as a filter that only allows Li$^+$ ions through. This means the anode surface, such as graphite, is protected from further interaction with the electrolyte and held together by the SEI layer meaning exfoliation is prevented.
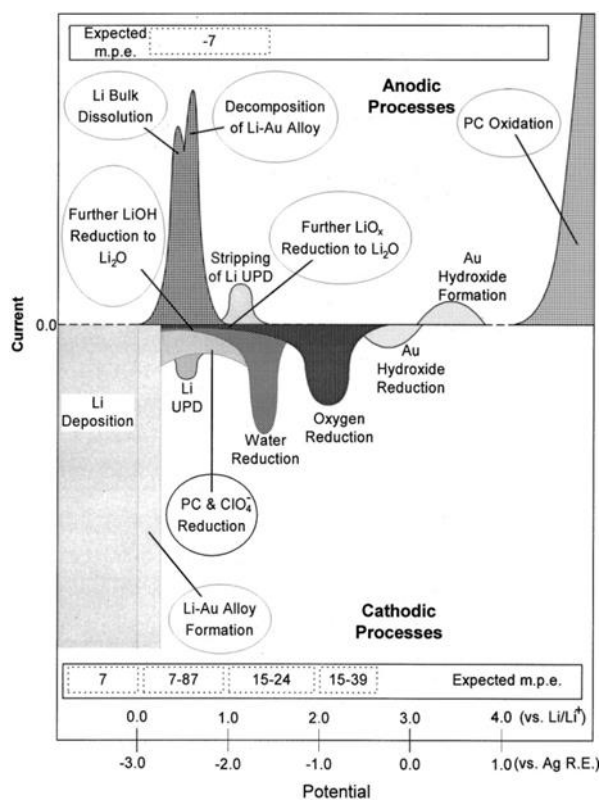
Figure 2.49: Schematic of the various electrochemical processes of a gold electrode in a PC/LiClO₄ solution. (Reproduced)[227c]

All solvents contribute to the SEI layer composition however EC is known to be critical in the formation of a stable SEI that results in low irreversible capacity in the initial cycles for SEI layer formation and low capacity fade for subsequent cycles[228]. Cyclic carbonates easily form a solvation shell around the Li^+ ions in comparison to linear carbonates[229]. PC is very similar in structure to EC and some of the critical characteristics for an electrolyte have more propitious values. PC has a lower melting point, better ionic conductivity at lower temperatures and a similar dielectric constant to EC[224]. The major constriction with the use of PC is its inability to form a stable SEI layer on a graphite anode which leads to exfoliation and severe capacity fade[18, 202, 230]. The inability of PC to form a stable SEI layer is due to the product of reduced PC, lithium propylene dicarbonate (LPDC), as the methyl group hinders the formation of a closely packed layer that is able to bond strongly to the graphite surface therefore making it more soluble in the electrolyte, Table 2.4[231]. There is no such methyl group present in the reduced product of EC, lithium ethylene dicarbonate (LEDC). LEDC is able to form a dense SEI layer that is strongly bonded to the anode surface and highly insoluble.

Table 2.4: Cyclic and linear solvents reduction products.

Solvent	Reduction product	Reduction product Structure
Ethylene Carbonate (EC)	Lithium ethylene dicarbonate (LEDC)	
Propylene Carbonate (PC)	Lithium propylene dicarbonate (LPDC)	
Dimethyl Carbonate (DMC)	Lithium methyl carbonate (LMC)	
Diethyl Carbonate (DEC)	Lithium ethyl carbonate (LEC)	
Ethylmethyl Carbonate (EMC)	LMC + LEC	

Performance enhancing electrolyte additives are an easy and cheap way to improve electrochemical performance. An electrolyte additive is classified as a substance that does not exceed > 10% in either volume (v/v %) or weight (w/w %) of the electrolyte. Additives that exceed 10% are considered co-solvents. Since electrolyte additives are almost completely consumed in either the formation of the SEI layer or the scavenging of the intermediate products from the solvent. It is almost impossible to detect these electrolyte additives in commercial batteries and are often a trade secret. The identity of such additives has been discovered either by a trial and error approach or by using theoretical calculations using LUMO or electron affinity[224]. Electrolyte additives can be broken down into 2 types, redox or reactive additives.

Redox additives are reduced/oxidised at specific potentials and are used to form a strong SEI layer on the anode or cathode prior to solvent reduction or attack respectively[232]. Redox additives are also used to prevent overcharging by undergoing a redox shuttle at a potential slightly higher than the cathode cut-off potential. The excess current forces the redox shuttle rather than forcing excess intercalation/deintercalation which is detrimental to cycle life[233]. These additives have a reactive electron withdrawing groups that react at higher potentials. The redox additives used to protect the anode and cathode are generally polymerised easily such as vinylene carbonate (VC), vinyl ethylene carbonate (VEC) and fluorinated ethylene

carbonate (FEC) for SEI layer formation on the anode and 1,3-propane sulfone (PS) for the cathode[234]. Interestingly VC has shown to be critical in the cycle stability of Ge, a next generation anode material, as its presence results in the transformation of a nanowire architecture into a porous architecture which ensures mechanical stability during cycling[60]. Lithium salts have also been used to form a more stable SEI layer on the anode and cathode depending on the salts anion properties. $LiNO_2$ with VC has been used to improve the SEI layer formed at lower potentials while LiBOB salt uses the BOB$^-$ anion to combine with the transition metal to form a stable insoluble layer on the cathode[235].

Reactive electrolyte additives are used to stabilise the SEI by scavenging intermediate products such as anions or water molecules from the solvent. They can also react with parts of SEI composition to form a more stable and thin SEI layer such as lithium alkyloxide and lithium alkyl dicarbonate. Anions such as F$^-$, O_2^- and O_2^{2-} are critical in the formation of a typical SEI layer that is made up of Li_2CO_3, Li_2O, Li_2O_2 and LiF[236]. Crystal LiF is known to be diminishing to the stability of the SEI layer[237]. The most common anion receptor is tris(pentafluorophenyl)borane (TPFPB) where it reduces the amount of LiF formed by scavenging F$^-$ ions and significantly improves the overall electrochemical performance of the battery, Figure 2.50[238]. Other additives used to scavenge destructive anions and intermediates are hexamethyldisilazane for water and heptamethyldisilazane for HF[239]. Phosphorous based flame-retardant electrolyte additives also work on the principle of scavenging[240]. At elevated temperatures phosphorous compounds are evaporated and undergo homolytic cleavage and form P$^•$ radicals which scavenge the reactive hydrogen and oxygen radicals that are critical for the combustion chain reaction, Figure 2.51
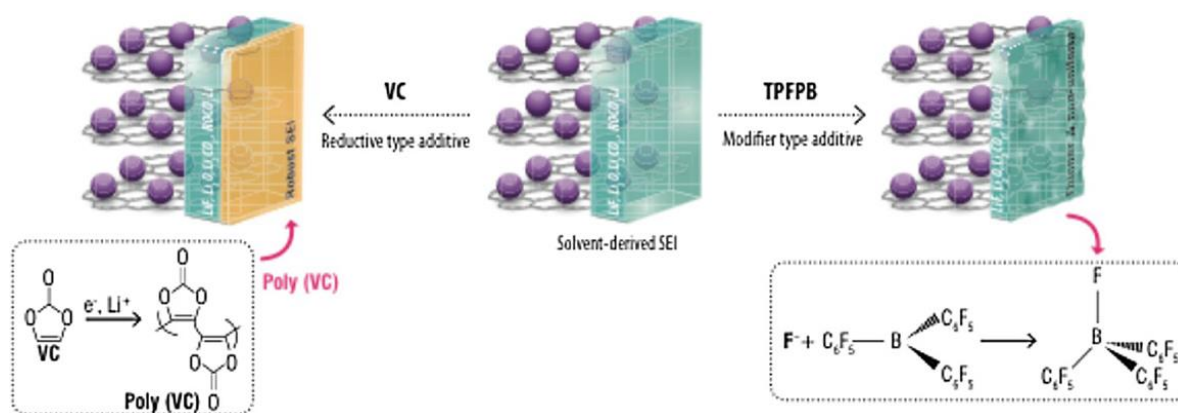
Figure 2.50: Schematic illustration of the effect VC electrolyte additive (redox additive) has on the formation of an SEI layer prior to solvent decomposition and the effect TPFPB electrolyte additive (reactive additive) has on the formation of the SEI layer by scavenging F$^-$ ions in the electrolyte. (Reproduced)[224]
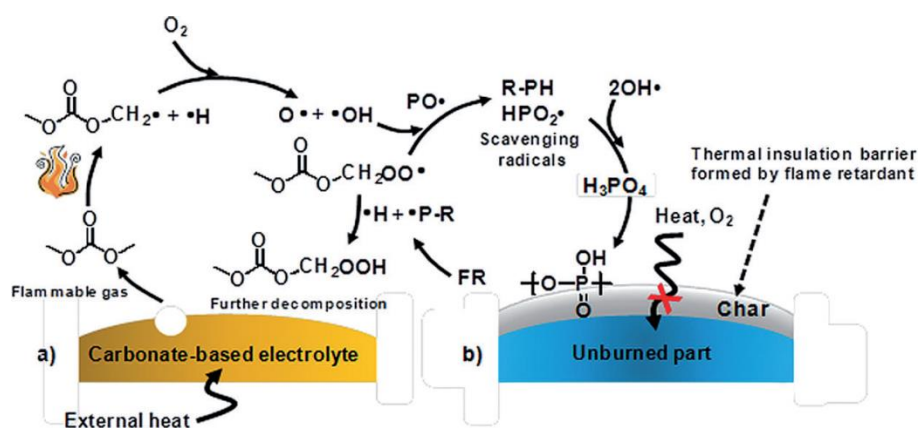
Figure 2.51: Schematic representation of: **a,** Thermal decomposition of conventional electrolyte based on carbonate solvents. **b,** Flame retarding by phosphorous flame retardant (FR) containing electrolyte. (Reproduced)[241]

Aqueous Electrolyte

The desire to replace organic solvents used in lithium ion batteries is driven by the safety concerns and costs associated with such solvents. A number of well documented reports have been published such as, Samsung Galaxy Note 7 recall in 2016 and most recently HP's recall of Notebook Computers due to faults in some of the lithium ion batteries in their electronic devices that caused them to catch fire[242]. The 4 main reasons that lead to battery damage and ultimately fire or explosions using the flammable organic solvents are:

1. Overcharging (Gas Ignition)
2. Overheating (Volatilisation of organic solvent)
3. Short circuit (Thermal runaway)
4. Mechanical Abuse

Aqueous or water based electrolytes are not flammable, have a high thermal capacitance, a natural cooling effect, are abundant and environmentally friendly. Aqueous electrolytes are used in the majority of other secondary battery technologies[243]. Switching to an aqueous electrolyte would dramatically reduce costs; 80-90% of the total cost of organic based systems is on materials and fabrication processes[244]. With an aqueous electrolyte the expensive lithium salts used in organic electrolytes such as $LiPF_6$ can be replaced with cheaper salts such as $LiNO_3$ and Li_2SO_4. The fabrication process can be performed in an ambient environment rather than a strictly controlled dry room environment. These issues of safety and cost are at the forefront when deploying lithium ion batteries in high power applications like grid energy storage and electric vehicles.

Besides safety and costs the other main advantages of aqueous electrolytes is their high ionic conductivity of Li^+ ions and solubility of lithium salts. The ionic conductivity (10^{-1} S/cm) is at least an order of magnitude greater than typical organic electrolytes (10^{-2} - 10^{-3} S/cm)[246]. Kohlrausch's law describes that the ionic conductivity is proportional to the concentration of the salt until an optimum concentration is reached[245a]. A high solubility of lithium salt means more charge carriers and therefore a higher conductivity. The optimum concentration is often near the saturation point as the excess salt will be in molecular form and makes it difficult for ions to flow. Unlike organic electrolytes, the decomposition products of water cannot deposit in a dense solid-state and a SEI layer cannot be formed on the electrode surface. The absence of an SEI layer means that the activation energy at the interface is almost half that in an organic electrolyte and therefore results in a lower internal resistance, Figure 2.52[245b, 247]. The charge transfer across the electrode/electrolyte interface can occur more easily resulting in faster kinetics and as a consequence a higher utilisation of the active electrode material at high C-rates.
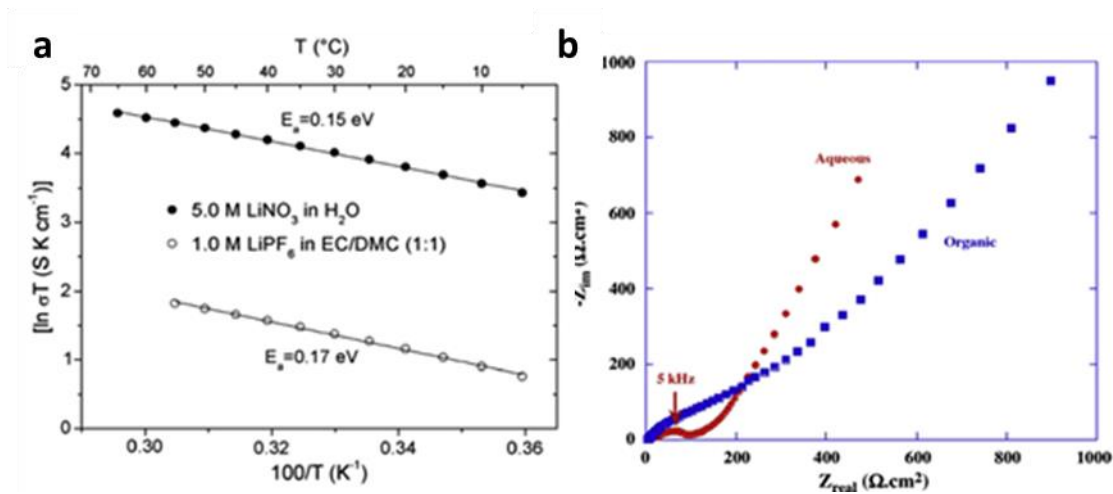
Figure 2.52: a, Arrhenius plot of 5 M LiNO$_3$ aqueous electrolyte and of 1 M LiPF$_6$ in EC/DMC (1:1). **b,** EIS for a thin LFP film 450 nm thick in 1 M LiNO$_3$ aqueous electrolyte and in 1 M LiClO$_4$ in EC/DMC (1:1). (Reproduced)[245]

Dahn et al. first showed that Li$_2$Mn$_2$O$_4$ cathode can be fabricated by lithiating LMO electrochemically from an aqueous electrolyte solution of 1 M LiOH[248]. This discovery not only showed a low cost way of fabricating cathode for lithium ion batteries but also showed that lithium intercalation can take place in an aqueous environment. They went on to propose and develop the first aqueous lithium-ion battery in 1995[249]. A cell was made up of composite electrodes that contained a LMO cathode, VO$_2$ (B) anode and 5 M LiNO$_3$ aqueous electrolyte. The battery had an operating potential of 1.5 V but a cycle life of only 20 cycles

before rapid capacity fade. Aqueous electrolyte cells that contained LMO cathode and γ-Li$_x$MnO$_2$ anode were also analysed and gave a 0.8 V operating potential with a similar cycle life. The work also highlights that Li$^+$ ion intercalation is the major reaction taking place at the electrode materials and mass transport in the electrode is via the same mechanism that occurs in organic electrolytes.

The disadvantages identified with aqueous lithium ion batteries are its small electrochemical window of 1.23 V and low cyclability. The smaller electrochemical window reduces their energy density and low cycle life limits there applications, Figure 2.53. The number of papers that have been published in recent years on aqueous lithium ion batteries has grown, with publications citing enhanced cyclability and higher rate capabilities, Figure 2.54[251]. A better understanding of the effects that the electrode and electrolyte salt have on the electrochemical performance of an aqueous lithium ion battery has led to renewed interest and potentially new applications.
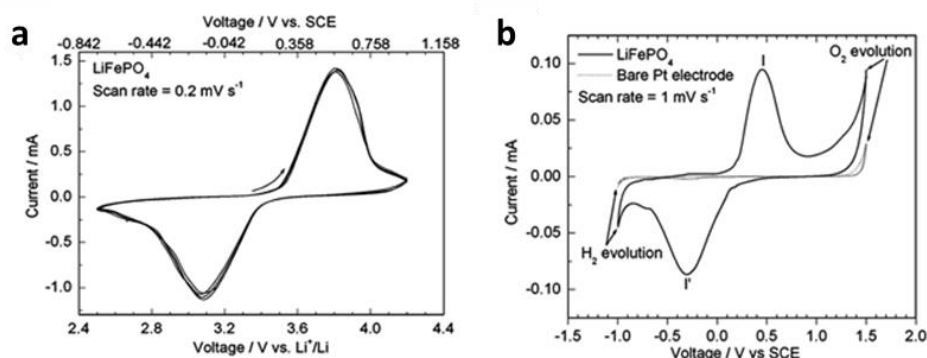
Figure 2.53: a, CV of LFP in 1 M LiPF$_6$-EC/DMC (1:1) nonaqueous electrolyte. **b,** CV of LFP in 1 M Li$_2$SO$_4$ aqueous electrolyte with O$_2$ and H$_2$ evolution occurring outside the 2 V aqueous stability window. (Reproduced)[250]
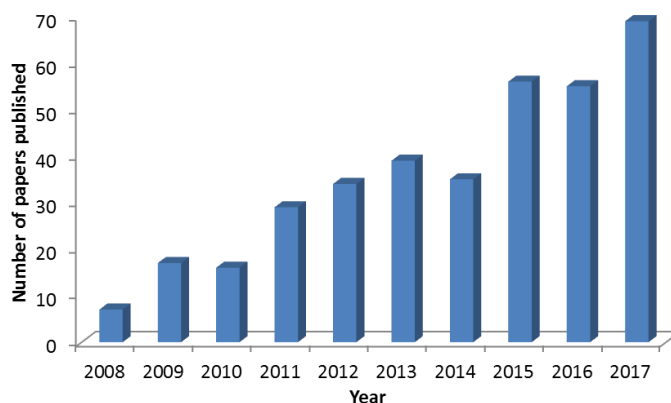
Figure 2.54: Number of papers (article, review and meeting) published on aqueous rechargeable lithium-ion battery in the period of 2008-2017 (10 years). Source: Web of Science database. Data are updated on February 2018

Recent advances in nanofabrication have revealed some interesting electrochemical properties of nanoscale materials in aqueous electrolyte. Pseudocapacitance, or the storage of charge on the surface of an electrode, is a non-diffusion controlled process and is dependent on the surface area of the electrode[252]. Pseudocapacitance is a typical transport mechanism in capacitors and allows for high power performance. The charge storage mechanism in most lithium ion intercalation electrodes is limited by solid-state diffusion and gives batteries their high energy density characteristics. Intercalation pseudocapacitive occurs where the storage of charge is in the crystalline structure but is not controlled by the solid state diffusion within the electrode[253]. Intercalation pseudocapacitive behaviour of lithium ion electrodes is rarely observed but there have been reports for a number of materials that exhibit this behaviour in organic electrolytes[254]. The combination of the typical faradaic behaviour in battery type (diffusion controlled) and supercapacitor type (non-diffusion controlled) materials offers a means of obtaining both a high energy and high power density in the one electrode. A recent report of thin-film LMO (90 nm), a typical cathode material, in an aqueous electrolyte shows intercalation pseudocapacitive properties[255]. Nanosized electrodes are sometimes misrepresented as exhibiting intercalation pseudocapacitive behaviour due to their high rate capabilities however the peak current is linearly dependent on the square root of the scan rate which is a characteristic of diffusion controlled kinetics. The slope of the line from the log of the Power Law relationship equation is used to determine the kinetics of the reaction, where a slope of 1 is non-diffusion controlled and 0.5 is diffusion controlled. The slope for thin-film LMO in an aqueous electrolyte was 0.87 and the contribution from both diffusion controlled and non-diffusion controlled kinetics was equal at a scan rate of 1 mV/s. Non-diffusion controlled kinetics were dominant from 5 mV/s and increased in dominance with increasing

scan rates. The characteristic redox peaks and potential plateaux were still seen at 100 mV/s and *384 C* (10 sec) respectively indicating exceptional lithium transport, Figure 2.55. The long term stability is also seen with only a 14% capacity drop after 3,500 cycles from the initial capacity of 67.2 mAh/g.
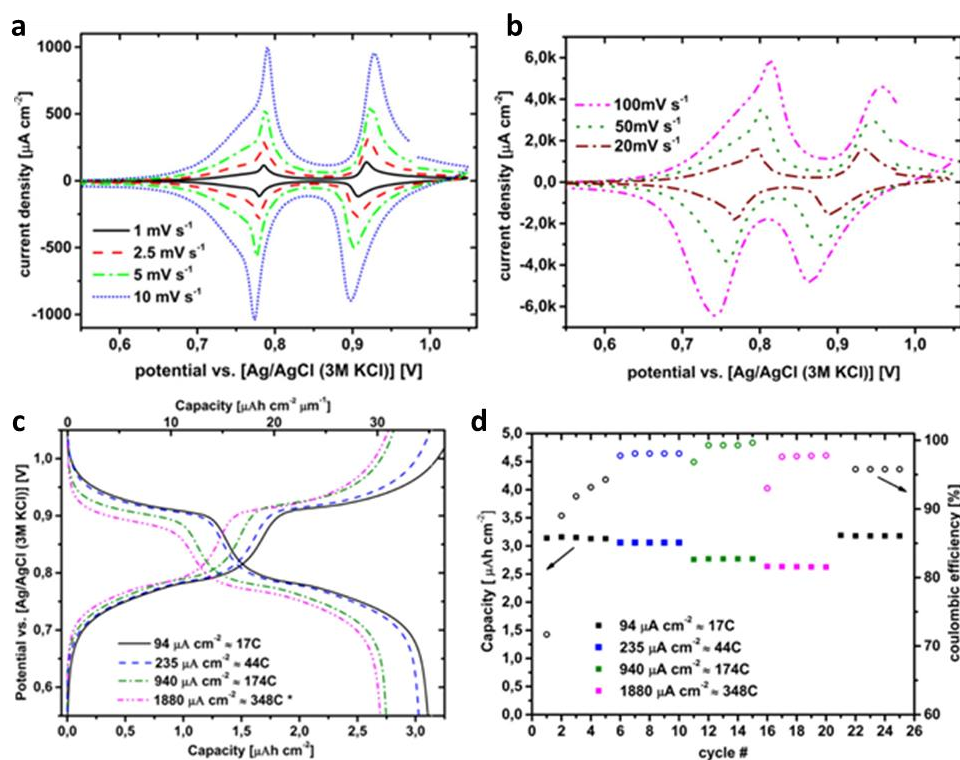
Figure 2.55: CV of LMO thin film at scan rates: **a,** 1, 2.5, 5, 10 mV/s and **b,** 20, 50, 100 mV/s. **c,** Galvanostatic profiles at C-rates *17, 44, 174,* and *348 C*. **d,** Rate performance at C-rates *17, 44, 174,* and *348 C*. (Reproduced)[255]

The three core components of the cell, water, lithium salt and electrode all have limitation that together result in low cyclability and limited cell potential. The electrochemical potential window is often expanded just by the presence of the electrode due to the kinetic effect during cycling[246]. The pH of the aqueous electrolyte does not affect the size of the electrochemical window but does shift its potential range in accordance with the Pourbaix diagram of water, Figure 2.56[256]. Typically the electrodes suitable for use in an aqueous electrolyte are the cathodes that are used in the organic electrolyte such as $LiCoO_2$, LMO, LFP and V_2O_5[257]. The pH of the electrolyte is critical as it determines the electrodes within the stability window and the electrode materials solubility. The polar nature of water renders it a good solvent as it can accommodate simple negative and positive ions while it also breaks weak bonds in solids in favour of forming stronger bonds to itself[258]. The high rate capabilities mentioned above due to the lack of an SEI layer forming on the electrode is also

a contributing factor to the low cyclability. The water molecules are in direct contact and can potentially dissolve the electrode material depending on its solubility and the pH of the electrolyte. LFP has a high affinity for water and reacts irreversible with it, causing Fe dissolution and electrode degradation[259]. In alkaline solutions PO_4^{3-} dissolves readily which again would cause electrode degradation[260]. V_2O_5 is slightly soluble in water (0.07 g/100 ml) which corresponds to a significant amount of electrode material resulting in poor cycle performance[261].
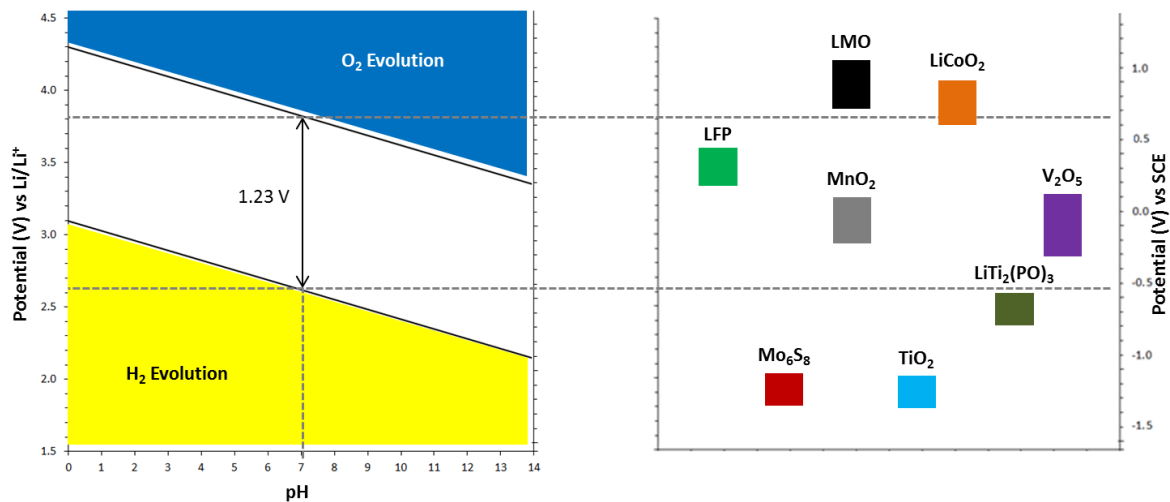
Figure 2.56: Pourbaix stability potential diagram of water and potentials of Li-ion electrodes vs Li metal (left) and SCE (right).

The intercalation/de-intercalation of Li^+ ions in an aqueous environment is a lot more complex than in organic environments are, as there are more side reactions that could potentially influence cell performance[247-248]. Protons (H^+) are present in aqueous electrolytes and could potentially intercalate in parallel with the Li^+ into the electrode. H^+ ion that intercalate into the electrode would be taking up the insertion site of Li^+. The crystalline structure of the electrode is known to determine if H^+ intercalation takes place in the electrode[262]. First principles calculations suggest that layered oxides ($LiCoO_2$) are more favourable than spinel (LMO) and olivine oxides (LFP) in accepting H^+ ions, $LiCoO_2 >$ LMO $>$ LFP[263]. $LiCoO_2$ has a flexible structure which allows either Li^+ or H^+ insertion without deformation of the octahedral structure while LFP has a very stiff structure meaning the Fe-P polyhedral needs to be under excessive strain to accept a H^+ proton. First principles also predict that a diffusion barrier forms on the surface of $LiCoO_2$ when cycled in saturated H_2 solution[262]. Experimental reports have supported the trend as H^+ insertion is observed in a low pH solution during deep cycling of $LiCoO_2$ while no H^+ insertion is seen for LMO and

LFP. An extensive study on the degradation of LiCoO2 highlighted that an amorphous thin film formed on the electrode as LiCoO2 is reduced to CoO that increased with cycle number and was an ionic insulator, Figure 2.57[264].
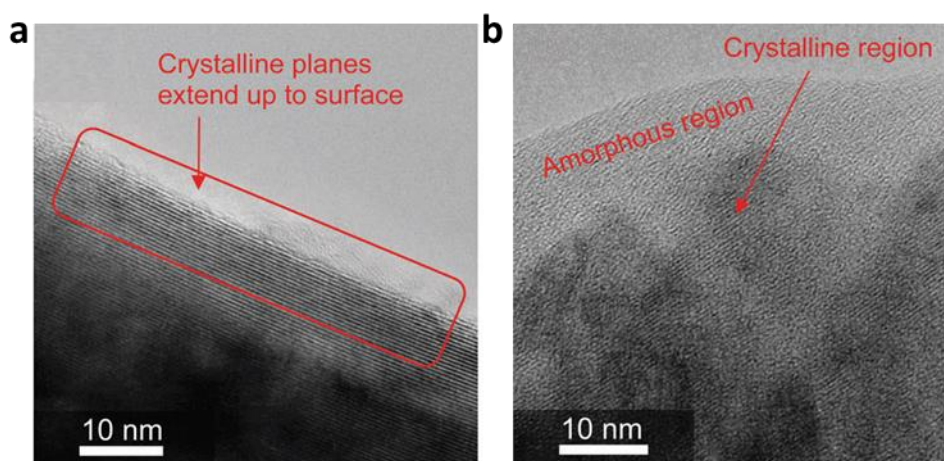
Figure 2.57: a, TEM of uncycled LiCoO2. **b,** TEM of cycled LiCoO2 in 1 M LiNO3 for 1500 cycles. (Reproduced)[264]

There are a number of other components in an electrolyte that can affect the performance of an aqueous battery such as the type and concentration of the lithium salt and dissolved oxygen[251a, 265]. The most common lithium salts used in aqueous lithium batteries are $LiNO_3$ and Li_2SO_4. The saturation concentration of Li_2SO_4 (3 M) is more stable than the saturation concentration of $LiNO_3$ (9 M) as large crystals can form on the electrode surface and block electrolyte access due to recrystallisation of the $LiNO_3$ caused by the slow evaporation of water, Figure 2.58[264]. Li_2SO_4 has a lower solubility and solvation energy that results in the precipitation of small crystals that do not block electrolyte access. A solution of 5 M $LiNO_3$ shows better electrochemical performance that Li_2SO_4 as this concentration is low enough to prevent the precipitation of large crystal but large enough to prevent sufficient interaction between the electrode surface and solvent[266]. The ionic conductivity of a 5 M $LiNO_3$ is 110 mS/cm[245a]. At lower concentrations of both salts the electrode degradation is more prominent as an increase in polarisation is seen with increasing cycle number. At higher concentrations the improved electrochemical performance is due to there being more anions present in the electrolyte which limits the interaction between the water molecules and the electrode surface and as a result decrease oxidation.
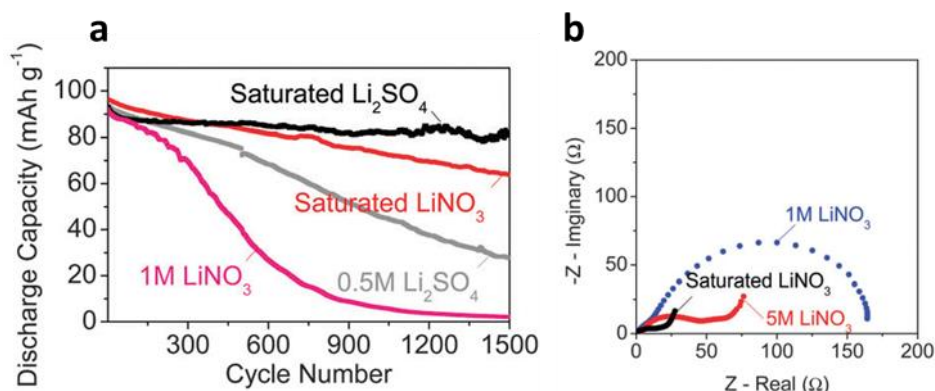
Figure 2.58: a, Cycle performance of LiCoO$_2$ in various aqueous solutions of LiNO$_3$ and Li$_2$SO$_4$. **b,** EIS of LiCO$_2$ in different concentrations of LiNO$_3$ after 500 cycles. (Reproduced)[264]

The main strategies to overcome the issues mentioned above are the formation of an SEI layer on the electrode or by disrupting or limiting the water molecules transport in the electrolyte towards the electrode and to preventing unwanted interactions between the electrode and the water. The SEI layer is formed by coating the electrode as part of the fabrication process or by adding an electrolyte additive that can form a protective coating during the first cycle. Sol-gel synthesis of electrodes is an example of where an SEI layer is formed inadvertently[267]. The chelating agents used in the sol-gel synthesis degrade and form a carbon coating onto the electrode material which protects the electrode material from unwanted side reaction with the water molecules. The carbon coating also has an added benefit of improving conductivity and preventing any agglomeration of electrode particles. Lanthanum trifluoride (LaF$_3$) has been used as an artificial SEI layer for LMO cathode in an aqueous electrolyte[268]. LaF$_3$ is coated onto the LMO by co-precipitation with a 3 wt. % of LaF$_3$ to LMO being the optimum coating for electrochemical performance and cycle life. The LaF$_3$ coating enhances Li$^+$ conductivity and reduced Mn dissolution by minimising the contact area between the LMO and electrolyte. VC electrolyte additive has shown to have a positive influence on the electrochemical performance of Li$_{1.05}$Cr$_{0.10}$Mn$_{1.85}$O$_4$ cathode in an aqueous electrolyte[269]. A 1 wt. % of VC to saturated LiNO$_3$ results in only an 11.5% and 18% capacity fade after 50 and 100 cycles respectively with an initial capacity of 112 mAh/g, Figure 2.59. An initial capacity of 80 mAh/g and after 50 cycles a capacity of 45 mAh/g is seen with no VC.
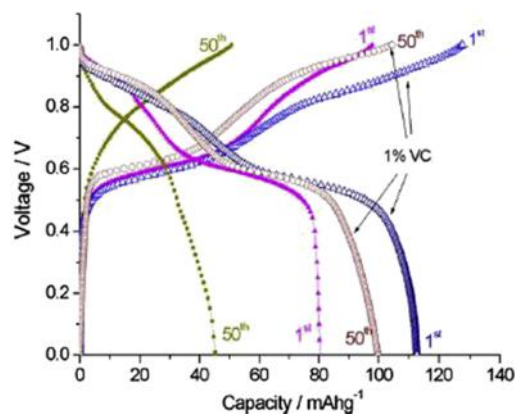
Figure 2.59: Galvanostatic profile of $Li_{1.05}Cr_{0.10}Mn_{1.85}O_4$ for the 1st and 50th cycle in 9 M $LiNO_3$ aqueous electrolyte without and with 1 wt.% VC at a rate of 50 mA/g. (Reproduced)[269]

Recent work by Wang et al. has shown that a Li metal anode can be used in an aqueous electrolyte[270]. The Li metal must be coated in a polymer gel electrolyte (PGE) first and then in a LiSICON solid state electrolyte film. The PGE and LiSICON coating permits the reaction at the Li metal anode to take place without hydrogen evolution by only allowing Li^+ ion transportation to the anode from the aqueous bulk electrolyte and also by preventing dendrite formation on the Li metal anode, Figure 2.60. The main purpose the PGE is to ensure that there are no side reactions between the Li metal and LiSICON film that can hinder the transport of Li^+ ions to the anode. The cross-over effect of Li^+ ions through the coating between the anode and aqueous electrolyte is similar to the effect that membranes have. Li^+ ions are stable in the aqueous electrolyte as they have a higher potential while the Li^+ ions in the coating have a lower potential but are not in contact with water molecules in the aqueous electrolyte and do not produce hydrogen as a result. A full cell of Li Metal/PGE/LiSICON/0.5 M Li_2SO_4/LMO gave a stable capacity of 110 mAh/g for 200 cycles at 500 mA/g (75 wt. % loading of LMO at *4.5 C* or 13 min).
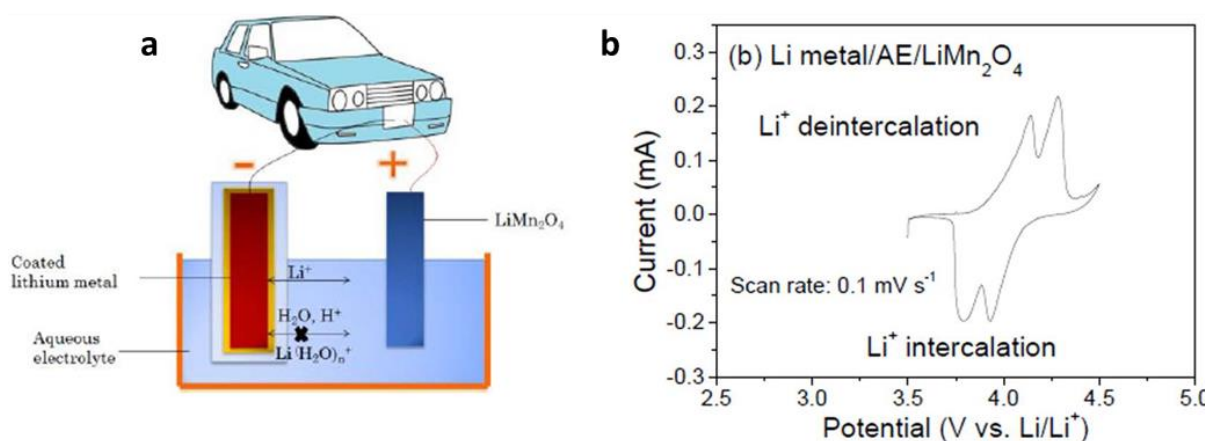
Figure 2.60: a, Schematic illustration of aqueous rechargeable lithium batteries (ARLB) using the coated lithium metal as anode, LiMn2O4 as cathode and 0.5 M Li2SO4 aqueous electrolyte. **b,** CV of the ARLB at the scan rate of 0.1 mV/s. (Reproduced)[270]

The water molecules transport can be disrupted/limited by adding a bulky anion additive to protect the Li^+ ions from interaction with them and therefore less water molecules are in contact with the electrode surface when the Li^+ is intercalated at the electrode surface. LNMO a high voltage cathode (4.5 V) was tested in a variety of aqueous electrolytes[271]. Only oxygen evolution was seen for both a 0.5 M and saturated solution of $LiNO_3$ and began at 1.3 V (vs Ag/AgCl). In accordance with the Nernst equation the electrode potential increased with salt concentration and since LNMO is already a high potential cathode, increasing the Li^+ concentration to suppress oxygen evolution would only result in pushing the electrode potential further into the oxygen evolution region. Disodium propane-1,3-disulfonate (PDSS) is added to 0.5 M $LiNO_3$ and results in the suppression of oxygen evolution and the appearance of a pair of redox peaks at around 1.5 V (vs Ag/AgCl), Figure 2.61. The peaks disappear after 5 cycles which is thought to be because the pH in close proximity to the electrode surface decreases due a side reaction during oxygen evolution. This drop in pH causes the LNMO to dissolve and limit the cycle life. A 0.25 M lithium-phosphate buffer solution consisting of LiOH and H_3PO_4 in a molar ratio of 3:2 was added to stabilise the pH during cycling and supply the Li^+ ions for intercalation while the saturated PDSS suppressed oxygen evolution. The pair of redox peaks is seen for the lithiation/delithiation of LNMO and also with an extended cycle life. The ionic conductivity of the 0.25 M Li-PO4 buffer + saturated PDSS was measured at 110 mS/cm which is similar to the reported conductivity of 5 M $LiNO_3$. Higher concentrations of lithium salt help to stabilise the electrochemical performance.
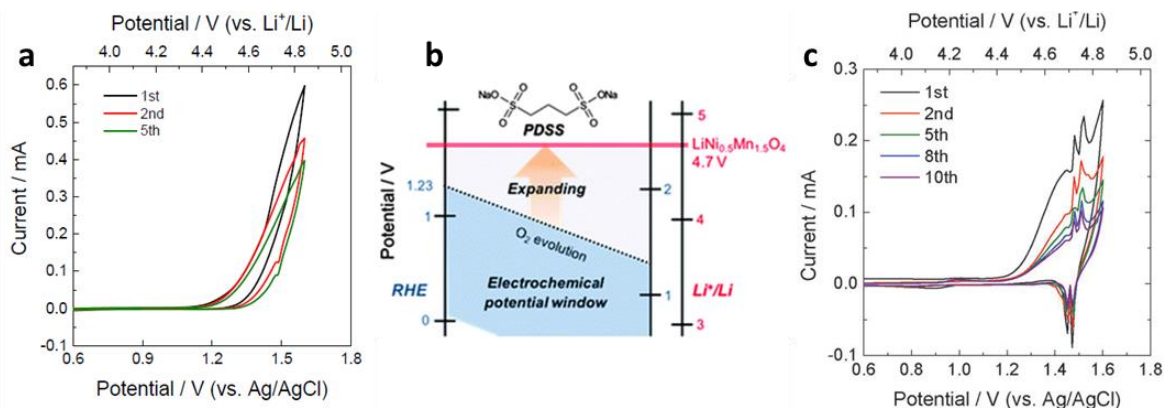
Figure 2.61: a, CV of LNMO in 0.25 M Li-PO4 aqueous solution. **b,** Schematic of the effect of PDSS on the oxygen evolution potential in an aqueous electrolyte. **c,** CV of LNMO in 0.25 M Li-PO4 buffer and saturated PDSS aqueous solution. (Reproduced)[271]

The anion of lithium salt provides a solvation sheath for the Li$^+$ ions and barrier to the water molecules during the lithiation process at the inner-Helmholtz region and reduces the interaction between the electrode and water molecules[272]. An extension of this concept was introduced in 2015 by Wang et al. which they referred to as "Water-in-salt" (WiS)[273] in a solution where the salt content is greater in both weight and volume than the solvent. A solution of > 5 m (m = mol/kg) LiTFSI is defined as a water-in salt solution. Interionic interactions become more dominant than solvent-ion interactions resulting in unusual properties. Thermal analysis of 20 and 21 m LiTFSI solutions showed that the solutions can be super-cooled down to -90°C with no crystallisation and are considered true liquid at room temperature. Raman analysis reveals that at concentrations of 21 m the spectrum of the S-N-S vibrational band is almost identical to that of crystalline LiTFSI. While ^{17}O NMR reveals that at concentration > 10 m the oxygen on the TFSI$^-$ ion coordinates to the Li$^+$ ion. Both these results suggest why at increasing concentrations the solution transforms into a semi solid like state where a percolated TFSI$^-$ network is eventually formed and each Li$^+$ ion is surrounded by at least one TFSI$^-$ ion. It is worth noting that the interaction between Li$^+$ ion and TFSI$^-$ ion is very similar to the interaction observed in ionic liquids[274]. At concentration > 20 m the simulations predict that at least two TFSI$^-$ ions surround the Li$^+$ ion which leads to a higher probability of TFSI$^-$ reduction, Figure 2.62. Quantum chemical calculations also suggest that the reduction potential of the TFSI$^-$ ion is increased to around 2.9 V due to its interaction with the Li$^+$ ion (Li$_2$(TFSI)(H$_2$O)$_x$). The reduction potential of the TFSI$^-$ ion is higher than the hydrogen evolution potential 2.63 V. The reduction of the TFSI$^-$ ion results in a passivation LiF rich layer on the electrode which acts as an electron barrier and suppresses hydrogen

evolution to 1.9 V. No passivation layer is seen on the cathode, however, oxygen evolution is suppressed to 4.9 V which is probably due to the increase in TFSI⁻ ions in the inner-Helmholtz layer and the reduced amount of water molecules coordinated to the Li⁺ ions. The result of the SEI formation and the unique interaction at the electrodes interface result in an electrochemical window of ~ 3.0 V.
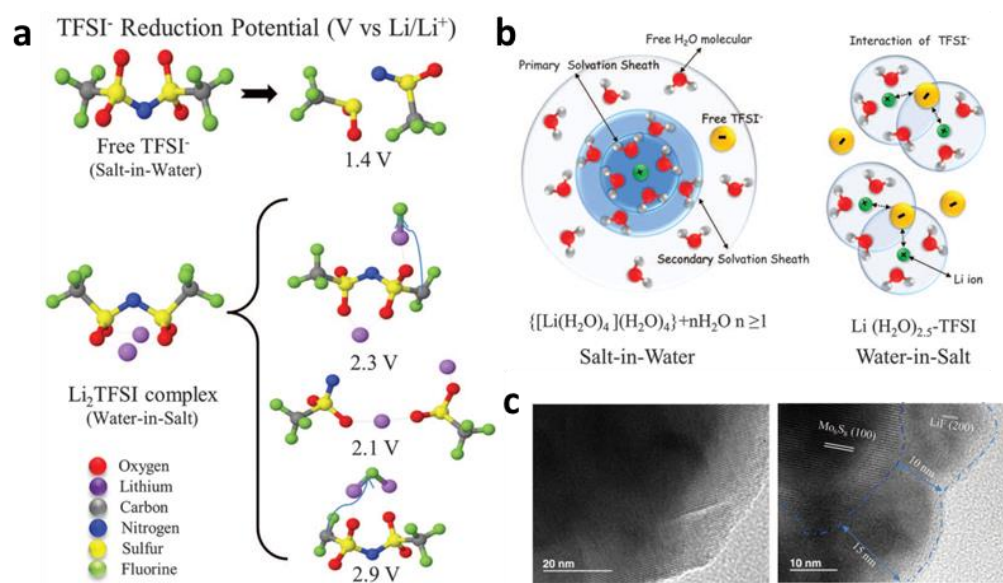
Figure 2.62: a, Predicted reduction potentials from G4MP2 quantum chemistry calculations. **b,** Illustration of the evolution of the Li⁺ primary solvation sheath in diluted and water-in-salt solutions. **c,** TEM images of pristine Mo_6S_8 (left) and cycled Mo_6S_8 (right) with SEI of LiF. (Reproduced)[273]

Half-cell and full cell analysis of LMO and Mo_6S_8 was carried out to investigate the extended electrochemical window of the WiS electrolyte, Figure 2.63. Only one lithiation/delithiation process was seen at 5 m concentration, however, the characteristic two lithiation/delithiation processes of Mo_6S_8 are seen for a concentration > 10 m. The second lithiation/delithiation process is seen at higher concentrations in accordance with the Nernst equation as a factor of 10 increase in Li⁺ activity results in an increase in redox potential of 59.1 mV. The extremely high concentration of the WiS solution pushes the redox potential of the Mo_6S_8 into the electrochemical stability window of the electrolyte while also protecting the anode with the formation of an SEI layer and supressing hydrogen evolution. The ionic conductivity of a 21 m solution is 10 mS/cm which is slightly higher than standard organic electrolytes. The full cell showed excellent cycle stability at both low and high rates. In a cathode:anode mass ratio of 1:2 a capacity of 47 mAh/g was obtained in the initial cycle at *0.15 C* (~6.5 hr) with a

capacity retention of 78% after 100 cycles. Capacity retention of 68% after 1,000 cycles was achieved at the higher rate of *4.5 C* (~13 min).
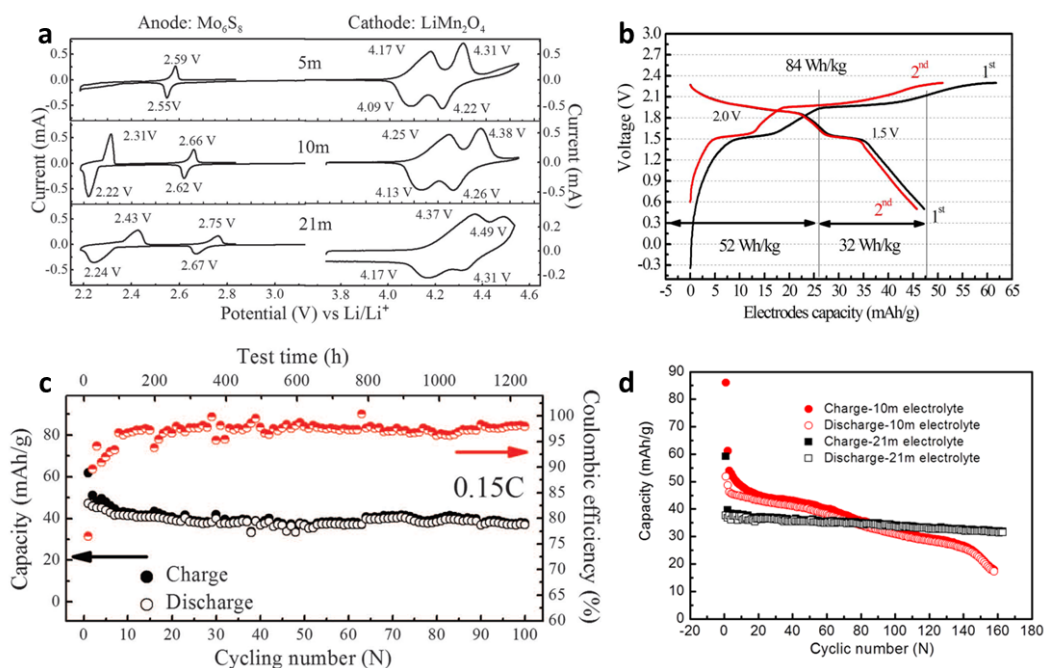
Figure 2.63: a, Electrochemical stability window of $LiMn_2O_4$ and Mo_6S_8 electrodes in various concentrations of LiTFSI aqueous electrolyte at 0.1 mV/s scan rate. **b,** Galvanostatic profile of a full cell of LMO and Mo_6S_8 at *0.15 C* in 21 m LiTFSI electrolyte. **c,** Cycle stability of full WiS battery at *0.15 C*. **d,** Comparison of cycle stability of 10 m and 21 m LiTFSI aqueous solution. (Reproduced)[273]

Lithium salts need to be highly soluble, stable against hydrolysis, undergo electrochemical reduction at an appropriate potential and the reduced component to be an insoluble solid in water. LiTFSI belongs to the fluoroalkyl sulfonimide lithium salts family that meets these requirements. Lithium trifluoromethane sulfone, $LiSO_3CF_3$ (LiOTf), belongs to the fluoroalkyl sulfonate lithium salt group and has shown an almost indistinguishable electrochemical response. Wang et al. subsequently continued on the work of further expanding the electrochemical window of aqueous batteries by taking inspiration from that hydrated salts can dissolve unhydrated salts of similar chemical properties[275]. A hydrated salt can also be considered a saturated electrolyte and they implemented this strategy by talking a 21 m LiTFSI WiS electrolyte to dissolve LiOTf[276]. They successfully dissolved 7 m of LiOTf into the WiS and created a mixed salt aqueous electrolyte termed "water-in-bisalt" (WiBS). The hydrogen evolution shifted down to 1.83 V and the cathodic current at 1.5 V decreased substantially to 4 mA/cm^2 from 10 mA/cm^2, Figure 2.64. The increase in molality resulted in an increase in the lithiation voltage of electrodes meaning the Mo_6S_8

100

anode could be replaced with TiO_2 as the lithiation voltage increased from 1.8 V to 2.0 V. TiO_2 is known for its catalytic water-splitting properties which is a detrimental characteristic for an anode in aqueous electrolyte as hydrogen evolution needs to be suppressed not enhanced. A thin layer of carbon is coated onto the TiO_2 anode which helps to increase conductivity but more importantly is inert electrocatalytically and hinders the catalytic properties as the electrolytes contact with the TiO_2 is reduced. The average voltage of a LMO/TiO_2 cell in a WiBS is 2.1 V with an actual energy density of 100 Wh/kg. The coulombic efficiency (CE) stabilises much faster and showed better cycle stability, 0.22% capacity fade/cycle, for the WiBS electrolyte (80% CE, 1st cycle → 99% CE, 40th cycle) than the WIS electrolyte (57.8% CE, 1st cycle → 97% CE, 60th cycle) indicating that the SEI layer formed much easier and as a more protective layer.
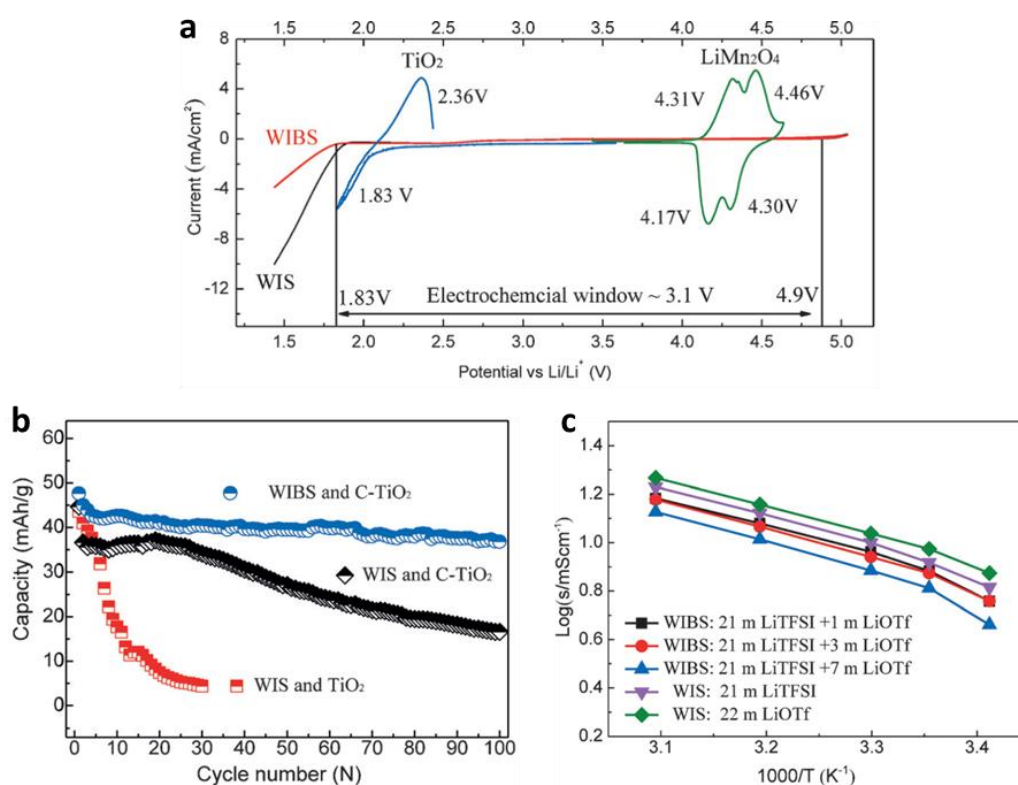
Figure 2.64: a, Electrochemical stability windows of WiS and WiBS electrolytes on a stainless steel grid at 10 mV/s, and the 1st CV profile of C-TiO_2 and LMO electrodes at 0.1 mV/s in the WiBS electrolyte. **b,** Cycle stability of TiO_2 and C-TiO_2 in WiS and WiBS. **c,** Arrhenius plot of WiS and WiBS electrolytes. (Reproduced)[276]

Wang et al. have since reported the use of a tris(trimethylsilyl) borate (TMSB) as an electrolyte additive in WIS to form a cathode electrolyte interface (CEI) on $LiCoO_2$ to solve the cycle stability issues associated with the electrode in aqueous electrolytes[277]. A 2.5 V cell of $LiCoO_2$/Mo_6S_8 with an energy density of 120 Wh/kg for 1,000 cycles at a capacity

fade of 0.013% per cycle. Most recently Wang et al. published a paper claiming a 4.0 V aqueous battery[278]. The low voltage anode of Li metal or graphite is coated in a highly fluorinated ether (HFE) gel made up of 0.5 M LiTFSI and 10 wt.% PEO. The HFE gel coating and a gel WiBS is also used to prevent hydrogen evolution and extend the electrochemical window, Figure 2.65. A graphite anode obtained a capacity of 325 mAh/g in the first cycle with a CE of 85% which increased to 99.3% and 99.5% for the second and third cycle, respectively, Figure 2.66. A full cell shows significant capacity fade during cycling with a ~10% capacity fade after 70 cycles, however the fact that graphite and Li metal can be cycled in an aqueous electrolyte demonstrates significant progress in the field.
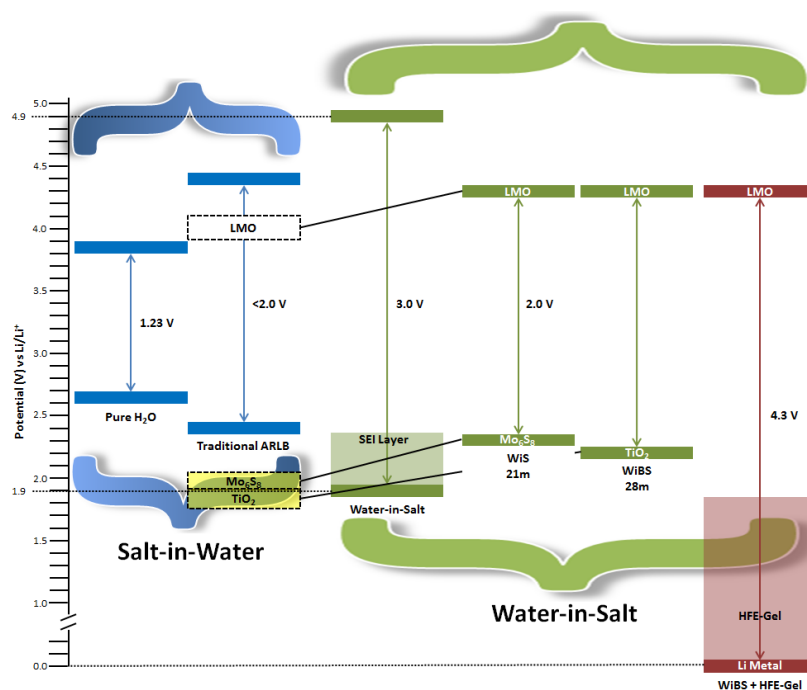
Figure 2.65: Schematic of the comparison between the electrochemical stability window of salt-in-water, WiS, WiBS and WiBS + HFE-Gel.
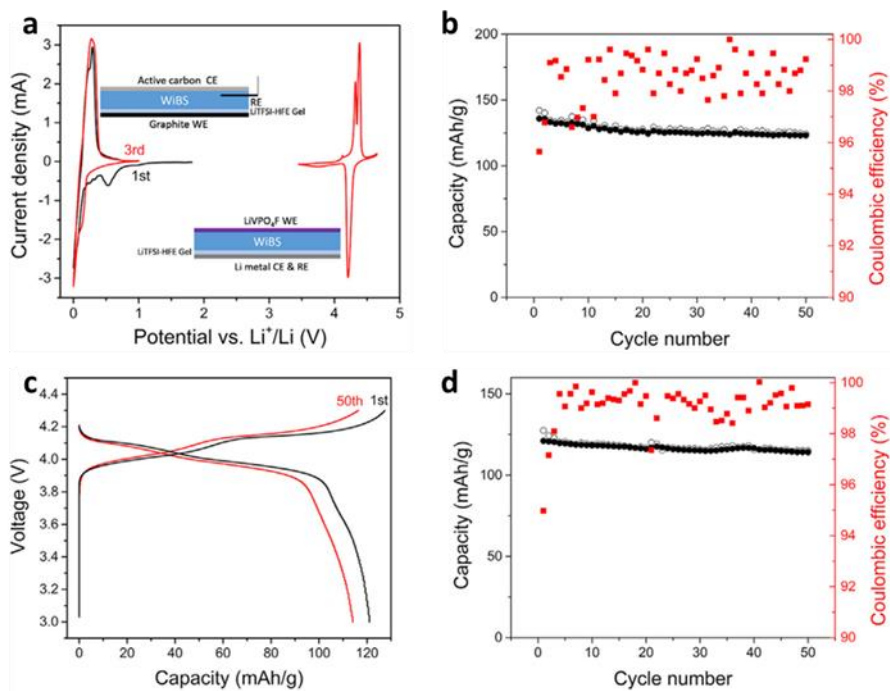
Figure 2.66: a, CV of a 3-electrode setup of graphite pre-coated with LiTFSI-HFE gel as the working electrode, activated carbon counter electrode and Ag/AgCl reference electrode. A CV of a 2-electrode setup of LiVPO₄F as the working electrode and lithium foil pre-coated with LiTFSI-HFE gel as the counter and reference electrode. **b,** Cycle stability of LiVPO₄F vs LiTFSI-HFE gel coated Li metal in WiBS at a *0.3 C* rate. **c,** Galvanostatic profile of LMO vs LiTFSI-HFE gel coated Li metal in WiBS at a *0.3 C* rate. **d,** Cycle stability of LMO vs LiTFSI-HFE gel coated Li metal in WiBS at a *0.3 C* rate. (Reproduced)[278]

Summary of Work

Chapter 2 is a review of the literature in areas of focus for this thesis to date. Chapter 3 discusses the fundamental principles of the electrochemical and characterisation techniques used in this study.

COMSOL Multiphysics was used to compare the effect that electrode architecture coupled with various electrolyte conductivities have on the battery performance in chapter 4. The battery performance of a typical all solid-state microbattery was used as a standard. The effects of improved electrolyte characteristics on the battery performance were investigated in the standard thin-film microbattery, 3D and 3D core-shell nanoarchitectures.

Starting with anode materials for high capacity and long cycle life, 3D Cu nanotubes were investigated as a current collector for Ge thin films in order to act as mechanical support and increase the amount of Ge per area is presented in chapter 5. SEM was used to investigate the coverage of the DC sputtered Ge deposit upon the electrodeposited Cu nanotubes. The electrochemical performance is studied with the cyclic voltammetry and chronopotentiometry techniques.

Chapter 6 then investigates the electrochemical properties of nanoscale films of $LiCoO_2$. In order to ensure the cell performance is solely dependent on the electrochemical performance of the nanoscale $LiCoO_2$ and not the ion transport in the electrolyte analysis was performed in an aqueous electrolyte. The effect the substrate and the RTA conditions have on the crystalline structure of nanoscale $LiCoO_2$ were also investigated.

Chapter 7 discuss the use of V_2O_5 as an electrode in aqueous environment and its electrochemical properties. TiO_2 protective coatings and various concentrations of VC electrolyte additive were investigated in order to improve cycle life as V_2O_5 is slightly soluble in an aqueous environment.

Chapter 8 draws conclusion from the conducted work, summarises the achievements and presents an outlook for future work.

References:

[1] *The battery has become our steady travel companion*. 2017. http://www.buchmann.ca/buchmann/battery-has-become-our-steady-travel-companion

[2] *Secondary battery sales statistics by volume*. 2017. http://www.baj.or.jp/e/statistics/06.html

[3] H. Ikeda, T. Saito, H. Tamura, in *Manganese Dioxide Symposium, Electrochemical Society Cleveland Section I. C. Sample Office, Vol. 1* (Eds.: A. Kozawa, R. Brodd), I.C. MnO$_2$ Sample Office, Cleveland, Ohio, **1975**.

[4] F. Orsini, A. du Pasquier, B. Beaudouin, J. M. Tarascon, M. Trentin, N. Langenhuizen, E. de Beer, P. Notten, *J. Power Sources* **1999**, *81*, 918-921.

[5] J. M. Tarascon, M. Armand, *Nature* **2001**, *414*, 359-367.

[6] a) J. Broadhead, A. Butherus, Rechargable nonaqueous battery, **1974**, US 3791867 A; b) J. Broadhead, S. J. F. J. Di, F. A. Trumbore, Non-aqueous battery using chalcogenide electrode, **1975**, US 3864167 A

[7] a) K. Mizushima, P. C. Jones, P. J. Wiseman, J. B. Goodenough, *Mat. Res. Bull.* **1980**, *15*, 783-789; b) M. M. Thackeray, W. I. F. David, P. G. Bruce, J. B. Goodenough, *Mater. Res. Bull.* **1983**, *18*, 461-472.

[8] a) D. W. Murphy, R. J. Cava, S. M. Zahurak, A. Santoro, *Solid State Ionics* **1983**, *9-10*, 413-417; b) M. Lazzari, B. Scrosati, *J. Electrochem. Soc.* **1980**, *127*, 773-774.

[9] B. M. L. Rao, R. W. Francis, H. A. Christopher, *J. Electrochem. Soc.* **1977**, *124*, 1490-1492.

[10] R. Yazami, P. Touzain, *J. Power Sources* **1983**, *9*, 365-371.

[11] M. Armand, J. M. Chabagno, M. J. Duclot, in *Fast Ion Transport in Solids Electrodes and Electrolytes* (Eds.: P. Vashista, J. N. Mundy, G. K. Shenoy), North-Holland, Amsterdam, **1979**, pp. 131-136.

[12] a) S. Basu, Ambient temperature rechargeable battery, **1983**, US 4423125 A; b) M. Mohri, N. Yanagisawa, Y. Tajima, H. Tanaka, T. Mitate, S. Nakajima, M. Yoshida, Y. Yoshimoto, T. Suzuki, H. Wada, *J. Power Sources* **1989**, *26*, 545-551.

[13] T. Nagaura, K. Tozawa, *Prog. Batteries Solar Cells* **1990**, *9*, 209-209.

[14] J. M. Tarascon, A. S. Gozdz, C. Schmutz, F. Shokoohi, P. C. Warren, *Solid State Ionics* **1996**, *86-8*, 49-54.

[15] R. M. Dell, D. A. J. Rand, Royal Society of Chemistry, **2001**, pp. 10-21.

[16] H. Selig, L. B. Ebert, in *Advances in Inorganic Chemistry and Radiochemistry, Vol. 23* (Eds.: H. J. Emeléus, A. G. Sharpe), Academic Press, **1980**, pp. 281-327.

[17] a) J. R. Dahn, A. K. Sleigh, H. Shi, J. N. Reimers, Q. Zhong, B. M. Way, *Electrochim. Acta* **1993**, *38*, 1179-1191; b) Z. X. Shu, R. S. McMillan, J. J. Murray, *J. Electrochem. Soc.* **1993**, *140*, 922-927; c) J. M. Tarascon, D. Guyomard, *Electrochim. Acta* **1993**, *38*, 1221-1231; d) K. Sawai, Y. Iwakoshi, T. Ohzuku, *Solid State Ionics* **1994**, *69*, 273-283.

[18] R. Fong, U. von Sacken, J. R. Dahn, *J. Electrochem. Soc.* **1990**, *137*, 2009-2013.

[19] a) H. Nozaki, K. Nagaoka, K. Hoshi, N. Ohta, M. Inagaki, *J. Power Sources* **2009**, *194*, 486-493; b) Y.-S. Park, H. J. Bang, S.-M. Oh, Y.-K. Sun, S.-M. Lee, *J. Power Sources* **2009**, *190*, 553-557.

[20] T. Takamura, K. Sumiya, J. Suzuki, C. Yamada, K. Sekine, *J. Power Sources* **1999**, *81-82*, 368-372.

[21] K. Teshima, H. Inagaki, S. Tanaka, K. Yubuta, M. Hozumi, K. Kohama, T. Shishido, S. Oishi, *Crystal Growth & Design* **2011**, *11*, 4401-4405.

[22]   a) K. M. Colbow, J. R. Dahn, R. R. Haering, *J. Power Sources* **1989**, *26*, 397-402; b) T. Ohzuku, A. Ueda, N. Yamamoto, *J. Electrochem. Soc.* **1995**, *142*, 1431-1435.

[23]   a) Y. Toyoguchi, S. Nankai, J. Yamaura, T. Matsui, T. Ijima, *Extended Abstracts, Osaka* **1983**, 205; b) Y. Toyoguchi, J. Yamaura, T. Matsui, T. Ijima, J. Gabano, Z. Takehara, P. Bro, *PV88-6, The Electrochemical Society, Pennington, NJ* **1988**, 659; c) Z. Takehara, *J. Power Sources* **1989**, *26*, 257-266.

[24]   a) M. Winter, J. O. Besenhard, *Electrochim. Acta* **1999**, *45*, 31-50; b) A. N. Dey, *J. Electrochem. Soc.* **1971**, *118*, 1547-1549.

[25]   a) W.-J. Zhang, *J. Power Sources* **2011**, *196*, 13-24; b) A. Dhanabalan, X. Li, R. Agrawal, C. Chen, C. Wang, *Nanomaterials* **2013**, *3*, 606-614; c) J. Kong, W. A. Yee, Y. Wei, L. Yang, J. M. Ang, S. L. Phua, S. Y. Wong, R. Zhou, Y. Dong, X. Li, X. Lu, *Nanoscale* **2013**, *5*, 2967-2973.

[26]   a) R. Teki, M. K. Datta, R. Krishnan, T. C. Parker, T.-M. Lu, P. N. Kumta, N. Koratkar, *Small* **2009**, *5*, 2236-2242; b) C. K. Chan, X. F. Zhang, Y. Cui, *Nano Lett.* **2008**, *8*, 307-309; c) I. A. Courtney, J. R. Dahn, *J. Electrochem. Soc.* **1997**, *144*, 2045-2052; d) Y. Idota, T. Kubota, A. Matsufuji, Y. Maekawa, T. Miyasaka, *Science* **1997**, *276*, 1395-1397.

[27]   U. Kasavajjula, C. Wang, A. J. Appleby, *J. Power Sources* **2007**, *163*, 1003-1039.

[28]   a) R. A. Sharma, R. N. Seefurth, *J. Electrochem. Soc.* **1976**, *123*, 1763-1768; b) H. Okamoto, *Journal of Phase Equilibria and Diffusion* **2009**, *30*, 118-119.

[29]   H. Wu, Y. Cui, *Nano Today* **2012**, *7*, 414-429.

[30]   a) P. Limthongkul, Y.-I. Jang, N. J. Dudney, Y.-M. Chiang, *J. Power Sources* **2003**, *119-121*, 604-609; b) M. Gu, Z. Wang, J. G. Connell, D. E. Perea, L. J. Lauhon, F. Gao, C. Wang, *ACS Nano* **2013**, *7*, 6303-6309.

[31]   a) P. Limthongkul, Y.-I. Jang, N. J. Dudney, Y.-M. Chiang, *Acta Mater.* **2003**, *51*, 1103-1113; b) J. Li, J. R. Dahn, *J. Electrochem. Soc.* **2007**, *154*, A156-A161; c) H. Li, X. Huang, L. Chen, G. Zhou, Z. Zhang, D. Yu, Y. Jun Mo, N. Pei, *Solid State Ionics* **2000**, *135*, 181-191.

[32]   C. K. Chan, H. Peng, G. Liu, K. McIlwrath, X. F. Zhang, R. A. Huggins, Y. Cui, *Nat. Nanotechnol.* **2007**, *3*, 31.

[33]   X. H. Liu, L. Zhong, S. Huang, S. X. Mao, T. Zhu, J. Y. Huang, *ACS Nano* **2012**, *6*, 1522-1531.

[34]   N. Lin, Y. Han, L. Wang, J. Zhou, J. Zhou, Y. Zhu, Y. Qian, *Angew. Chem. Int. Ed.* **2015**, *54*, 3822-3825.

[35]   a) X. H. Liu, F. Fan, H. Yang, S. Zhang, J. Y. Huang, T. Zhu, *ACS Nano* **2013**, *7*, 1495-1503; b) J. W. Wang, Y. He, F. Fan, X. H. Liu, S. Xia, Y. Liu, C. T. Harris, H. Li, J. Y. Huang, S. X. Mao, T. Zhu, *Nano Lett.* **2013**, *13*, 709-715.

[36]   T.-L. Chan, J. R. Chelikowsky, *Nano Lett.* **2010**, *10*, 821-825.

[37]   X. H. Liu, H. Zheng, L. Zhong, S. Huang, K. Karki, L. Q. Zhang, Y. Liu, A. Kushima, W. T. Liang, J. W. Wang, J.-H. Cho, E. Epstein, S. A. Dayeh, S. T. Picraux, T. Zhu, J. Li, J. P. Sullivan, J. Cumings, C. Wang, S. X. Mao, Z. Z. Ye, S. Zhang, J. Y. Huang, *Nano Lett.* **2011**, *11*, 3312-3318.

[38]   a) E. Mullane, T. Kennedy, H. Geaney, C. Dickinson, K. M. Ryan, *Chem. Mater.* **2013**, *25*, 1816-1822; b) A. M. Chockla, K. C. Klavetter, C. B. Mullins, B. A. Korgel, *Chem. Mater.* **2012**, *24*, 3738-3745.

[39]   X. Su, Q. Wu, J. Li, X. Xiao, A. Lott, W. Lu, B. W. Sheldon, J. Wu, *Advanced Energy Materials* **2014**, *4*, 1300882-n/a.

[40]   Y. Wang, H. Li, P. He, E. Hosono, H. Zhou, *Nanoscale* **2010**, *2*, 1294-1305.

[41]   H. Wu, G. Chan, J. W. Choi, I. Ryu, Y. Yao, M. T. McDowell, S. W. Lee, A. Jackson, Y. Yang, L. Hu, Y. Cui, *Nat. Nanotechnol.* **2012**, *7*, 310.

[42]   Z.-L. Xu, X. Liu, Y. Luo, L. Zhou, J.-K. Kim, *Prog. Mater Sci.* **2017**, *90*, 1-44.

[43]   a) M. Zhang, T. Zhang, Y. Ma, Y. Chen, *Energy Storage Materials* **2016**, *4*, 1-14; b) F. Luo, B. Liu, J. Zheng, G. Chu, K. Zhong, H. Li, X. Huang, L. Chen, *J. Electrochem. Soc.* **2015**, *162*, A2509-A2528.

[44]   Z. Lu, N. Liu, H.-W. Lee, J. Zhao, W. Li, Y. Li, Y. Cui, *ACS Nano* **2015**, *9*, 2540-2547.

[45]   L. Pan, H. Wang, D. Gao, S. Chen, L. Tan, L. Li, *Chem. Commun.* **2014**, *50*, 5878-5880.

[46]   a) Y. Kamata, *Mater. Today* **2008**, *11*, 30-38; b) C. S. Fuller, J. C. Severiens, *Phys. Rev.* **1954**, *96*, 21-24.

[47]   a) C.-M. Park, J.-H. Kim, H. Kim, H.-J. Sohn, *Chem. Soc. Rev.* **2010**, *39*, 3115-3141; b) A. M. Chockla, K. C. Klavetter, C. B. Mullins, B. A. Korgel, *ACS Appl. Mater. Interfaces* **2012**, *4*, 4658-4664.

[48]   a) G. H. Wang, C. Y. Shi, L. Zhao, H. W. Diao, W. J. Wang, *J. Alloys Compd.* **2016**, *658*, 543-547; b) Y. Liu, S. Zhang, T. Zhu, *ChemElectroChem* **2014**, *1*, 706-713; c) A. D. Collord, H. W. Hillhouse, *Chem. Mater.* **2016**, *28*, 2067-2073.

[49]   J. Graetz, C. C. Ahn, R. Yazami, B. Fultz, *J. Electrochem. Soc.* **2004**, *151*, A698-A702.

[50]   B. Laforge, L. Levan-Jodin, R. Salot, A. Billard, *J. Electrochem. Soc.* **2008**, *155*, A181-A188.

[51]   L. Baggetto, P. H. L. Notten, *J. Electrochem. Soc.* **2009**, *156*, A169-A175.

[52]   a) A. Al-Obeidi, D. Kramer, C. V. Thompson, R. Mönig, *J. Power Sources* **2015**, *297*, 472-480; b) S. P. V. Nadimpalli, R. Tripuraneni, V. A. Sethuraman, *J. Electrochem. Soc.* **2015**, *162*, A2840-A2846.

[53]   a) X. H. Liu, J. Y. Huang, *Energy Environ. Sci.* **2011**, *4*, 3844-3860; b) X. H. Liu, Y. Liu, A. Kushima, S. Zhang, T. Zhu, J. Li, J. Y. Huang, *Advanced Energy Materials* **2012**, *2*, 722-741.

[54]   X. H. Liu, S. Huang, S. T. Picraux, J. Li, T. Zhu, J. Y. Huang, *Nano Lett.* **2011**, *11*, 3991-3997.

[55]   R. A. Susantyoko, X. Wang, L. Sun, W. Sasangka, E. Fitzgerald, Q. Zhang, *Nano Energy* **2015**, *12*, 521-527.

[56]   X. H. Liu, J. W. Wang, S. Huang, F. Fan, X. Huang, Y. Liu, S. Krylyuk, J. Yoo, S. A. Dayeh, A. V. Davydov, S. X. Mao, S. T. Picraux, S. Zhang, J. Li, T. Zhu, J. Y. Huang, *Nat. Nanotechnol.* **2012**, *7*, 749.

[57]   M. K. Y. Chan, B. R. Long, A. A. Gewirth, J. P. Greeley, *The Journal of Physical Chemistry Letters* **2011**, *2*, 3092-3095.

[58]   W. Liang, H. Yang, F. Fan, Y. Liu, X. H. Liu, J. Y. Huang, T. Zhu, S. Zhang, *ACS Nano* **2013**, *7*, 3427-3433.

[59]   A. M. Chockla, T. D. Bogart, C. M. Hessel, K. C. Klavetter, C. B. Mullins, B. A. Korgel, *J. Phys. Chem. C* **2012**, *116*, 18079-18086.

[60]   T. Kennedy, E. Mullane, H. Geaney, M. Osiak, C. O'Dwyer, K. M. Ryan, *Nano Lett.* **2014**, *14*, 716-723.

[61]   M.-H. Park, Y. Cho, K. Kim, J. Kim, M. Liu, J. Cho, *Angew. Chem. Int. Ed.* **2011**, *50*, 9647-9650.

[62]   a) H. Peng, C. Xie, D. T. Schoen, K. McIlwrath, X. F. Zhang, Y. Cui, *Nano Lett.* **2007**, *7*, 3734-3738; b) H. J. Fan, M. Knez, R. Scholz, D. Hesse, K. Nielsch, M. Zacharias, U. Gösele, *Nano Lett.* **2007**, *7*, 993-997; c) H. Jin fan, M. Knez, R. Scholz, K. Nielsch, E. Pippel, D. Hesse, M. Zacharias, U. Gösele, *Nature Materials* **2006**, *5*, 627.

[63]   T. Kennedy, M. Bezuidenhout, K. Palaniappan, K. Stokes, M. Brandon, K. M. Ryan, *ACS Nano* **2015**, *9*, 7456-7465.

[64]   I.-S. Hwang, J.-C. Kim, S.-D. Seo, S. Lee, J.-H. Lee, D.-W. Kim, *Chem. Commun.* **2012**, *48*, 7061-7063.

[65]   R. Hu, H. Liu, M. Zeng, J. Liu, M. Zhu, *Chin. Sci. Bull.* **2012**, *57*, 4119-4130.

[66]   a) J. Wang, I. D. Raistrick, R. A. Huggins, *J. Electrochem. Soc.* **1986**, *133*, 457-460; b) A. Anani, S. Crouch-Baker, R. A. Huggins, *J. Electrochem. Soc.* **1987**, *134*, 3098-3102; c) F. M. Courtel, Y. Abu-Lebdeh, in *Nanotechnology for Lithium-Ion Batteries* (Eds.: Y. Abu-Lebdeh, I. Davidson), Springer US, Boston, MA, **2013**, pp. 67-83.

[67]   a) M. Inaba, T. Uno, A. Tasaka, *J. Power Sources* **2005**, *146*, 473-477; b) J. Hassoun, P. Reale, S. Panero, *J. Power Sources* **2007**, *174*, 321-327.

[68]   L. Y. Beaulieu, T. D. Hatchard, A. Bonakdarpour, M. D. Fleischauer, J. R. Dahn, *J. Electrochem. Soc.* **2003**, *150*, A1457-A1464.

[69]   a) I. A. Courtney, J. S. Tse, O. Mao, J. Hafner, J. R. Dahn, *Physical Review B* **1998**, *58*, 15583-15588; b) I. A. Courtney, J. R. Dahn, *J. Electrochem. Soc.* **1997**, *144*, 2045-2052.

[70]   K.-F. Chiu, H. C. Lin, K. M. Lin, T. Y. Lin, D. T. Shieh, *J. Electrochem. Soc.* **2006**, *153*, A1038-A1042.

[71]   M. Mohamedi, S.-J. Lee, D. Takahashi, M. Nishizawa, T. Itoh, I. Uchida, *Electrochim. Acta* **2001**, *46*, 1161-1168.

[72]   J.-j. Zhang, Y.-y. Xia, *J. Electrochem. Soc.* **2006**, *153*, A1466.

[73]   O. Mao, R. A. Dunlap, J. R. Dahn, *J. Electrochem. Soc.* **1999**, *146*, 405-413.

[74]   H. Mukaibo, T. Momma, T. Osaka, *J. Power Sources* **2005**, *146*, 457-463.

[75]   K. D. Kepler, J. T. Vaughey, M. M. Thackeray, *Electrochem. Solid-State Lett.* **1999**, *2*, 307-309.

[76]   a) *Sony's New Nexelion Hybrid Lithium Ion Batteries to have 30% more Capacity than Conventional Offering*. 2005. https://www.sony.net/SonyInfo/News/Press/200502/05-006E/; b) H. Inoue, in *International Meeting on Lithium Batteries, Vol. Abstract No. 228*, Biarritz, France, **2006**; c) H. Inoue, S. Mizutani, H. Ishihara, S. Hatake, *Meeting Abstracts* **2008**, *MA2008-02*, 1160; d) H. Inoue, T. Takada, Y. Kudo, *Electrochemistry* **2008**, *76*, 358-362.

[77]   A. D. W. Todd, P. P. Ferguson, M. D. Fleischauer, J. R. Dahn, *International Journal of Energy Research* **2010**, *34*, 535-555.

[78]   P. P. Ferguson, P. Liao, R. A. Dunlap, J. R. Dahn, *J. Electrochem. Soc.* **2009**, *156*, A13-A17.

[79]   T. Reddy, D. Linden, in *Linden's Handbook of Batteries, Fourth Edition* (Eds.: J. Dahn, G. M. Ehrlich), McGraw Hill Professional, Access Engineering, **2010**, pp. 26.21-26.79.

[80]   a) M. S. Islam, C. A. J. Fisher, *Chem. Soc. Rev.* **2014**, *43*, 185-204; b) M. S. Whittingham, Y. Song, S. Lutta, P. Y. Zavalij, N. A. Chernova, *J. Mater. Chem.* **2005**, *15*, 3362-3379.

[81]   D. O'Hare, *Inorganic materials*, Wiley, Chichester, **1992**.

[82]   a) P. Liu, S.-H. Lee, Y. Yan, C. Edwin Tracy, J. A. Turner, *J. Power Sources* **2006**, *158*, 659-662; b) J. Yamaki, M. Makidera, T. Kawamura, M. Egashira, S. Okada, *J. Power Sources* **2006**, *153*, 245-250.

[83]   S. A. Solin, in *Intercalation in Layered Materials* (Ed.: M. S. Dresselhaus), Springer US, Boston, MA, **1986**, pp. 145-154.

[84]   a) Z. Chen, Y. Qin, K. Amine, Y. K. Sun, *J. Mater. Chem.* **2010**, *20*, 7606-7612; b) Z. Chen, J. R. Dahn, *Electrochem. Solid-State Lett.* **2003**, *6*, A221-A224; c) Z. Chen, J. R. Dahn, *Electrochem. Solid-State Lett.* **2002**, *5*, A213-A216.

[85]   a) M. M. Thackeray, S.-H. Kang, C. S. Johnson, J. T. Vaughey, R. Benedek, S. A. Hackney, *J. Mater. Chem.* **2007**, *17*, 3112-3125; b) N. Yabuuchi, K. Yoshii, S.-T. Myung, I. Nakai, S. Komaba, *J. Am. Chem. Soc.* **2011**, *133*, 4404-4419.

[86]   a) Z. Lu, J. R. Dahn, *J. Electrochem. Soc.* **2002**, *149*, A815-A822; b) Z. Chen, Y.-K. Sun, K. Amine, *J. Electrochem. Soc.* **2006**, *153*, A1818-A1822.

[87]   C. Kim, T. Fujino, K. Miyashita, T. Hayashi, M. Endo, M. S. Dresselhaus, *J. Electrochem. Soc.* **2000**, *147*, 1257-1264.

[88]   J. N. Reimers, J. R. Dahn, *J. Electrochem. Soc.* **1992**, *139*, 2091-2097.

[89]   a) H. Gabrisch, R. Yazami, B. Fultz, *J. Electrochem. Soc.* **2004**, *151*, A891-A897; b) H. Wang, Y. I. Jang, B. Huang, D. R. Sadoway, Y. M. Chiang, *J. Electrochem. Soc.* **1999**, *146*, 473-480; c) H. Gabrisch, R. Yazami, B. Fultz, *J. Power Sources* **2003**, *119-121*, 674-679.

[90]   M. S. Whittingham, *Chem. Rev.* **2004**, *104*, 4271-4302.

[91]   a) W. D. Johnston, R. R. Heikes, D. Sestrich, *J. Phys. Chem. Solids* **1958**, *7*, 1-13; b) M. Yoshio, H. Tanaka, K. Tominaga, H. Noguchi, *J. Power Sources* **1992**, *40*, 347-353; c) M. Antaya, J. R. Dahn, J. S. Preston, E. Rossen, J. N. Reimers, *J. Electrochem. Soc.* **1993**, *140*, 575-578; d) P. Fragnaud, R. Nagarajan, D. M. Schleich, D. Vujic, *J. Power Sources* **1995**, *54*, 362-366; e) E. Zhecheva, R. Stoyanova, M. Gorova, R. Alcántara, J. Morales, J. L. Tirado, *Chem. Mater.* **1996**, *8*, 1429-1440; f) E.-D. Jeong, M.-S. Won, Y.-B. Shim, *J. Power Sources* **1998**, *70*, 70-77; g) P. N. Kumta, D. Gallet, A. Waghray, G. E. Blomgren, M. P. Setter, *J. Power Sources* **1998**, *72*, 91-98.

[92]   E. Antolini, *Solid State Ionics* **2004**, *170*, 159-171.

[93]   J. B. Bates, N. J. Dudney, B. J. Neudecker, F. X. Hart, H. P. Jun, S. A. Hackney, *J. Electrochem. Soc.* **2000**, *147*, 59-70.

[94]   Y. Yoon, C. Park, J. Kim, D. Shin, *J. Power Sources* **2013**, *226*, 186-190.

[95]   C.-L. Liao, K.-Z. Fung, *J. Power Sources* **2004**, *128*, 263-269.

[96]   Y. S. Yoon, S. H. Lee, S. B. Cho, S. C. Nam, *J. Electrochem. Soc.* **2011**, *158*, A1313-A1319.

[97]   a) K. Gerasopoulos, E. Pomerantseva, M. McCarthy, A. Brown, C. Wang, J. Culver, R. Ghodssi, *ACS Nano* **2012**, *6*, 6422-6432; b) Y. Liu, W. Zhang, Y. Zhu, Y. Luo, Y. Xu, A. Brown, J. N. Culver, C. A. Lundgren, K. Xu, Y. Wang, C. Wang, *Nano Lett.* **2013**, *13*, 293-300.

[98]   H. Xia, Y. Wan, W. Assenmacher, W. Mader, G. Yuan, L. Lu, *NPG Asia Mater* **2014**, *6*, e126.

[99]   M. M. Shaijumon, E. Perre, B. Daffos, P.-L. Taberna, J.-M. Tarascon, P. Simon, *Adv. Mater.* **2010**, *22*, 4978-4981.

[100]   I. D. Scott, Y. S. Jung, A. S. Cavanagh, Y. Yan, A. C. Dillon, S. M. George, S.-H. Lee, *Nano Lett.* **2011**, *11*, 414-418.

[101]   H.-M. Cheng, F.-M. Wang, J. P. Chu, R. Santhanam, J. Rick, S.-C. Lo, *J. Phys. Chem. C* **2012**, *116*, 7629-7637.

[102]   J. Kim, M. Noh, J. Cho, H. Kim, K.-B. Kim, *J. Electrochem. Soc.* **2005**, *152*, A1142-A1148.

[103]   T. Fang, J.-G. Duh, S.-R. Sheen, *J. Electrochem. Soc.* **2005**, *152*, A1701-A1706.

[104]   *Why Everyone Wants to Get Their Hands on Cobalt*. 2017. http://themarketmogul.com/hands-on-cobalt/

[105]   *Cobalt*. 2017. http://tradingeconomics.com/commodity/cobalt

[106] T. Ohzuku, A. Ueda, M. Nagayama, *J. Electrochem. Soc.* **1993**, *140*, 1862-1870.

[107] K. Kang, Y. S. Meng, J. Bréger, C. P. Grey, G. Ceder, *Science* **2006**, *311*, 977-980.

[108] K. Takada, N. Aotani, K. Iwamoto, S. Kondo, *Solid State Ionics* **1995**, *79*, 284-287.

[109] a) A. Rougier, P. Gravereau, C. Delmas, *J. Electrochem. Soc.* **1996**, *143*, 1168-1175; b) J. R. Dahn, U. von Sacken, C. A. Michal, *Solid State Ionics* **1990**, *44*, 87-97.

[110] S. Yamada, M. Fujiwara, M. Kanda, *J. Power Sources* **1995**, *54*, 209-213.

[111] a) J. Cho, H. Jung, Y. Park, G. Kim, H. S. Lim, *J. Electrochem. Soc.* **2000**, *147*, 15-20; b) J. R. Dahn, E. W. Fuller, M. Obrovac, U. von Sacken, *Solid State Ionics* **1994**, *69*, 265-270.

[112] *Breakdown of raw materials in Tesla's batteries and possible bottlenecks*. 2016. https://electrek.co/2016/11/01/breakdown-raw-materials-tesla-batteries-possible-bottleneck/

[113] M. R. Palacín, D. Larcher, A. Audemer, N. Sac-Épée, G. G. Amatucci, J. M. Tarascon, *J. Electrochem. Soc.* **1997**, *144*, 4226-4236.

[114] a) C. Pouillerie, L. Croguennec, C. Delmas, *Solid State Ionics* **2000**, *132*, 15-29; b) Y. Gao, M. V. Yakovleva, W. B. Ebner, *Electrochem. Solid-State Lett.* **1998**, *1*, 117-119; c) C. Pouillerie, F. Perton, P. Biensan, J. P. Pérès, M. Broussely, C. Delmas, *J. Power Sources* **2001**, *96*, 293-302; d) C. H. Chen, J. Liu, M. E. Stoll, G. Henriksen, D. R. Vissers, K. Amine, *J. Power Sources* **2004**, *128*, 278-285.

[115] I. Nakai, T. Nakagome, *Electrochem. Solid-State Lett.* **1998**, *1*, 259-261.

[116] a) M. G. Kim, H. J. Shin, J.-H. Kim, S.-H. Park, Y.-K. Sun, *J. Electrochem. Soc.* **2005**, *152*, A1320-A1328; b) B. J. Hwang, Y. W. Tsai, D. Carlier, G. Ceder, *Chem. Mater.* **2003**, *15*, 3676-3682.

[117] Y.-K. Sun, S.-T. Myung, B.-C. Park, J. Prakash, I. Belharouak, K. Amine, *Nature Materials* **2009**, *8*, 320.

[118] a) J. Tu, X. B. Zhao, G. S. Cao, D. G. Zhuang, T. J. Zhu, J. P. Tu, *Electrochim. Acta* **2006**, *51*, 6456-6462; b) M. M. Thackeray, *Prog. Solid State Chem.* **1997**, *25*, 1-71.

[119] W. Liu, G. C. Farrington, F. Chaput, B. Dunn, *J. Electrochem. Soc.* **1996**, *143*, 879-884.

[120] W. S. Yang, G. Zhang, S. G. Lu, J. Y. Xie, Q. G. Liu, *Solid State Ionics* **1999**, *121*, 85-89.

[121] O. K. Park, Y. Cho, S. Lee, H.-C. Yoo, H.-K. Song, J. Cho, *Energy Environ. Sci.* **2011**, *4*, 1621-1633.

[122] K. Naoaki, K. Shinichi, K. Yoichi, K. Makoto, *Chem. Lett.* **2000**, *29*, 1154-1155.

[123] X. Hao, X. Lin, W. Lu, B. M. Bartlett, *ACS Appl. Mater. Interfaces* **2014**, *6*, 10849-10857.

[124] a) J.-W. Song, C. C. Nguyen, H. Choi, K.-H. Lee, K.-H. Han, Y.-J. Kim, S. Choy, S.-W. Song, *J. Electrochem. Soc.* **2011**, *158*, A458-A464; b) Y. L. Ding, J. Xie, G. S. Cao, T. J. Zhu, H. M. Yu, X. B. Zhao, *J. Phys. Chem. C* **2011**, *115*, 9821-9825.

[125] Z. Chen, K. Amine, *J. Electrochem. Soc.* **2006**, *153*, A1279-A1283.

[126] M. Okubo, Y. Mizuno, H. Yamada, J. Kim, E. Hosono, H. Zhou, T. Kudo, I. Honma, *ACS Nano* **2010**, *4*, 741-752.

[127] E. Hosono, T. Kudo, I. Honma, H. Matsuda, H. Zhou, *Nano Lett.* **2009**, *9*, 1045-1051.

[128] H.-W. Lee, P. Muralidharan, R. Ruffo, C. M. Mari, Y. Cui, D. K. Kim, *Nano Lett.* **2010**, *10*, 3852-3856.

[129] K. Ariyoshi, E. Iwata, M. Kuniyoshi, H. Wakabayashi, T. Ohzuku, *Electrochem. Solid-State Lett.* **2006**, *9*, A557-A560.

[130] Y. Yang, C. Xie, R. Ruffo, H. Peng, D. K. Kim, Y. Cui, *Nano Lett.* **2009**, *9*, 4109-4114.

[131] H. Shigemura, H. Sakaebe, H. Kageyama, H. Kobayashi, A. R. West, R. Kanno, S. Morimoto, S. Nasu, M. Tabuchi, *J. Electrochem. Soc.* **2001**, *148*, A730-A736.

[132] a) N. Amdouni, F. Gendron, A. Mauger, C. Julien, in *Materials Research Society Symposium Proceedings, Vol. 973*, Warrendale, Pa.; Materials Research Society; 1999, **2007**, p. 67; b) C. Wang, S. Lu, S. Kan, J. Pang, W. Jin, X. Zhang, *J. Power Sources* **2009**, *189*, 607-610; c) P. Arora, B. N. Popov, R. E. White, *J. Electrochem. Soc.* **1998**, *145*, 807-815; d) H. Huang, C. Wang, W. K. Zhang, Y. P. Gan, L. Kang, *J. Power Sources* **2008**, *184*, 583-588.

[133] J. B. Goodenough, in *Advances in Lithium-Ion Batteries* (Eds.: W. A. van Schalkwijk, B. Scrosati), Springer US, Boston, MA, **2002**, pp. 135-154.

[134] a) J. H. Kim, S. T. Myung, C. S. Yoon, S. G. Kang, Y. K. Sun, *Chem. Mater.* **2004**, *16*, 906-914; b) K. M. Shaju, P. G. Bruce, *Dalton Transactions* **2008**, 5471-5475.

[135] M. Kunduraci, G. G. Amatucci, *J. Electrochem. Soc.* **2006**, *153*, A1345-A1352.

[136] H. Xia, Y. S. Meng, L. Lu, G. Ceder, *J. Electrochem. Soc.* **2007**, *154*, A737-A743.

[137] Q. Zhong, A. Bonakdarpour, M. Zhang, Y. Gao, J. R. Dahn, *J. Electrochem. Soc.* **1997**, *144*, 205-213.

[138] R. Santhanam, B. Rambabu, *J. Power Sources* **2010**, *195*, 5442-5451.

[139] R. Alcántara, M. Jaraba, P. Lavela, J. L. Tirado, P. Biensan, A. de Guibert, C. Jordy, J. P. Peres, *Chem. Mater.* **2003**, *15*, 2376-2382.

[140] J.-H. Kim, S.-T. Myung, C. S. Yoon, I.-H. Oh, Y.-K. Sun, *J. Electrochem. Soc.* **2004**, *151*, A1911-A1918.

[141] J. Liu, A. Manthiram, *J. Phys. Chem. C* **2009**, *113*, 15073-15079.

[142] B. León, J. M. Lloris, C. P. Vicente, J. L. Tirado, *Electrochem. Solid-State Lett.* **2006**, *9*, A96-A100.

[143] a) H. Wang, H. Xia, M. O. Lai, L. Lu, *Electrochem. Commun.* **2009**, *11*, 1539-1542; b) C. Locati, U. Lafont, L. Simonin, F. Ooms, E. M. Kelder, *J. Power Sources* **2007**, *174*, 847-851; c) M. Aklalouch, J. M. Amarilla, R. M. Rojas, I. Saadoune, J. M. Rojo, *J. Power Sources* **2008**, *185*, 501-511; d) X. X. Xu, J. Yang, Y. Q. Wang, Y. N. NuLi, J. L. Wang, *J. Power Sources* **2007**, *174*, 1113-1116.

[144] S. H. Oh, K. Y. Chung, S. H. Jeon, C. S. Kim, W. I. Cho, B. W. Cho, *J. Alloys Compd.* **2009**, *469*, 244-250.

[145] a) Y. K. Sun, K. J. Hong, J. Prakash, K. Amine, *Electrochem. Commun.* **2002**, *4*, 344-348; b) Y.-K. Sun, Y.-S. Lee, M. Yoshio, K. Amine, *J. Electrochem. Soc.* **2003**, *150*, L11.

[146] Y.-K. Sun, Y.-S. Lee, M. Yoshio, K. Amine, *Electrochem. Solid-State Lett.* **2002**, *5*, A99-A102.

[147] a) Y. Fan, J. Wang, Z. Tang, W. He, J. Zhang, *Electrochim. Acta* **2007**, *52*, 3870-3875; b) J. Arrebola, A. Caballero, L. Hernán, J. Morales, E. Rodríguez Castellón, J. R. Ramos Barrado, *J. Electrochem. Soc.* **2007**, *154*, A178-A184; c) J. Arrebola, A. Caballero, L. Hernán, J. Morales, E. Rodríguez Castellón, *Electrochem. Solid-State Lett.* **2005**, *8*, A303-A307.

[148] Y. Kobayashi, H. Miyashiro, K. Takei, H. Shigemura, M. Tabuchi, H. Kageyama, T. Iwahori, *J. Electrochem. Soc.* **2003**, *150*, A1577-A1582.

[149] T. V. S. L. Satyavani, A. Srinivas Kumar, P. S. V. Subba Rao, *Engineering Science and Technology, an International Journal* **2016**, *19*, 178-188.

[150] K. Tang, J. Sun, X. Yu, H. Li, X. Huang, *Electrochim. Acta* **2009**, *54*, 6565-6569.

[151] A. K. Padhi, K. S. Nanjundaswamy, J. B. Goodenough, *J. Electrochem. Soc.* **1997**, *144*, 1188-1194.

[152] Z. Gong, Y. Yang, *Energy Environ. Sci.* **2011**, *4*, 3223-3242.

[153] B. Ellis, L. K. Perry, D. H. Ryan, L. F. Nazar, *J. Am. Chem. Soc.* **2006**, *128*, 11416-11422.

[154] Y. Feng, G. Shenguang, L. Bing, S. Gengzhi, M. Riguo, Z. Lianxi, *Current Inorganic Chemistry* **2012**, *2*, 194-212.

[155] a) N. Meethong, Y.-H. Kao, M. Tang, H.-Y. Huang, W. C. Carter, Y.-M. Chiang, *Chem. Mater.* **2008**, *20*, 6189-6198; b) J. L. Allen, T. R. Jow, J. Wolfenstine, *J. Solid State Electrochem.* **2008**, *12*, 1031-1033; c) R. Dedryvère, M. Maccario, L. Croguennec, F. Le Cras, C. Delmas, D. Gonbeau, *Chem. Mater.* **2008**, *20*, 7164-7170; d) Z. Yang, Y. Dai, S. Wang, J. Yu, *J. Mater. Chem. A* **2016**, *4*, 18210-18222.

[156] R. Malik, F. Zhou, G. Ceder, *Nature Materials* **2011**, *10*, 587.

[157] S. Yang, Y. Song, P. Y. Zavalij, M. Stanley Whittingham, *Electrochem. Commun.* **2002**, *4*, 239-244.

[158] a) B. Hu, G. Tao, *J. Mater. Chem. A* **2015**, *3*, 20399-20407; b) M. S. Islam, D. J. Driscoll, C. A. J. Fisher, P. R. Slater, *Chem. Mater.* **2005**, *17*, 5085-5092; c) R. Malik, D. Burch, M. Bazant, G. Ceder, *Nano Lett.* **2010**, *10*, 4123-4127; d) J. Maier, R. Amin, *J. Electrochem. Soc.* **2008**, *155*, A339-A344.

[159] C. Zhu, Y. Yu, L. Gu, K. Weichert, J. Maier, *Angew. Chem. Int. Ed.* **2011**, *50*, 6278-6282.

[160] S.-B. Park, C.-K. Park, J.-T. Hwang, W.-I. Cho, H. Jang, *Bull. Korean Chem. Soc.* **2011**, *32*, 536-540.

[161] a) H. Liu, J. Xie, K. Wang, *Solid State Ionics* **2008**, *179*, 1768-1771; b) W. Ojczyk, J. Marzec, K. Świerczek, W. Zając, M. Molenda, R. Dziembaj, J. Molenda, *J. Power Sources* **2007**, *173*, 700-706.

[162] M.-S. Song, D.-Y. Kim, Y.-M. Kang, Y.-I. Kim, J.-Y. Lee, H.-S. Kwon, *J. Power Sources* **2008**, *180*, 546-552.

[163] Y. Lin, Y. Lin, T. Zhou, G. Zhao, Y. Huang, Z. Huang, *J. Power Sources* **2013**, *226*, 20-26.

[164] B. Kang, G. Ceder, *Nature* **2009**, *458*, 190.

[165] a) F. Omenya, N. A. Chernova, S. Upreti, P. Y. Zavalij, K.-W. Nam, X.-Q. Yang, M. S. Whittingham, *Chem. Mater.* **2011**, *23*, 4733-4740; b) L.-L. Zhang, G. Liang, A. Ignatov, M. C. Croft, X.-Q. Xiong, I. M. Hung, Y.-H. Huang, X.-L. Hu, W.-X. Zhang, Y.-L. Peng, *J. Phys. Chem. C* **2011**, *115*, 13520-13527.

[166] N. Hua, C. Wang, X. Kang, T. Wumair, Y. Han, *J. Alloys Compd.* **2010**, *503*, 204-208.

[167] J. Hong, C. S. Wang, X. Chen, S. Upreti, M. S. Whittingham, *Electrochem. Solid-State Lett.* **2009**, *12*, A33-A38.

[168] a) S.-W. Kim, J. Kim, H. Gwon, K. Kang, *J. Electrochem. Soc.* **2009**, *156*, A635-A638; b) N. N. Bramnik, K. Nikolowski, D. M. Trots, H. Ehrenberg, *Electrochem. Solid-State Lett.* **2008**, *11*, A89-A93; c) Y. Zhang, Y. Pan, J. Liu, G. Wang, D. Cao, *Chemical Research in Chinese Universities* **2015**, *31*, 117-122.

[169] a) Y. Wang, G. Cao, *Chem. Mater.* **2006**, *18*, 2787-2804; b) C. Delmas, H. Cognac-Auradou, J. M. Cocciantelli, M. Ménétrier, J. P. Doumerc, *Solid State Ionics* **1994**, *69*, 257-264.

[170] M. S. Whittingham, *J. Electrochem. Soc.* **1976**, *123*, 315-320.

[171] C. O'Dwyer, V. Lavayen, S. B. Newcomb, M. A. Santa Ana, E. Benavente, G. González, C. M. Sotomayor Torres, *J. Electrochem. Soc.* **2007**, *154*, K29-K35.

[172] R. J. Cava, A. Santoro, D. W. Murphy, S. M. Zahurak, R. M. Fleming, P. Marsh, R. S. Roth, *J. Solid State Chem.* **1986**, *65*, 63-71.

[173] J. M. Cocciantelli, M. Ménétrier, C. Delmas, J. P. Doumerc, M. Pouchard, M. Broussely, J. Labat, *Solid State Ionics* **1995**, *78*, 143-150.

[174] J. M. Cocciantelli, J. P. Doumerc, M. Pouchard, M. Broussely, J. Labat, *J. Power Sources* **1991**, *34*, 103-111.

[175] a) C. Leger, S. Bach, P. Soudan, J.-P. Pereira-Ramos, *J. Electrochem. Soc.* **2005**, *152*, A236-A241; b) C. Delmas, S. Brèthes, M. Ménétrier, *J. Power Sources* **1991**, *34*, 113-118.

[176] a) X. Rui, J. Zhu, W. Liu, H. Tan, D. Sim, C. Xu, H. Zhang, J. Ma, H. H. Hng, T. M. Lim, Q. Yan, *RSC Advances* **2011**, *1*, 117-122; b) T. Watanabe, Y. Ikeda, T. Ono, M. Hibino, M. Hosoda, K. Sakai, T. Kudo, *Solid State Ionics* **2002**, *151*, 313-320; c) J. Liu, Y. Zhou, J. Wang, Y. Pan, D. Xue, *Chem. Commun.* **2011**, *47*, 10380-10382.

[177] D. Chao, X. Xia, J. Liu, Z. Fan, C. F. Ng, J. Lin, H. Zhang, Z. X. Shen, H. J. Fan, *Adv. Mater.* **2014**, *26*, 5794-5800.

[178] Y.-Z. Zheng, H. Ding, E. Uchaker, X. Tao, J.-F. Chen, Q. Zhang, G. Cao, *J. Mater. Chem. A* **2015**, *3*, 1979-1985.

[179] a) H. Zeng, D. Liu, Y. Zhang, K. A. See, Y.-S. Jun, G. Wu, J. A. Gerbec, X. Ji, G. D. Stucky, *Chem. Mater.* **2015**, *27*, 7331-7336; b) F. Coustier, J. Hill, B. B. Owens, S. Passerini, W. H. Smyrl, *J. Electrochem. Soc.* **1999**, *146*, 1355-1360.

[180] Y. Li, J. Yao, E. Uchaker, M. Zhang, J. Tian, X. Liu, G. Cao, *J. Phys. Chem. C* **2013**, *117*, 23507-23514.

[181] Z. Li, C. Zhang, C. Liu, H. Fu, X. Nan, K. Wang, X. Li, W. Ma, X. Lu, G. Cao, *Electrochim. Acta* **2016**, *222*, 1831-1838.

[182] a) G. Blomgren, Marcel Dekker, NY, **1999**; b) D. Aurbach, I. Weissman, Marcel Dekker, NY, **1999**.

[183] K. Xu, *Chem. Rev.* **2004**, *104*, 4303-4418.

[184] M. Morita, T. Shibata, N. Yoshimoto, M. Ishikawa, *Electrochim. Acta* **2002**, *47*, 2787-2793.

[185] M. Marcinek, J. Syzdek, M. Marczewski, M. Piszcz, L. Niedzicki, M. Kalita, A. Plewa-Marczewska, A. Bitner, P. Wieczorek, T. Trzeciak, M. Kasprzyk, P.Łężak, Z. Zukowska, A. Zalewska, W. Wieczorek, *Solid State Ionics* **2015**, *276*, 107-126.

[186] L. Niedzicki, S. Grugeon, S. Laruelle, P. Judeinstein, M. Bukowska, J. Prejzner, P. Szczeciñski, W. Wieczorek, M. Armand, *J. Power Sources* **2011**, *196*, 8696-8700.

[187] B. Ravdel, K. M. Abraham, R. Gitzendanner, J. DiCarlo, B. Lucht, C. Campion, *J. Power Sources* **2003**, *119-121*, 805-810.

[188] S. E. Sloop, J. B. Kerr, K. Kinoshita, *J. Power Sources* **2003**, *119-121*, 330-337.

[189] K. Amine, J. Liu, I. Belharouak, *Electrochem. Commun.* **2005**, *7*, 669-673.

[190] D. Aurbach, A. Zaban, Y. Ein-Eli, I. Weissman, O. Chusid, B. Markovsky, M. Levi, E. Levi, A. Schechter, E. Granot, *J. Power Sources* **1997**, *68*, 91-98.

[191] a) E. W. Lawless, C. J. W. Wiegand, Y. Mizumoto, C. Weis, *Inorg. Chem.* **1971**, *10*, 1084-1086; b) C. Nanjundiah, J. L. Goldman, L. A. Dominey, V. R. Koch, *J. Electrochem. Soc.* **1988**, *135*, 2914-2917.

[192] V. R. Koch, *J. Electrochem. Soc.* **1979**, *126*, 181-187.

[193] a) S. S. Zhang, K. Xu, T. R. Jow, *J. Electrochem. Soc.* **2002**, *149*, A586-A590; b) S. S. Zhang, T. R. Jow, *J. Power Sources* **2002**, *109*, 458-464.

[194] a) D. P. Abraham, M. M. Furczon, S. H. Kang, D. W. Dees, A. N. Jansen, *J. Power Sources* **2008**, *180*, 612-620; b) M. Nie, B. L. Lucht, *J. Electrochem. Soc.* **2014**, *161*, A1001-A1006.

[195] a) J. S. Gnanaraj, E. Zinigrad, L. Asraf, H. E. Gottlieb, M. Sprecher, D. Aurbach, M. Schmidt, *J. Power Sources* **2003**, *119-121*, 794-798; b) C. Iwakura, Y. Fukumoto, H. Inoue, S. Ohashi, S. Kobayashi, H. Tada, M. Abe, *J. Power Sources* **1997**, *68*, 301-303; c) R. Marom, O. Haik, D. Aurbach, I. C. Halalay, *J. Electrochem. Soc.* **2010**, *157*, A972-A983.

[196] G. H. Newman, R. W. Francis, L. H. Gaines, B. M. L. Rao, *J. Electrochem. Soc.* **1980**, *127*, 2025-2027.

[197] J. Foropoulos, D. D. DesMarteau, *Inorg. Chem.* **1984**, *23*, 3720-3723.

[198] a) D. Di Censo, I. Exnar, M. Graetzel, *Electrochem. Commun.* **2005**, *7*, 1000-1006; b) A. Webber, *J. Electrochem. Soc.* **1991**, *138*, 2586-2590; c) Z. Lu, L. Yang, Y. Guo, *J. Power Sources* **2006**, *156*, 555-559; d) S. F. Lux, L. Terborg, O. Hachmöller, T. Placke, H.-W. Meyer, S. Passerini, M. Winter, S. Nowak, *J. Electrochem. Soc.* **2013**, *160*, A1694-A1700.

[199] a) H. Yang, K. Kwon, T. M. Devine, J. W. Evans, *J. Electrochem. Soc.* **2000**, *147*, 4399-4407; b) X. Zhang, B. Winget, M. Doeff, J. W. Evans, T. M. Devine, *J. Electrochem. Soc.* **2005**, *152*, B448-B454; c) L. J. Krause, W. Lamanna, J. Summerfield, M. Engle, G. Korba, R. Loch, R. Atanasoski, *J. Power Sources* **1997**, *68*, 320-325.

[200] K. Matsumoto, K. Inoue, K. Nakahara, R. Yuge, T. Noguchi, K. Utsugi, *J. Power Sources* **2013**, *231*, 234-238.

[201] J. Kalhoff, D. Bresser, M. Bolloli, F. Alloin, J.-Y. Sanchez, S. Passerini, *ChemSusChem* **2014**, *7*, 2939-2946.

[202] K. Xu, *Chem. Rev.* **2014**, *114*, 11503-11618.

[203] M. Schmidt, U. Heider, A. Kuehner, R. Oesten, M. Jungnitz, N. Ignat'ev, P. Sartori, *J. Power Sources* **2001**, *97-98*, 557-560.

[204] a) J. S. Gnanaraj, M. D. Levi, Y. Gofer, D. Aurbach, M. Schmidt, *J. Electrochem. Soc.* **2003**, *150*, A445-A454; b) J. S. Gnanaraj, E. Zinigrad, L. Asraf, M. Sprecher, H. E. Gottlieb, W. Geissler, M. Schmidt, D. Aurbach, *Electrochem. Commun.* **2003**, *5*, 946-951.

[205] a) S. Zhang, K. Xu, T. Jow, *J. Solid State Electrochem.* **2003**, *7*, 147-151; b) S. S. Zhang, K. Xu, T. R. Jow, *Electrochem. Commun.* **2002**, *4*, 928-932; c) Z. Liu, J. Chai, G. Xu, Q. Wang, G. Cui, *Coord. Chem. Rev.* **2015**, *292*, 56-73.

[206] U. Wietelmann, U. Lischka, M. Wegner, Lithium bisoxalatoborate, the production thereof and its use as a conducting salt, **2003**,

[207] a) S.-T. Myung, H. Natsui, Y.-K. Sun, H. Yashiro, *J. Power Sources* **2010**, *195*, 8297-8301; b) K. Xu, S. Zhang, T. R. Jow, W. Xu, C. A. Angell, *Electrochem. Solid-State Lett.* **2002**, *5*, A26-A29; c) X. Zhang, T. M. Devine, *J. Electrochem. Soc.* **2006**, *153*, B365-B369.

[208] a) J.-C. Panitz, U. Wietelmann, M. Wachtler, S. Ströbele, M. Wohlfahrt-Mehrens, *J. Power Sources* **2006**, *153*, 396-401; b) K. Xu, S. Zhang, T. R. Jow, *Electrochem. Solid-State Lett.* **2003**, *6*, A117-A120; c) L. Larush-Asraf, M. Biton, H. Teller, E. Zinigrad, D. Aurbach, *J. Power Sources* **2007**, *174*, 400-407.

[209] Z.-M. Xue, B.-B. Sun, W. Zhou, C.-H. Chen, *J. Power Sources* **2011**, *196*, 8710-8713.

[210] K. Xu, *J. Electrochem. Soc.* **2008**, *155*, A733-A738.

[211] H.-B. Han, S.-S. Zhou, D.-J. Zhang, S.-W. Feng, L.-F. Li, K. Liu, W.-F. Feng, J. Nie, H. Li, X.-J. Huang, M. Armand, Z.-B. Zhou, *J. Power Sources* **2011**, *196*, 3623-3632.

[212] K. Naoi, M. Mori, Y. Naruoka, W. M. Lamanna, R. Atanasoski, *J. Electrochem. Soc.* **1999**, *146*, 462-469.

[213] L. Li, S. Zhou, H. Han, H. Li, J. Nie, M. Armand, Z. Zhou, X. Huang, *J. Electrochem. Soc.* **2011**, *158*, A74-A82.

[214] a) P. Murmann, P. Niehoff, R. Schmitz, S. Nowak, H. Gores, N. Ignatiev, P. Sartori, M. Winter, R. Schmitz, *Electrochim. Acta* **2013**, *114*, 658-666; b) J. S. Gnanaraj, E. Zinigrad, M. D. Levi, D. Aurbach, M. Schmidt, *J. Power Sources* **2003**, *119-121*, 799-804.

[215] S.-T. Myung, H. Yashiro, *J. Power Sources* **2014**, *271*, 167-173.

[216] a) M. Armand, P. Johansson, *J. Power Sources* **2008**, *178*, 821-825; b) P. Johansson, H. Nilsson, P. Jacobsson, M. Armand, *PCCP* **2004**, *6*, 895-899.

[217] a) L. Niedzicki, G. Z. Żukowska, M. Bukowska, P. Szczeciński, S. Grugeon, S. Laruelle, M. Armand, S. Panero, B. Scrosati, M. Marcinek, W. Wieczorek, *Electrochim. Acta* **2010**, *55*, 1450-1454; b) S. Paillet, G. Schmidt, S. Ladouceur, J. Fréchette, F. Barray, D. Clément, P. Hovington, A. Guerfi, A. Vijh, I. Cayrefourcq, K. Zaghib, *J. Power Sources* **2015**, *294*, 507-515.

[218] S. Paillet, G. Schmidt, S. Ladouceur, J. Fréchette, F. Barray, D. Clément, P. Hovington, A. Guerfi, A. Vijh, I. Cayrefourcq, K. Zaghib, *J. Power Sources* **2015**, *299*, 309-314.

[219] a) L. Niedzicki, E. Karpierz, A. Bitner, M. Kasprzyk, G. Z. Zukowska, M. Marcinek, W. Wieczorek, *Electrochim. Acta* **2014**, *117*, 224-229; b) L. Niedzicki, M. Kasprzyk, K. Kuziak, G. Z. Żukowska, M. Marcinek, W. Wieczorek, M. Armand, *J. Power Sources* **2011**, *196*, 1386-1391.

[220] J. Scheers, Chalmers University of Technology **2011**.

[221] M. Salomon, H.-p. Lin, E. J. Plichta, M. Hendrickson, in *Advances in Lithium-Ion Batteries* (Eds.: W. A. van Schalkwijk, B. Scrosati), Springer US, Boston, MA, **2002**, pp. 309-344.

[222] A. Abouimrane, J. Ding, I. J. Davidson, *J. Power Sources* **2009**, *189*, 693-696.

[223] a) F. Schipper, D. Aurbach, *Russ. J. Electrochem.* **2016**, *52*, 1095-1121; b) D. Aurbach, A. Schechter, in *Lithium Batteries: Science and Technology* (Eds.: G.-A. Nazri, G. Pistoia), Springer US, Boston, MA, **2003**, pp. 530-573; c) J.-i. Yamaki, in *Advances in Lithium-Ion Batteries* (Eds.: W. A. van Schalkwijk, B. Scrosati), Springer US, Boston, MA, **2002**, pp. 155-183; d) M. Nazri, in *Lithium Batteries: Science and Technology* (Eds.: G.-A. Nazri, G. Pistoia), Springer US, Boston, MA, **2003**, pp. 509-529.

[224] J. Kalhoff, G. G. Eshetu, D. Bresser, S. Passerini, *ChemSusChem* **2015**, *8*, 2154-2175.

[225] G. Xiong, A. Kundu, T. S. Fisher, in *Thermal Effects in Supercapacitors*, Springer International Publishing, Cham, **2015**, pp. 27-69.

[226] M. Grützke, X. Mönnighoff, F. Horsthemke, V. Kraft, M. Winter, S. Nowak, *RSC Advances* **2015**, *5*, 43209-43217.

[227] a) D. Aurbach, Y. Talyosef, B. Markovsky, E. Markevich, E. Zinigrad, L. Asraf, J. S. Gnanaraj, H.-J. Kim, *Electrochim. Acta* **2004**, *50*, 247-254; b) M. Moshkovich, M. Cojocaru, H. E. Gottlieb, D. Aurbach, *J. Electroanal. Chem.* **2001**, *497*, 84-96; c) M. Moshkovich, Y. Gofer, D. Aurbach, *J. Electrochem. Soc.* **2001**, *148*, E155-E167.

[228] a) E. Peled, *J. Electrochem. Soc.* **1979**, *126*, 2047-2051; b) Y. Ein-Eli, *Electrochem. Solid-State Lett.* **1999**, *2*, 212-214.

[229] K. Xu, Y. Lam, S. S. Zhang, T. R. Jow, T. B. Curtis, *J. Phys. Chem. C* **2007**, *111*, 7411-7421.

[230] a) M. Winter, K.-C. Moeller, J. O. Besenhard, in *Lithium Batteries: Science and Technology* (Eds.: G.-A. Nazri, G. Pistoia), Springer US, Boston, MA, **2003**, pp. 145-194; b) D. Aurbach, H. Teller, M. Koltypin, E. Levi, *J. Power Sources* **2003**, *119-121*, 2-7.

[231] O. V. Bushkova, T. V. Yaroslavtseva, Y. A. Dobrovolsky, *Russ. J. Electrochem.* **2017**, *53*, 677-699.

[232] S. S. Zhang, *J. Power Sources* **2006**, *162*, 1379-1394.

[233] B. R. Thomas, in *Linden's Handbook of Batteries, Fourth Edition*, McGraw Hill Professional, Access Engineering, **2011**.

[234] a) B. Simon, J.-P. Boeuve, Rechargeable lithium electrochemical cell, **1997**, 5,626,981; b) D. Aurbach, K. Gamolsky, B. Markovsky, Y. Gofer, M. Schmidt, U. Heider, *Electrochim. Acta* **2002**, *47*, 1423-1439; c) H.-H. Lee, Y.-Y. Wang, C.-C. Wan, M.-H. Yang, H.-C. Wu, D.-T. Shieh, *J. Appl. Electrochem.* **2005**, *35*, 615-623; d) I. A. Profatilova, C. Stock, A. Schmitz, S. Passerini, M. Winter, *J. Power Sources* **2013**, *222*, 140-149; e) G. Chen, G. V. Zhuang, T. J. Richardson, G. Liu, P. N. Ross, *Electrochem. Solid-State Lett.* **2005**, *8*, A344-A347; f) G. G. Eshetu, S. Grugeon, G. Gachot, D. Mathiron, M. Armand, S. Laruelle, *Electrochim. Acta* **2013**, *102*, 133-141; g) H. Lee, S. Choi, S. Choi, H.-J. Kim, Y. Choi, S. Yoon, J.-J. Cho, *Electrochem. Commun.* **2007**, *9*, 801-806; h) J. Pires, L. Timperman, A. Castets, J. S. Pena, E. Dumont, S. Levasseur, R. Dedryvere, C. Tessier, M. Anouti, *RSC Advances* **2015**, *5*, 42088-42094.

[235] a) J. Guo, Z. Wen, M. Wu, J. Jin, Y. Liu, *Electrochem. Commun.* **2015**, *51*, 59-63; b) Y. Ji, S. Li, G. Zhong, Z. Zhang, Y. Li, M. J. McDonald, Y. Yang, *J. Electrochem. Soc.* **2015**, *162*, A7015-A7023.

[236] J. Zheng, J. Xiao, M. Gu, P. Zuo, C. Wang, J.-G. Zhang, *J. Power Sources* **2014**, *250*, 313-318.

[237] A. M. Andersson, K. Edström, *J. Electrochem. Soc.* **2001**, *148*, A1100-A1109.

[238] a) X. Sun, H. S. Lee, X.-Q. Yang, J. McBreen, *Electrochem. Solid-State Lett.* **2002**, *5*, A248-A251; b) M. Herstedt, M. Stjerndahl, T. Gustafsson, K. Edström, *Electrochem. Commun.* **2003**, *5*, 467-472; c) Z. Chen, K. Amine, *J. Electrochem. Soc.* **2006**, *153*, A1221-A1225.

[239] a) H. Yamane, T. Inoue, M. Fujita, M. Sano, *J. Power Sources* **2001**, *99*, 60-65; b) Y. Li, R. Zhang, J. Liu, C. Yang, *J. Power Sources* **2009**, *189*, 685-688.

[240] X. Wang, E. Yasukawa, S. Kasuya *J. Electrochem. Soc.* **2001**, *148*, A1058-A1065.

[241] N. S. Choi, Z. Chen, S. A. Freunberger, X. Ji, Y. K. Sun, K. Amine, G. Yushin, L. F. Nazar, J. Cho, P. G. Bruce, *Angew. Chem. Int. Ed. Engl.* **2012**, *51*, 9994-10024.

[242] a) *Samsung Expands Recall to All Galaxy Note7 Devices*. 2016. http://www.samsung.com/us/note7recall/; b) *HP Notebook Computer and Mobile Workstation Battery Safety Recall and Replacement Program*. 2017. https://batteryprogram687.ext.hp.com/en-GB/

[243] B. R. Thomas, in *Linden's Handbook of Batteries, Fourth Edition*, McGraw Hill Professional, Access Engineering, **2011**.

[244] L. L. Gaines, R. M. Cuenca, Argonne National Laboratory, Argonne, IL USA, **2000**, p. 73.

[245] a) R. Ruffo, F. La Mantia, C. Wessells, R. A. Huggins, Y. Cui, *Solid State Ionics* **2011**, *192*, 289-292; b) F. Sauvage, L. Laffont, J. M. Tarascon, E. Baudrin, *J. Power Sources* **2008**, *175*, 495-501.

[246] N. Alias, A. A. Mohamad, *J. Power Sources* **2015**, *274*, 237-251.

[247] H. Manjunatha, G. S. Suresh, T. V. Venkatesha, *J. Solid State Electrochem.* **2011**, *15*, 431-445.

[248] W. Li, W. R. McKinnon, J. R. Dahn, *J. Electrochem. Soc.* **1994**, *141*, 2310-2316.

[249] W. Li, J. R. Dahn, *J. Electrochem. Soc.* **1995**, *142*, 1742-1746.

[250] C. H. Mi, X. G. Zhang, H. L. Li, *J. Electroanal. Chem.* **2007**, *602*, 245-254.

[251] a) J.-Y. Luo, W.-J. Cui, P. He, Y.-Y. Xia, *Nature Chemistry* **2010**, *2*, 760; b) M. Zhao, B. Zhang, G. Huang, H. Zhang, X. Song, *J. Power Sources* **2013**, *232*, 181-186; c) P. He, X. Zhang, Y.-G. Wang, L. Cheng, Y.-Y. Xia, *J. Electrochem. Soc.* **2008**, *155*, A144-A150.

[252] B. E. Conway, in *Electrochemical Supercapacitors: Scientific Fundamentals and Technological Applications*, Springer US, Boston, MA, **1999**, pp. 221-257.

[253] V. Augustyn, J. Come, M. A. Lowe, J. W. Kim, P. L. Taberna, S. H. Tolbert, H. D. Abruna, P. Simon, B. Dunn, *Nature materials* **2013**, *12*, 518-522.

[254] a) V. Augustyn, P. Simon, B. Dunn, *Energy Environ. Sci.* **2014**, *7*, 1597-1614; b) M. Sathiya, A. S. Prakash, K. Ramesha, J. M. Tarascon, A. K. Shukla, *J. Am. Chem. Soc.* **2011**, *133*, 16291-16299; c) K. Brezesinski, J. Wang, J. Haetge, C. Reitz, S. O. Steinmueller, S. H. Tolbert, B. M. Smarsly, B. Dunn, T. Brezesinski, *J. Am. Chem. Soc.* **2010**, *132*, 6982-6990; d) M. Zukalová, M. Kalbáč, L. Kavan, I. Exnar, M. Graetzel, *Chem. Mater.* **2005**, *17*, 1248-1255; e) K. Naoi, K. Kisu, E. Iwama, S. Nakashima, Y. Sakai, Y. Orikasa, P. Leone, N. Dupre, T. Brousse, P. Rozier, W. Naoi, P. Simon, *Energy Environ. Sci.* **2016**, *9*, 2143-2151.

[255] M. Fehse, R. Trócoli, E. Ventosa, E. Hernández, A. Sepúlveda, A. Morata, A. Tarancón, *ACS Appl. Mater. Interfaces* **2017**, *9*, 5295-5301.

[256] M. Pourbaix, *Atlas of electrochemical equilibria in aqueous solutions*, Pergamon Press, Oxford; New York, **1966**.

[257] R. Ruffo, C. Wessells, R. A. Huggins, Y. Cui, *Electrochem. Commun.* **2009**, *11*, 247-249.

[258] D. Zhou, S. Liu, H. Wang, G. Yan, *J. Power Sources* **2013**, *227*, 111-117.

[259] W. Porcher, P. Moreau, B. Lestriez, S. Jouanneau, F. Le Cras, D. Guyomard, *Ionics* **2008**, *14*, 583-587.

[260] D. Y. W. Yu, K. Donoue, T. Kadohata, T. Murata, S. Matsuta, S. Fujitani, *J. Electrochem. Soc.* **2008**, *155*, A526-A530.

[261] H. Wang, Y. Zeng, K. Huang, S. Liu, L. Chen, *Electrochim. Acta* **2007**, *52*, 5102-5107.

[262] J. Choi, E. Alvarez, T. A. Arunkumar, A. Manthiram, *Electrochem. Solid-State Lett.* **2006**, *9*, A241-A244.

[263] R. Benedek, M. M. Thackeray, A. van de Walle, *Chem. Mater.* **2008**, *20*, 5485-5490.

[264] A. Ramanujapuram, D. Gordon, A. Magasinski, B. Ward, N. Nitta, C. Huang, G. Yushin, *Energy Environ. Sci.* **2016**, *9*, 1841-1848.

[265] L. Tian, A. Yuan, *J. Power Sources* **2009**, *192*, 693-697.

[266] C. Wessells, R. Ruffo, R. A. Huggins, Y. Cui, *Electrochem. Solid-State Lett.* **2010**, *13*, A59-A61.

[267] a) S. Kandhasamy, A. Pandey, M. Minakshi, *Electrochim. Acta* **2012**, *60*, 170-176; b) S. Kandhasamy, P. Singh, S. Thurgate, M. Ionescu, D. Appadoo, M. Minakshi, *Electrochim. Acta* **2012**, *82*, 302-308; c) N. Alias, A. A. Mohamad, *Ceram. Int.* **2014**, *40*, 13089-13096.

[268] Q. Zhu, S. Zheng, X. Lu, Y. Wan, Q. Chen, J. Yang, L.-z. Zhang, Z. Lu, *J. Alloys Compd.* **2016**, *654*, 384-391.

[269] I. B. Stojković, N. D. Cvjetićanin, S. V. Mentus, *Electrochem. Commun.* **2010**, *12*, 371-373.

[270] X. Wang, Y. Hou, Y. Zhu, Y. Wu, R. Holze, *Scientific Reports* **2013**, *3*, 1401.

[271] K. Miyazaki, T. Shimada, S. Ito, Y. Yokoyama, T. Fukutsuka, T. Abe, *Chem. Commun.* **2016**, *52*, 4979-4982.

[272] J. O. M. Bockris, A. K. N. Reddy, in *Modern Electrochemistry 2A: Fundamentals of Electrodics*, Springer US, Boston, MA, **2000**, pp. 771-1033.

[273] L. Suo, O. Borodin, T. Gao, M. Olguin, J. Ho, X. Fan, C. Luo, C. Wang, K. Xu, *Science* **2015**, *350*, 938-943.

[274] C. A. Angell, N. Byrne, J.-P. Belieres, *Acc. Chem. Res.* **2007**, *40*, 1228-1236.

[275] C. A. Angell, *J. Electrochem. Soc.* **1965**, *112*, 1224-1227.

[276]   L. Suo, O. Borodin, W. Sun, X. Fan, C. Yang, F. Wang, T. Gao, Z. Ma, M. Schroeder, A. von Cresce, S. M. Russell, M. Armand, A. Angell, K. Xu, C. Wang, *Angew. Chem. Int. Ed. Engl.* **2016**, *55*, 7136-7141.

[277]   F. Wang, Y. Lin, L. Suo, X. Fan, T. Gao, C. Yang, F. Han, Y. Qi, K. Xu, C. Wang, *Energy Environ. Sci.* **2016**, *9*, 3666-3673.

[278]   C. Yang, J. Chen, T. Qing, X. Fan, W. Sun, A. von Cresce, M. S. Ding, O. Borodin, J. Vatamanu, M. A. Schroeder, N. Eidson, C. Wang, K. Xu, *Joule* **2017**, *1*, 122-132.

Chapter 3 Electrochemical & Physical Techniques

Electrochemical Techniques

Cyclic voltammetry

Cyclic voltammetry (CV) is an electrochemical technique that can be used to test a variety of parameters of an electroactive species[1]. The reactions at the electrode can be qualitatively diagnosed and quantified using CV. The working electrode potential is linearly scanned in voltammetry and the resulting current between it and the counter electrode is measured and displayed in a voltammogram. The potential difference is measured between the working and reference electrode. In a CV the potential is linearly scanned from an initial potential to a set potential and is then reversed back to either its initial or another final potential. Ideally the initial potential is chosen where no Faradaic process occurs, as the products from the forward scan can be compared against the products in the reverse scan. This allows for the equilibrium potentials (E_{eq}) to be determined, the detection of chemical reactions prior to or following the electrochemical reaction and the electron transfer kinetics to be quantified.

The initial potential chosen, for a solution that only contains the oxidised form of a redox couple, is more positive than the E_{eq} of the redox couple, Figure 3.1. The E_{eq} is usually the cross over potential at zero current. The initial potential is scanned towards (lower potentials) the redox couple potential. At the initial potential the bulk solution only contains the oxidised species so that there is only a background current reading. As the redox couple potential is approached there is a conversion of the oxidised species to its reduced form which results in an exponential increase in reduction current with the potential and establishes concentration gradients for the oxidised and reduced species. The electroactive species diffuse in the concentration gradients and the corresponding peak current indicates that the overpotential is negative enough to convert any oxidised species that reach the electrode surface instantaneously to the reduced species. The subsequent current is then dependent on the mass transfer of the oxidised species to the electrode surface. When the scan is reversed for a reversible redox couple the reaction slows down and the current approaches zero on the current axes, i.e. E_{eq}. The first reaction is then reversed and the current increases beyond zero

and the reduced species is converted back to the oxidised form indicated by the resultant peak where the reduced species are instantaneously oxidised when in contact with the electrode. The symmetry of a CV is a good indication of the degree of reversibility of the system. A reversible reaction system is only affected by the mass transfer process only, the redox species are defined by the Nernst equation and the peak current by the Randles-Sevcik equation. The peak potentials are independent of the scan rate and have a peak separation of $\leq \frac{59\,mV}{n}$.
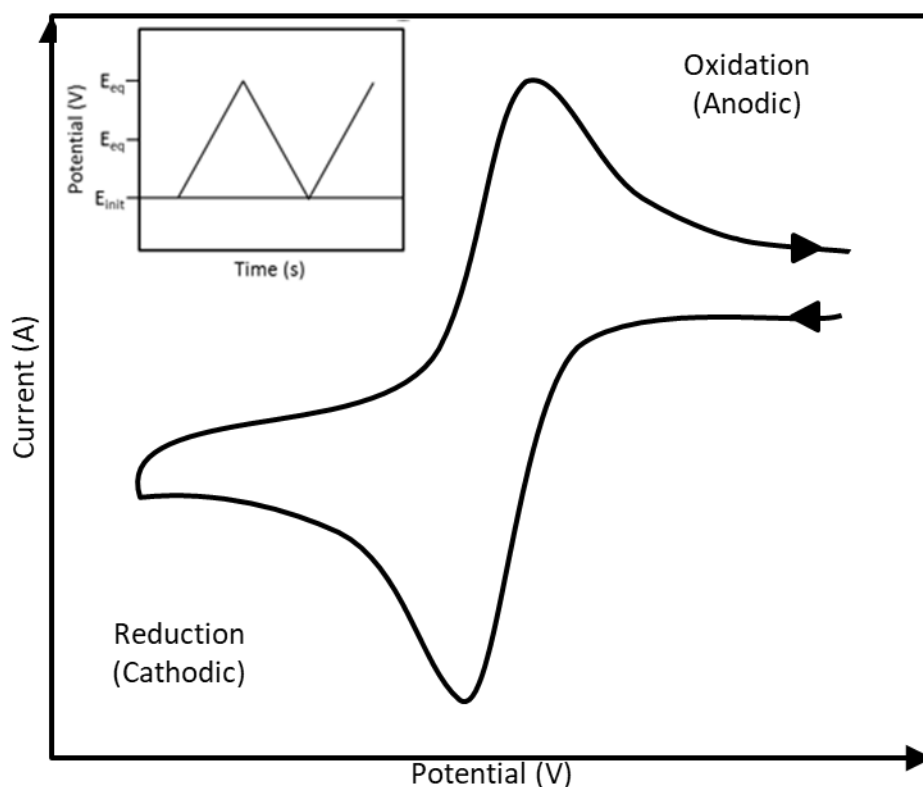
Figure 3.1: Typical current response in a CV for a redox couple for which both species are soluble. Inserted is the potential versus time diagram of a CV technique.

The potential of a CV is changed at a constant scan rate meaning the surface area under the current profile is proportional to the charge in the reaction. The size of the diffusion layer at the electrode surface depends on the scan rate. For a slow scan rate the diffusion layer will grow further away from the electrode in comparison to a fast scan, meaning the flux at the electrode surface is significantly smaller for a slow scan rate. Consequently the flux is proportional to the current resulting in smaller currents at slower scan rates. This technique is applied in the electrochemical performance analysis of electrodes for Li-ion batteries as the

capacity of the electrode can be calculated from the insertion/de-insertion Li^+ ion peaks in a CV. Cathodic current values indicate Li^+ insertion into the working electrode or surface reactions e.g. SEI layer formation. Anodic current values indicate Li^+ extraction from the working electrode or oxidation of the electrolyte.

Chronopotentiometry

In chronopotentiometry (CP) a constant current is applied to an electrochemical cell and the resulting potential is measured for a defined period of time or to a set potential[2]. CP, like CV, is useful for investigating reactions occurring at the working electrode. CP has the advantage that the reaction rate is fixed (current density) and the corresponding potential is measured, which is the sum of the kinetic and thermodynamic reactions, Figure 3.2. CP plots are usually called charge-discharge or galvanostatic cycling plots which have the measured potential plotted against time which can also be represented as the capacity (mAh/g) of the electrode. The information that can be obtained from a galvanostatic profile includes:

1. Capacity at a given potential.
2. Formation of redox species, indicated by plateaux in the curve.
3. Average cell potential.
4. Specific energy, e.g. gravimetric (Wh/kg)
5. Polarisation, which is indicated by the difference in plateaux potentials of the charge and discharge profiles.
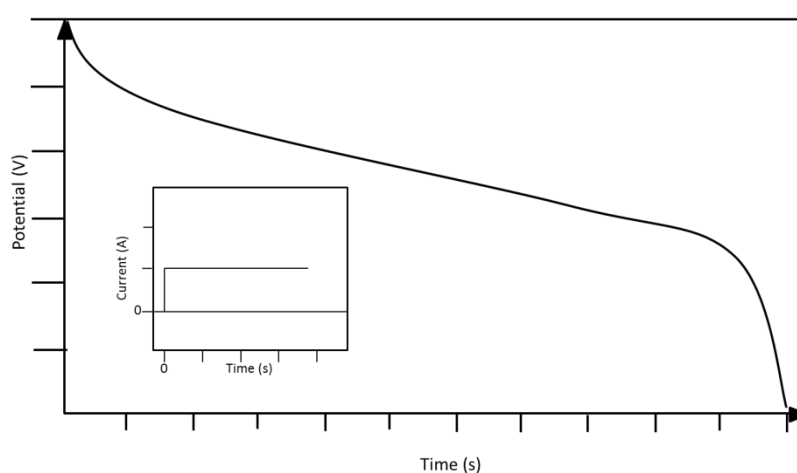
Figure 3.2: Typical galvanostatic profile of Li-ion battery being discharged. Inset is the current versus time diagram of a CP technique.

The Ohmic drop is constant during a CP technique as it is equal to the combination of the current and solution resistance, which can be compensated for with a constant current. The rate capability of an electrode can also be measured by recording and comparing the capacity at various current densities. The mathematical formulation used in solving the diffusion equation is simpler than the formulation used for constant potential techniques as closed form analytical solutions are typically utilised. Surface boundary conditions are based on concentration gradients at the electrode surface while prior knowledge of electron transfer rate reaction is not required in the solution unlike constant potential techniques.

Double-layer charging effects are a significant issue with the CP technique as the potential is constantly changing meaning a non-faradaic current is always contributing to the charging of double-layer capacitance throughout the experiment for which it is difficult to compensate.

Chronoamperometry

Chronoamperometry (CA) is a versatile technique used to study various processes such as the kinetics of diffusion processes, chemical reactions, adsorptions and provide quantitative information about an electrochemical nucleation and growth process. CA involves a potential applied in steps rather than linearly as seen for CVs. The potential of the working electrode is stepped from a potential where there is no Faradaic reaction to a potential where a Faradaic reaction takes place and is held. The current response is plotted as a function of time.

The response from a species in an electrolyte where the O and R forms are soluble in the electrolyte when the potential applied is significantly lower than the E_{eq} a rapid reduction of the O species occurs as soon as it reaches the electrode. This results in a region where the concentration of the electroactive species becomes gradually lower near the electrode surface resulting in a concentration gradient. This region called a depletion layer, which grows out into the bulk solution over time as the potential is applied and results in a decrease in current response over time,Figure 3.3a. The depletion layer is dependent on the interaction between the charge transfer and mass transport.
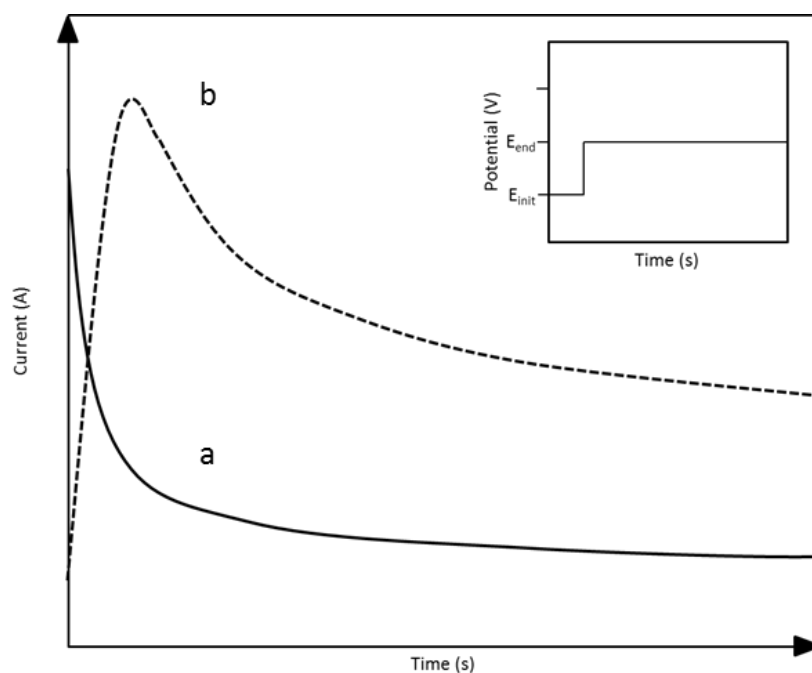
Figure 3.3: CA current profile for **(a)** a redox couple and **(b)** a metal deposition process in a solution. Inset is the potential versus time diagram of a CA technique.

A deposition process differs as the R form is non-soluble and its nuclei bond to the electrode surface and grow independently, Figure 3.3b. When a potential is applied the initial increase in current is rapid due to the nucleation and growth of the metal deposit. When nuclei are deposited and grow where they can have either a 2D or 3D structure resulting in an increase in surface area and therefore an increase in the current response. A depletion layer is formed around these 3D structures (hemispherical) which are isolated initially and grow independently[3]. As the nuclei grow and get closer to other nuclei or growth sites the depletion layers begin to overlap and combine resulting eventually in a planar flux and reduced surface area in comparison to the initial 3D nuclei, Figure 3.4[4]. The Cottrell equation describes the current decay with time at a planar electrode without imposed convection. The transition from the formation of the 3D nuclei to the planar diffusion is reflected in the current response with the initial rise to the eventual fall in current. The maximum current represents the point at which the diffusing electroactive species consists of similar planar and hemispherical modes[5]. The diffusion controlled growth of metal deposits has been theoretically modelled with modifications based on planar diffusion flux[6]. The initial current response includes the charging current in response to the potential step and decreases exponentially in the first few milliseconds. At prolonged hold times convection

currents can develop in the solution due to the density gradients that formed from the electrolysis products that cause positive deviations from the theoretical current.
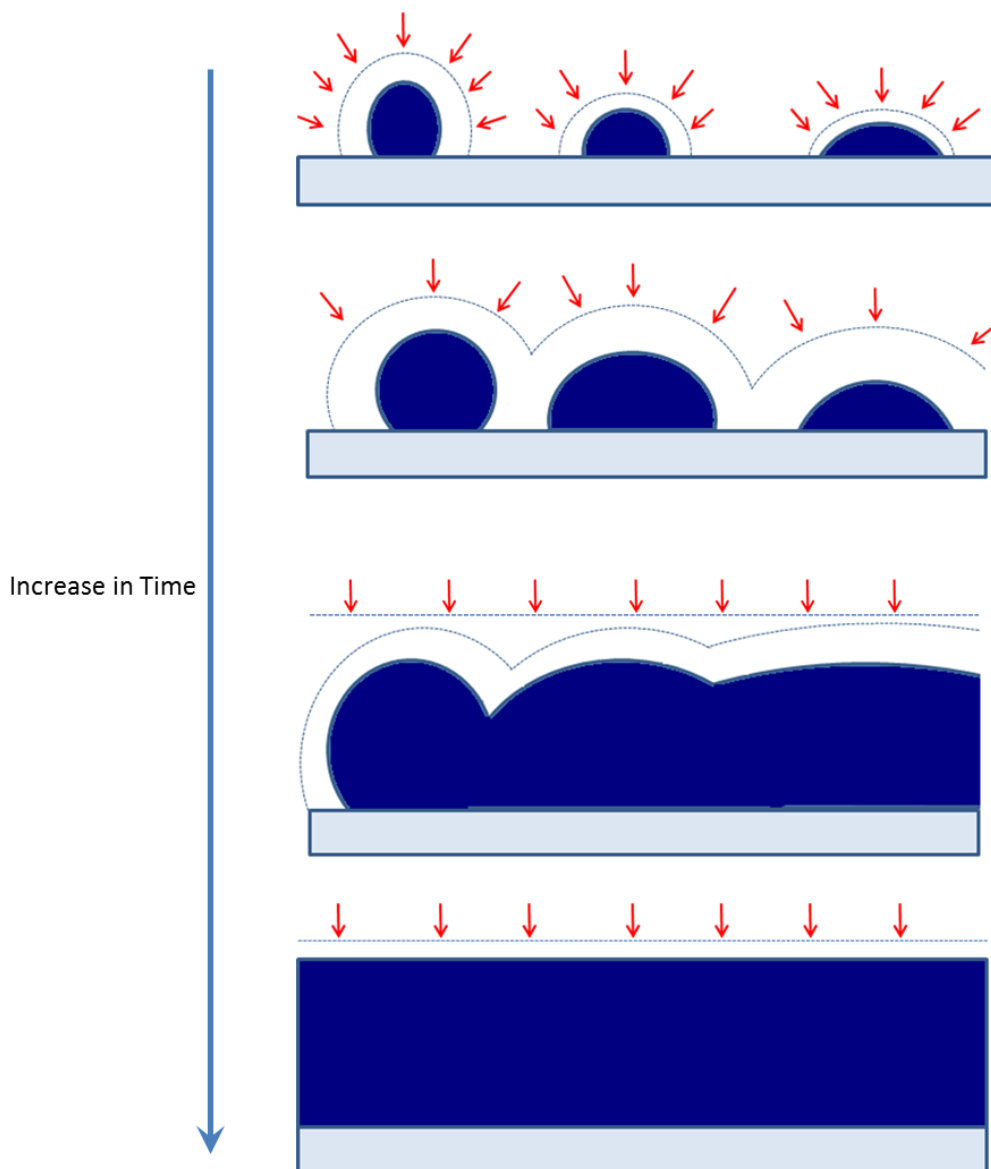
Figure 3.4: The time dependent behaviour of the flux of electroactive material during the electrodeposition on a foreign substrate.

GITT

Li-ion diffusion into the bulk of the electrode is described using the chemical diffusion coefficient of the electrode material. The chemical diffusion coefficient is a critical parameter in determining the electrochemical performance of the electrode material. Galvanostatic intermittent titration technique (GITT) can be used to determine the kinetic and thermodynamic characteristics of an electrode material. GITT involves applying a pulse

current followed by a relaxation step (i.e. no current). When a current is applied the initial cell potential change is proportional to the iR drop, where R is the made-up of the charge transfer and uncompensated resistance. After the initial change in potential the potential continues to change at a slower rate as the concentration gradient is maintain constant due to the current applied. During the initial stage of the relaxation step the potential change is proportional to the iR drop and subsequent change in potential is due to the composition of the electrode becomes homogeneous and as it goes to the open cell potential to reach equilibrium. The sequence of applying a current and then allowing the relaxation step is repeated until the electrode is fully charged/discharged.

The chemical diffusion of each step can be calculated using Equation 3.1 if small current is applied for short intervals:

$$D = \frac{4}{\pi\tau}\left(\frac{n_m V_m}{S}\right)^2\left(\frac{\Delta E_s}{\Delta E_t}\right)^2 \qquad 3.1$$

Where τ is the duration of the current pulse (s), n_m is the number of moles (mol), V_m is the molar volume of the electrode (cm^3/mol), S is the electrode/electrolyte interface area (cm^2), ΔE_s is the steady-state voltage change due to the applied current pulse and ΔE_t is the voltage change, not including the iR drop, due to the applied current.

EIS

The impedance of a system is its ability to resist a flowing electrical current. Electrochemical impedance spectroscopy (EIS) used general in a battery is the when an alternating current (AC) potential is applied over a large range of frequency to an electrochemical system and the current response is measured. By applying the signal over a large range of frequencies the impedance as a function of frequency is generated since impedance is dependent on frequency. The rates of the electrochemical reactions are non-linear as the reactions are exponentially dependent on the potential. EIS theory is based on linear responses which results in the AC potential being kept restricted to under 10 mV to maintain a linear response from the electrochemical system.

The equivalent circuit models, which consist of known passive elements, are used to interpret the impedance data. The electrochemical reaction that takes place in battery cell consists of a charge transfer at the electrode/electrolyte interface. The charge transfer is a faradaic process and has a resistance (R_{ct}). All electrodes have a double layer capacitance (C_{dl}) which is

independent of the faradic process. The current must pass through the electrolyte which has a resistance (R_s) and the total current is the sum of the double layer charging and faradaic currents. Mass transport of reactants also play a role in the electrochemical process that gives rise to diffusion impedance. The Warburg impedance element (Z_w) is used to describe a semi-infinite diffusion process. All these elements combine for a battery result in an equivalent circuit called the Randles equivalent circuit.

Impedance can be represented in Cartesian coordinates which is made-up of a real (Z_{re}) and imaginary ($-Z_{im}$) parts. These two elements plotted against each other, respectively, is called a Nyquist plot. Nyquist plots give a quick overview of the data and can be interpreted easily. The overall shape is characteristic of specific mechanisms which can be broken down into two limiting cases. At low frequencies the Z_w term becomes dominant resulting in a straight line which is characteristic of a diffusion-controlled electrode process. A semi-circle is seen at high frequencies as Z_w becomes negligible. The values of R_s and R_{ct} can be extrapolated from where the semi-circle intercepts the Z_{re} axis and C_{dl} can be calculated from the frequency at the maximum $-Z_{im}$ value of the semi-circle.

Physical Material Characterisation and Deposition

Scanning electron microscope and Energy dispersive X-ray spectrometry

The scanning electron microscope (SEM) is used to observe and characterise materials at the nanometre to micron scale by using electrons rather than light photons to form an image[7], Figure 3.5. An electron gun is used to produce a highly energised electron beam in a raster across the target sample surface. The electron gun is a tungsten filament loop cathode from which a thermionically emitted electron beam is produced when a high voltage is applied. The electron beam is accelerated down a vertical column by applying a large negative bias to the anode in order to repel and accelerate the negatively charged electrons. The column is made up of electromagnetic fields and objective lenses that focus the beam towards the target sample. The imaging is conducted under vacuum to avoid secondary reactions of gases with the electron beam. The focused electron beam will hit the sample surface and penetrate a determined depth (1–7 μm), depending on the beam's energy and inversely to the specimen's atomic number. The interactions between the sample and the electron beam will generate elastic and inelastic scattering effects and are collected by a detector. The elastic scattering effects correspond to backscattered electrons while inelastic effects are due to secondary electrons. The secondary electrons are ejected before they have a chance to spread within the sample and therefore generate a high resolution signal. The contrasts between these two signals make up the changes in elevation on the sample surface in the generated image.
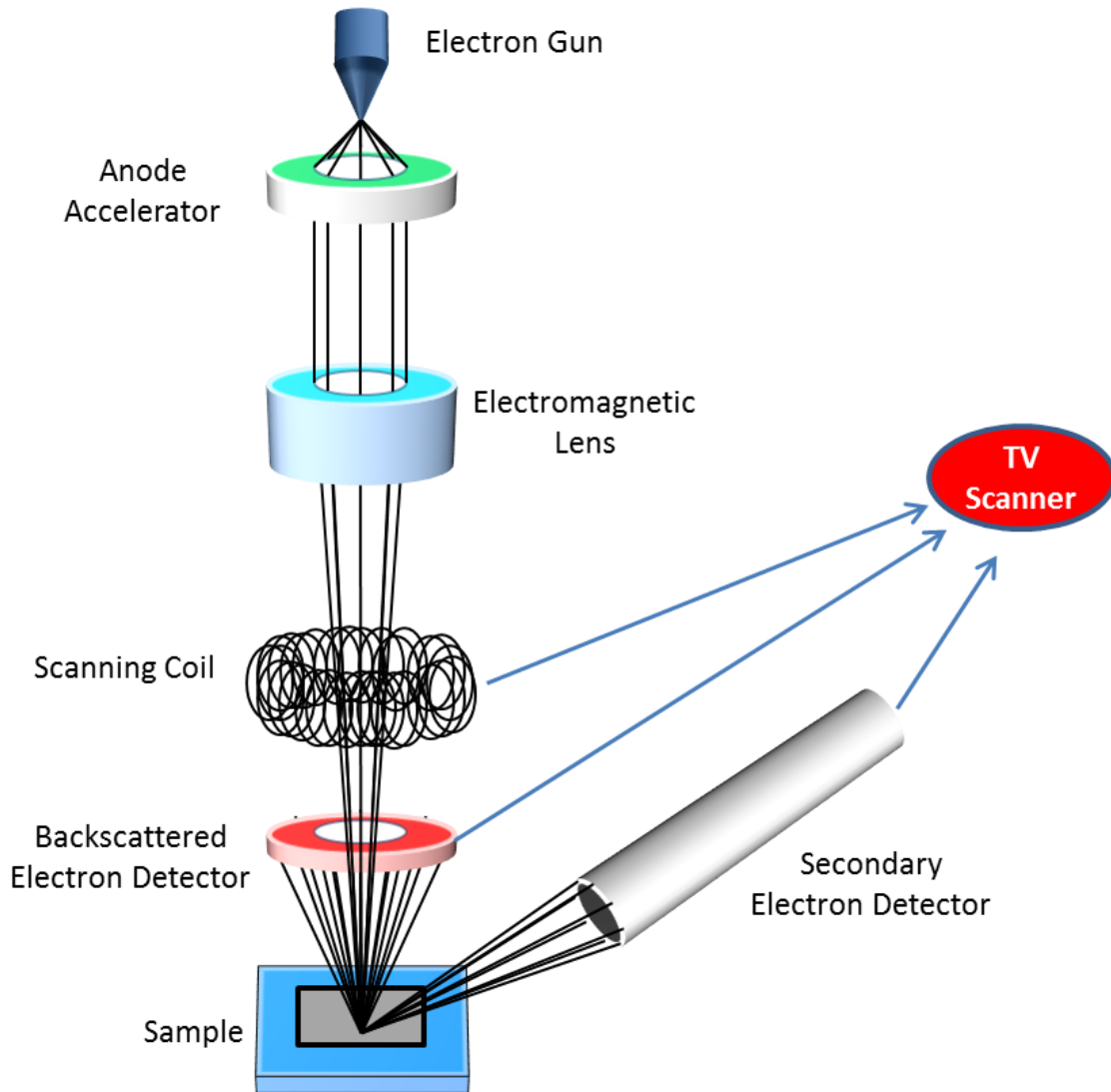
Figure 3.5: A schematic illustration of the working principle of an SEM.

The four parameters that affect the resolution of image produced are:

1. Electron probe spot size. (Diameter of final electron beam)
2. Electron probe current. (Final current of beam at the sample surface)
3. Electron probe convergence angle.

   (Half angle of the cone of electrons converging on the sample)
4. Electron beam accelerating voltage.

In order to view the smallest detail on the sample surface the spot size needs to be less than or equal to the size of the feature being examined. The smallest spot size with a sufficient beam current results in a high resolution image. Large beam currents are required to surpass the visibility threshold so that even if the smallest spot size is chosen a detailed image cannot be

observed without an appropriate current. The electron probe's convergence angle affects the depth of field of an image. When the convergence angle is small the beam diameter only changes slightly over a large vertical distance, resulting in a simultaneous focus on surface features of different heights. Small accelerating voltages result in minimal electron penetration of the sample surface resulting in a more detailed surface image. At increased accelerating voltages the electron beam penetrates deeper resulting in less surface details. A balance is needed between the parameters in order to obtain an image that has sufficient detail and resolution as small spot sizes give high resolution but require large beam currents which results in less surface details and vice versa[8].

Highly energised backscattered electrons can cause ionisation of the atoms in the material before leaving the surface. The relaxation of these ions results in X-rays being emitted which are characteristic of the relaxed atoms chemical nature and are captured using an energy dispersive X-ray spectrometry (EDX). Elements present in the sample have their abundance measured and are identified by comparing a material database of characteristic atomic X-rays with the emitted X-rays.

X-ray Diffraction

X-ray diffraction (XRD) is a non-destructive analytical technique used to study material crystal structure and atomic spacing. The wavelength of an X-ray is approximately 1 Å which is about the same size as the typical distance between atoms in a crystalline solid, making them ideal for structure and atomic spacing investigation[9]. When an X-ray beam makes contact with an atom it interacts with the electrons which alters (diffracts) the path of the X-ray beam. The diffracted X-rays will interfere with other diffracted X-rays as a result of the interaction with the atom.

A solid described as amorphous has atoms arrange randomly while a crystalline solid has atoms arranged in a periodic pattern. A crystalline solid only diffracts X-rays in a certain direction depending on the lattice planes due to its ordered structure resulting in the diffracted X-rays that interfere with each other and produce an emitted diffracted X-ray (constructive interference)[10], Figure 3.6a. Typically diffracted X-rays from an amorphous solid will have scattering in multiple directions resulting in numerous X-rays interfering with each other and effectively cancelling each other out (destructive interference), Figure 3.6b.
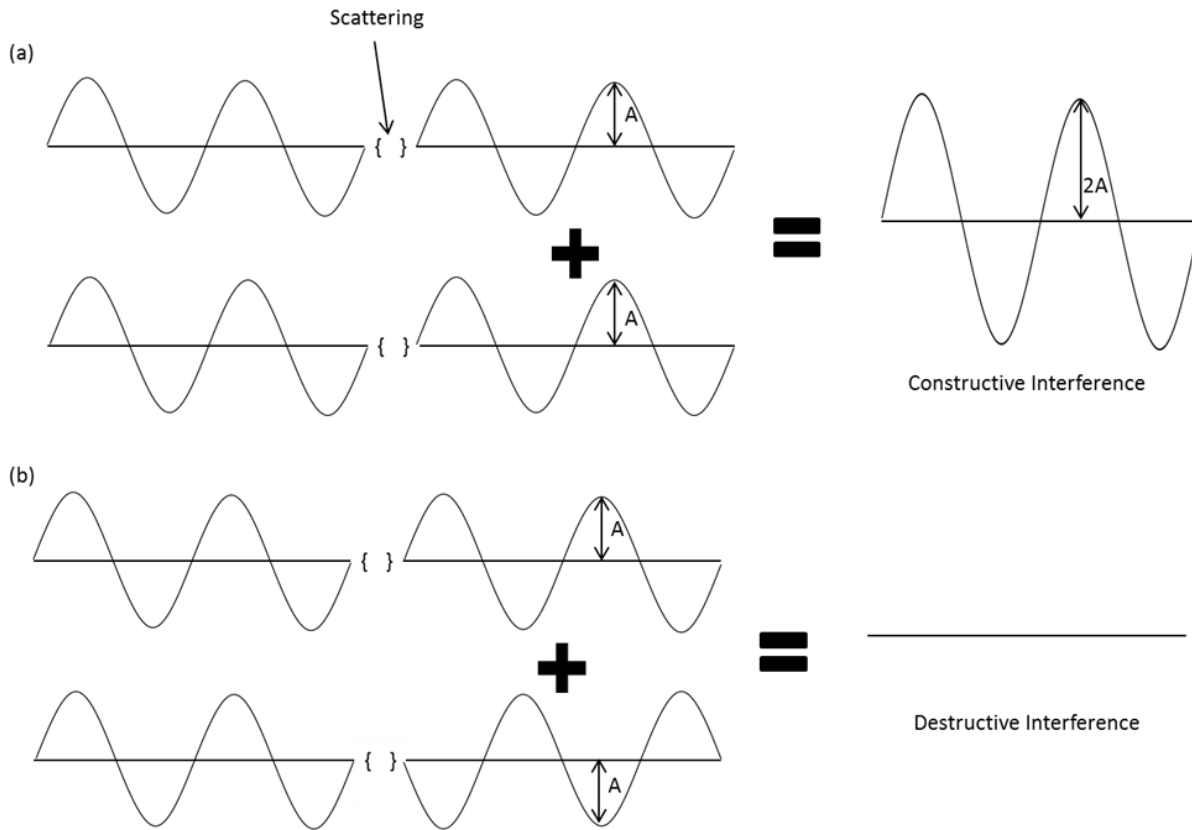
Figure 3.6: (a) Graphic description of how two waves with the same wavelength remain in phase after scattering and constructively interfere with each other. **(b)** shows how two waves with the same wavelength become out of phase when scattered and destructively interfere with one another.

When the scattered X-rays interfere constructively in a crystalline lattice and produce a diffracted X-ray, the wavelength of the X-ray is related to the diffraction angle and the lattice spacing of the sample according to Bragg's Law.

$$n\lambda = 2d \sin \theta \qquad\qquad 3.2$$
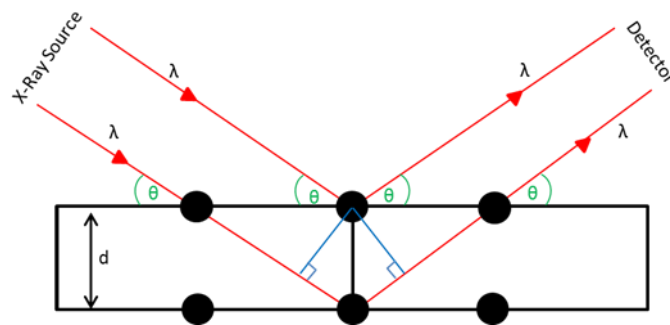
Figure 3.7: Schematic representation of the diffraction of a monochromatic light by crystal planes.

Where *n* is an order of reflection and an integer, λ is the wavelength of the X-ray, *d* is the inter-plane distance between lattice plane and θ is the angle between the crystalline planes and the X-ray beam. The crystalline planes are integers described using Miller indices, (h k l), and are obtained by getting the reciprocal value of the intersection (a b c) of an axis (x y z) with a plane of interest. The indices values are used to calculate the inter-plane spacing meaning the diffraction angles detected from known crystalline planes allows for the lattice parameter to be calculated depending on the type of unit cell structure, e.g. cubic (Equation 3.3) and orthogonal (Equation 3.4) structures.

$$\frac{1}{d^2} = \frac{h^2 + k^2 + l^2}{a^2}$$
$\qquad$ 3.3

$$\frac{1}{d^2} = \frac{h^2}{a^2} + \frac{k^2}{b^2} + \frac{l^2}{c^2}$$
$\qquad$ 3.4
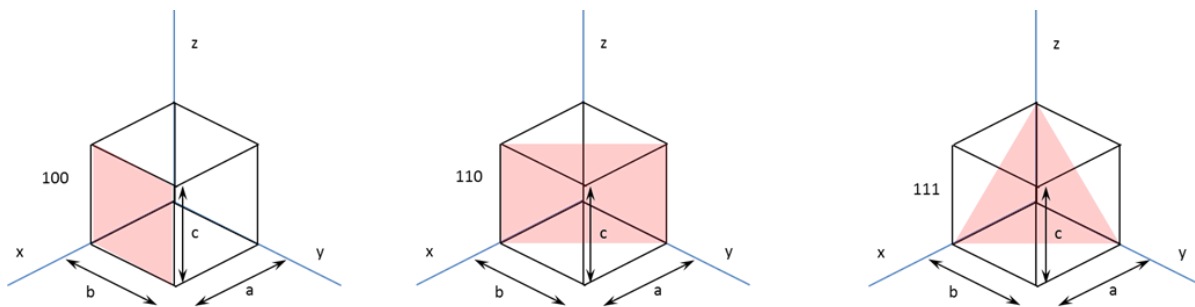
Figure 3.8: Schematic representation of planes inside a cubic structure.

A detector is used to record and process the diffracted X-ray signals. The detector is mounted on an arm that rotates at an angle of *2θ* with respect to the X-ray beam. The intensity of the signals detected depends on the atomic position within the lattice planes of the sample. The typical X-ray used is from a Cu anode as the K_α radiation beam, corresponding to the transition from 2p to 1s orbital, has a wavelength of 1.54 Å which is close to typical distances between atoms in a lattice, thus ensuring interference occurs. A K_β radiation beam is also produced due to the transition between the 3p and 1s orbital and has a wavelength of 1.39 Å but is selectively filtered to increase the monochromaticity of the incident beam.

Raman

Raman spectroscopy, like XRD, is a non-destructive analytical technique used on materials to study their chemical structure and physical form from their characteristic spectral pattern. When light is shone on a material, the photons are absorbed, scattered or have no interaction i.e. pass through. A photon is absorbed if its energy matches the energy gap between the ground state and excited state of the molecule. The loss in radiation between the incident and reflected/transmitted light beam corresponds to the absorption energy. Infrared (IR) spectroscopy is based on this principle as vibration transition energies correspond to IR spectrum wavelengths. The photons of light can also be scattered by interacting with the materials molecules. The scattered photons are collected at a certain angle to the incident light beam and are dependent on the wavelength of the incident beam as it is proportional to the fourth power of the frequency, Equation 3.5[11].

$$I \propto \frac{1}{\lambda^4} \qquad \qquad 3.5$$

The scattering of light with no shift in frequency is known as Rayleigh scattering and is an elastic effect, Figure 3.9. The inelastic scattering of light results in a change in frequency and known as Raman scattering which can be broken down into two groups. Stokes Raman scattering is when the photon loses energy to the molecule meaning the molecule remains at a higher excited state and a lower frequency to the incident beam. Anti-Stokes Raman scattering is when the photon gains energy from the molecule and has a higher frequency than the incident beam. Anti-Stoke scattering is not common at ambient temperatures as molecules predominantly exist in their ground state due to the thermal energy being lower than the normal modes energy. Raman spectroscopy is a highly sensitive technique in determining difference between similar molecules and chemical species where the change in energy of the photon is related to the nature of each bond and vibration and thus highlighting any phase changes, stress or strains within the material.
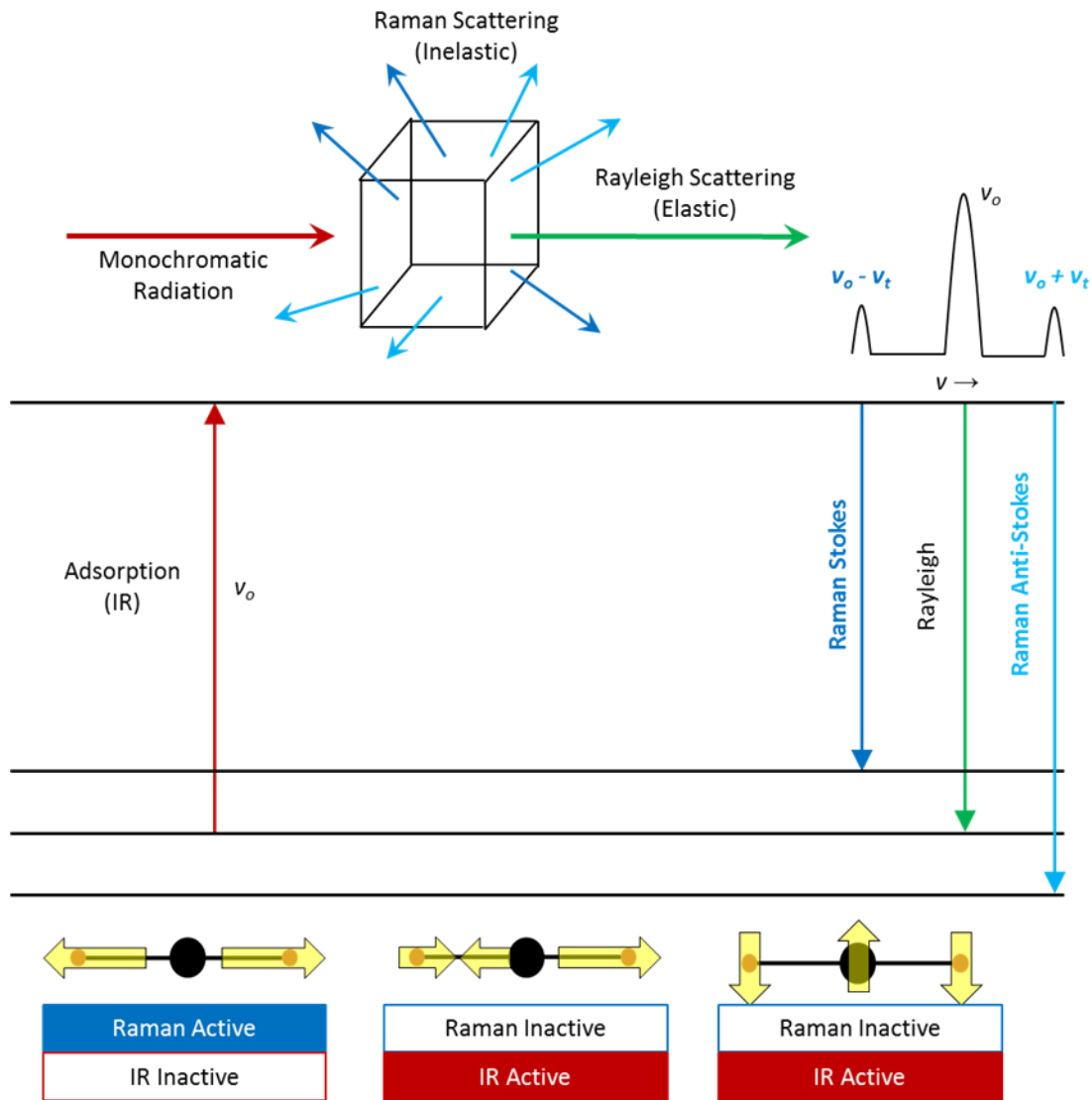
Figure 3.9: Schematic illustration of the working principle of Raman spectroscopy via Energy diagrams and rule of mutual exclusion

Scattering is not caused by an oscillating dipole (μ) phenomenon like IR spectroscopy. Isotropic polarizability of an atom causes the atom to act like an antenna and results in the scattering of photons at the same frequency (v) as the incident beam i.e. Rayleigh scattering. The polarizability (α) of a molecule that is anisotropic results in Raman scattering. Anisotropic polarizability is dependent on the rotational and vibrational coordination of a molecule. The incident light beam is oscillating and when it comes in contact with an atom/molecule electric field (E_o) it causes the field to oscillate and induces polarization, Equation 3.6[12].

$$\mu_{ind} = \alpha E_0 \cos(2\pi vt)$$ 3.6

A molecule can be both IR and Raman active however the rule of mutual exclusion states that in a centrosymmetric molecule e.g. CO_2, a vibrational mode may be either IR active or Raman active but not both.

Surface profilometer

A profilometer is an instrument used to measure the surface profile of films e.g. surface height and roughness. There are two types of profilometers: contact and non-contact. The contact profilometer uses a diamond stylus that is in physical contact with the sample surface and is mechanically moved over the surface of the film laterally at a specific distance and with contact force. A feedback loop is used to monitor the force that pushes up against the stylus due to the surface of film as it is scanned. The arm that holds the stylus is set at a specific amount of torque (set-point) and any changes in the z-axis of the arm can be used to obtain a reconstructed image of the surface, Figure 3.10. As the stylus is in direct contact with the surface it is a highly sensitive technique whose resolution is dependent on the shape and radius of the stylus. The direct contact with the sample surface the technique can also be destructive to very soft surfaces.
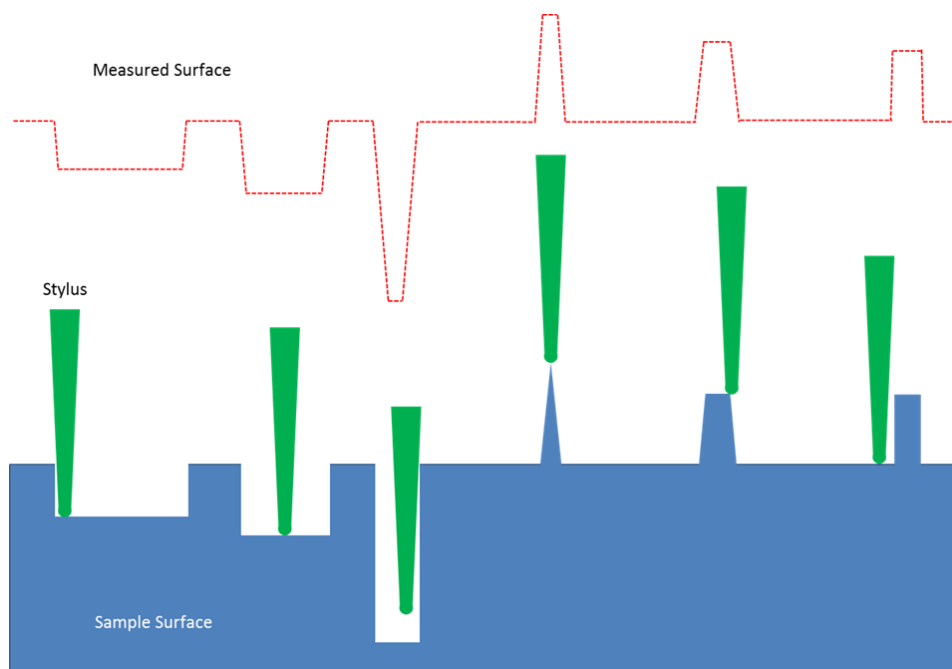
Figure 3.10: Schematic of the working principle of a contact surface profilometer.

Non-contact profilometers use light instead of physical contact of a stylus. The light hits the surface and the time it takes for the light to return is used and input to a model to make a reconstruction of the surface. The advantages to this technique are that it is not destructive,

high resolution and high speed in comparison to contact profilometers. Highly sloped substrates are difficult to process as all of light is reflected away from the objective if the surface does not have enough texture.

A profilometer is an ideal instrument for measuring the thicknesses of deposited layers and also the quality of deposited film with regards to roughness and smoothness. A typical profilometer can measure vertical features ranging from 10 nm to 1 mm.

Sputter deposition

Physical vapour deposition (PVD) is a technique in which a thin film is deposited onto a substrate by the condensation of the material of interest in its vaporised form. The vapour is produced by using elevated temperatures and pressures as the process environment. The main categories of PVD are sputter deposition, thermal evaporation, electron beam deposition and pulsed laser deposition.

Sputtering is a common technique used to deposit thin films of elemental or compound materials. The sputtering process involves atoms ejected from a solid target material due to the bombardment of the target by energetic particles. Ionized gas can be generated by applying a DC voltage between a target and substrate that forms a hot gas-like phase consisting of ions and electrons known as a plasma. It is created in a pressurised chamber (10^{-3} mbar) and in an inert gas atmosphere (Ar, N_2). The charged gas atoms accelerate towards and collide with the atoms of the cathode target material and subsequently release those atoms. The ejected atoms travel across the vacuum and inert gas atmosphere where they condense on the cooler surface of the substrate of interest to form a thin film deposit. The electrons created in the plasma accelerate in the opposite direction of the ions towards the anode substrate where they collide with gas atoms and thus create more free ions and electrons to ensure the continuation of the sputter process. This is the simplest version of the sputter process and is limited by low deposition rates, low ionization efficiency in the plasma and high substrate heating effects.

Magnetron sputtering is the addition of a magnetic field parallel to the target surface which interacts with secondary electrons that are emitted during ion bombardment and confines them in the vicinity of the target's surface. The addition of the magnet increases both the ionization efficiency, and deposition rate and lowers the heating effects subjected to the substrate[13]. The magnets increase the probability of collisions and thus the density of the

plasma close to the target's surface in comparison to the non-magnetron sputter process, Figure 3.11. The magnetic field is created by placing one magnetic pole as a ring along the outer edge of the target and the other pole along the central axis of the target. Unbalanced magnetron sputtering can occur when the outer magnetic field is stronger than the central pole which results in an expansion of the plasma between the target and substrate while also eliminating the need for an external bias on the substrate to achieve thin film deposition[14].
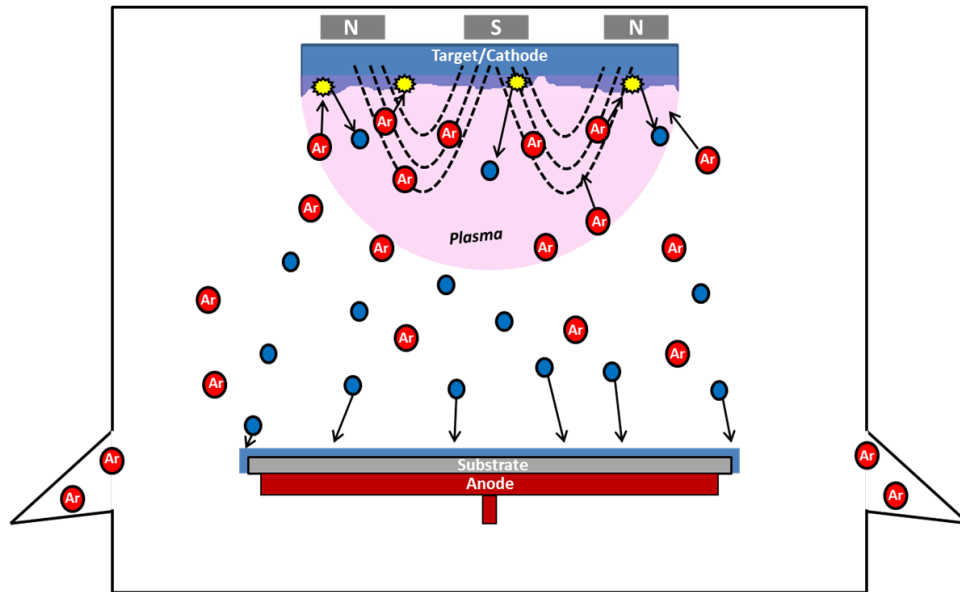
Figure 3.11: Schematic representation of a DC magnetron sputtering process in an Ar atmosphere.

Deposition of conductive materials can be achieved using a DC power supply while insulating and conductive targets use a RF power supply by applying an alternating current with frequencies higher than 50 kHz[14]. Elemental and compound materials can be deposited using sputtering as the vaporised material is the same composition as the target material. When sputtering compound materials the elemental composition of the target must be considered as elements tend to have different volatilities which can lead to loss in stoichiometry in the deposited thin-film compared to the target. Compensation for these losses can be implemented by increasing the stoichiometry in the target material or by including reactive gases such as O_2 or N_2. Reactive gases are also used to deposit either oxides or nitrides of the target material. The reactive gases combine with the incoming atoms to form the oxide or nitride when condensing on the substrate[15].

References

[1]   A. J. Bard, L. R. Faulkner, *Electrochemical Methods: Fundamentals and Applications, 2nd Edition*, Wiley, New York, NY, **2001**.

[2]   R. K. Jain, H. C. Gaur, B. J. Welch, *J. Electroanal. Chem. Interfacial. Electrochem.* **1977**, *79*, 211-236.

[3]   E. Budevski, G. Staikov, W. J. Lorenz, *Electrochemical phase formation and growth: An introduction to the initial stages of metal deposition*, VCH Publishers, New York, NY, **1996**.

[4]   a) G. Gunawardena, G. Hills, I. Montenegro, B. Scharifker, *J. Electroanal. Chem. Interfacial. Electrochem.* **1982**, *138*, 255-271; b) B. Scharifker, G. Hills, *Electrochim. Acta* **1983**, *28*, 879-889.

[5]   B. R. Scharifker, J. Mostany, *J. Electroanal. Chem. Interfacial. Electrochem.* **1984**, *177*, 13-23.

[6]   a) L. Heerman, A. Tarallo, *J. Electroanal. Chem.* **1999**, *470*, 70-76; b) L. Heerman, A. Tarallo, *Electrochem. Commun.* **2000**, *2*, 85-89; c) E. Matthijs, S. Langerock, E. Michailova, L. Heerman, *J. Electroanal. Chem.* **2004**, *570*, 123-133.

[7]   J. I. Goldstein, D. E. Newbury, P. Echlin, D. C. Joy, C. E. Lyman, E. Lifshin, L. Sawyer, J. R. Michael, in *Scanning Electron Microscopy and X-ray Microanalysis: Third Edition*, Springer US, Boston, MA, **2003**, pp. 21-60.

[8]   J. Goldstein, *Scanning Electron Microscopy and X-ray Microanalysis: Third Edition*, Springer US, Boston, MA, **2003**.

[9]   a) J. A. Kaduk, *Acta Crystallogr. Sect. A: Found. Crystallogr.* **1994**, *50*, 259-259; b) B. D. Cullity, *Elements of x-ray diffraction*, Addison-Wesley Publishing Company, Inc., Reading, MA, **1978**; c) R. C. Graham, *Soil Science* **1999**, *164*, 72-73.

[10]   W. D. Callister, W. D. C. William D., *Materials Science and Engineering: An Introduction, 7th Edition*, John Wiley & Sons, New York, NY, **2007**.

[11]   E. Smith, G. Dent, *Modern Raman Spectroscopy: A Practical Approach*, Wiley, West Sussex, England, **2005**.

[12]   F. Siebert, P. Hildebrandt, in *Vibrational Spectroscopy in Life Science* (Eds.: F. Siebert, P. Hildebrandt), **2008**.

[13]   P. J. Kelly, R. D. Arnell, *Vacuum* **2000**, *56*, 159-172.

[14]   D. M. Mattox, *Handbook of physical vapor deposition (PVD) processing*, Second Edition ed., William Andrew, Oxford, UK, **2010**.

[15]   a) J. Musil, S. Kadlec, *Vacuum* **1990**, *40*, 435-444; b) F. R. Flory, *Thin Films for Optical Systems*, Taylor & Francis, New York, NY, **1995**.

Chapter 4 COMSOL Multiphysics Simulations of Thin-Film, 3D and 3D Core-Shell Nanoarchitectures

Abstract

Finite element simulations are presented, showing material utilisation and electrochemical cell behaviour of a rechargeable Li-ion microbattery in planar thin-film, 3D and 3D core-shell nanoarchitectures. The materials simulated are non-porous additive-free $LiCoO_2$, lithium metal and solid-state, polymer, polymer-gel and liquid electrolytes. The concentration profile of the $LiCoO_2$ during discharge and areal energy versus areal power in a Ragone plot for each of the different architectures is compared. It is shown that the planar thin-film architecture gave better cell performance when used with the solid-state electrolyte with all three architectures showing material utilisation of the cathode at the closest point to the anode. The 3D and 3D core-shell nanoarchitectures show better battery performance for the polymer electrolyte than the planar thin film, with the 3D nanoarchitecture being the best. The 3D core-shell nanoarchitecture shows a significant improvement in performance by comparison with the thin-film and 3D nanoarchitecture when a polymer-gel or a liquid electrolyte are used. The 3D nanoarchitecture shows a slight decline in performance when going from a polymer-gel electrolyte to a liquid electrolyte with faster Li-ion transport. The 3D core-shell nanoarchitecture shows improved cell performance with faster Li-ion transport. The adoption of 3D nanoarchitectures with suitable electrolytes can have a significant improvement in battery areal energy and power performance.

Introduction

The internet of things (IoT) scenario is the seamless mass distribution of sensors into everyday objects which enable a smart, efficient and connected world. These sensors are becoming smaller ($<1mm^3$) and more energy efficient creating a demand for micro energy supplies. Energy harvesters are now able to harvest enough energy from the sensors environment to power these sensors and create an efficient energy cycle[1]. Electrical energy

storage technology is needed to enable the commercialisation of energy harvesters as an energy source for IoT sensors due to the intermittency of sources in the environment such as solar or vibrational energy harvesters. A hybrid system would result in a smaller battery capacity requirement and sensors with a life-time in years rather than months.

However, meeting the energy and power densities (rate at which energy can be accessed) requirements for these devices is proving challenging. Lithium-ion batteries are a mature technology and a leading contender for integration with microelectronic devices for the energy storage provision. Planar thin-film solid-state batteries processed on silicon substrates with excellent cycle life are being developed for such devices but generally suffer from limited areal capacity and low power capabilities[2]. This necessitates complex power management circuits and additional components to ensure compatibility, thus drastically increasing the size of the device. Typical thin-film solid-state batteries are made up of an electrolyte that has low lithium ion conductivity. The cathode material is a solid additive-free metal oxide with poor ionic and electronic conductivity which limits the thickness to micrometers ($<5\mu m$) in a 2D geometry, therefore limiting the energy storage per area (Wh/cm^2).

Micro and nano-scale fabrication techniques have advanced in recent years and it is now possible to fabricate complex 3D micro and nanoarchitectures[3]. 3D architectures can decrease the distance between anode and cathode while also increasing the surface area of the electrodes. This decrease in distance and increase in surface area means a shorter ion transport distance and improved current distribution which results in higher power densities. A range of complex 3D architectures have been proposed as suitable geometries for lithium-ion batteries with high energy and power densities[4]. Depending on the critical material characteristics of the anode, cathode and electrolyte the 3D architectures may actually have a deleterious effect on cell performance if not optimised.

Mathematical modelling is used to describe the underlying electrochemical characteristics to optimise the 3D architecture. Finite element analysis (FEA) is a powerful tool for designing and optimising battery design, highlighting the key material and operational parameters to tailor the battery designs for various applications. FEA was used by Hart et al. to optimise the electrode array configuration in a 3D microbattery and highlighted the significant impact that non-uniform primary current distribution has on the battery performance[5]. Zadin et al. provided simulations of 3D microarchitectures such as concentric pillars, interdigitated

trenches and pillars using both non-porous and porous electrode electrochemistry models[6]. Miranda et al. investigated the effect of different geometries from conventional layered geometries to unconventional geometries such as antenna and gear shaped electrodes[7]. They also look at how the battery performance could be tailored for certain applications by modifying the dimensions of the geometries.

FEA of Li-ion batteries are generally built on the foundation of the work carried out by Newman and co-workers who developed the isothermal electrochemical model[8]. The charge and transport of battery species are dictated by the concentration gradient of lithium ions and the electrochemical potential gradient. There are a number of phases in a battery, anode, cathode and electrolyte, which need to be considered when implementing the conversion principles and equations to describe the transport of species and charge. The mass transport in the electrolyte, potential difference and profile in the anode and cathode materials are critical in predicting the battery performance. Newman et al. highlighted the significant effect that electrode porosity has on cell performance[9]. FEA simulations using COMSOL have been presented by Danilov et al. for all solid-state Li-ion batteries[10]. The aim of this work is to compare the electrochemical performance of planar thin-film microbatteries to 3D nanoarchitecture Li-ion batteries for solid-state, polymer, polymer-gel and liquid electrolytes.

Simulation

Theoretical Considerations

Conventional Li-ion battery materials characteristics were used in this study. The anode electrode is metallic lithium and the cathode electrode is $LiCoO_2$. The electrode materials are considered to be non-porous and additive-free. This means that Li-ion transport can only be considered at the electrolyte/electrode interface. The electrolytes used can be grouped into solid-state, polymer, polymer-gel and liquid electrolytes. The solid-state electrolyte material is based on an amorphous LiPON, derived from Li_3PO_4 sputter targets in a nitrogen environment and the polymer, polymer-gel and liquid electrolyte material based on 1M $LiPF_6$ salt dissolved polymer and solvent. The electrochemical reaction that takes place at each electrode is:

$$xLi^+ + xe^- + Li_{1-x}CoO_2 \rightarrow LiCoO_2 \qquad (0 \leq x < 0.5) \qquad \text{4.1}$$

$$Li \leftrightarrow Li^+ + e^-$$

<div align="right">4.2</div>

Li-ion concentration in LiCoO$_2$ is at its maximum when the battery is fully discharged and at its lowest when the battery is fully charged.

Mathematical model

Multiphysics simulations were computed using COMSOL Multiphysics® Version 5.0 software. The lithium-ion battery and transport of diluted species modules have predefined mathematical equations which were used to describe mass transport in the electrolyte and electrode, respectively. In this work a combination of the Doyle et al. and Danilov et al models describe the main equations that dictate the operation of a battery[8, 10]. The following assumptions are made for this mathematical model:

1. Diffusion coefficients and conductivities are constant for the materials in their respective regions.
2. Ion movement in the solid non-porous electrodes is described by diffusion.
3. No side reactions are considered.
4. The electrolyte is in electroneutrality at all times.
5. No volume changes occur in the electrodes.
6. At the electrolyte/electrode interface the charge transfer processes are described using Butler-Volmer kinetics:

$$J = i_0 \left[exp\left(F\alpha_a \frac{\eta}{RT} \right) - exp\left(-F\alpha_c \frac{\eta}{RT} \right) \right]$$

<div align="right">4.3</div>

where J is the current density at the electrolyte/electrode interface, i_0 is the exchange current density and α_a and α_c are the anodic and cathodic transfer coefficients where $\alpha_c = 1 - \alpha_a$.

7. The transference number (t_0) and the activity coefficient $\left(\frac{\partial ln f}{\partial ln(c_{Li\_ion})} \right)$ throughout the electrolyte are constant with the activity of salt in electrolyte being (f).

The surface overpotential, η, at the interface is:

$$\eta = \varphi_{Li} - \varphi_{Li\_ion} - U_{oc}$$

<div align="right">4.4</div>

where φ_{Li} and φ_{Li_ion} are the potentials of the electrode and electrolyte respectively and U_{oc} is the open circuit potential function. The equilibrium and electric potential for lithium metal anode electrode is set to 0. The equilibrium potential for LiCoO₂ cathode electrode is dependent upon its ion concentration.

The exchange current density is described by:

$$i_0 = Fk\big((c_{-Li})(c_{Li\_ion})\big)^{\alpha_a}(c_{Li})^{\alpha_c} \qquad\qquad 4.5$$

where k is the Butler-Volmer reaction rate coefficient, c_{-Li} is the remaining available ion concentration in the electrode, c_{Li_ion} is the dissociated ion concentration in the electrolyte and c_{Li} is the ion concentration in the electrode. c_{-Li} can be rewritten as $c_{-Li} = \big(c_{Li\_max} - c_{Li}\big)$ where c_{Li_max} is the maximum ion concentration in the electrode. The exchange current density, Equation 4.5, for the cathode electrode can be rewritten as:

$$i_{0\_pos} = Fk_{pos}\left[\left(\frac{c_{Li\_max} - c_{Li}}{c_{Li\_max} - c_{Li\_min}}\right)\left(\frac{c_{Li\_ion}}{c_{0\_Li\_ion\_init}}\right)\right]^{\alpha_{a\_pos}}\left(\frac{c_{Li} - c_{Li\_min}}{c_{Li\_max} - c_{Li\_min}}\right)^{\alpha_{c\_pos}} \qquad 4.6$$

where c_{Li_min} is the minimum ion concentration in the electrode and $c_{0\_Li\_ion\_init}$ is the total ion concentration in the electrolyte. The exchange current density for the anode electrode can be simplified since the anode material is lithium metal:

$$i_{0\_neg} = Fk_{neg}\left(\frac{c_{Li\_ion}}{c_{Li\_ion\_init}}\right)^{\alpha_{a\_neg}} \qquad\qquad 4.7$$

where both c_{-Li} and c_{Li} become negligible as the activity of lithium metal is considered unity.

The potential of the electrodes (φ_{Li}) is calculated using Ohm's law and since the anode material is lithium metal only the cathode is considered.

$$\nabla.\big(\sigma_{Li\_pos}\nabla\varphi_{Li}\big) = 0 \qquad\qquad 4.8$$

$$\vec{n}.\big(\sigma_{Li\_pos}\nabla\varphi_{Li}\big) = J \qquad\qquad 4.9$$

The potential of the electrolyte (φ_{Li_ion}) is calculated using Ohm's law and the concentrated solution theory:

$$\nabla . \left(\sigma_{Li\_ion} \nabla \varphi_{Li\_ion} - \sigma_{diff} \nabla ln(c_{Li_{ion}}) \right) = 0 \qquad \text{4.10}$$

$$\vec{n} . \left(\sigma_{Li\_ion} \nabla \varphi_{Li\_ion} - \sigma_{diff} \nabla ln(c_{Li_{ion}}) \right) = -J \qquad \text{4.11}$$

where σ_{Li_ion}, σ_{diff} and $\vec{n}$ are the electrolyte ionic conductivity, diffusional conductivity and the normal unit vector respectively. The diffusional conductivity is calculated from:

$$\sigma_{diff} = \frac{2RT\sigma_{Li\_ion}}{F}(1 - t_0)\left(1 + \frac{\partial lnf}{\partial ln(c_{Li\_ion})}\right) \qquad \text{4.12}$$

as the activity coefficient is assumed constant when the partial term in Equation 4.12 is removed.

The transport of lithium through the cathode electrode is calculated using the concentrated solution theory i.e. Fick's law:

$$\frac{\partial c}{\partial t} = \nabla\left(D_{Li\_pos}\nabla c_{Li}\right) \qquad \text{4.13}$$

$$\vec{n} . \nabla c_{Li} = \frac{J}{FD_{Li\_pos}} \qquad \text{4.14}$$

where D_{Li_pos} is the diffusion coefficient of lithium in the cathode electrode and Equation 4.14 describes the boundary condition at the electrolyte/electrode interface.

Typical lithium conducting solid-state electrolytes are glass-like. This glass-forming system operates in which the lithium ions are transported in a shuttle type movement, where the bridging oxygen atoms in a quasi-two-dimensional polymeric network are depolymerized in the presence of a modifier to non-bridging oxygen atoms. The ionized reaction, Equation 4.15, therefore is the transformation of immobile oxygen-bound lithium (Li^0) to mobile lithium (Li^+) with resultant negative charge (n^-) chemically associated to the nearest non-bridging oxygen atom.

$$Li^0 \leftrightarrow Li^+ + n^- \qquad \text{4.15}$$

k_d is the dissociation rate coefficient of Li^0 and k_r is the recombination rate coefficient of ($Li^+ + n^-$). The overall rate of the dissociation reaction is:

$$r_{Li\_ion} = k_d\left(c_{0\_Li\_ion\_init} - c_{Li\_ion}\right) - k_r(c_{Li^+})(c_{n^-}) \qquad \text{4.16}$$

When the solid-state electrolyte is at equilibrium the fraction of Li^+ in $c_{0\_Li\_ion\_init}$ is δ. Since the electrolyte is assumed to be electroneutral the equilibrium of the mobile charge carriers and immobile lithium is:

$$c_{Li^+}^{Eq} = c_{n^-}^{Eq} = \delta c_{0\_Li\_ion\_init} \qquad 4.17$$

$$c_{Li^0}^{Eq} = (1-\delta)c_{0\_Li\_ion\_init} \qquad 4.18$$

$$k_d c_{Li^0}^{Eq} = k_r c_{Li^+}^{Eq} c_{n^-}^{Eq} \qquad 4.19$$

Combining Equations 4.17, 4.18 and 4.19 gives the dissociation rate of reaction in the solid-state electrolyte:

$$k_d = \frac{k_r c_{0\_Li\_ion\_init}\delta^2}{(1-\delta)} \qquad 4.20$$

The transport of lithium through the solid-state electrolyte is calculated using the concentrated solution theory and the electrolyte rate coefficient:

$$\frac{\partial c}{\partial t} = \nabla\left(D_{Li\_ion}\nabla c_{Li\_ion}\right) + r_{Li\_ion} \qquad 4.21$$

The rate coefficient is not utilised when a liquid electrolyte is used as it is assumed to be fully dissociated. The boundary condition at the electrolyte/electrode interface, anion diffusion, has to be taken into account and is balanced by migration $(1-t_0)$.

$$\vec{n}.\nabla c_{Li\_ion} = \frac{J(1-t_0)}{F D_{Li\_ion}} \qquad 4.22$$

Table 4.1: COMSOL multiphysics general parameters

Symbol	Description	Value	Reference
c_{Li_max}	Maximum Li concentration in cathode	50.88 mol dm^{-3}	[11]
k_{pos}	Butler-Volmer cathode reaction rate coefficient	5.1×10^{-4} mol m^{-2} s^{-1}	[12]
k_{neg}	Butler-Volmer anode reaction rate coefficient	1×10^{-2} mol m^{-2} s^{-1}	[12]
σ_{Li_pos}	Cathode electrical conductivity	1×10^{-5} S cm^{-1}	[13]
D_{Li_pos}	Cathode diffusion Coefficient	2.93×10^{-10} cm^2 s^{-1}	[14]
σ_{Li_neg}	Anode electrical conductivity	1.05×10^5 S cm^{-1}	[15]
α_{a_pos}	Cathode transfer coefficient	0.6	[10]
α_{a_neg}	Anode transfer coefficient	0.5	[12]
t_0	Transference number	0.5	[6a]
T	Temperature	298.15K	

Table 4.2: Electrolyte parameters

Symbol	Description	Value	Reference
$c_{0\_Li\_ion\_init}$	Total concentration of Li-ions in solid electrolyte	60100 mol m^{-3}	[10]
k_r	Li-ion recombination reaction rate in solid electrolyte	0.9x10^{-8} m^3 mol^{-1} s^{-1}	[10]
δ	Fraction of free Li-ions in equilibrium solid electrolyte	0.18	[10]
$c_{Li\_ion\_init}$	Concentration of dissociated Li-ions in solid electrolyte	$\delta^* c_{0\_Li\_ion\_init}$	[10]
	Concentration of dissociated Li-ions in liquid electrolyte	1000 mol m^{-3}	[16]
D_{Li_ion}	Diffusion coefficient in solid electrolyte	1x10^{-11} cm^2 s^{-1}	[17]
	Diffusion coefficient in polymer electrolyte	1x10^{-9} cm^2 s^{-1}	[18]
	Diffusion coefficient in polymer-gel electrolyte	1x10^{-8} cm^2 s^{-1}	[18]
	Diffusion coefficient in liquid electrolyte	1x10^{-7} cm^2 s^{-1}	[16]
σ_{Li_ion}	Ionic conductivity of solid electrolyte	1x10^{-6} S cm^{-1}	[17]
	Ionic conductivity of polymer electrolyte	1x10^{-5} S cm^{-1}	[18]
	Ionic conductivity of polymer-gel electrolyte	1x10^{-4} S cm^{-1}	[18]
	Ionic conductivity of liquid electrolyte	1x10^{-3} S cm^{-1}	[16]

Geometric models

The geometric models used in these studies are the planar thin-film microbattery, 3D and 3D core-shell nanoarchitectures; see Figure 4.1. The thin-film microbattery geometry comprised of 2.5 µm thick electrodes separated by 1.25 µm of electrolyte. In the model the width of the microbattery is just a fraction of a typical planar thin-film.
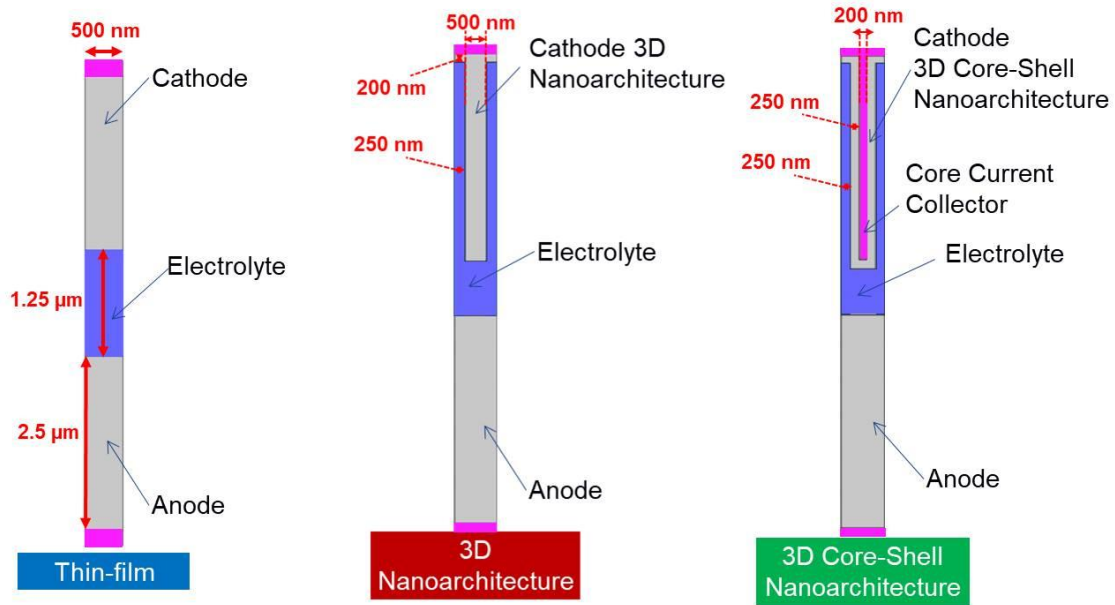
Figure 4.1: Types of architectures; Thin-film, 3D and 3D core-shell nanoarchitectures.

The 3D nanoarchitecture battery geometry is composed of anode and cathode materials in 3D electrodes with a width of 500 nm, the tops of the electrodes are separated by 1.25 µm and have a spacing of 250 nm filled with electrolyte. The 3D core-shell nanoarchitecture geometry is comprised of a 3D current collector uniformly covered in anode and cathode material. The 3D current collector has a width of 200 nm, covered in 250 nm thick electrode material and a 250 nm spacing filled with electrolyte. The 2D model used in these simulations used an out-of-plane thickness of 100 µm. The stated battery capacity is based on a full discharge in 7,200 seconds, equivalent to a 0.5 C-Rate. The anode and cathode are directly opposite each other for all 3 geometries, this is of particular importance for the 3D and 3D core-shell nanoarchitectures for practical fabrication.

For solid-state batteries, areal capacity (capacity per overall cell area) is the most important characteristic since area is at a premium; therefore it is important to compare not just the gravimetric energy density but also the areal capacity of the geometries. The stated areal capacity (0.5 C) of the thin-film microbattery is the same for the 3D and 3D core-shell nanoarchitectures in order to compare battery performance.

For this study an extremely fine edge mesh was used at the electrode/electrolyte boundaries while the mesh for the remaining geometry was extra fine free triangular mesh. A parametric sweep was used to vary the discharge C-rate. The time dependent study was between 0 and 7,200 seconds with a relative tolerance of 10^{-4} and a timestep of $<1\times10^{-7}$ s as a stop condition.

Results and discussion

Current thin-film microbatteries use a solid-state electrolyte that has a low ionic conductivity so electrolytes with a higher ionic conductivity were investigated in thin-film geometry. The effect of an increase in ionic conductivity on the galvanostatic profile, Figure 4.2, results in less voltage drop at higher discharge currents but no change in capacity due to it being limited by the rate of diffusion in the cathode. This results in only a slight increase in the areal power and energy with the increase in ionic conductivity of the electrolyte as seen in the Ragone plot, Figure 4.3, due to the slight increase in operational potential given that there is no change in the concentration profile corresponding to no change in capacity at specific discharge rates.
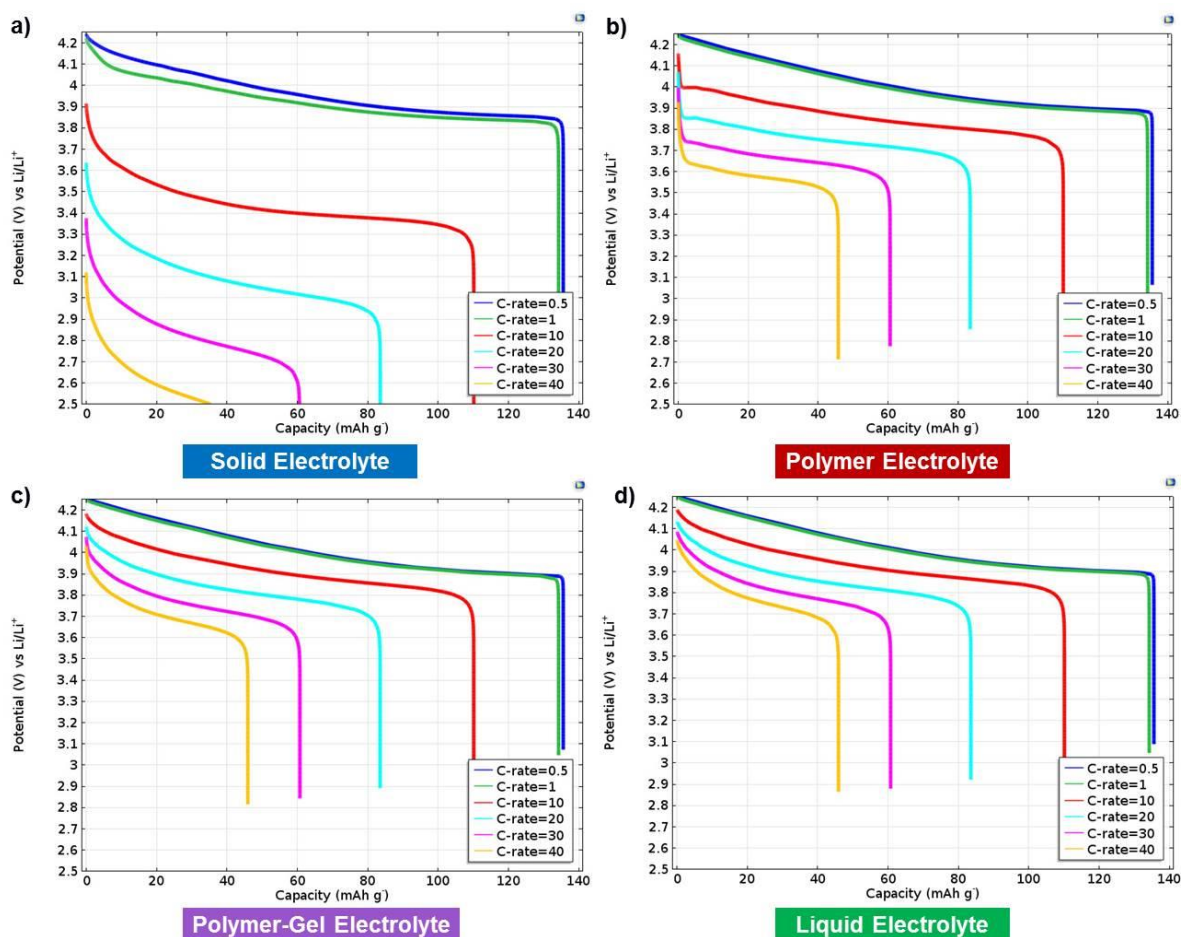

Figure 4.2: Galvanostatic discharge profiles of a thin-film microbattery in: **a)** solid, **b)** polymer, **c)** polymer-gel and **d)** liquid electrolyte.
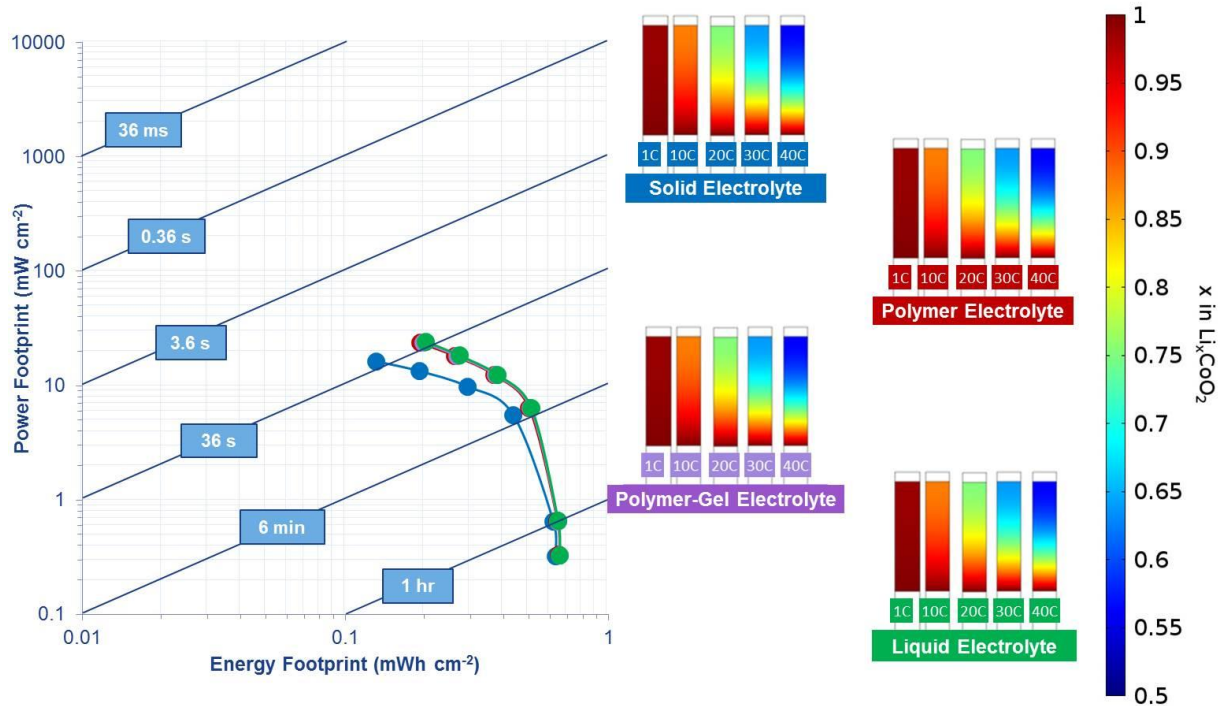
Figure 4.3: Ragone plot and lithium concentration profile in the cathode at discharge termination of thin-film microbattery with a solid, polymer, polymer-gel and liquid electrolyte.

To compare a thin-film microbattery with the nanoarchitectures of a 3D and 3D core-shell battery on a practical level, the areal capacity at a 0.5 C-Rate of the 3D and 3D core-shell must match the areal capacity of the thin-film microbattery. The geometries of the 3D and 3D core-shell nanoarchitectures both require an increase in electrode area to allow for the electrolyte to make contact in and around the base of the nanoarchitectures. The 3D core-shell nanoarchitecture requires an additional increase in elctrode area by comparison with the 3D nanoarchitecture to take into account the area of the core current collector, Table 4.3. Increasing the amount of active electrode material offsets this increase in area. Since the cell area is fixed the additional active electrode material is accounted for by increasing in the electrode height as seen in Figure 4.4.
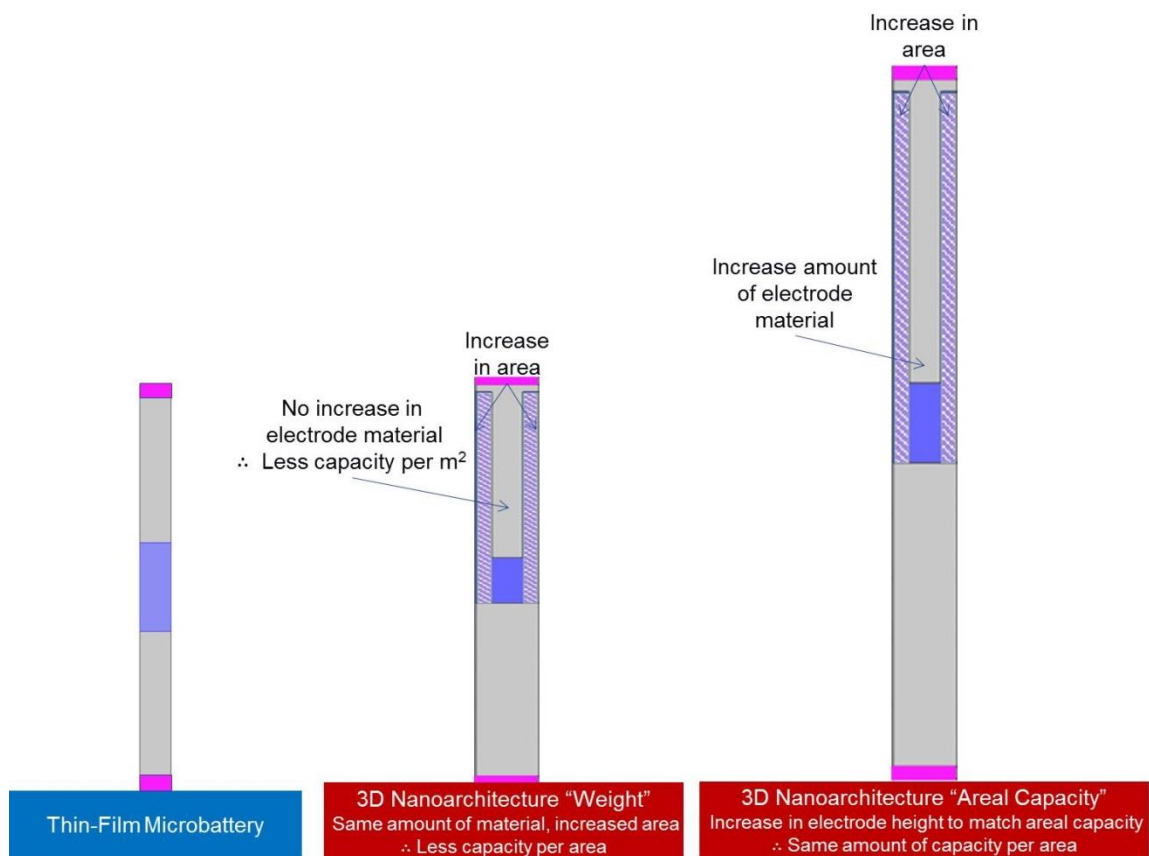
Figure 4.4: The effect on geometry of a 3D nanoarchitecture to match the areal capacity of planar thin-film microbattery.

Table 4.3: Architecture Vs Discharge current

Architecture	Cell Width	Discharge Current (1C)	Current Density
Thin-Film	500 nm	0.08441 nA	1.69×10^{-4} A m-
3D Nanoarchitecture	1000 nm	0.16882 nA	1.69×10^{-4} A m-
3D Core-Shell Nanoarchitecture	1200 nm	0.20260 nA	1.69×10^{-4} A m-

The effect that geometries have on the overall capacity of the battery is dependent on the electrolyte used. As seen in the Ragone plot in Figure 4.5 the thin-film microbattery geometry gives superior areal power values as opposed to the 3D and 3D core-shell nanoarchitectures when a solid-state electrolyte is used. This is due to low values of ionic conductivity and diffusion coefficient for the solid-state electrolyte. The low values for these critical parameters mean that it is faster for the Li^+ ions to diffuse through the cathode material rather than the electrolyte. This negates any advantages associated with the nanoarchitectures such as the electrolyte in contact with a larger electrode surface area become negligible due to the

150

increase in the nanoarchitectures height to match the capacity of a thin-film microbattery. As it is faster for the Li$^+$ ions to travel through the cathode material, lithiation is focused on the closest point to the anode electrode which is the tip on the nanoarchitectures. The concentrated lithiation on the top of the nanoarchitecture results in a larger overpotential, i.e. potential drop, at the same discharge rates when compared to thin-film geometry as the internal resistance is greater as shown in Figure 4.6 due to thicker electrodes for the nanoarchitectures.

Figure 4.5: Ragone plot and lithium concentration profile at discharge termination of thin-film, 3D and 3D core-shell nanoarchitectures with a solid-state electrolyte.
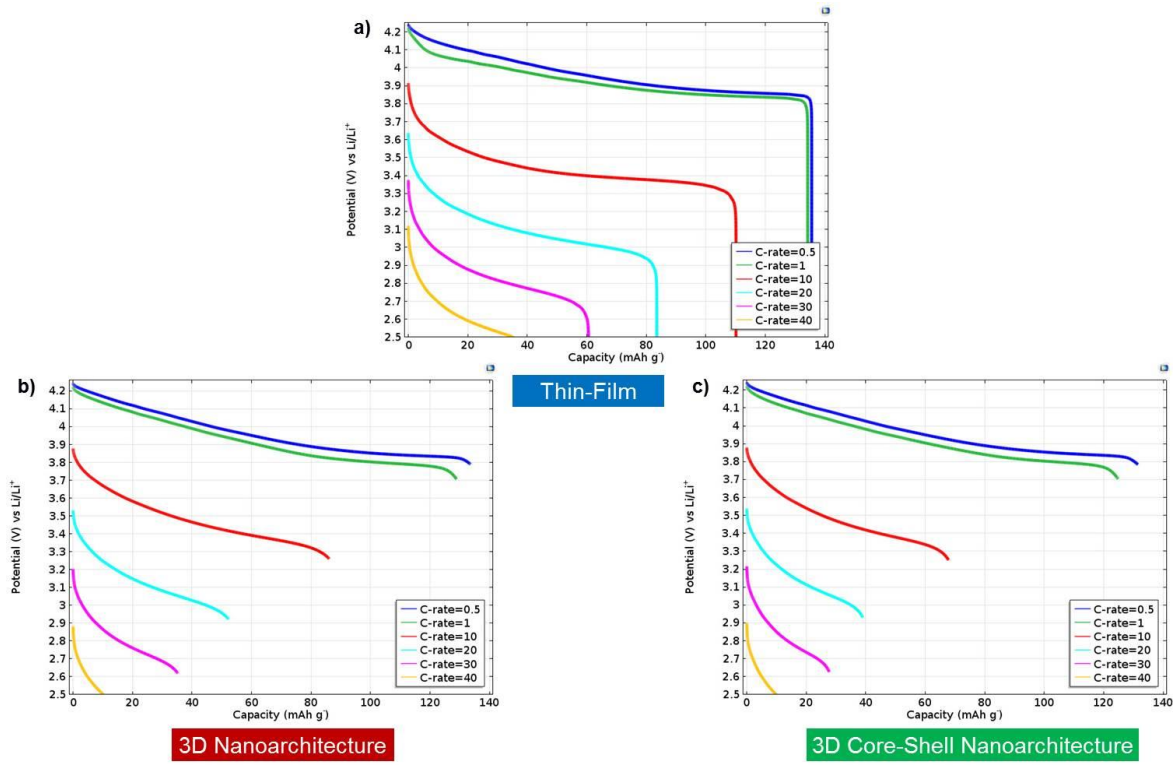
Figure 4.6: Galvanostatic discharge profiles of geometries in a solid-state electrolyte: a) thin-film, b) 3D nanoarchitecture, c) 3D core-shell nanoarchitecture.

As seen with the thin-film geometry the potential drop decreases with improved electrolyte parameters at increased current densities for both nanoarchitectures in the galvanostatic discharge curves in the polymer electrolyte in Figure 4.7. However, unlike the thin-film geometry the nanoarchitectures also increase in capacity.
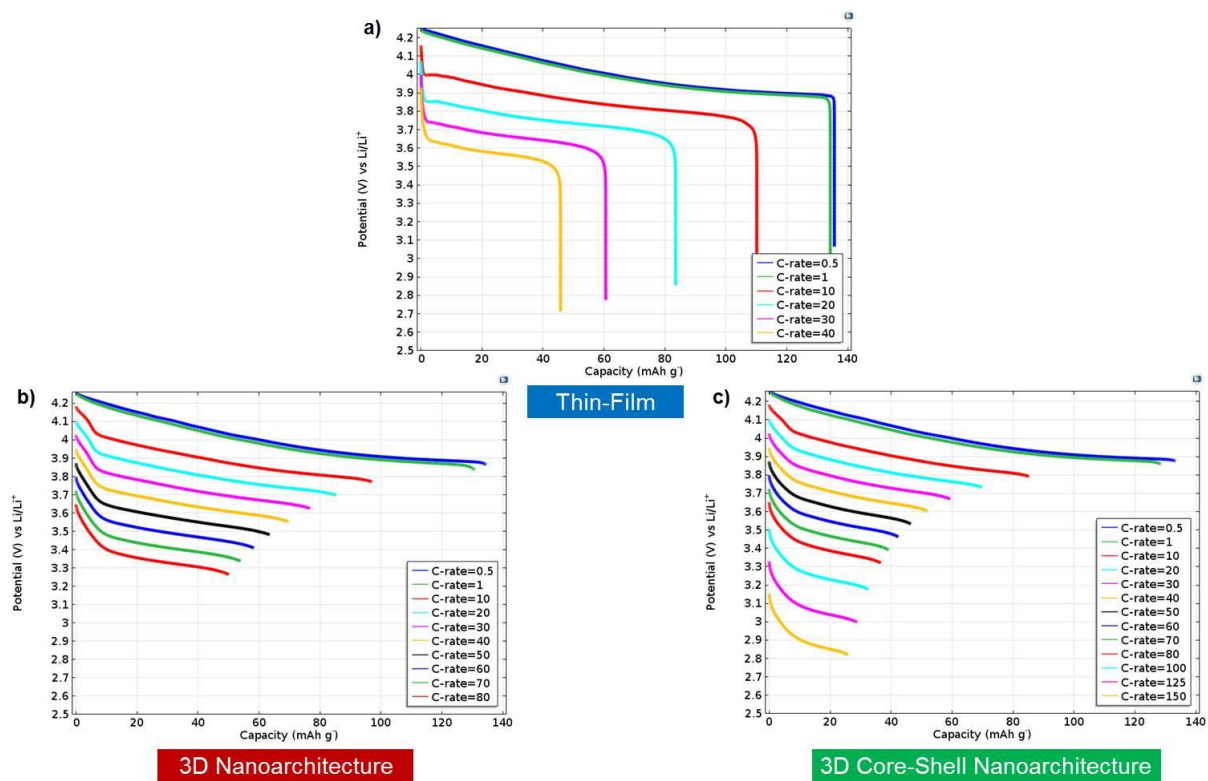
Figure 4.7: Galvanostatic discharge profiles of geometries in a polymer electrolyte: a) thin-film, b) 3D nanoarchitecture, c) 3D core-shell nanoarchitecture.

In Figure 4.8 the advantages of additional surface area in contact with the electrolyte are seen for 3D and 3D core-shell nanoarchitectures when polymer electrolyte characteristics are used. The 3D nanoarchitecture shows the best power performance in comparison to thin-film microbattery and the 3D core-shell nanoarchitecture. Even though both the 3D and 3D core-shell nanoarchitectures have additional surface area exposed, the core current collector has a negative effect on performance. The additional area for the core current collector comes at a cost resulting in a taller electrode which leads to less uniform lithiation and a further transport distance in comparison to the 3D nanoarchitecture even at lower C-rates resulting in lower areal power capabilities.
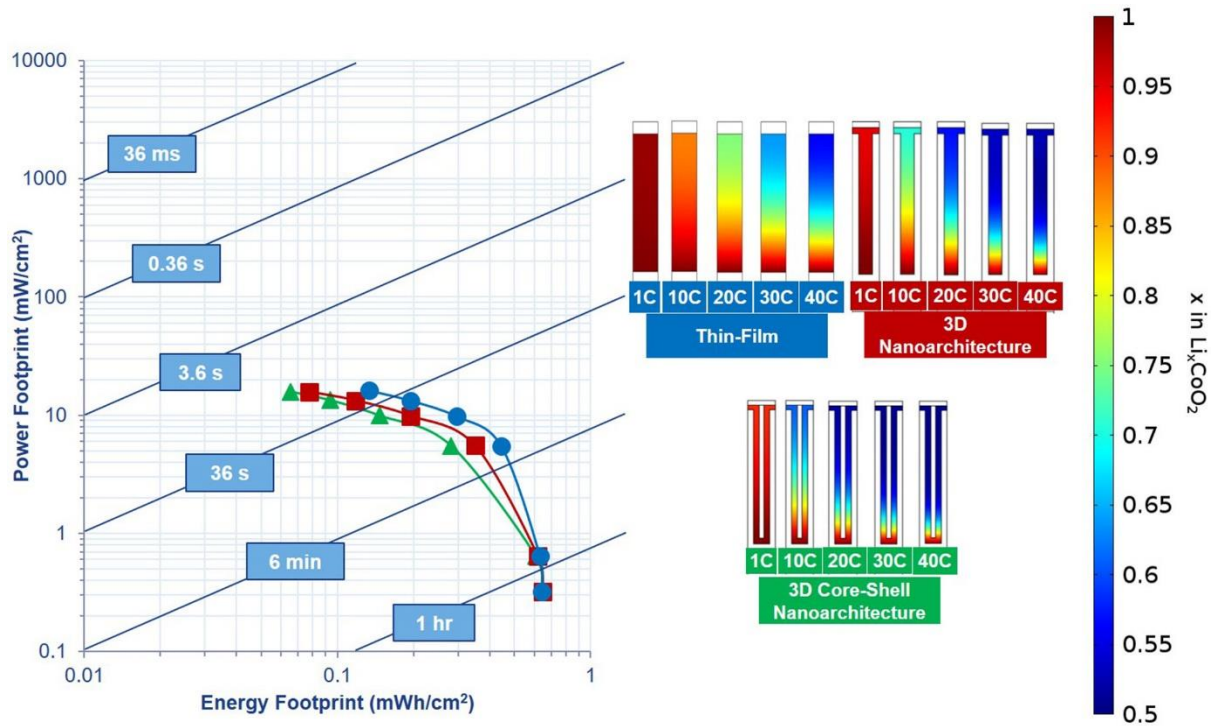
Figure 4.8: Ragone plot and lithium concentration profile in the cathode at discharge termination of thin-film, 3D and 3D core-shell nanoarchitectures with a polymer electrolyte.

The concentration profile of the 3D nanoarchitecture with a polymer electrolyte in Figure 4.8, shows that at higher C-rates an increased amount of non-utilised electrode material exists at the centre of the 3D nanoarchitecture in contrast to the base and tip of the nanoarchitecture. This is because the transport rate of the Li^+ ions through the electrolyte and the electrode are similar. The electrolyte allows for the transport of the Li^+ ions to the base of the electrode and closest to the current collector, while the diffusion of Li^+ ions through the electrode material is also favourable.

The Ragone plot for the polymer-gel electrolyte is shown in Figure 4.9 with a larger improvement in the areal power and energy values for the nanoarchitectures by comparison with the polymer electrolyte. The benefit of the core current collector can be seen in this plot and the advantages that the 3D core-shell nanoarchitecture has over the 3D nanoarchitecture. The core current collector improves the electronic transport, the distance between the electrode/electrolyte interface and the current collector is much smaller in comparison to the 3D nanoarchitecture format which has the current collector contact at the base. This results in an improved lithiation distribution and a more gradual decline in performance at higher C-rates for the 3D core-shell nanoarchitecture. The improved characteristics of the polymer-gel electrolyte result in very good power and energy values for the 3D nanoarchitecture however these values diminish rapidly at increased C-rates in contrast to the 3D core-shell

nanoarchitecture due to the absence of the core current collector. The concentration profiles match up with the galvanostatic profiles seen in Figure 4.10 with a rapid drop in capacity at higher discharge rates for the 3D nanoarchitecture while a more gradual drop is seen for the 3D core-shell nanoarchitecture. The potential drop at higher discharge rates is also minimal due to the improved ionic conductivity and diffusion characteristics of the polymer-gel electrolyte.
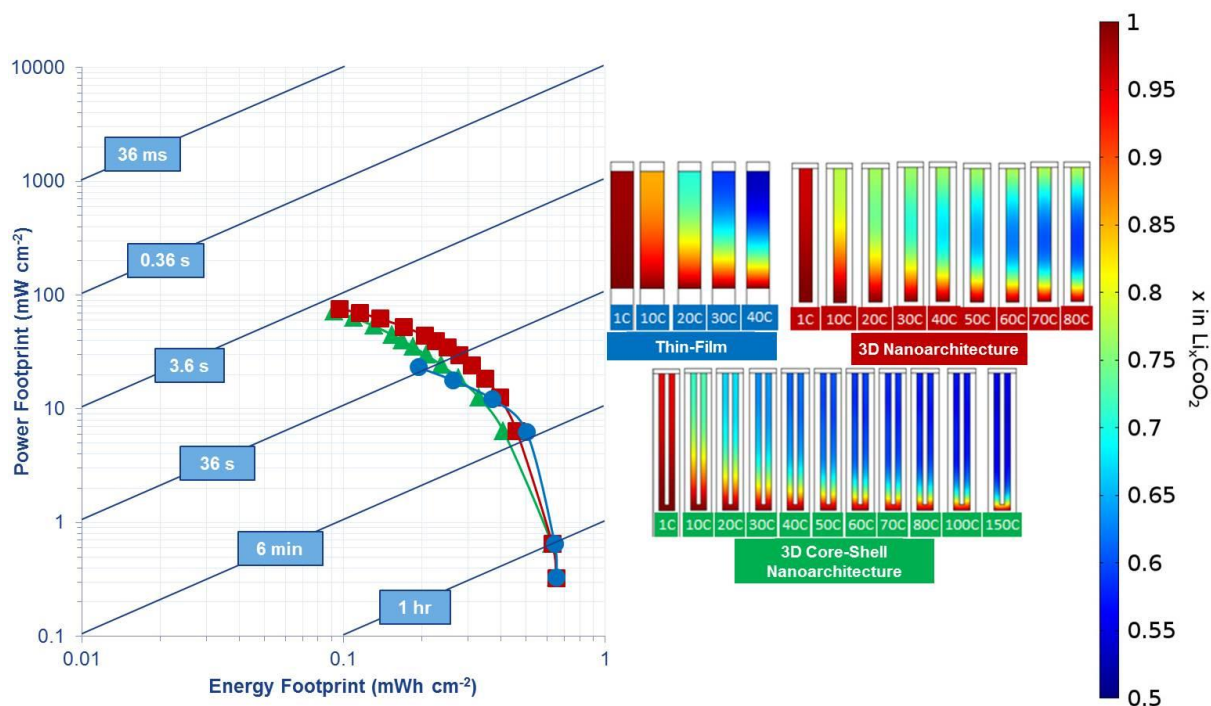

Figure 4.9: Ragone plot and lithium concentration profile in the cathode at discharge termination of thin-film, 3D nanoarchitecture and 3D core-shell nanoarchitecture with a polymer-gel electrolyte.

Figure 4.10: Galvanostatic discharge profiles of geometries in a polymer-gel electrolyte: a) thin-film, b) 3D nanoarchitecture, c) 3D core-shell nanoarchitecture.

The liquid electrolyte for the 3 geometries can be seen in Figure 4.11 and Figure 4.12. The positive attributes of the 3D core-shell nanoarchitecture are more prominent in this case and have a significant effect on the areal power and energy values. The liquid electrolyte makes the lithiation process more favourable assisting the Li$^+$ ions to diffuse through the electrolyte and uniformly around the electrode due to the core current collector followed by solid-state diffusion into the electrode material.

At the higher rates there is a change in concentration profiles and the resulting Ragone plots due to the uniformity of lithiation in the electrode. When lithiation is not uniform there is a variety of local reaction rates at the electrode, which limit the amount of current that can be passed by the battery. Areas with a higher reaction rate become fully lithiated faster than it takes for lithium to diffuse to areas of lower concentration in the electrode. The discharging process stops prematurely and not all of the material is accessed at the increased C-rates.
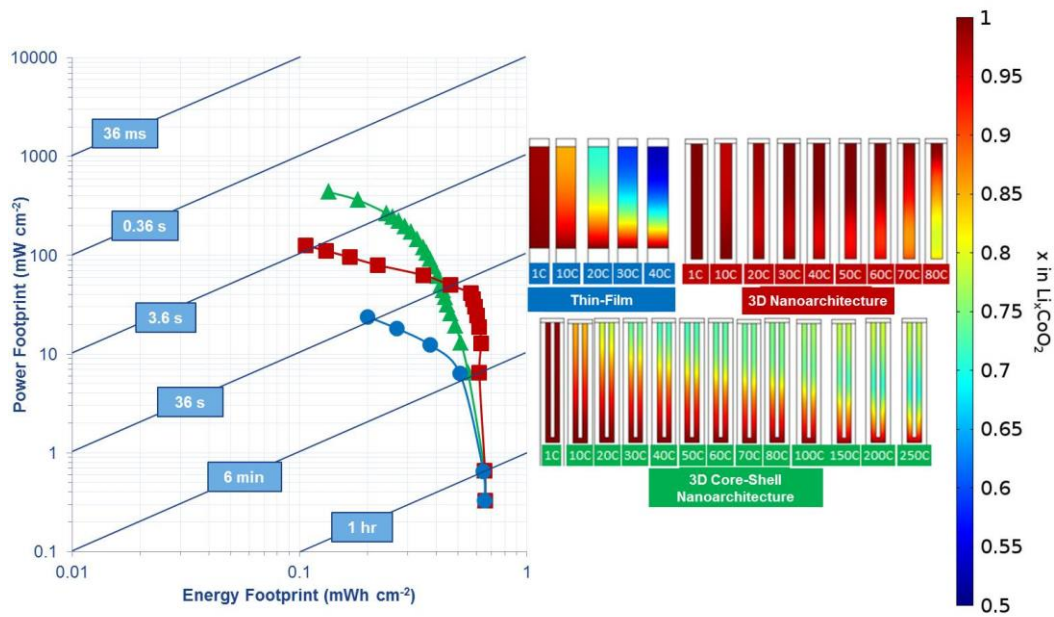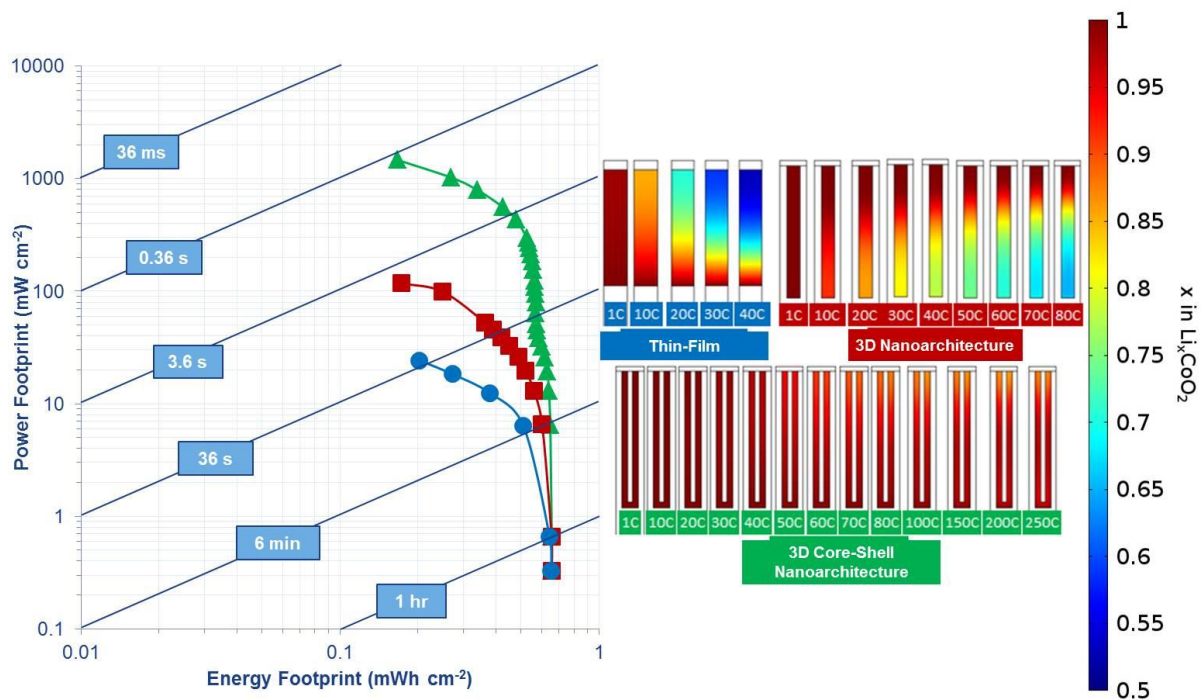
Figure 4.11: Ragone plot and lithium concentration profile at discharge termination of thin-film, 3D and 3D core-shell nanoarchitectures with a liquid electrolyte.
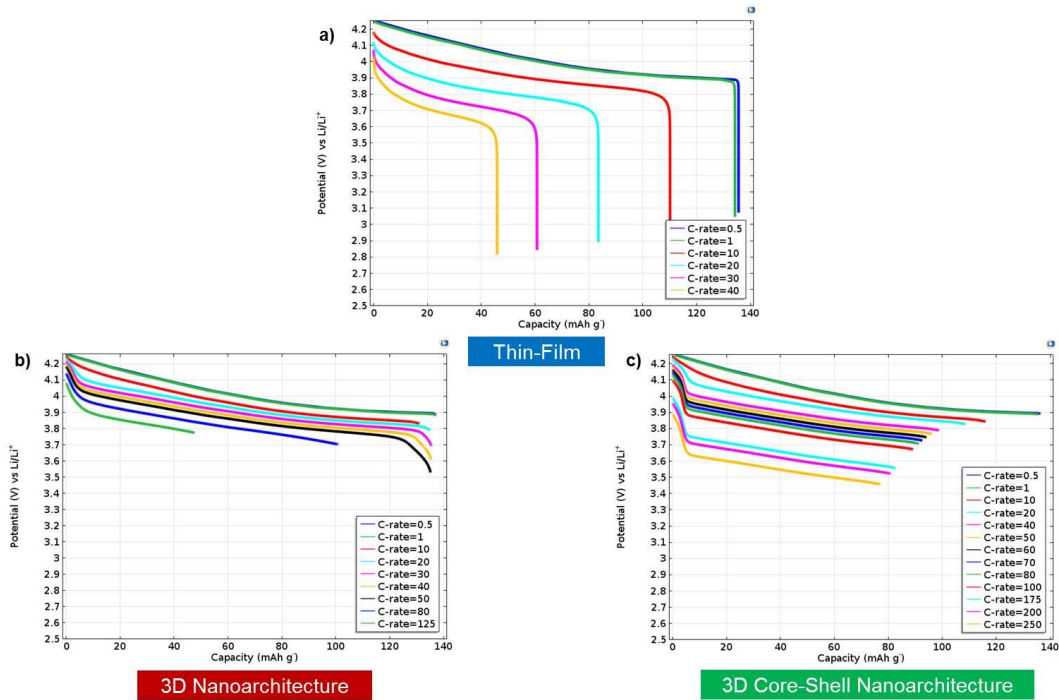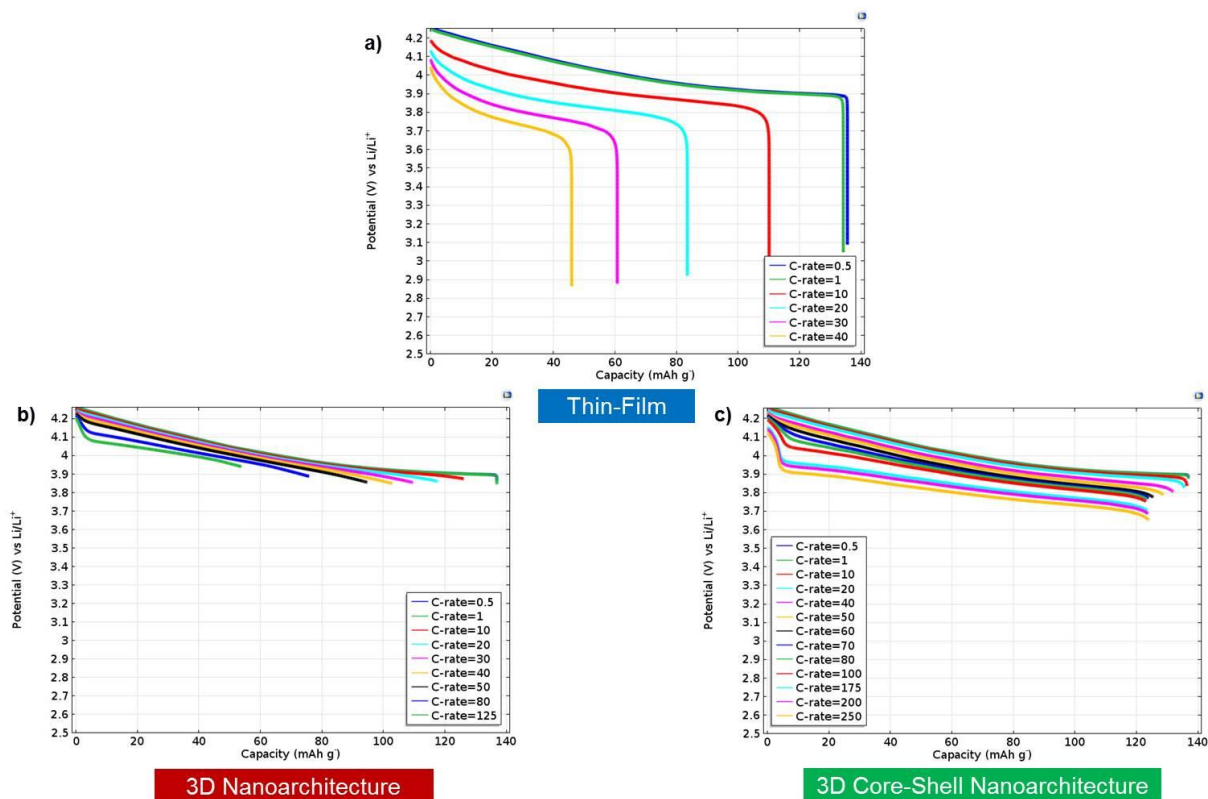
Figure 4.12: Galvanostatic discharge profiles of geometries in a liquid electrolyte: a) thin-film, b) 3D nanoarchitecture, c) 3D core-shell nanoarchitecture.

Figure 4.13 shows that 3D nanoarchitecture becomes the performance limiting factor and electrolyte characteristics have little or no effect on the cell performance. There is little difference between a 3D nanoarchitectures used with a polymer-gel and a liquid electrolyte. Both the polymer-gel and liquid electrolyte favour lithium transport through the electrolyte initially and lithiation at the closest point to the current collector which is at the base of the electrode. Interestingly, the polymer-gel electrolyte shows better performance at lower C-rates up to 80 C due to the coupling of lithium transport mechanisms. Similar transport rates through the electrolyte and electrode means high rates of lithiation occur at the base and tip of the 3D nanoarchitecture, respectively. This coupling of lithium transport mechanisms allows for more utilisation of electrode material at lower C-rates, however the slightly less favourable transport mechanism of lithium transport to the tip of 3D nanoarchitecture begins to diminish at increasing C-rates leaving just the lithium transport to the base of the 3D nanoarchitecture.

Figure 4.13: Ragone plot and lithium concentration profile in the cathode at discharge termination of 3D nanoarchitecture geometries with a solid, polymer, polymer-gel and liquid electrolyte.

The slightly slower transport of lithium in the polymer-gel electrolyte compared to the liquid electrolyte means there is a more significant drop off in performance at higher C-rates for the polymer-gel electrolyte. The opposite effect can be seen for the polymer electrolyte where the lithium transport to the base of the 3D nanoarchitecture is the least favourable transport mechanism and becomes negligible at higher C-rates. Since the critical kinetic parameters of the polymer electrolyte are lower than the polymer-gel the coupling effect of the lithium transport mechanism is more extreme for the concentration profile at higher C-rates. The liquid electrolyte shows a slightly negative effect at lower C-rates, in comparison to the polymer-gel electrolyte solely due to the battery geometry.

The 3D core-shell nanoarchitecture benefits most from enhanced electrolyte characteristics as seen in Figure 4.14. There is a significant increase in cell performance with improving electrolyte characteristics, which is due to the 3D core-shell nanoarchitecture providing more uniform lithiation especially when lithium diffusion through the electrolyte rather than the electrode is the limiting factor. The core current collector minimises the diffusion distance from electrolyte/electrode interface to current collector and has an equal distance from the side wall. When the solid electrolyte is used for the 3D core-shell nanoarchitecture the lithium diffusion through the electrode is faster than through the electrolyte. This causes high

local overpotentials at the tip of the 3D core-shell nanoarchitecture which ultimately ends the lithiation process early at increasing C-rates. A similar and delayed response is seen for the polymer electrolyte due to the better electrolyte characteristics. The polymer-gel electrolyte shows a different response. At the 250 C rate it can be seen that there is a slightly higher concentration of lithium near the base rather than the centre of the electrode. This is more than likely due to the larger electrode/current collector interface area at the base. A similar but more extreme result can also be seen for the 3D nanoarchitecture. The liquid electrolyte shows uniform lithiation throughout the electrode at high C-rates.
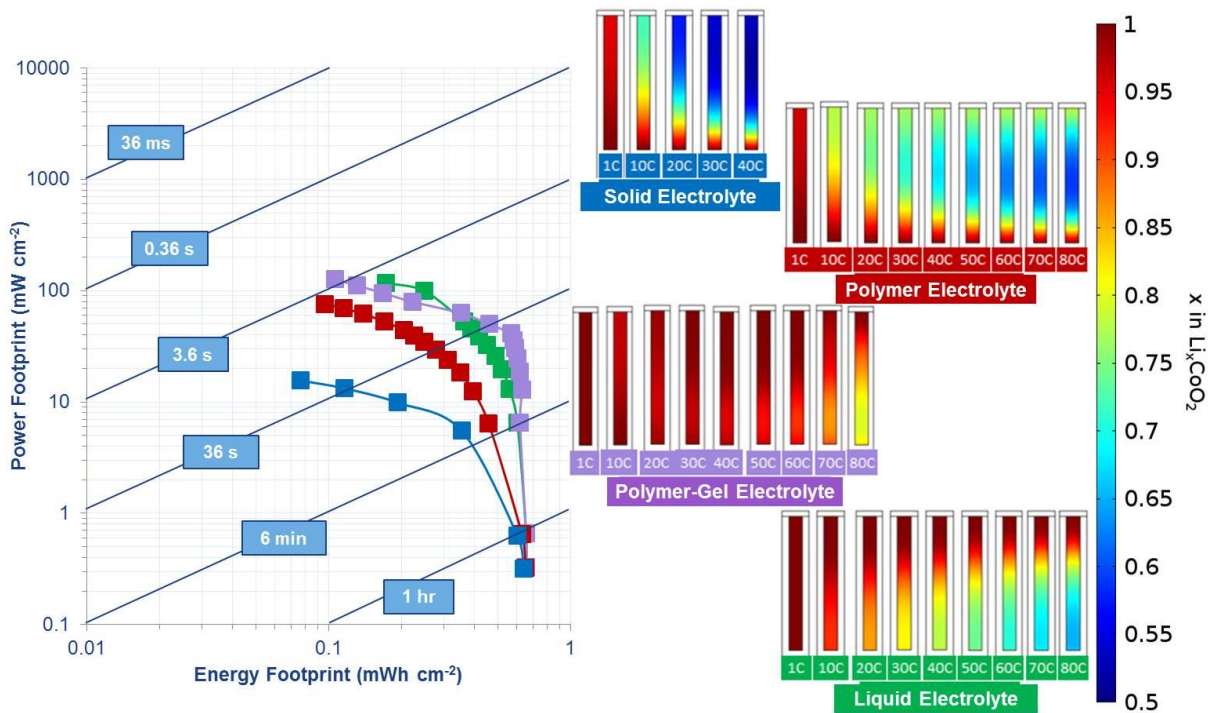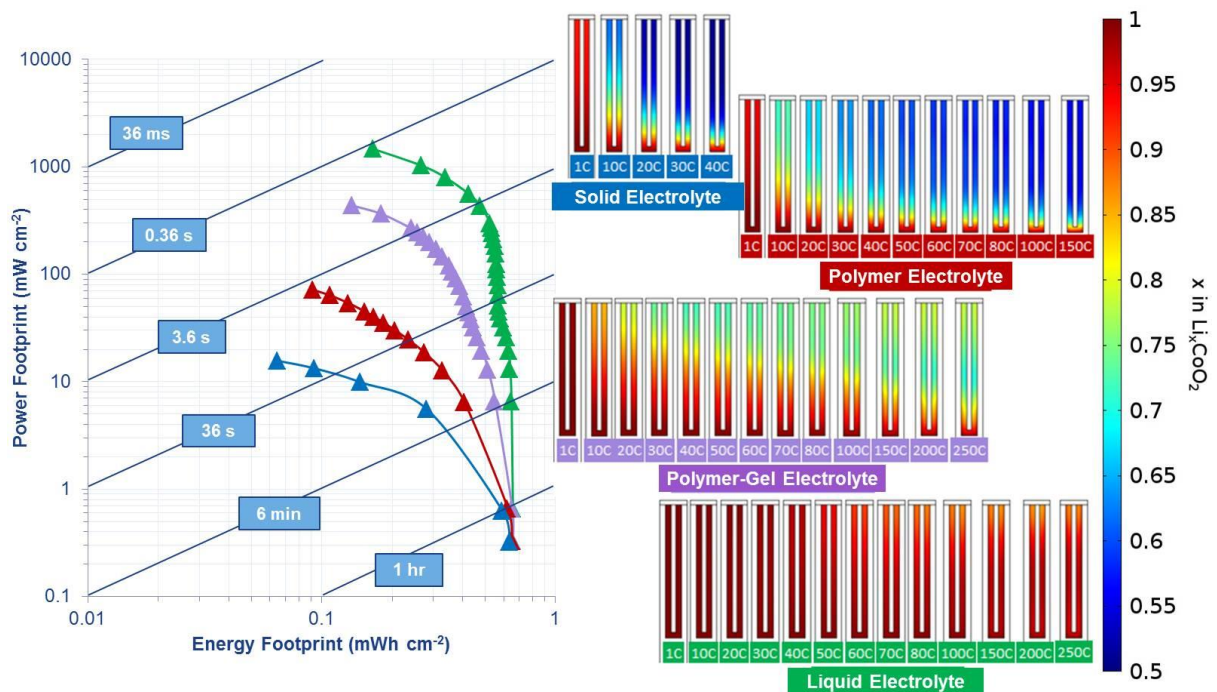

Figure 4.14: Ragone plot and lithium concentration profile in the cathode at discharge termination of 3D core-shell nanoarchitecture with a solid, polymer, polymer-gel and liquid electrolyte.

The liquid electrolyte coupled with the 3D core-shell nanoarchitecture gave the best performance. For a 1500 C (2.4 s) discharge rate, 42% (0.28 mWh/cm^2) of the battery is utilised with an areal power value of 862 mW/cm^2. This is a significant improvement from the planar thin-film battery with the solid-state electrolyte where a 20 C (180 s) discharge rate gave 47% (0.30 mWh/cm^2) of the batteries areal energy with an areal power of 9.71 mW/cm^2. Even when the electrolyte was changed to a liquid electrolyte only a slight improvement was seen in the battery cell performance, 30 C (120 s) discharge gave 42% (0.27 mWh/cm^2) of the total areal energy with an areal power of 18.35 mW/cm^2.

Conclusion

In this work, FEA has been used to compare the effect of different architectures on a range of electrolytes and the influence of the different electrolytes on the proposed architectures for microbatteries. The simulations were of a microbattery stack where non-porous additive-free $LiCoO_2$ is the cathode, lithium metal is the anode and solid-state, polymer, polymer-gel and liquid electrolytes were investigated. The architectures used are planar thin film, 3D and 3D core-shell nanoarchitectures where the anode and cathode are directly opposite each other for nanoarchitecture fabrication practicality. The simulations include Fick's diffusion law for lithium transport in the electrode, concentration solution theory for the transport of Li^+ ions in the electrolyte and the Butler-Volmer theory to describe the transport kinetics at the electrode/electrolyte interface.

When comparing the effect the geometries have on the solid-state electrolyte it can be concluded that thin-film microbatteries have slightly better performance in comparison with 3D and 3D core shell nanoarchitectures. This is because the electrodes height needed to be increased to accommodate the additional area of a 3D (electrolyte in contact with electrode sidewall) and 3D core-shell (addition on core current collector) nanoarchitectures to so that the capacity per area for all three geometries. The low transport characteristics of the solid-state electrolyte means the fastest transport mechanism for Li^+ ion is through the electrode rather than the electrolyte means that little lithiation takes place at the electrode sidewall. This means the increase in electrode height required for the nanoarchitectures does not create shorter Li^+ ion transport distances when used with a solid state electrolyte as lithiation is concentrated at the tip of the electrode while the increase in electrode height negatively impacts the performance of the battery as the electrons produced from lithiation at the tip of the electrode have a greater distance to travel to the base of the electrode. To summarise, lithiation of the electrode takes place at the tip of the electrode in all 3 geometries therefore the performance decreases with increasing electrode.

An improvement in the performance of the nanoarchitectured batteries can be seen with an improvement in electrolyte diffusion characteristics. It can be concluded that the geometric characteristics of the nanoarchitectures become dominant with improving electrolyte lithium ion transport. Interestingly this can be seen to have its own problems for the 3D nanoarchitecture where the lithium transport in the liquid electrolyte is fast, causing high lithium ion insertion at the base of the electrode, closest the current collector, resulting in

non-uniform utilisation of the 3D nanoarchitecture. The lithium transport in the polymer-gel electrolyte is slower but results in more uniform utilisation of the electrode material due to simultaneous lithium ion insertion at the base of the 3D nanoarchitecture and at the tip due to the slower transport properties of the polymer-gel making lithium ion insertion more favourable at increased distances from the current collector. This is in agreement with Zadin et al. who found that polymer electrolytes gave more uniform electrochemical activity than liquid electrolytes in 3D interdigitated microbatteries[6b].

The 3D core-shell nanoarchitecture does not have the same problems as the 3D nanoarchitecture with improving electrolyte characteristics. The core current collector ensures that lithium insertion is uniform because of the increase in electrode/current collector area resulting in shorter distance from the current collector to the electrode/electrolyte interface. This means that the 3D core-shell nanoarchitecture maximises the advantageous effect of increased surface area when lithium ion transport in the electrolyte is the dominant transport mechanism in the cell.

The simulations suggest the implementation of nanoarchitectures such as 3D and 3D core-shell nanoarchitectures when coupled with the appropriate electrolytes can have a significant advantage in terms of areal energy and power capabilities compared to thin-film geometry for a microbattery cell. The deployment of these architectures for microbatteries where area is at a premium and high power capabilities are desirable should result in better performing hybrid system and less complex power management systems.

References

[1]   P. V. Kamat, *J. Phys. Chem. C* **2008**, *112*, 18737-18753.
[2]   B. J. Neudecker, N. J. Dudney, J. B. Bates, *J. Electrochem. Soc.* **2000**, *147*, 517-523.
[3]   a) T. Chowdhury, D. P. Casey, J. F. Rohan, *Electrochem. Commun.* **2009**, *11*, 1203-1206; b) G. W. Rubloff, S. B. Lee, *Curr. Opin. Solid State Mater. Sci.* **2015**, *19*, 227-234; c) J. F. Rohan, M. Hasan, S. Patil, D. P. Casey, T. Clancy, in *ICT - Energy - Concepts Towards Zero - Power Information and Communication Technology*, InTech, Rijeka, Croatia, **2014**.
[4]   J. F. M. Oudenhoven, L. Baggetto, P. H. L. Notten, *Advanced Energy Materials* **2011**, *1*, 10-33.
[5]   R. W. Hart, H. S. White, B. Dunn, D. R. Rolison, *Electrochem. Commun.* **2003**, *5*, 120-123.
[6]   a) V. Zadin, H. Kasemagi, A. Aabloo, D. Brandell, *J. Power Sources* **2010**, *195*, 6218-6224; b) V. Zadin, D. Brandell, *Electrochim. Acta* **2011**, *57*, 237-243; c) V. Zadin, D. Brandell, H. Kasemägi, A. Aabloo, J. O. Thomas, *Solid State Ionics* **2011**,

192, 279-283; d) P. Priimägi, D. Brandell, S. Srivastav, A. Aabloo, H. Kasemägi, V. Zadin, *Electrochim. Acta* **2016**, *209*, 138-148.

[7]   D. Miranda, C. M. Costa, A. M. Almeida, S. Lanceros-Méndez, *Applied Energy* **2016**, *165*, 318-328.

[8]   M. Doyle, T. F. Fuller, J. Newman, *J. Electrochem. Soc.* **1993**, *140*, 1526-1533.

[9]   J. Newman, K. E. Thomas, H. Hafezi, D. R. Wheeler, *J. Power Sources* **2003**, *119*, 838-843.

[10]   D. Danilov, R. A. H. Niessen, P. H. L. Notten, *J. Electrochem. Soc.* **2011**, *158*, A215-A222.

[11]   T. M. Clancy, J. F. Rohan, *ChemElectroChem* **2018**, *5*, 3273-3278.

[12]   A. Bates, S. Mukherjee, N. Schuppert, B. Son, J. G. Kim, S. Park, *International Journal of Energy Research* **2015**, *39*, 1505-1518.

[13]   M. S. Whittingham, *Chem. Rev.* **2004**, *104*, 4271-4302.

[14]   Y. Matsuda, N. Kuwata, J. Kawamura, *Solid State Ionics* **2018**, *320*, 38-44.

[15]   G. K. Creffield, M. G. Down, R. J. Pulham, *J. Chem. Soc., Dalton Trans.* **1974**, 2325-2329.

[16]   M. Marcinek, J. Syzdek, M. Marczewski, M. Piszcz, L. Niedzicki, M. Kalita, A. Plewa-Marczewska, A. Bitner, P. Wieczorek, T. Trzeciak, M. Kasprzyk, P.Łężak, Z. Zukowska, A. Zalewska, W. Wieczorek, *Solid State Ionics* **2015**, *276*, 107-126.

[17]   Y. R. Su, J. C. Falgenhauer, C. Lupo, B. K. Meyer, D. Schlettwein, A. Polity, J. Janek, *Meeting Abstracts* **2015**, *MA2015-01*, 103.

[18]   L. Long, S. Wang, M. Xiao, Y. Meng, *J. Mater. Chem. A* **2016**, *4*, 10038-10069.

Chapter 5 Fabrication & Electrochemical Evaluation of Ge Core-Shell Anode Nanostructure

Abstract

3D core-shell lithium ion battery anodes were fabricated using sputter deposition for a lithium active energy dense Ge shell onto electrodeposited Cu nanotube core. A thin Ge coating on the Cu nanotubes resulted in the formation of an excess lithiated form of crystalline $Li_{15}Ge_4$ with enhanced capacity and excellent rate performance characteristics shown by cyclic voltammetry and galvanostatic cycling. Ge deposition upon the 3D Cu nanotubes resulted in an increase in capacity of 153% in comparison to the same depositing duration for Ge onto a planar Cu current collector. Rapid thermal annealing (RTA) of a thin film of Ge on a Cu current collector resulted in the formation of a nanoporous structure during lithium cycling with improved adhesion. The fabrication of an energy dense anode that is additive free with excellent rate characteristics makes them highly attractive for micro power applications such as wireless sensors where large currents are required for short periods of time and where they can be charged slowly with small currents from an energy harvester.

Introduction

Anode materials such as Si and Ge have similar physical and chemical properties and both can theoretically hold up to 4.4 Li^+ ions per atom ($Li_{22}M_5$, M = Si, Ge) resulting in high gravimetric capacities of 4,200 and 1,623 mAh/g, respectively. Both undergo a volume expansion of up to 300% which results in mechanical instability that leads to low cycle life in the bulk state due to delamination and structural disintegration from the current collector[1]. Ge is more expensive than Si but has a similar volumetric capacity of 8,645 mAh/cm^3 in comparison to 9,783 mAh/cm^3 for Si. The similar volumetric capacity values make Ge an ideal candidate for applications when the area of a device is at a premium due to Ge's superior material properties in comparison to Si. Ge has an electronic conductivity 10,000 times greater than Si and has a Li^+ ion diffusion coefficient that is 400 times faster[2]. These

properties enable fast transport of both electrons and Li$^+$ ions that results in an efficient charge transport material that can achieve both high power and energy densities[3]. The volume expansion during lithiation of Si is anisotropic meaning significant differences in expansion speeds along the <110> and <111> directions, this cause stresses to build up and eventual cracking and pulverisation of the Si electrode[4]. Ge by comparison is more resistant to cracking and pulverisation as lithiation is isotropic meaning there is no contribution to the overall stress in the film from non-uniform volume expansion[5]. The isotropic volume expansion is a very useful material property during lithiation that could enable a long cycle life for a high capacity Ge anode material.
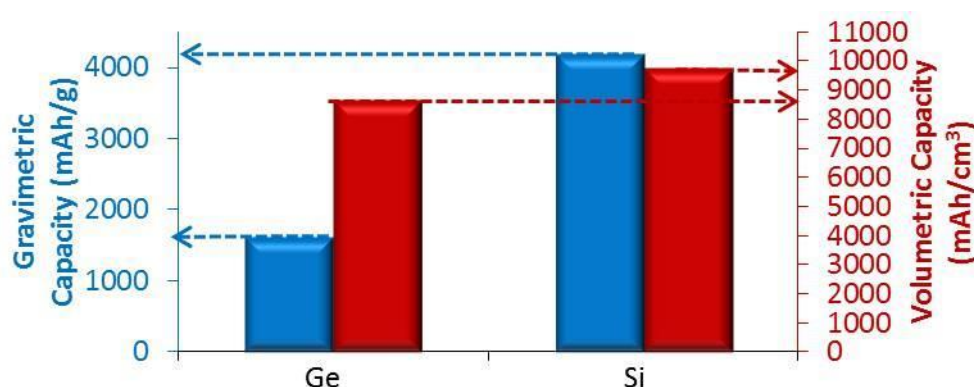
Figure 5.1: Theoretical gravimetric and volumetric capacity of Ge and Si anodes.

Graetz et al. were some of the first to investigate the lithiation process of thin-film Ge in 2004[2a]. An amorphous Ge film was deposited and cycled in an organic lithium electrolyte where it was revealed, using ex-situ XRD, that Ge transformed to crystalline Li$_x$Ge containing a mixture of Li$_{22}$Ge$_5$ and Li$_{15}$Ge$_4$ when lithiated to 0 V vs. Li/Li$^+$ and a mixture of crystalline and amorphous Ge upon delithiation to 1.5 V. Laforge et al. showed, using CV analysis, the effect of the thickness (2 μm, 800 nm, 400 nm and 200 nm) of Ge thin-films (Cu current collector) on the electrochemical performance where a decrease in thickness resulted in an increase in cycle life[6]. The transformation of a broad delithiation peak at 0.4 V to a sharp peak at 0.6 V is seen after fewer cycles for thinner Ge samples which is attributed to a decrease in compression stress levels for thinner Ge.

Baggetto et al. consolidated the results seen for Graetz at al. and Laforge et al. by using in-situ XRD and CV analysis with various lithiation cut-off potentials[7]. Li$_x$Ge remains amorphous to a 0.13 V lithiation cut-off potential with the resultant sharp lithiation and broad delithiation peak at 0.15 and 0.45 V, respectively. When the lithiation cut-off potential is

decreased to 0.02 V the XRD reveals the transformation of amorphous Li_xGe to crystalline $Li_{15}Ge_4$ and the CV profile maintains the sharp lithiation peak at 0.15 V and the replacement of the broad delithiation peak at 0.45 V with a sharp peak at 0.53 V. Therefore a broad delithiation peak at 0.40 - 0.45 V indicates an amorphous Li_xGe was formed during lithiation and a sharp delithiation peak at 0.53 - 0.6 V indicates the formation of crystalline $Li_{15}Ge_4$ during lithiation. Laforge et al. showed that a sharp delithiation peak at 0.6 V replaces the broad peak after fewer cycles with thinner Ge which suggests that crystalline Li_xGe is more easily formed with thinner Ge samples due to decreased compression stress levels in the thinner films. This also means Ge is able to accommodate 3.75 Li^+ per Ge atom and not 4.4 Li^+ atoms. Laforge stated that a mixture of $Li_{22}Ge_5$ (4.4 Li^+) and $Li_{15}Ge_4$ (3.75 Li^+) are the alloys formed during lithiation of Ge however the intensity of the $Li_{22}Ge_5$ XRD peak is relatively small in comparison to the $Li_{15}Ge_4$ XRD peak which suggest that $Li_{15}Ge_4$ is the dominant alloy formed during lithiation. This is in agreement with the results of Baggetto et al. using XRD and CV analysis and Al-Obeidi et al. using in-situ stress and CV analysis[8].

3D nanoarchitectures have been shown to alleviate the effect of volume expansion, enhancing mechanical stability at the nanoscale for high capacity electrodes as the expansion is not restricted to one direction as seen in planar geometries[9]. In-situ TEM analyse of a Ge nanowire highlighted the transformation of lithiated amorphous Ge to crystalline $Li_{15}Ge_4$ and the isotropic volume expansion[10]. The 3D geometry of a nanowire coupled with the isotropic properties of Ge results in less stress in the film and insignificant amounts of delamination. The enhanced mechanical stability of the Ge nanowire results in the formation of a nanoporous amorphous delithiated Ge nanowire as revealed by in-situ TEM with a pore memory effect. The formation of a nanoporous Ge nanowire with a pore memory effect allows for more "breathing space" during lithiation and decreased SEI formation that further enhances the cycle life and rate capabilities for the Ge nanowire.

3D geometries of Ge electrodes reported to date have included nanowires, nanotubes and direct deposition onto a 3D current collector[11]. Vapor-liquid-solid (VLS) method has been used to fabricate Ge nanowires using an Au, Sn or Cu_3Ge catalyst[1a, 12]. A Ge nanowire fabricated using a Sn nanoparticle catalyst with a 1:5 Sn:Ge mass ratio (0.22 mg/cm^2) gave a stable capacity of over 900 mAh/g at *C/2* for 1,100 cycles with the dense nanowire completely transformed to a nanoporous structure after 100 cycles. Ge nanotubes were fabricated by exploiting the Kirkendall effect in which Ge nanowires were coated with Sb and polyvinyl pyrrolidone and annealed at 700ºC in an Ar/H_2 environment and achieved a

600 mAh/g capacity after 25 cycles at a *20 C* rate[11b]. For a 50 nm Ge coating, on 40 – 50 nm diameter, 1 – 2 µm long Cu nanowires fabricated using a Cu backed AAO template[11c] capacities of 850 and 734 mAh/g were obtained after 80 cycles at a rate of *40 C* and *90 C*, respectively.

The formation of a porous structure from a planar Ge sample has also been reported[13]. The thin-film of Ge undergoes cracking but rather than delamination from the current collector as typically seen a porous structure was formed after numerous lithium cycling. This was attributed to the improved adhesion at the interface between the Ge and current collector caused by ion beam implantation of Ge$^+$ into the, as deposited Ge, resulting in an increase in concentration of Ge in the current collector at the interface. Susantyoko et al, investigated the annealing of Ge on stainless steel (SS) and SS/TiN current collectors[14]. The annealing of thin-films of Ge on SS resulted in the formation of non-uniform islands of intermetallic phases that acted like anchors to the SS current collector and drastically improved the cycle life and capacity stability of the sample. The implementation of the TiN layer, which is also a known diffusion barrier, resulted in the improvement in the cycle life and capacity compared to a non-annealed SS/Ge sample. An annealed sample of SS/TiN/Ge showed worse performance compared to an annealed SS/Ge sample, which implies that the non-uniform islands of intermetallic layers are critical for improved performance of Ge electrodes. Cu is the most common current collector for an anode electrode due to its high conductivity and its inactivity in the anode potential range. Cu_3Ge is formed after the thermal annealing of a Cu/Ge bilayer at relatively low temperatures with a reaction beginning at 100 ^{o}C[15]. Cu_3Ge is a low resistivity material with a large resistance to oxidation. It improves electrical contact between Ge and Cu and is Li inactive and therefore considered a conductive additive[16].

In this study, ultra thin-films of Ge were DC sputter deposited at room temperature onto planar Cu and Cu nanotubes current collectors and tested in a 1 M $LiPF_6$ EC:DEC (1:1) solution in which the electrochemical kinetics were investigated. The effect of an RTA process was also investigated with a view to improve the adhesion between the current collector and electrode and as a result the electrochemical performance.

Experimental

A stack of Ti (10 nm) and Cu (250 nm) was deposited on a 4" diameter silicon wafer using metal sputter targets (Kurt J. Lesker) in a DC magnetron (Quorum Q300T D) Dual sputter

coating system. The Ti layer acted as an adhesion layer between the SiO_2 substrate and Cu current collector.

Cu nanotubes were fabricated as follows. Cu electrodeposition was carried out in a 0.24 M $CuSO_4$ (Sigma Aldrich) and 1.8 M H_2SO_4 (Sigma Aldrich), poly ethylene glycol (PEG), (300 ppm) (SigmaUltra, MW 3350, powder) and Cl^- (50 ppm) as NaCl (BDH, analytical reagent grade) bath at room temperature with slow stirring of the solution. A constant current of 40 mA was applied for the Cu nanotubes electrodeposition using a potentiostat CH Instruments 660C in a two-electrode setup with Cu foil as the anode and an AAO (Aluminium Anodic Oxide) (Whatman® Anodisc, diameter 25 mm, pore size 0.02 μm, number of pores 1.00×10^9 pores/cm^2) template with a Ag backing as the cathode. After the Cu deposition, the AAO template was dissolved in a 1 M NaOH (Sigma Aldrich) solution for 50 min., washed with DI water, and dried in air.

Ge was DC sputter deposited using a 99.99% pure Ge target (Kurt J. Lesker) at a pressure and current of 1×10^{-2} mBar and 90 mA, respectively. All depositions were performed in an Ar environment. The thickness of a 6 min. deposition onto a planar Si/Cu current collector was assessed using a surface profilometer (Tencor alpha-step 200) and gave a thickness of 225 nm. Ge deposition times used on Cu nanotubes were 6, 12 and 24 min. It is assumed that Ge depositions of 12 and 24 min. on a planar substrate would give 400 and 900 nm, respectively, as 6 min. deposition on a planar substrate gives 225 nm.. The fabrication process for the Cu nanotube core/Ge shell anode is shown in Figure 5.2. The quartz crystal monitor on the DC sputter was used to deposit 470 nm of Ge onto a Si/Ni wafer with a 200 nm Cu coating and confirmed using the surface profilometer. The sample was RTA (Jipelec 150) under vacuum at 500°C for 5 min. with a ramp up of 10 °C/s.
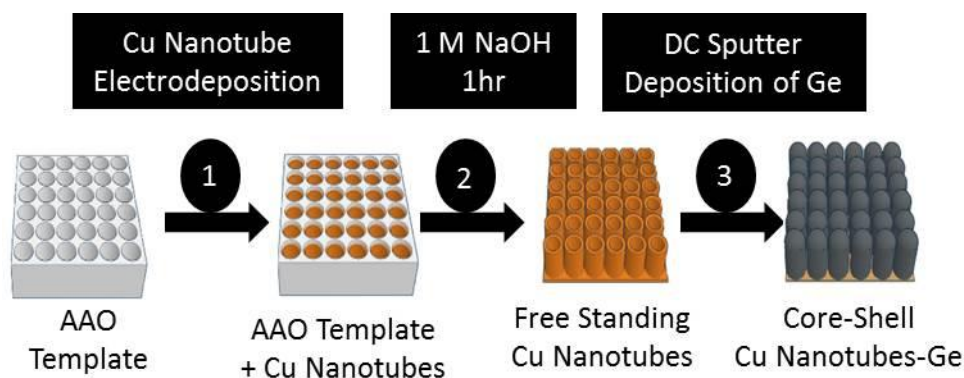
Figure 5.2: Schematic of fabrication of Cu nanotube core and Ge shell.

The structure and the morphology of the samples were analysed (FEI Nova 630 Nano-SEM) coupled with an energy dispersive X-ray (EDX) (Hitachi S4000), X-ray powder diffraction (XRD) (Philips PW3710-MPD with Cu K_α radiation, $l = 1.54056$ Å, at 45 kV (40 mA), and data was analysed using Philips X'Pert XRD software), Raman spectroscopy was performed on a Renishaw Invia, with 514 nm laser and four point probe resistivity analysis used an Agilent 34401A multimeter and Wayne Kerr Electronics, LS30-10 power supply.

Electrochemical measurements of the Li^+ capacity were assessed by cyclic voltammetry (CV) and galvanostatic intermittent titration technique (GITT) using a potentiostat (Bio-logic VSP) at various scan rates and discharge/charge currents, respectively. The scan rate was increased and varied by applying 0.10, 0.50, 1.00, 0.50, 0.10 and 0.05 mV/s for 5 cycles per scan rate. The CV's displayed have undergone background reduction due to the thin Cu_2O layer on the Cu nanotubes being Li active material in the electrochemical window of interest. A two electrode cell setup of lithium foil 0.25 mm thick (Sigma Aldrich) acted as counter and reference and 0.283 cm^2 (current density in terms of exposed cell area) of the anode was exposed as the working electrode in 1 M $LiPF_6$ in EC:DEC (1:1) (Sigma Aldrich) electrolyte assembled in an argon-filled glove box (M. Braun LABstar Glove Box) with O_2 and H_2O maintained below 0.1 ppm.

Results and discussion

Surface profilometer measurements determined a 6 min. DC sputter Ge deposition on a planar Cu/Ti/Si wafer stack gave a very smooth deposit that had a roughness of 0.40 nm which is in agreement with the top down SEM image. EDX and Raman analysis confirmed the presence of Ge with a broad Raman peak at 279 cm^{-1} attributed to the first order

transverse optical phonon mode of Ge and indicates an amorphous Ge film, Figure 5.3. XRD analysis did not detect a Ge peak which could be due to the penetration depth of the XRD and the thickness of the film but also could be indicative of an amorphous film.
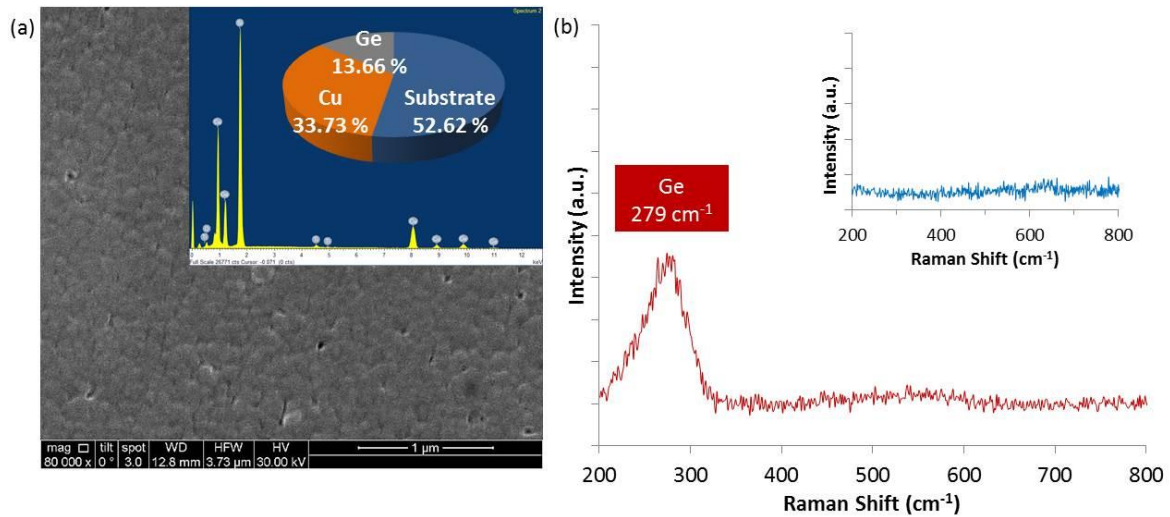
Figure 5.3: a, Top down SEM image with EDX analysis of 6 min. planar Ge. **b,** Raman analysis of 6 min. planar Ge sample, inserted Raman analysis of planar Cu substrate.

SEM and EDX analysis were used to confirm the deposition of Cu nanotubes and also used to analyse the uniformity of the Ge deposit upon the Cu nanotubes. Figure 5.4a is a SEM image and EDX data of the electrodeposited Cu nanotubes current collector. The image shows electrodeposited hollow Cu nanotubes, perpendicular to the Ag seed layer. The SEM and EDX image of the Cu nanotubes with 6, 12 and 24 min. DC sputtered Ge is shown in Figure 5.4b, Figure 5.4c and Figure 5.4d, respectively. The EDX confirms the presence of Ge and Cu as the prevalent elements while the SEM illustrates the deposition of Ge on the Cu nanotubes. Thicker Ge deposits at the top of the Cu nanotubes which eventually forms a thin layer for the longest deposit time of 24 min. The nanoscale spacing between the pores in AAO templates means that the spacing eventually gets blocked during the deposition due to a higher deposition rate at the point closest to the Ge target i.e. top of the nanotube. A larger spacing would give a more uniform deposit for a 24 min. deposition time.

Figure 5.4: SEM and EDX analysis of: **a,** Free standing Cu nanotubes, **b,** 6 min. Ge deposit onto Cu nanotubes**, c,** 12 min. Ge deposit onto Cu nanotubes, **d,** 24 min. Ge deposit onto Cu nanotubes.

The XRD analysis shown in Figure 5.5 shows a thin oxide layer exists on the Cu nanotubes. Cu nanotubes with Ge DC sputtered show the presence of a (111) Ge phase at 26^0 only for the 12 and 24 min. deposition times, Figure 5.5. The (111) Ge phase is typically found at 27^0 in the literature indicating that there is a peak shift of 1^0 perhaps due to stress on the lattice structure which is expected for thin films[17]. No Ge peak is seen for the 6 min. deposition which is due to the penetration depth of the XRD and the small quantity of Ge deposited, while the intensity of the Ge peaks increases for the 24 min. deposit in comparison to the 12

min. deposit. Raman spectroscopy exhibits a single peak at 290 cm^{-1} attributed to the Raman active first order transverse optical phonon mode of crystalline Ge[18]. This is slightly lower than the bulk Ge Raman peak quoted in the literature and also differs from the amorphous Ge deposited on a planar Cu substrate, which suggests that the Cu nanotubes promote the formation of a crystalline Ge film[19].

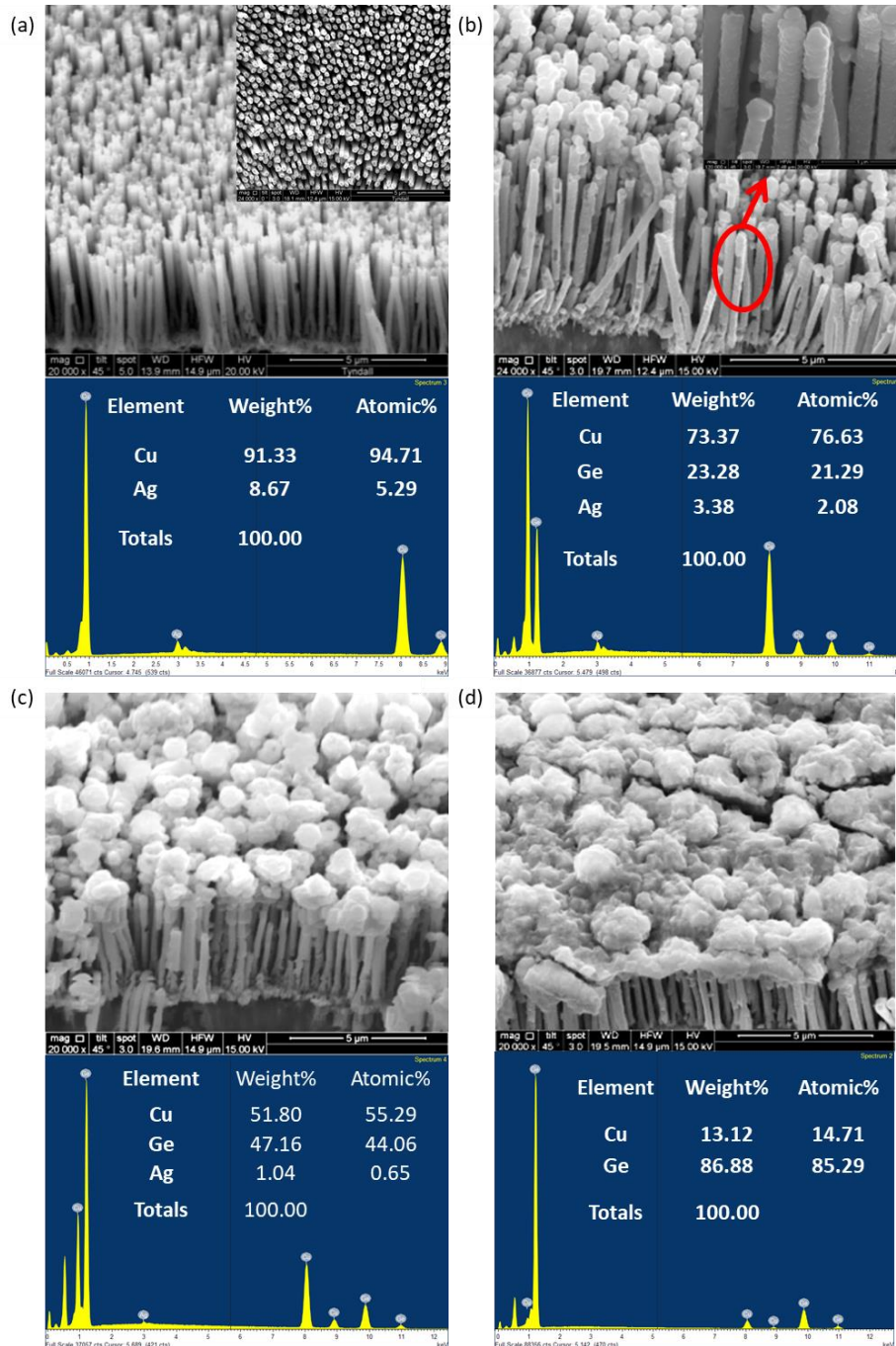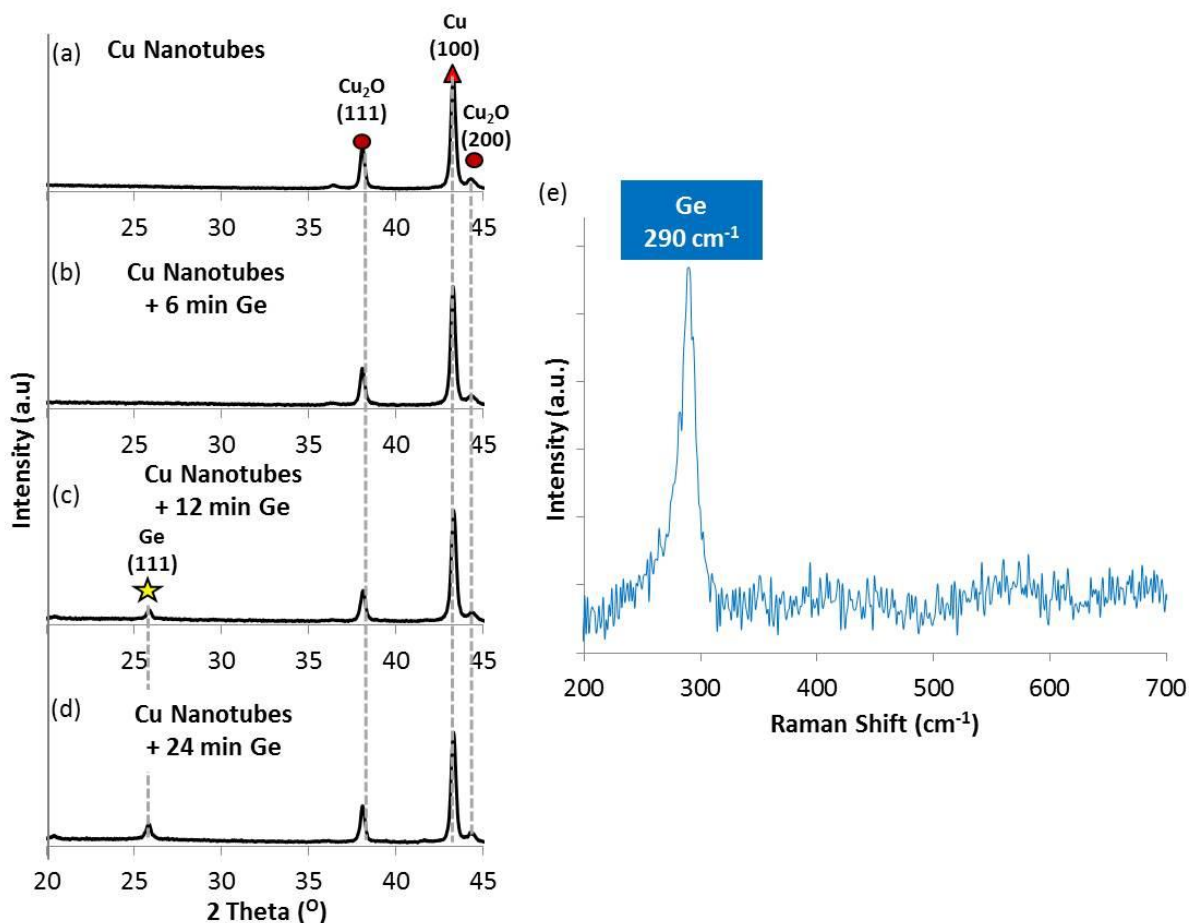**Figure 5.5:** XRD analysis of **a,** Free standing Cu nanotubes, **b,** 6 min. Ge deposit onto Cu nanotubes**, c,** 12 min. Ge deposit onto Cu nanotubes, **d,** 24 min. Ge deposit onto Cu nanotubes. **e,** Raman analysis of Ge deposited onto Cu nanotubes.

CV analysis of the 225 nm planar Ge film shows the initial cycle with cathodic peaks at (I) 0.54, (II) 0.29 and (III) 0.05 V are characteristic of Li-Ge alloying with a broad anodic peak at (IV) 0.47 V indicating delithiation of amorphous Li$_x$Ge at a scan rate of 0.05 mV/s, Figure 5.6a. There is a significant drop in the peak current and increase in anodic peak potential after 5 cycles which could be attributed to the formation of a resistive SEI layer preventing Li$^+$ ion diffusion and mechanical instability due to volume expansion. The anodic peak potential shifted to lower values while the current increased with cycle number for the next 5 cycles at 0.10 mV/s. The cycles began to stabilise at 0.50 mV/s leading to smaller current increases

with each cycle. This behaviour indicates that the first 5 cycles at 0.05 mV/s are needed for the planar Ge film to reach equilibrium.

The CV development of the 24 min. deposit of Ge on Cu nanotubes for a 0.05 mV/s scan rate is similar to the 6 min, Figure 5.6b. Ge deposit on a Cu planar substrate with the presence of the cathodic peaks at 0.50, 0.30 and 0.05 V, the broad anodic peak at 0.45 V and the drop in peak current with increasing cycle number. However, the drop in peak current is less severe and the CV stabilises after 3 cycles at 0.05 mV/s which is quicker in comparison to a planar current collector which could be attributed to volume expansion in multiple directions and the mechanical stability provided by the 3D structure of the Cu nanotubes. The cycle overlap was excellent for subsequent cycles and scan rates.

The initial CV's for the 12 min. Ge deposit on Cu nanotubes at 0.05 mV/s show the characteristic cathodic peaks at 0.51, 0.30 and 0.08 V and broad anodic peak at 0.45 V however the peak begins to sharpen while the peak current and potential increases with cycle number, Figure 5.6c. The sharp cathodic peak at 0.08 V splits into 2 peaks with the smaller peak at 0.05 V and the larger peak at 0.14 V while peak (I) at 0.51 V shifts to 0.62 V and decreases in intensity.

The CV development of the 6 min. Ge deposit on Cu nanotubes differs from the longer deposition times at a 0.05 mV/s, Figure 5.6d. There is no significant (I) cathodic peak in the 0.51 - 0.62 V range. Cathodic peaks at 0.36 and 0.152 V, respectively, are related to the characteristic peaks labelled (II) and (III). The broad anodic peak (IV) is seen at 0.4 V with the addition of a small peak (V) at 0.51 V. The potential of the initial cathodic peaks normally increases for the longer duration Ge deposits as the electrode forms a stable structure. However no such increase is seen for the 6 min. Ge deposit on Cu nanotubes as the initial potentials recorded match the stabilised potentials (6 mV increase in potential) of the longer duration Ge deposits. The broad (IV) anodic peak decreases in potential and sharpens while the intensity of the small (V) peak increases with cycle number. With increasing cycle number a redox couple is developed with a cathodic peak (VI) at 0.05 V and corresponding (VI') anodic peak at 0.12 V. The peak intensity of the redox couple increases with cycle number. The additional redox couple has not been reported before and we have attributed it to the over lithiation phase of crystalline $Li_{15}Ge_4$ suggested by Al-Obeidi et al. since the (V) anodic peak indicates delithiation of crystalline Li_xGe and is not present in the longer duration Ge deposits.
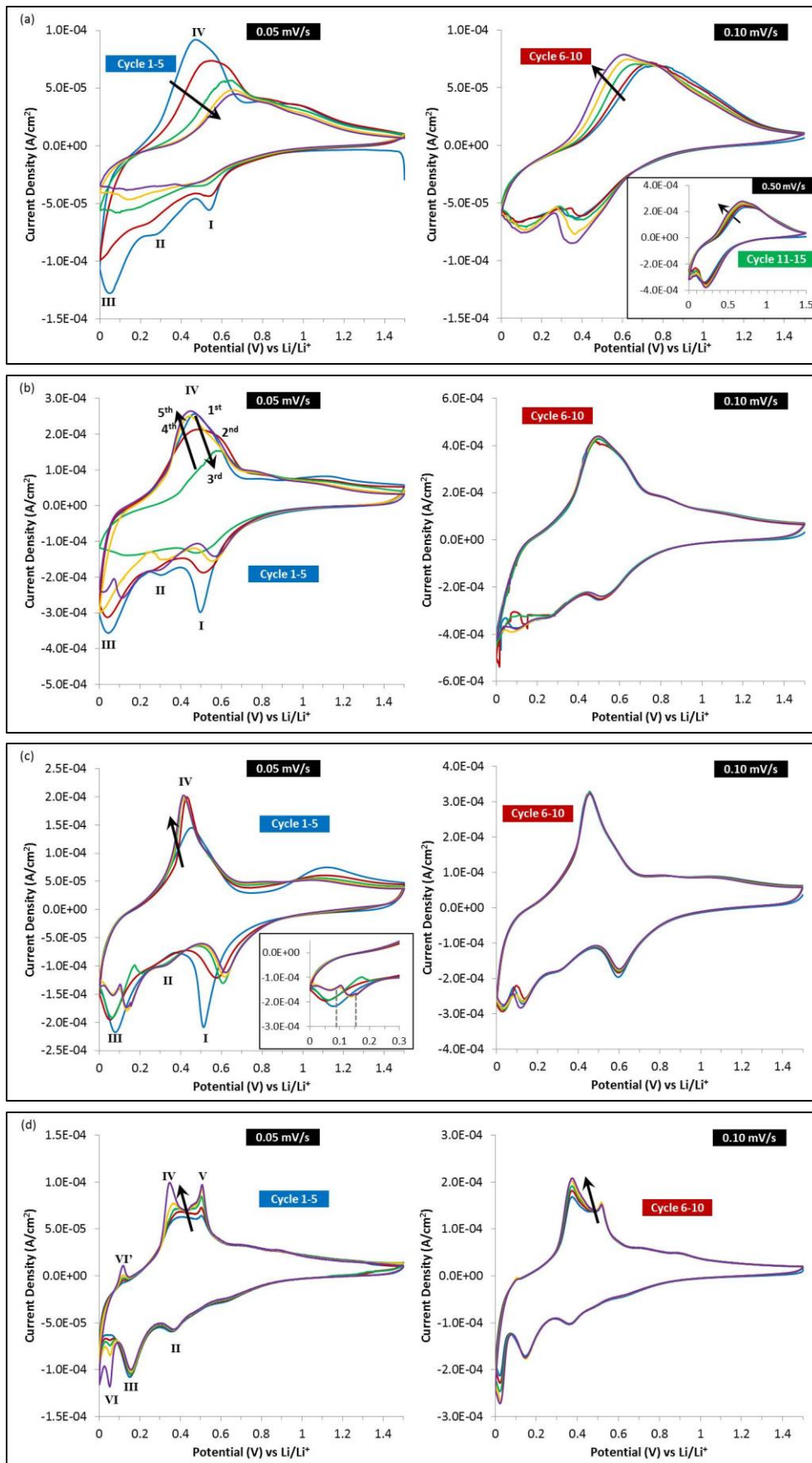
Figure 5.6: CV analysis of the first 1-5 and 6-10 cycles at 0.05 and 0.10 mV/s, respectively for: **a,** 6 min. planar Ge, insterted cycle 11-15 at 0.50 mV/s. **b,** 24 min. 3D Ge, **c,** 12 min. 3D Ge, **d, 6** min. 3D Ge.

174

Figure 5.7, compares CV cycles 16 to 35 at 1.00, 0.50, 0.10 and 0.05 mV/s scan rates each for 5 cycles for 6 min. planar, 24 min. 3D, 12 min. 3D and 6 min. 3D Ge deposits. All deposits show excellent cycle overlap for all scan rates. The final 0.05 mV/s scan rate data for all deposits show the characteristic peaks for Li-Ge de/alloying. It is worth noting that the (I) peak is no longer present for the 6 min. planar and 6 min. 3D samples.

The last 5 cycles compared to the first 5 cycles at 0.05 mV/s for the 6 min. planar sample show a smaller peak separation which indicates improved charge transfer and a decrease in overpotential. An SEM image of 6 min. planar Ge sample after the full range of CV cycling in Figure 5.8 shows the formation of islands that look similar to a porous network that was reported during the cycling on a 90 nm planar Ge thin-film electrode[13]. The formation of a porous network is due to the fast rate of Li^+ extraction from the electrode that produces vacancies to form pores[10]. This means the initial cycles are needed to form a stable 3D Ge porous structure for planar Ge thin-film electrodes.

As mentioned above, Figure 5.6d, the appearance of the redox couple peak, due to overlithiation of the crystalline $Li_{15}Ge_4$ phase, is seen in Figure 5.7d for the 6 min. 3D sample CV cycles at scan rates of 0.05 and 0.10 mV/s. The appearance of the (V) anodic peak at 0.51 V indicates the delithiation of crystalline Li_xGe. The (VI) cathodic peak also begins to appear for the 12 min. 3D sample during the 0.05 mV/s cycles in Figure 5.7c.
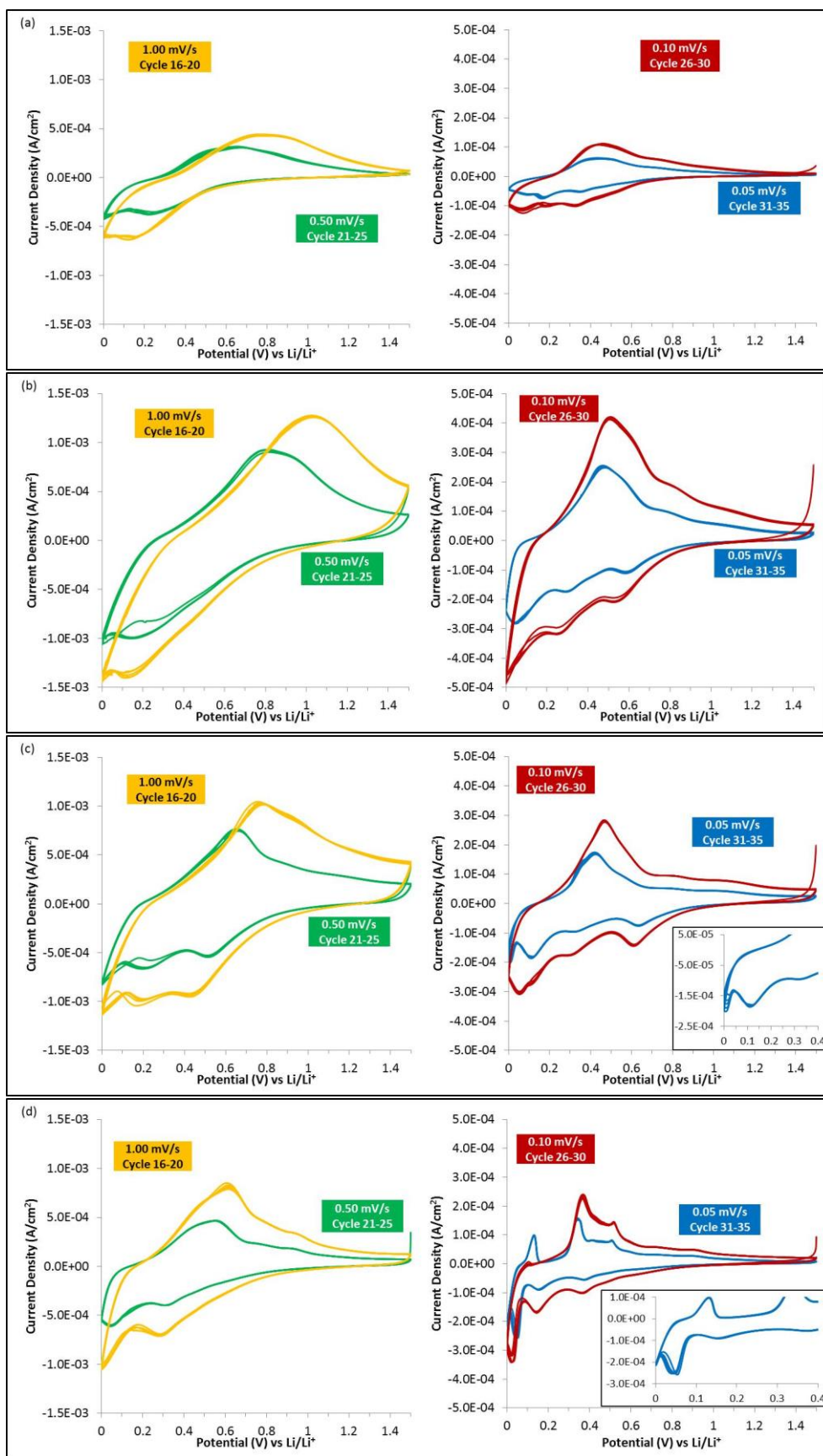
Figure 5.7: CV analysis of cycles 16-20, 21-25, 26-30 and 31-35 at 1.00, 0.50, 0.10 and 0.50 mV/s, respectively for: **a,** 6 min. planar Ge, **b,** 24 min. 3D Ge, **c,** 12 min. 3D Ge, inserted potential range 0.4-0.0 V. **d,** 6 min. 3D Ge, inserted potential range 0.4-0.0 V.

176
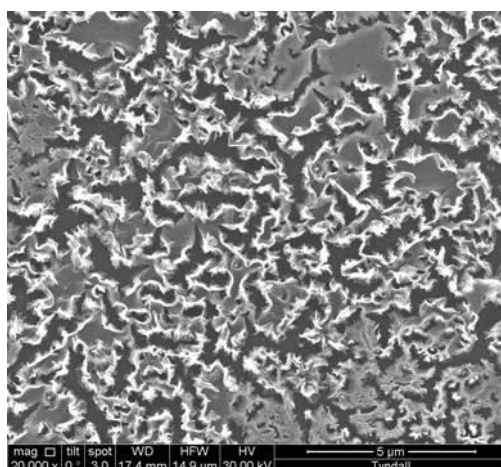
Figure 5.8: SEM image of 6 min. planar Ge after CV cycling.

The (IV) anodic peak potential increases with increasing scan rate due to an increase in overpotential for all samples, Figure 5.9. For the Ge deposition onto the 3D Cu nanotubes the difference in peak potential between the fastest and slowest scan rate is largest for the 24 min. 3D sample and smallest for the 6 min. 3D as expected since there is less material on the 3D resulting in a shorter diffusion distance. The 6 min. planar Ge deposit has a slightly larger difference in peak potential than the 12 min. 3D sample indicating that the 12 min. 3D sample with double the deposition time has similar rate capabilities to the 6 min. planar sample.
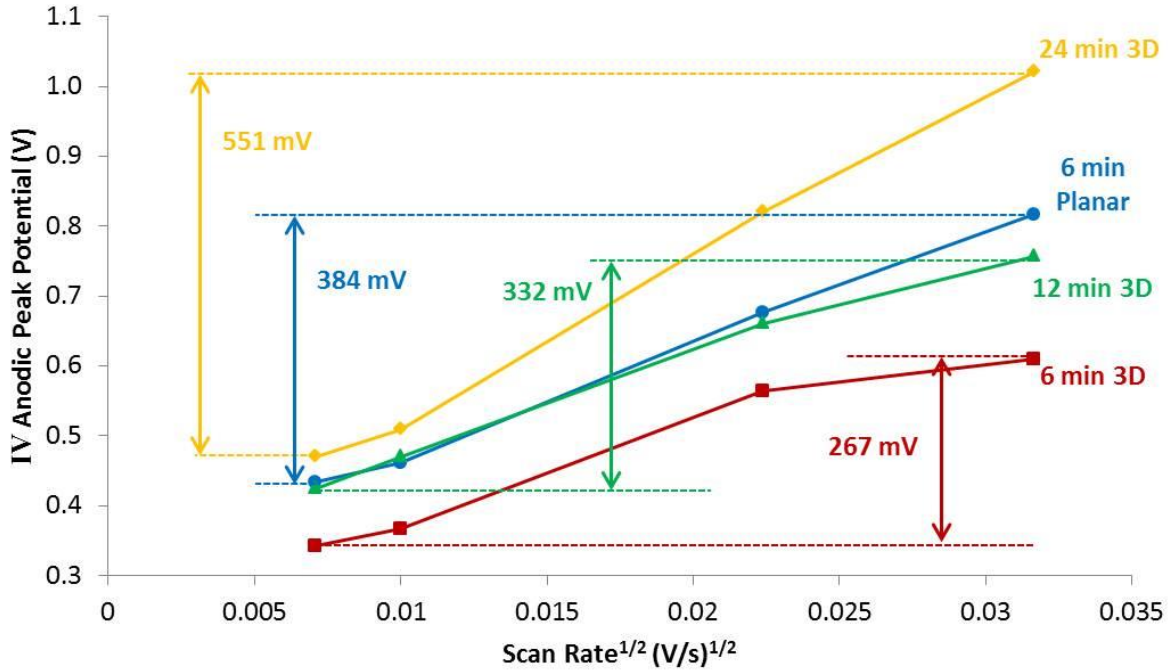
Figure 5.9: Peak shift. Comparison of IV peak potential trend with increasing scan rate.

Figure 5.10 shows the effect on capacity that a 3D substrate has by comparison with a planar substrate for the same Ge deposition time. The quantity of the 6 min. planar sample was calculated by using the area of the exposed electrode to the electrolyte and the average thickness of the Ge deposit (225 nm). Impressive capacity values of 695, 928, 1359 and 1498 mAh/g due to the formation of porous Ge island were obtained for the 6 min. planar Ge sample after stabilisation at 1.00, 0.50, 0.10 and 0.05 mV/s, respectively, equivalent to areal capacities of 83, 111, 163 and 176 μAh/cm^2. The thickness of the 6 min. 3D Ge sample is difficult to obtain due to the architecture of the Cu nanotube so the areal capacity values are used to compare planar and 3D deposits. The areal capacity of the 6 min. 3D Ge sample was 127, 146, 224 and 264 μAh/cm^2 for scan rates of 1.00, 0.50, 0.10 and 0.05 mV/s, respectively. This is an increase of 44 (153%), 35 (132%), 61 (138%) and 85 (147%) μAh/cm^2 for scan rates of 1.00, 0.50, 0.10 and 0.05 mV/s, respectively. The increase in areal capacity is due to more active material per area due to the 3D geometry of the Cu nanotubes and overlithiation of the crystalline $Li_{15}Ge_4$ phase (VI/VI') indicated in Figure 5.6d and Figure 5.7d.
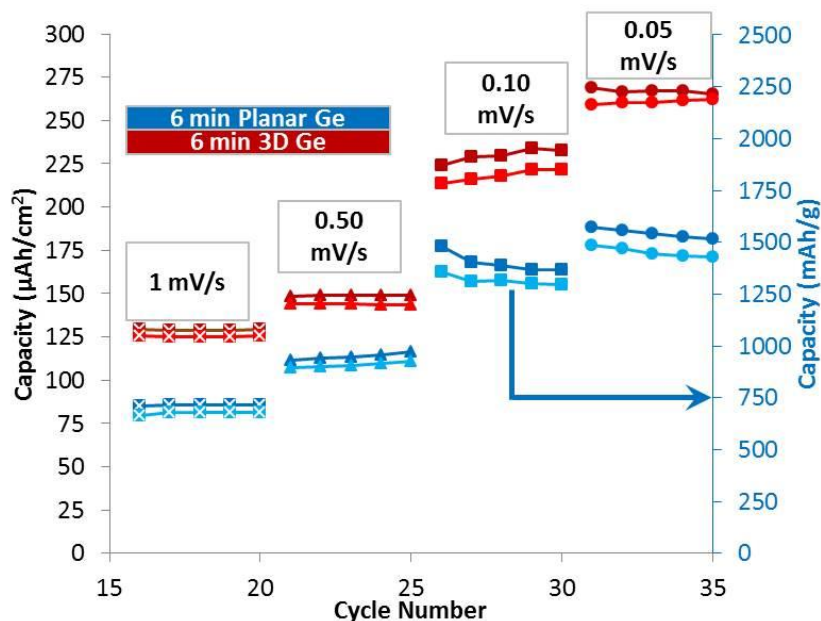
Figure 5.10: Comparison of the capacities for a planar and 3D substrate with a 6 min. Ge deposition time at scan rates of 1, 0.50, 0.10 and 0.05 mV/s. The blue y-axis is the capacity in mAh/g for the 6 min. planar Ge.

A comparison of the areal capacity for all the samples is shown in Figure 5.11. Doubling the deposition time, on the Cu nanotubes, from 6 min. to 12 min. results in an areal capacity increase of 163% for the slower scan rate of 0.05 mV/s. There is little change in the capacity increase percentage of 157% for a scan rate of 1.00 mV/s which is 20 times faster. Ideally the percentage increase should be 200% however, as noted from the CV in Figure 5.7c, there is minimal contribution from the over lithiation crystalline $Li_{15}Ge_4$ and the increase in film thickness on the 3D geometry explains why the ideal percentage increase is not reached. Quadrupling the deposition time, to 24 min., results in a capacity increase of 260% at 0.05 mV/s scan rate. However, the faster scan rate of 1.00 mV/s results in a smaller increase of 194%. The reason for the smaller increase in capacity at the higher scan rate for the 24 min. 3D Ge sample is due to the increase in material per area that resulted in the formation of a planar thin film on top on the Cu nanotubes seen in Figure 5.4d rather than a conformal coating. The thin-film of Ge formed on the Cu nanotubes negates the advantages associated with the 3D geometry over a planar geometry and the electrode acts more like a 2D thin-film electrode with the associated capacity limitations.

179
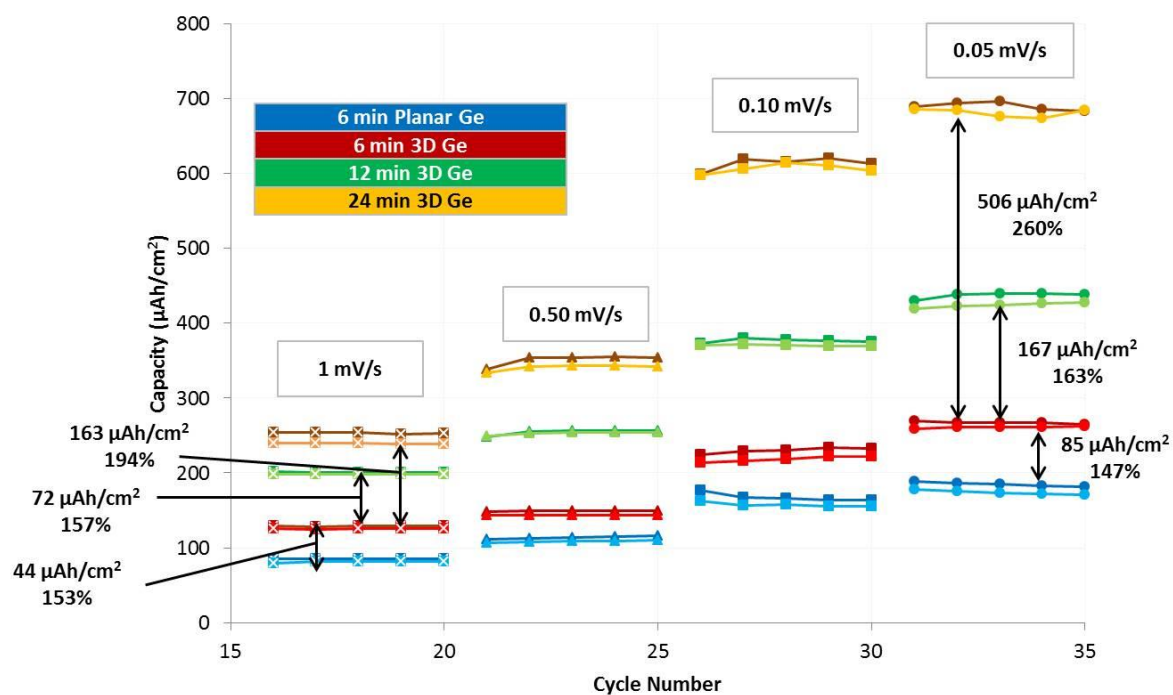
Figure 5.11: Capacity comparison at scan rates of 1, 0.50, 0.10 and 0.05 mV/s for the 6 min. planar Ge, 6 min. 3D Ge, 12 min. 3D Ge and 24 min. 3D Ge samples.

The same 6, 12 and 24 min. 3D Ge samples used for the CV analysis were used for galvanostatic cycling at constant current. The 6 min. 3D Ge sample was cycled 5 times at currents of 20, 30, 50, 75, 50, 30, 20 μA. Figure 5.12a shows the galvanostatic profile of the 3rd cycle for each applied current and an inserted graph of the capacity per cycle number. There is a difference in the galvanostatic profiles between the lower current of 20 and 30 μA and the higher currents of 50 and 75 μA. Close to the voltage cut-off during lithiation there is a slight increase in the potential for a short period that then begins to decrease again for the lower currents with a corresponding plateau during delithiation at 0.30 V. This loop at the end of the lithiation profile and additional plateau in the delithiation profile are attributed to the excess lithiation of the $Li_{15}Ge_4$ that was also seen in the CV profile (Figure 5.7d) at slower scan rates. The loop and additional plateau are not present for the higher currents of 50 and 75 μA which explains why the drop in capacity for the 30 (190 μA/cm^2) to 50 μA (137 μA/cm^2) currents is larger than that for the 50 to 75 μA (125 μA/cm^2). There is an increase in the potential at higher currents as expected however the increase is minimal (20 μA, 0.35 V and 75 μA, 0.45 V).

The galvanostatic profiles for the 3rd cycle of each current applied to the 12 min. 3D Ge and 24 min. 3D Ge samples are shown in Figure 5.12b and Figure 5.12c, respectively. The rate capabilities of the samples were investigated by cycling at each current for 5 cycles at

currents of 30, 50, 80, 120, 80, 50, 30 µA and 50, 80, 110, 160, 110, 80, 50 µA, for the 12 min. 3D Ge and 24 min. 3D Ge samples, respectively. The drop in capacity is more consistent with the change in current for the 12 min. 3D Ge and 24 min. 3D Ge samples and there is no loop at the end of the discharge curve and additional plateau seen in the 6 min. 3D Ge sample, (Figure 5.12a). The drop in potential at higher currents is larger for both samples in comparison to the 6 min. 3D Ge sample due to the increase in the quantity of material per area which increases in the resistance and causes an increase in overpotential.

Figure 5.12: Galvanostatic profiles with capacity data galvanostatic profiles: **a,** 6 min. 3D Ge, **b,** 12 min. 3D Ge, **c,** 24 min. 3D Ge.

Previous studies have shown that Ge electrodes can be discharged at high currents while maintaining high and stable capacities if charged at low currents[2a, 3b, 11a]. The charge current was kept constant at 20 µA for all cycles while the discharge currents used were 200, 300, 500, 750 and 20 µA for 5 cycles per current. The capacities obtained for the high discharge currents while maintaining a characteristic profile are impressive, with values of 146, 12, 99 and 81 µAh/cm^2 for currents of 200, 300, 500 and 750 µA, respectively, indicating fast Li$^+$ ion transport within the 6 min. 3D electrode, Figure 5.13a. Assuming the same amount of Ge was deposited onto the 6 min. 3D sample as the 6 min. planar (225 nm) then the discharge currents used would be equivalent to 3.6C (16 min.), 5.5C (11 min.), 9.1C (7 min.) and 13.7C (4 min.) for 200, 300, 500 and 750 µA, respectively. At larger discharge currents and a small charge current for the 12 min 3D, Figure 5.13b and 24 min 3D, Figure 5.13c, Ge samples the drop in capacity becomes more prominent with increasing current. The difference between the capacity at a discharge current of 750 µA for the 12 min. 3D Ge (121.05 µAh/cm^2) and 24 min. 3D Ge (144.37 µAh/cm^2) is 23.32 µAh/cm^2 and relatively small when considering the deposition time was doubled, indicating that a significant amount of the deposited Ge is not utilised for the 24 min. 3D Ge sample.
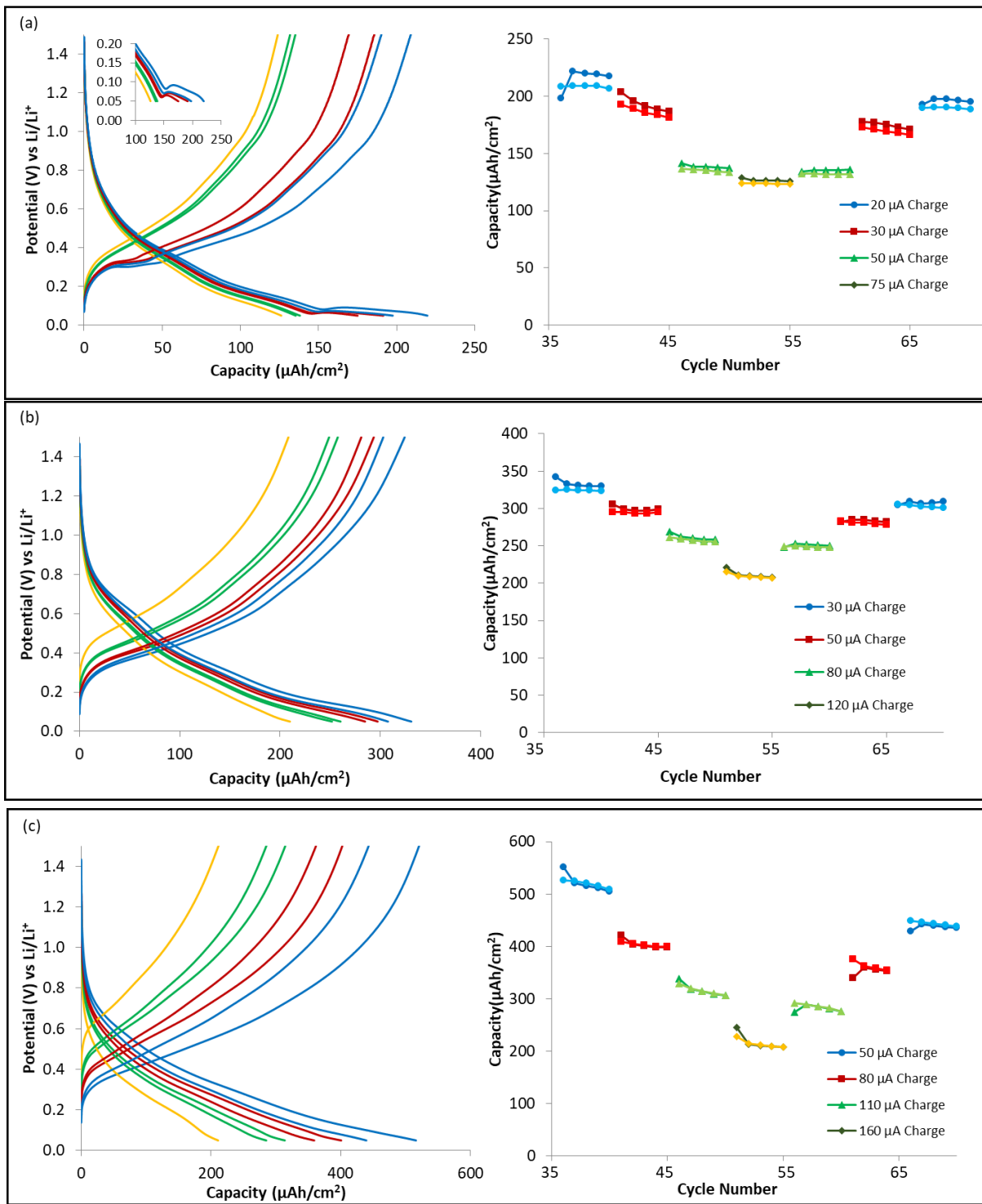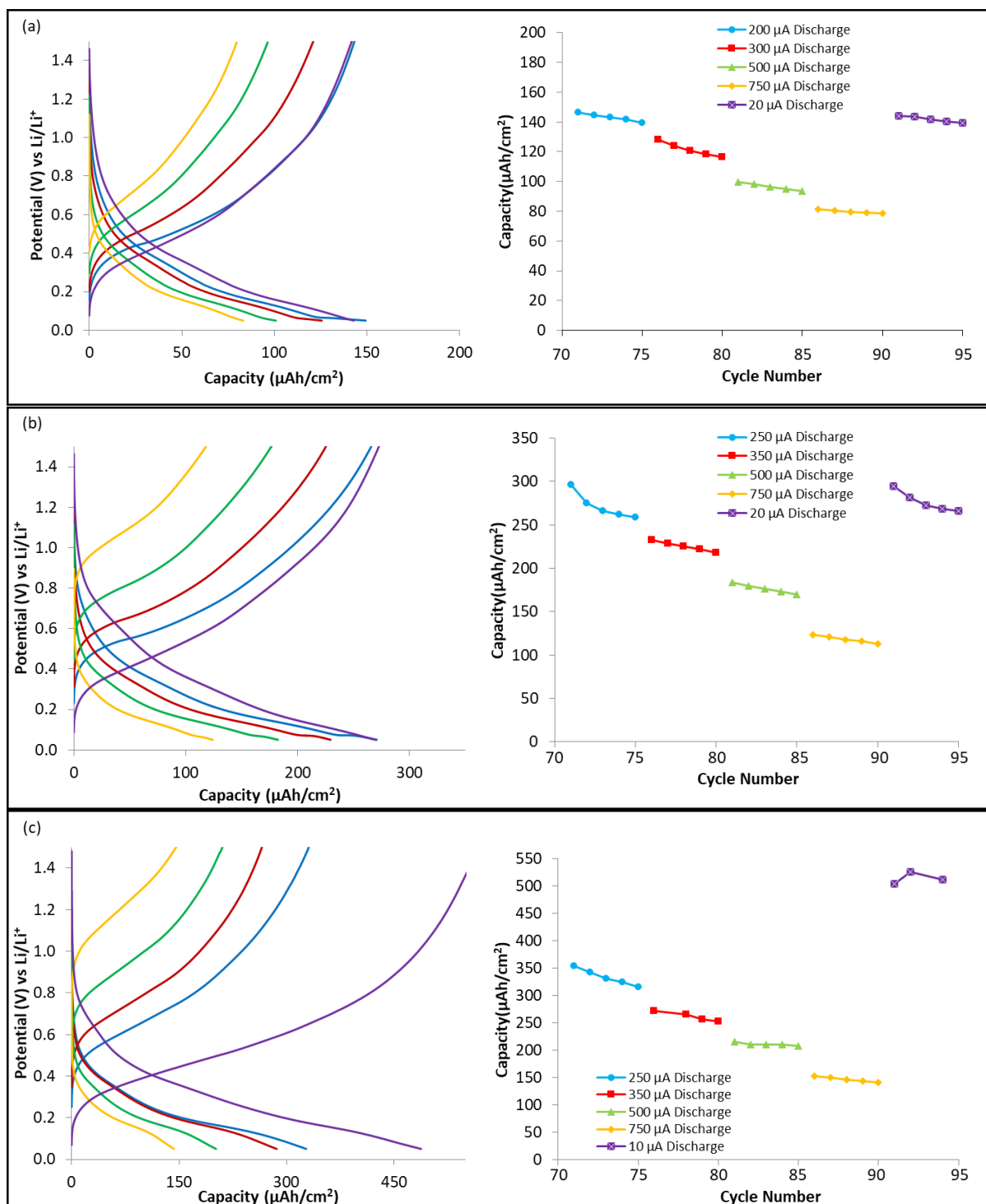
Figure 5.13: Galvanostatic profiles with capacity data galvanostatic profiles: **a,** 6 min. 3D Ge, **b,** 12 min. 3D Ge, **c,** 24 min. 3D Ge.

The chemical diffusion coefficient (D_{Li}) of Li in Ge was measured using GITT with a 20 μA pulse for 10 min. followed by a rest period of 10 min. and Equation 5.1[20].

$$D_{Li} = \frac{4}{\pi\tau}\left(\frac{n_m V_m}{S}\right)^2 \left(\frac{\Delta E_s}{\Delta E_t}\right)^2 \qquad\qquad 5.1$$

τ is the duration of the current pulse (s); n_m is the number of moles of electrode material (mol); V_m is the molar volume of the electrode material (cm^3/mol); S is the electrode/electrolyte contact area (cm^2); ΔE_s is the steady-state voltage change due to the current pulse and ΔE_t is the voltage change during the current pulse having addressed the iR drop, Figure 5.14. Ge has two D_{Li} depending on the Li concentrations, at low concentration and high concentrations the D_{Li} measured was 2×10^{-10} cm^2/s and 8×10^{-12} cm^2/s, respectively, which is in agreement with values reported in the literature[6]. Four point probe conductivity measurements gave a value of 1×10^{-2} S/cm which is in the same order of magnitude as bulk Ge, ~ 10^{-2} S/cm and one order higher than Ge nanowires reported in the literature[21].
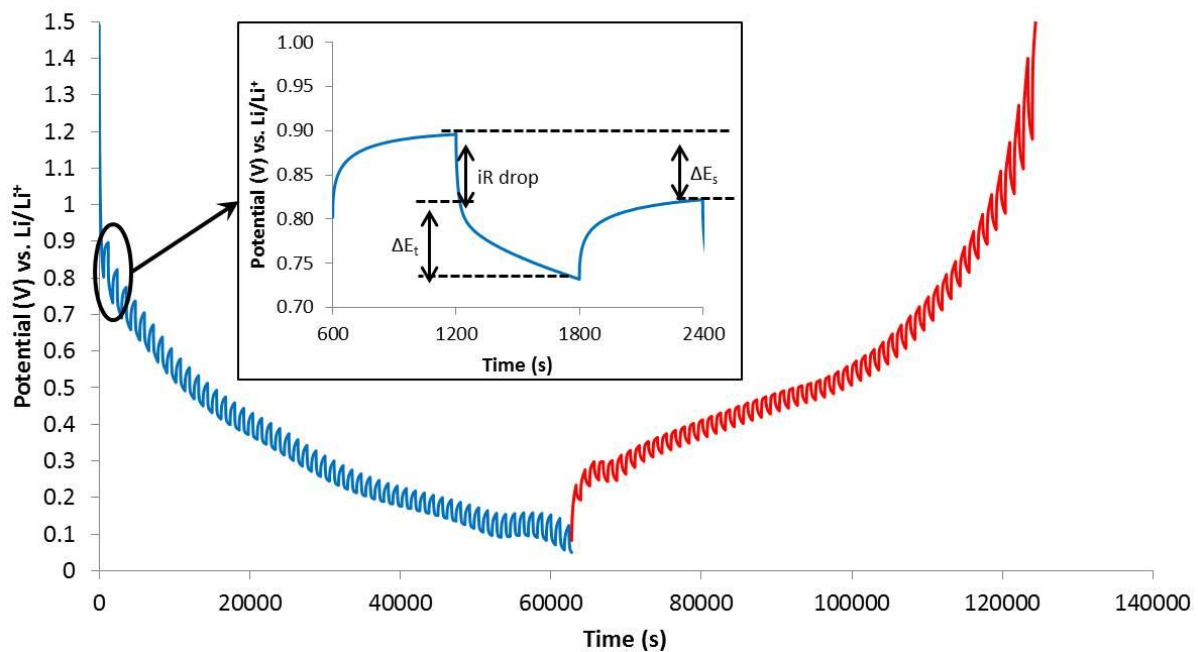
Figure 5.14: GITT profile (20μA charge/discharge and rest for 10 min squarewave) for charging and discharging used to calculate Li^{+} ion diffusion coefficient in Ge. Inset is a magnified image of how ΔE_t and ΔE_s are calculated from the GITT profile.

RTA was investigated as a way of improving adhesion of the Ge to the Cu to form a stable interface during cycling and to improve cycle life and capacity by preventing delamination of Ge commonly seen for high capacity alloying electrodes. Since both Cu and Ge are consumed during the formation of Cu_3Ge, with a conversion ratio of 1:1.55 for Cu:Cu_3Ge, Cu

needs to be the limiting material in the reaction in order to ensure that the Li^+ ion active Ge is not consumed. Newly formed Cu_3Ge can delaminate from Si substrates during formation and so to improve adhesion to the Si wafer the initial Cu current collector was deposited onto a Ni coated Si wafer with a Ti adhesion layer. Cu only alloys with Ni at temperatures above the annealing temperature of Cu/Ge bilayer and is non-reactive with Li. As the 200 nm Cu is the limiting material and is expected to be fully consumed during RTA to form 307 nm layer of Cu_3Ge with 128 nm of the 470 nm deposited Ge also consumed meaning 342 nm of active Ge anode material should remain. However, for the purposes of this experiment the capacity measured is in relation to the initial amount of Ge deposited as no quantitative composition analysis were performed on this sample.

XRD and Raman analysis were performed on a stack of Si/Ti/Cu/Ge that was subjected to RTA at 500°C in vacuum with the Cu deposit being the limiting material. The data confirms the presence of Ge while also highlighting its conversion from amorphous to crystalline in Figure 5.15.
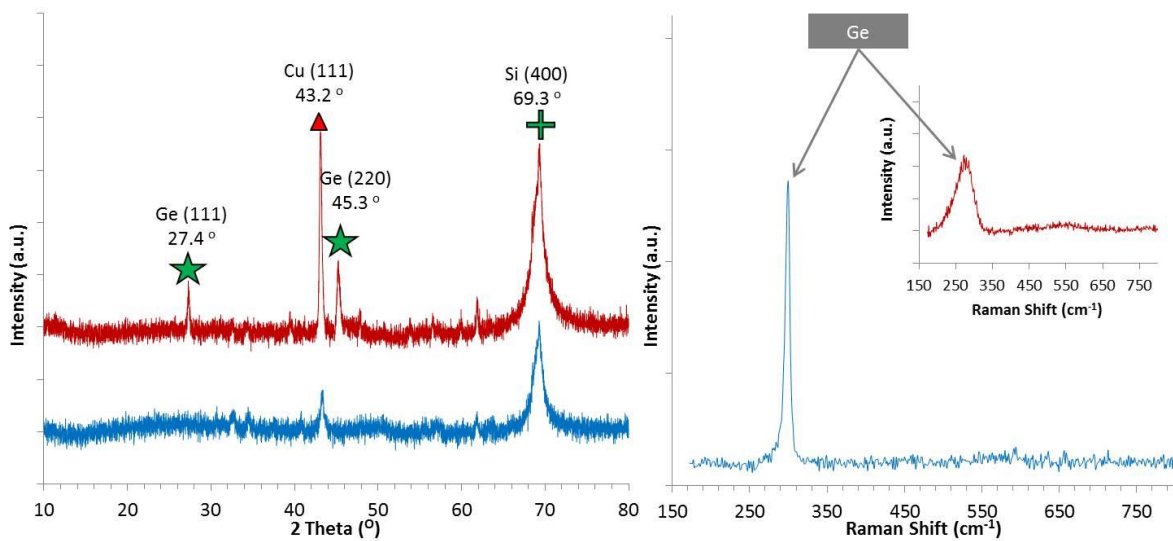
Figure 5.15: XRD and Raman analysis of 470 nm Ge deposited onto Cu prior (blue) and post RTA at 500°C (red).

Figure 5.16 shows the capacity obtained after CV cycling at scan rate of 0.05, 0.10, 0.50 and 1.00 mV/s and that the capacity begins to increase after 37 cycles. The improved adhesion to the substrate allows numerous cycles without severe capacity loss. The SEM image of the sample after cycling, Figure 5.17, highlights the formation of a porous structure which explains the improved capacity after the initial cycling and cycle stability thereafter as the improved adhesion allows for the formation of a 3D nanoporous structure. This increases the

surface area and amount of Ge material exposed to the electrolyte and availability for lithiation, therefore increasing the capacity. The 6 min. Ge deposit on planar Cu is almost half the thickness of the RTA sample and would therefore be expected to have a longer cycle life before capacity fade. The improved capacity with cycling of the RTA sample is in contrast to the 6 min. planar Ge deposit where the capacity starts to decrease after 26 cycles, Figure 5.10. A comparison of the SEM images after cycling indicate the improved adhesion for the RTA sample due to the formation of a porous structure, while the 6 min. planar Ge deposit surface cracks with the forms islands, Figure 5.8, which can result in delamination of Ge from the current collector.
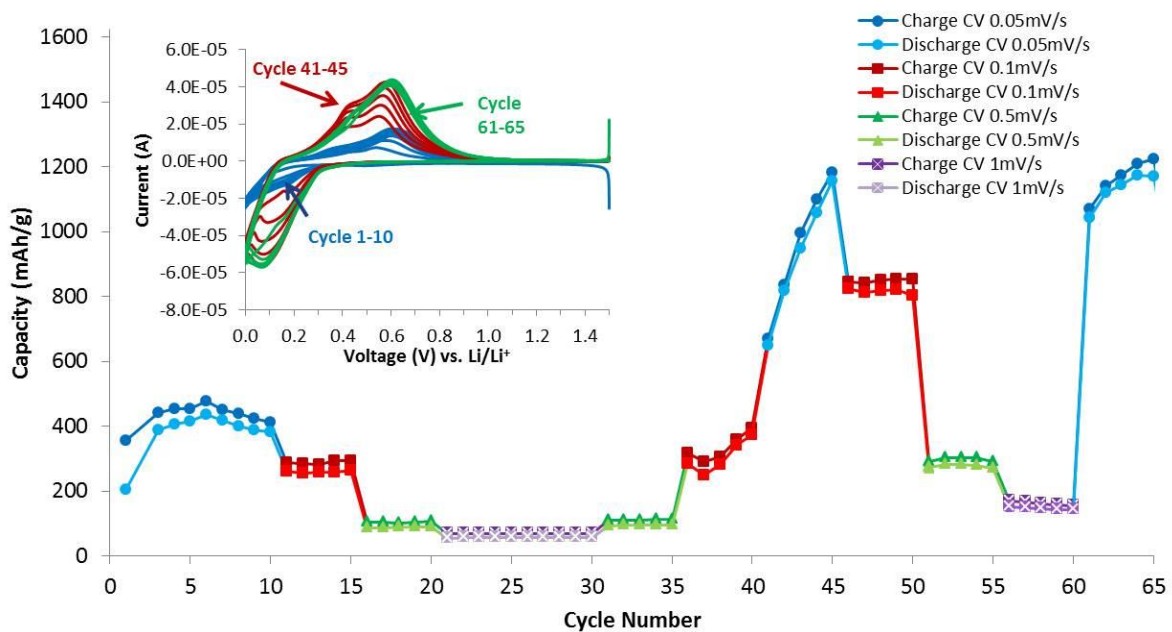
Figure 5.16: Capacity for a 470 nm Ge RTA sample at scan rates of 0.05, 0.10, 0.50 and 1.00 mV/s. Inset are the CV's at a 0.05 mV/s scan rate for cycles 1-10, 41-45 and 61-65.
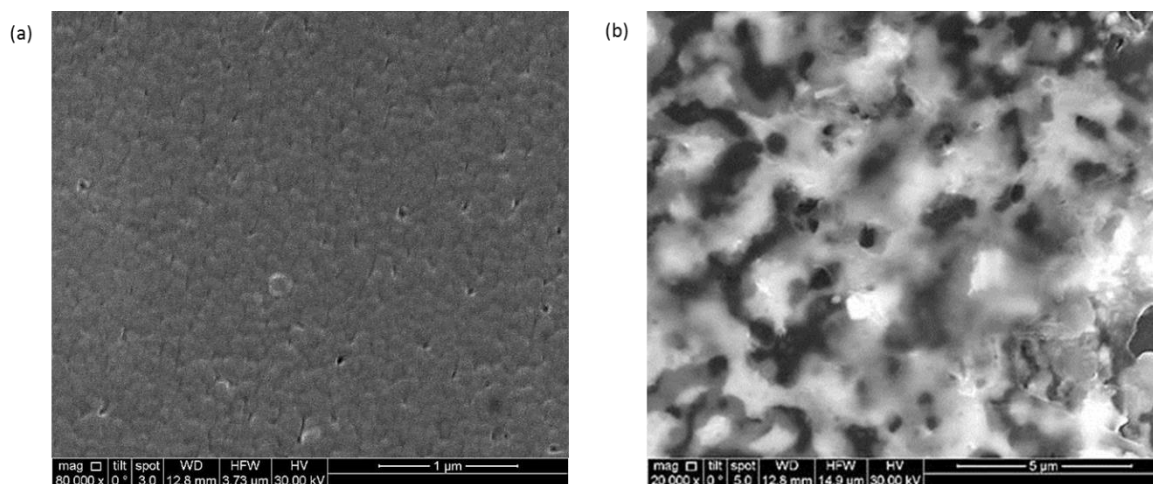
Figure 5.17: SEM image of 470 nm Ge RTA (a) before and (b) after CV cycling.

Conclusion

In summary, a 3D core-shell Cu/Ge nanowire was fabricated by DC sputtering Ge onto Cu nanotubes. When used as a lithium ion anode and compared with the same Ge deposition time upon a planar Cu substrate an increase in capacity of 153% is seen with improved rate capabilities. The nano-film planar deposit shows good capacity and cycle efficiency once a nanoporous-like structure is formed. Deposition upon a 3D Cu nanotube substrate means a thinner Ge can be utilised that results in improved rate capabilities due to shorter Li^+ ion diffusion lengths and mechanical stability due to the space around the nanotubes which afford Ge space to 'breathe'. They also ensure a larger mass loading i.e. increase in the quantity of Ge per area due to the nature of the 3D nanotubes. This structure results, in a delithiation peak which has not been reported to date, to the best of our knowledge, which we have attributed to the delithiation of the crystalline $Li_{15}Ge_4$ phase that was initially excessively lithiated. This suggests that not only is there an increase in the mass loading by comparison with a similar deposit upon a planar sample but also the ability to excessively lithiate the crystalline $Li_{15}Ge_4$ phase results in an increase in capacity.

RTA annealing of Ge on a planar Cu substrate has been shown to form a nanoporous-like structure during lithium cycling. This is thought to be due to the improved adhesion which permits Ge to form such a structure rather than delaminate and results in an increase in capacity rather than a decrease with increasing cycle number. Further study is required to understand the exact changes the sample undergoes both during RTA and lithium cycling. Future recommended work would include quantitative material analysis (TEM) at the Cu/Ge interface after RTA while also measuring the adhesion strength and varying the RTA

temperature in order to find the optimal parameters that give the best electrochemical performance with minimal Ge consumption. In-situ SEM cycling would also be recommended in order to observe the changes in morphology during lithiation/delithiation as a result of the improve adhesion.

References

[1]   a) C. K. Chan, X. F. Zhang, Y. Cui, *Nano Lett.* **2008**, *8*, 307-309; b) C. K. Chan, H. Peng, G. Liu, K. McIlwrath, X. F. Zhang, R. A. Huggins, Y. Cui, *Nat. Nanotechnol.* **2007**, *3*, 31; c) L. Pan, H. Wang, D. Gao, S. Chen, L. Tan, L. Li, *Chem. Commun.* **2014**, *50*, 5878-5880.

[2]   a) J. Graetz, C. C. Ahn, R. Yazami, B. Fultz, *J. Electrochem. Soc.* **2004**, *151*, A698-A702; b) D. Wang, Y.-L. Chang, Q. Wang, J. Cao, D. B. Farmer, R. G. Gordon, H. Dai, *J. Am. Chem. Soc.* **2004**, *126*, 11602-11611.

[3]   a) C.-M. Park, J.-H. Kim, H. Kim, H.-J. Sohn, *Chem. Soc. Rev.* **2010**, *39*, 3115-3141; b) A. M. Chockla, K. C. Klavetter, C. B. Mullins, B. A. Korgel, *ACS Appl. Mater. Interfaces* **2012**, *4*, 4658-4664.

[4]   X. H. Liu, J. W. Wang, S. Huang, F. Fan, X. Huang, Y. Liu, S. Krylyuk, J. Yoo, S. A. Dayeh, A. V. Davydov, S. X. Mao, S. T. Picraux, S. Zhang, J. Li, T. Zhu, J. Y. Huang, *Nat. Nanotechnol.* **2012**, *7*, 749.

[5]   W. Liang, H. Yang, F. Fan, Y. Liu, X. H. Liu, J. Y. Huang, T. Zhu, S. Zhang, *ACS Nano* **2013**, *7*, 3427-3433.

[6]   B. Laforge, L. Levan-Jodin, R. Salot, A. Billard, *J. Electrochem. Soc.* **2008**, *155*, A181-A188.

[7]   L. Baggetto, P. H. L. Notten, *J. Electrochem. Soc.* **2009**, *156*, A169-A175.

[8]   A. Al-Obeidi, D. Kramer, C. V. Thompson, R. Mönig, *J. Power Sources* **2015**, *297*, 472-480.

[9]   M. Hasan, T. Chowdhury, J. F. Rohan, *J. Electrochem. Soc.* **2010**, *157*, A682-A688.

[10]   X. H. Liu, S. Huang, S. T. Picraux, J. Li, T. Zhu, J. Y. Huang, *Nano Lett.* **2011**, *11*, 3991-3997.

[11]   a) T. Kennedy, E. Mullane, H. Geaney, M. Osiak, C. O'Dwyer, K. M. Ryan, *Nano Lett.* **2014**, *14*, 716-723; b) M.-H. Park, Y. Cho, K. Kim, J. Kim, M. Liu, J. Cho, *Angew. Chem. Int. Ed.* **2011**, *50*, 9647-9650; c) I.-S. Hwang, J.-C. Kim, S.-D. Seo, S. Lee, J.-H. Lee, D.-W. Kim, *Chem. Commun.* **2012**, *48*, 7061-7063.

[12]   a) E. Mullane, T. Kennedy, H. Geaney, C. Dickinson, K. M. Ryan, *Chem. Mater.* **2013**, *25*, 1816-1822; b) E. Mullane, T. Kennedy, H. Geaney, K. M. Ryan, *ACS Appl. Mater. Interfaces* **2014**, *6*, 18800-18807.

[13]   N. G. Rudawski, B. R. Yates, M. R. Holzworth, K. S. Jones, R. G. Elliman, A. A. Volinsky, *J. Power Sources* **2013**, *223*, 336-340.

[14]   R. A. Susantyoko, X. Wang, L. Sun, W. Sasangka, E. Fitzgerald, Q. Zhang, *Nano Energy* **2015**, *12*, 521-527.

[15]   Z. Wang, G. Ramanath, L. H. Allen, A. Rockett, J. P. Doyle, B. G. Svensson, *J. Appl. Phys.* **1997**, *82*, 3281-3286.

[16]   a) T. Burchhart, A. Lugstein, Y. J. Hyun, G. Hochleitner, E. Bertagnolli, *Nano Lett.* **2009**, *9*, 3739-3742; b) I. Jyothi, V. Janardhanam, J. Y. Hwang, W.-K. Lee, Y. C. Park, H. C. Kang, S.-N. Lee, C.-J. Choi, *J. Alloys Compd.* **2016**, *655*, 198-202; c) O.

B. Chae, S. Park, J. H. Ku, J. H. Ryu, S. M. Oh, *Electrochim. Acta* **2010**, *55*, 2894-2900.

[17]   a) R. A. DiLeo, S. Frisco, M. J. Ganter, R. E. Rogers, R. P. Raffaelle, B. J. Landi, *J. Phys. Chem. C* **2011**, *115*, 22609-22614; b) S. Fan, L. Y. Lim, Y. Y. Tay, S. S. Pramana, X. Rui, M. K. Samani, Q. Yan, B. K. Tay, M. F. Toney, H. H. Hng, *J. Mater. Chem. A* **2013**, *1*, 14577-14585.

[18]   V. Ho, W. Choi, C. Heng, V. Ng, *Mater. Phys. Mech.* **2001**, *4*, 42-45.

[19]   P. K. Giri, S. Dhara, *J Nanomater* **2012**, *2012*, 1-5, Article No.: 6.

[20]   a) Y. Zhu, C. Wang, *J. Phys. Chem. C* **2010**, *114*, 2830-2841; b) W. Weppner, R. A. Huggins, *J. Electrochem. Soc.* **1977**, *124*, 1569-1578; c) C. J. Wen, B. A. Boukamp, R. A. Huggins, W. Weppner, *J. Electrochem. Soc.* **1979**, *126*, 2258-2266.

[21]   S. Barth, M. M. Koleśnik, K. Donegan, V. Krstić, J. D. Holmes, *Chem. Mater.* **2011**, *23*, 3335-3340.

Chapter 6 Ultra-Fast Cycling of Nanoscale Thin-Film LiCoO₂ Cathode

Abstract

Additive-free nanoscale LiCoO₂ thin-films deposited on Si substrates using DC sputtering show exceptional electrochemical performance due to the unique kinetics of the nanoscale thin-film in an aqueous environment. At extremely high potential cycling scan rates and galvanostatic constant current densities of up to 100 mV/s and 200 C respectively, a capacity retention equivalent to 97 mAh/g (4.8 µAh/cm^2, 48.3 µAh/cm^{2}µm) is obtained. A significant contribution of non-diffusion control in the kinetics of the LiCoO₂ electrode reactions is shown.

Introduction

The 'Internet of Things' scenario envisions billions of wireless sensors acting as the environmental interface to provide data that will, amongst other benefits, reduce analysis costs, improve safety and predict future trends. Non-rechargeable batteries are the predominant energy source for today's commercial wireless sensors and both the energy and power demands dramatically reduce the lifetime of the primary batteries. The value of the useful data gathered is offset by the frequent battery replacement necessitated by their short lifetimes. The ultimate challenge facing the mass distribution of wireless sensors is matching the energy and power requirements to the lifetime of the microdevices[1].

To extend the lifetime, smaller and more energy efficient sensor components and drive electronics are being developed with lower power and energy requirements. Of the available battery technologies Li-ion provides the highest energy density (~270 Wh/kg) which is essential for miniaturisation and device integration[2]. The limitations of typical organic solvent–based Li-ion batteries include a modest cycle life (<1,000) and low power density (<1,000 W/kg) which can hamper device operation particularly during the energy intensive periods of sensor measurement and wireless communication. Hybrid systems comprising a significantly smaller energy storage element coupled to an energy harvester are of interest to enable wireless operation over the lifetime of the device[3].

Microbatteries, such as solid-state Li-ion batteries, present a number of potential advantages in the transition from primary to rechargeable batteries for hybrid powered wireless sensors[4]. They have a larger potential energy density due to the removal of inactive binder and conductive additive materials in the cathodes and they offer the potential for Li metal anodes. The solid-state electrolyte significantly improves cycle life ($\geq$ 5,000)[5]. The drawbacks which have limited their use in commercial systems include the need to maintain thin electrodes (at the micron level) particularly for the low electronic conductivity oxide cathodes typically utilised. A cathode with limited thickness and conductivity in combination with a low ionic conductivity solid-state electrolyte results in poor power capabilities and a significant potential drop can occur during high current operation. A small form factor capable of high current operation is critical in the development of the next-generation hybrid systems. Dedicated micro power management systems are also required to deal with these issues and that of intermittent energy supply from the harvester which can add further volume and complexity to the system[6].

In a typical thin-film microbattery the faradaic reaction and ion transport are primarily controlled by the solid-state diffusion kinetics in the electrode material. Changing the geometry, size and thickness of the electrodes will have a direct effect on the battery capabilities. The current is limited by the ion diffusion in the electrode. Cathodes tend to be the limiting electrode material in batteries due their low electrical conductivity (oxide materials) and lower energy density compared to typical anode materials. 3D architectures with a large aspect ratio coupled to nanoscale films are a possible strategy to enable high currents for a hybrid system[7]. In this strategy the areal energy is primarily dependent on the aspect ratio of the 3D architectures and the areal power on the thickness of the electrodes. Using the approximation[8] for time (τ) to diffuse in a material of dimension l ($\tau \approx l^2/D$), where D is the diffusion coefficient, it can be estimated that the time taken for Li$^+$ to diffuse in typical battery materials of micron dimension will be two to three orders of magnitude longer with a corresponding lower power capability than for a nanoscale ($\leq$ 100 nm) material.

Recent research has shown nanoscale film electrodes are not solely diffusion controlled and that pseudo-capacitive intercalation has a significant contribution on the electrochemical performance[9]. Solid-state and organic electrolytes by comparison with aqueous electrolytes tend to have low ionic conductivity and diffusion characteristics which have a significant effect on cell performance. The high ionic conductivity and diffusion coefficient of an aqueous electrolyte means that the electrochemical performance is primarily dependent upon

the rate of lithiation and delithiation rather than the ion transport in the electrolyte. Analysis of a nanoscale film electrode in an aqueous electrolyte enables the analysis of the electrode performance without the resistive complications of an organic or solid state electrolyte.

The concept of aqueous rechargeable Li-ion batteries was first introduced in 1994 with the use of $LiMn_2O_4$ and $VO_2(B)$ giving a cell potential of 1.5 V for 25 cycles[10]. This smaller potential window limits the suitable electrode materials. One of the most common cathode materials, $LiCoO_2$ (3.9 V vs Li^+/Li) used in organic systems can also be utilised in aqueous systems[11]. As with organic electrolytes side reactions due to the aqueous environment can complicate the lithium intercalation reaction mechanism[12]. As described in a recent review the number of papers published on aqueous lithium battery systems has increased tenfold over a ten year period[13]. While the research into thin-film $LiCoO_2$ has been thorough in organic and solid state electrolytes, there has been limited analysis for aqueous electrolytes. The majority of analysis on $LiCoO_2$ in an aqueous electrolyte has been directed towards bulky composite electrodes[14]. Such electrodes are porous and contain inactive additives unlike the solid-state thin film materials required for high-power microbatteries.

The nanoscale $LiCoO_2$ thin-films described here were deposited using standard DC sputter processing appropriate for thin film microbattery applications. An aqueous electrolyte is used to investigate the electrochemical properties of a nanoscale $LiCoO_2$ thin-film in order to ensure the performance of the electrochemical cell is solely dependent on the electrode and not influenced by the resistive electrolytes typically used in the investigation of Li-ion electrodes. Cyclic voltammetry and galvanostatic cycling demonstrated charging in less than 18 s, and similarly discharging in the same timeframe, without altering the characteristic electrochemical profile of $LiCoO_2$.

Experimental

$LiCoO_2$ was deposited, using a $LiCoO_2$ (99.9% purity) sputter target (Kurt J. Lesker) over the substrate at a pressure and current of $5x10^{-3}$ mBar and 150 mA, respectively. The $LiCoO_2$ target was cleaned prior to deposition by pre-sputtering for 15 minutes. Deposition was performed in an Ar environment and deposit thickness monitored using a quartz-crystal monitor system. Deposition thickness values were confirmed using a surface profilometer (Tencor alpha-step 200). DC sputtered $LiCoO_2$ is amorphous and is crystallised using rapid thermal annealing (RTA) (Jipelec 150) which has not been investigated previously for

aqueous $LiCoO_2$ cathode systems. RTA offers a short operational time and lower energy consumption by comparison with a furnace.

$LiCoO_2$ was deposited on the following substrates to examine their effect on the material and electrochemical characteristics of $LiCoO_2$ and determine if the substrate was compatible with the RTA process.:

Sample Number	Substrate
1	Borosilicate glass slide
2	Borosilicate glass slide/Ni
3	$Si/SiO_2/Ni$
4	$Si/SiO_2/Al$
5	$Si/SiO_2/Pt$
6	Borosilicate glass slide/Au
7	$Si/SiO_2/Au$
8	$Si/SiO_2/Ni/TiO_2/Au$
9	$Si/SiO_2/NiO/Au$
10	$Si/SiO_2/NiO/TiO_2/Au$

All deposits on borosilicate glass slides or Si wafers with a 1 µm thermal annealed SiO_2 utilised metal sputter targets (Kurt J. Lesker) in a DC magnetron (Quorum Q300T D Dual) sputter coating system. For all Si/SiO_2 wafer samples a Ti (10 nm) layer was deposited to act as an adhesion layer between the SiO_2 substrate and current collector. Au, Pt, Al and Ni were also studied as possible current collectors. The NiO and TiO_2 metal oxides were deposited by DC sputtering either Ni or Ti and RTA in an O_2 environment.

The structure and the morphology of the samples were analysed with a scanning electron microscope (FEI Nova 630 Nano-SEM) coupled with an energy dispersive X-ray (EDX)

(Hitachi S4000). Transmission electron microscopy (TEM) (was performed using a JEOL 2100 High Resolution TEM), For X-ray diffraction (XRD) a Philips PW3710-MPD with Cu Kα radiation, l = 1.54056 Å, at 45 kV (40 mA) was used and data analysed using Philips X'Pert XRD software). Raman spectroscopy was performed with a Renishaw Invia, 514 nm laser.

Electrochemical measurements were controlled using a CH Instruments 660B potentiostat and a three electrode cell. Cyclic voltammetry (CV) was performed on the $LiCoO_2$ cathode over the potential window of 0.45 to 1.05 V against a saturated calomel electrode (SCE). Galvanostatic cycling was carried out in a potential window of 0.25 to 1.05 V vs SCE at C-rates of 3, 5, 10, 20, 50, 100 and 200 C in which 1 C is equivalent to $LiCoO_2$ being either fully charged or discharged (137 mA/g) within 1 hour. The electrolyte was 5 M $LiNO_3$ aqueous solution at a pH of 7 purged with N_2 gas prior to cycling to reduce the amount of dissolved oxygen.

Delithiated $LiMn_2O_4$ was utilised as the counter electrode. A high concentration of $LiNO_3$, neutral pH and little or no dissolved O_2 is critical to remove/suppress the side reactions that are associated with aqueous electrolytes[13]. The use of delithiated $LiMn_2O_4$ as a counter electrode rather than a metal counter, (e.g. Pt), is required to achieve stable electrochemical behaviour for extended cycling[13, 14b, 14e, 15]. A metal counter electrode would have no storage capacity for the Li^+ extracted from the working electrode and would most likely evolve gas as the counter electrode reaction perturbing the electrolyte composition. The delithiated $LiMn_2O_4$ allows for Li^+ to cycle between the electrodes and operates without any significant changes to the chemical or physical properties of the electrolyte. The electrochemical measurements were carried out under ambient air and at 21 °C.

Results and discussion

Raman and XRD analysis were predominately used to characterise the $LiCoO_2$ film after annealing in an RTA oven to 600 °C for 3 min with a ramp up of 10 °C/s. A borosilicate glass slide was first used as a substrate in order to minimise any possibility of interlayer diffusion and RTA was either performed in an Ar or O_2 environment. As shown in Figure 6.1 the RTA atmospheric environment has little effect on the material characteristics while the spectrum profile indicates that the RTA of $LiCoO_2$ on a borosilicate glass slide substrate results in the formation of Co_3O_4 rather than crystalline $LiCoO_2$[16].
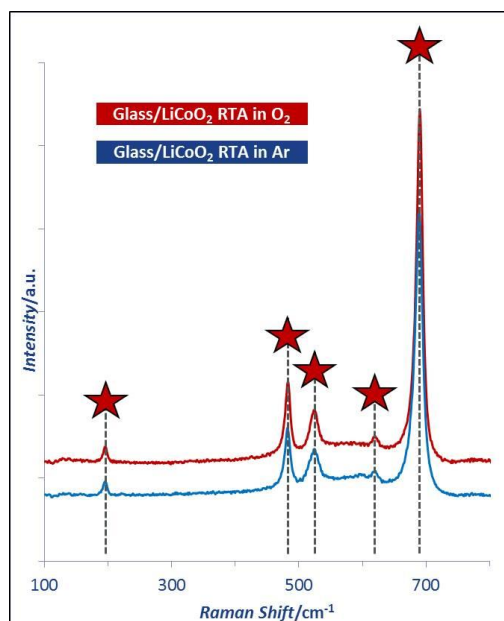
Figure 6.1: Raman spectrum of rapid thermal annealed (RTA) 100 nm LiCoO$_2$ film to 600°C on a borosilicate glass slide on both an O$_2$ and Ar environment for 3 min.

Figure 6.2a also indicates that Ni is not suitable as a current collector as the large broad peak at 510 cm^{-1} indicates the formation of Li$_2$O while the Co$_3$O$_4$ peak is also present at 665 cm^{-1}, with both being inactive Li-ion by-products of LiCoO$_2$ XRD analysis inserted in Figure 6.2 shows that the deposited Ni current collector is crystallised in the Ar RTA environment and is converted to NiO in an O$_2$ environment at 600°C. Crystalline Ni peaks are indicated at 44.5° (111) and 52.0° (200) while NiO peaks are seen at 37.3° (111) and 43.3° (200). A stepwise approach was utilised on a Si/SiO$_2$/Ni/LiCoO$_2$ substrate to minimise the effect a rapid ramp-up could have on the Ni/LiCoO$_2$. Figure 6.2b shows a Raman spectrum of the results from an RTA with a stepwise ramp up of 50 °C steps with a 60 s hold. The lower starting ramp-up temperature results in a sharper Li$_2$O peak. All spectra show a sharp Si peak at 520 cm^{-1} which suggests aggregation of the Ni current collector to expose the Si substrate.
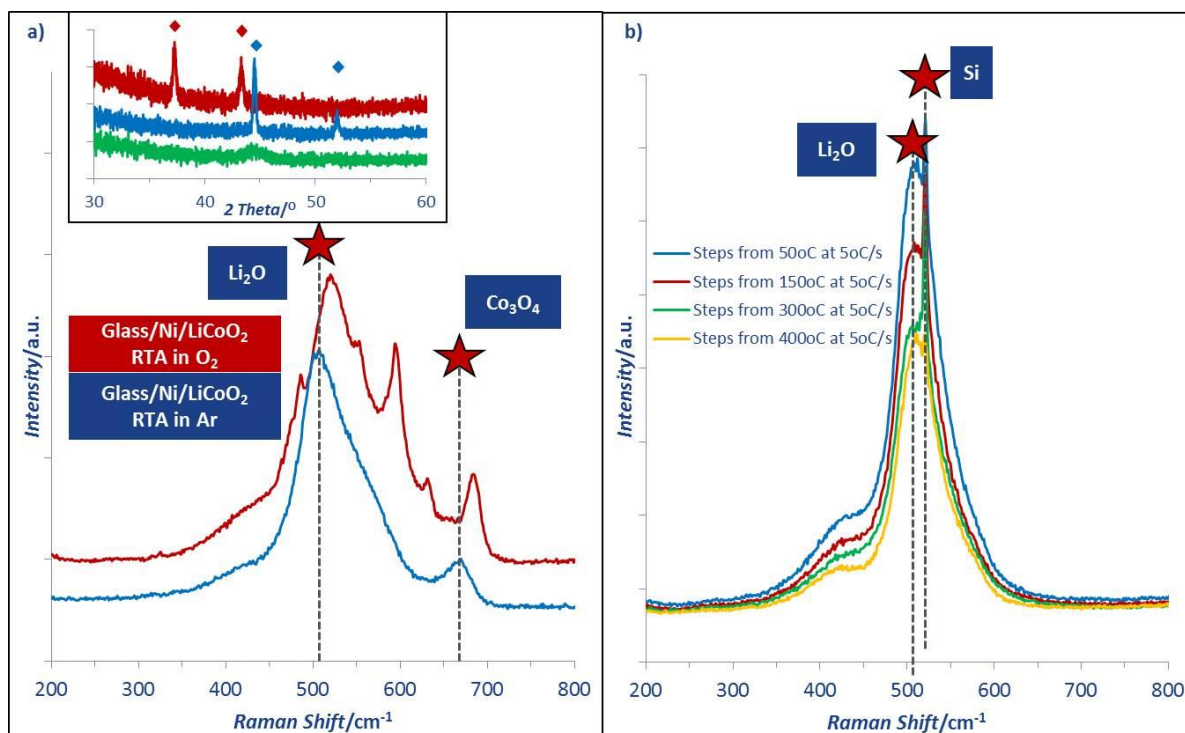
Figure 6.2: Raman spectra **(a)** 100 nm LiCoO$_2$ films RTA to 600°C on borosilicate glass slide/Ni in an O$_2$ and Ar environment for 3 min, **(b)** 100 nm LiCoO$_2$ samples on Si/SiO$_2$/Ni with and RTA recipe of 50°C steps held for 60 s at various starting temperatures to 600°C in an Ar environment for 3 min.

Al is the most common current collector for cathode electrodes in Li-ion batteries however Pt is preferred in solid-state batteries due to the additional processing not affecting the crystallisation of the additive-free thin-film. Al oxidises readily and has a melting point 660 °C which is close to the crystallisation temperature on LiCoO$_2$. LiCoO$_2$ was RTA in an Ar environment to 600 °C on Si/SiO$_2$/Al in order to prevent oxidation of Al and crystallise LiCoO$_2$. The Raman spectrum of the LiCoO$_2$ was not the characteristic profile seen for a crystalline LiCoO$_2$ sample with a broad peak at 510 cm^{-1} indicating the formation of Li$_2$O. The RTA annealing temperature was lowered initially and was then increased stepwise with ex-situ Raman analysis performed after every step in order to determine if the required annealing temperature was lower as a result of the Al current collector. For each sample an anneal time of 3 minutes and ramp up rate of 10 °C/s was used. The initial annealing temperature was 400 °C and increased to 420, 440, 550 and 600 °C. As seen in Figure 6.3a the Raman spectrum shows a broad peak at 595 cm^{-1} after a 400 °C anneal, the peak becomes sharper with increasing temperature with the development of a second peak at 486 cm^{-1} beginning at 420 °C. At 550 °C the characteristic profile of crystalline LiCoO$_2$ is fully developed with the appearance of sharp peaks. The Raman spectrum at 600 °C shows the appearance of an additional peak at 520 cm^{-1} which is characteristic of Si, indicating either

cracking or delamination of the LiCoO$_2$ film. A fresh 100 nm LiCoO$_2$ sample on an Al current collector annealed to 550 ºC in one step did not yield LiCoO$_2$ peaks, Figure 6.3b. This indicates that it is not just the annealing temperature that has an effect on the crystallinity of LiCoO$_2$. A further LiCoO$_2$ sample was subjected to an RTA to 550 ºC with 50 ºC steps beginning at 400 ºC that lasted 60 s. The resultant Raman spectrum gave the characteristic profile of crystalline LiCoO$_2$ with sharp intense peaks at 486 and 595 cm^{-1}. This confirms that Al can be used as a current collector for LiCoO$_2$ cathode that require RTA.
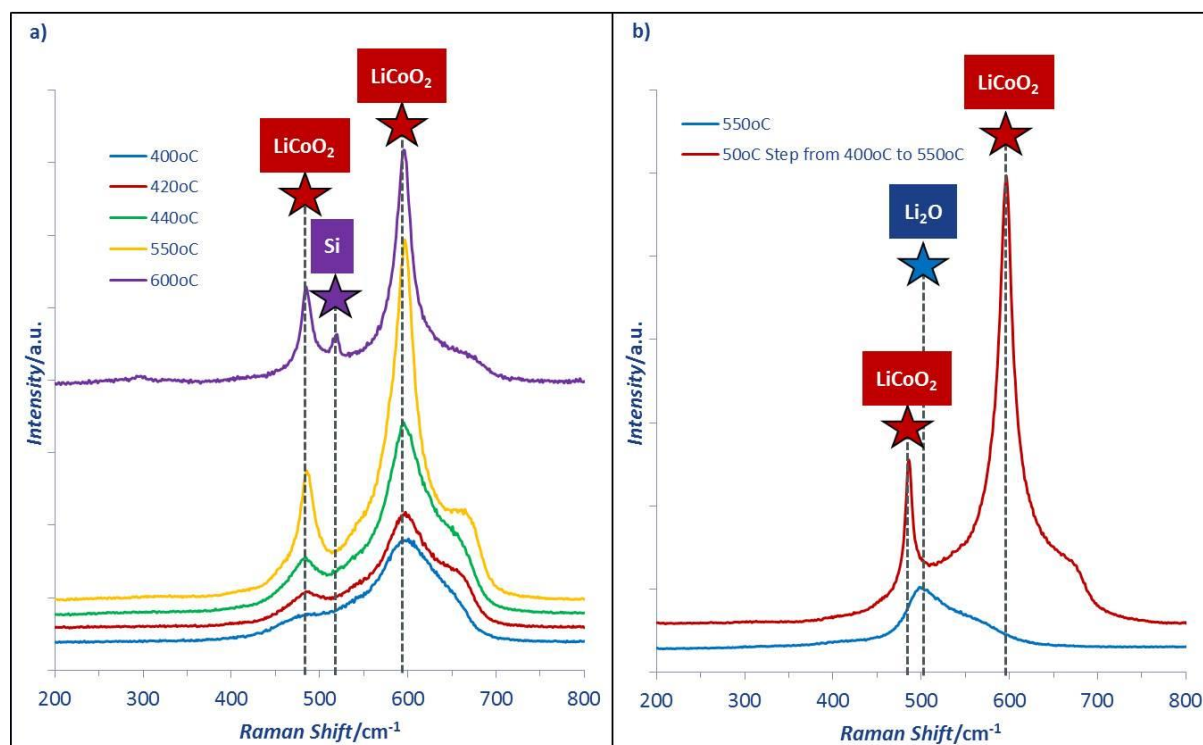
Figure 6.3: Raman spectrum **(a)** 100 nm LiCoO$_2$ film on Si/SiO$_2$/Al of RTA in an Ar environment for 3 min at various temperatures, **(b)** Comparison of 100 nm LiCoO$_2$ RTA to 550ºC in an Ar environment for 3 min with a ramp-up of 10ºC/s and a ramp-up of 10ºC/s with 60 s stabilising steps every 50ºC from 400ºC.

RTA of LiCoO$_2$ on Pt and Au also results in the required crystalline structure and space group of R$\overline{3}$m, as verified by the presence of the A$_{1g}$ (487 cm^{-1}) and E$_g$ peaks (596 cm^{-1}), for Li-ion batteries as seen in Figure 6.4. This could be due to the Pt and Au being relatively unreactive metals with no side reactions and minimum induced stress on the LiCoO$_2$ thin-film as there are no changes to the film structure of the current collector.
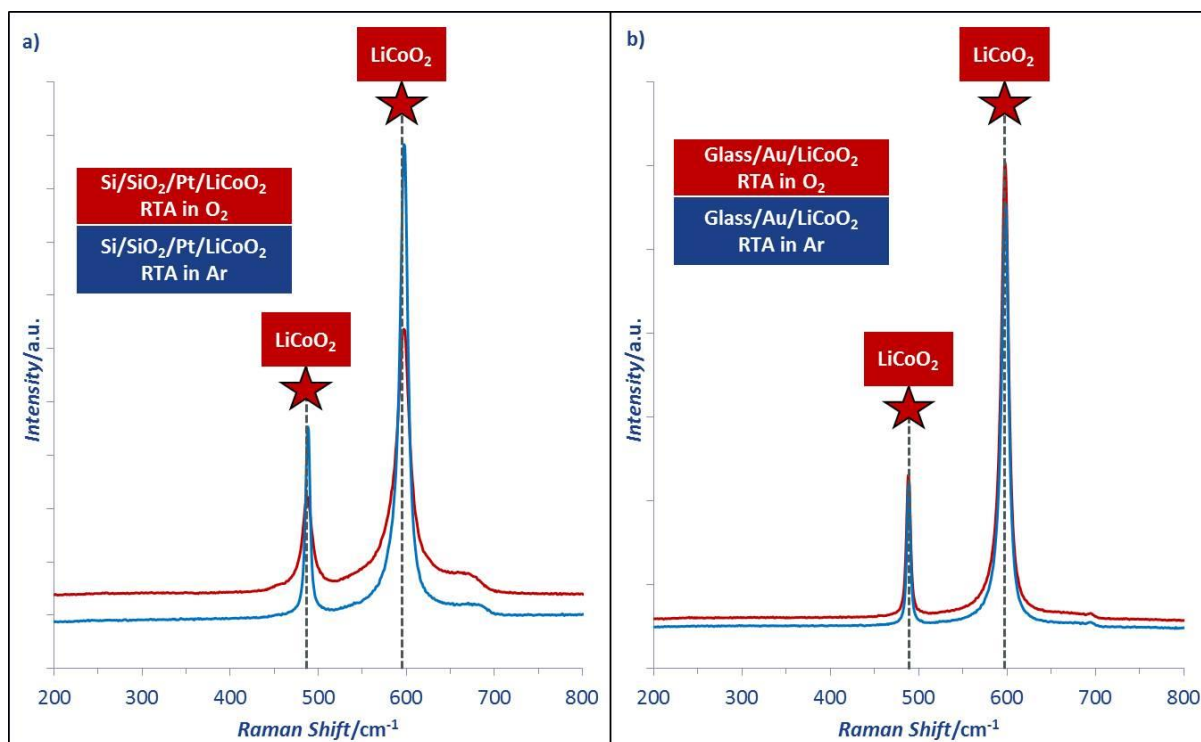
Figure 6.4: Raman spectrum of 100 nm LiCoO$_2$ film RTA to 600°C in an O$_2$ and Ar environment for 3 min on **(a)** Si/SiO$_2$/Pt and **(b)** borosilicate glass slide/Au.

Figure 6.5a shows the XRD pattern of a typical LiCoO$_2$ thin-film deposited by DC magnetron sputtering. XRD shows crystalline phases of (003) and (104) reflections that have an intensity ratio (I$_{(003)}$/I$_{(104)}$) of 0.67, indicating that (104) is the dominant phase present and that there is cation mixing within the hexagonal lattice[17]. The (101) and (104) crystalline phases are preferred for LiCoO$_2$ as a lithium battery electrode in which the layered structure is at 10° and 35° to the surface, respectively, meaning increased rate capabilities[18]. The (003) crystalline phase on the other hand where the layered structure is at 90° to the surface limits the lithiation/delithiation which can only occur at cracks in the surface[19].

Initially solid-state deposition of LiCoO$_2$ thin-films with a thickness of $\leq$ 500 nm were (003) dominated with layers $\geq$ 1 μm preferring (101) and (104) orientations however other factors such as deposition technique, substrate, gas pressure etc. also have a significant influence on crystalline lattice[18a, 20]. Figure 6.5b shows the Raman spectrum of a high quality thin-film of LiCoO$_2$ as indicated by the presence of the A$_{1g}$ and E$_g$ peaks. The E$_g$ peak at 596 cm^{-1} is associated with the stretching of the Co-O bond and the A$_{1g}$ peak at 487 cm^{-1} with the bending of the O-Co-O bonds. The ratio between the intensity of E$_g$ and A$_{1g}$ peaks is (I$_{(Eg)}$ /I$_{(A1g)}$) 0.62, which indicates there is a small amount of c-axis orientation with a random orientation in the film[21]. The vibration of oxygen atoms at the ab and c -axes are related to

the E_g and A_{1g} peaks, respectively, and the results are in agreement with the XRD analysis[22]. The full width half maximum (FWHM) of less than 12 cm^{-1} for the A_{1g} peak is a good indication of the thin-film quality[23].
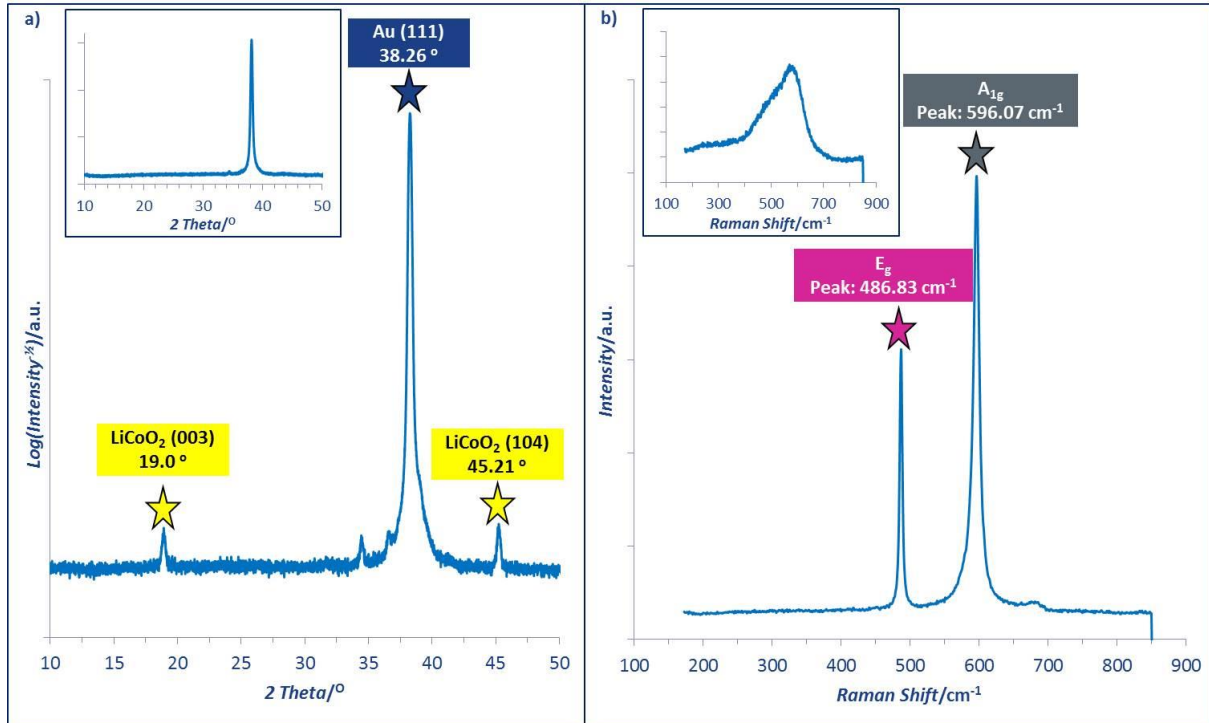
Figure 6.5: XRD (a) and Raman (b) of rapid thermal annealed (RTA) 100 nm $LiCoO_2$ film. Inset images are of as-deposited 100 nm $LiCoO_2$ film with intensity on the y axes in arbitrary units.

A plan view SEM and cross-sectional TEM image for the $LiCoO_2$ deposit is shown in Figure 6.6. The SEM image indicates large grains without a preferred orientation while the cross-section shows a rough $LiCoO_2$ surface with an average thickness of 100 nm on 100 nm of Au and 6 nm of Ti in agreement with surface profilometry measurements.
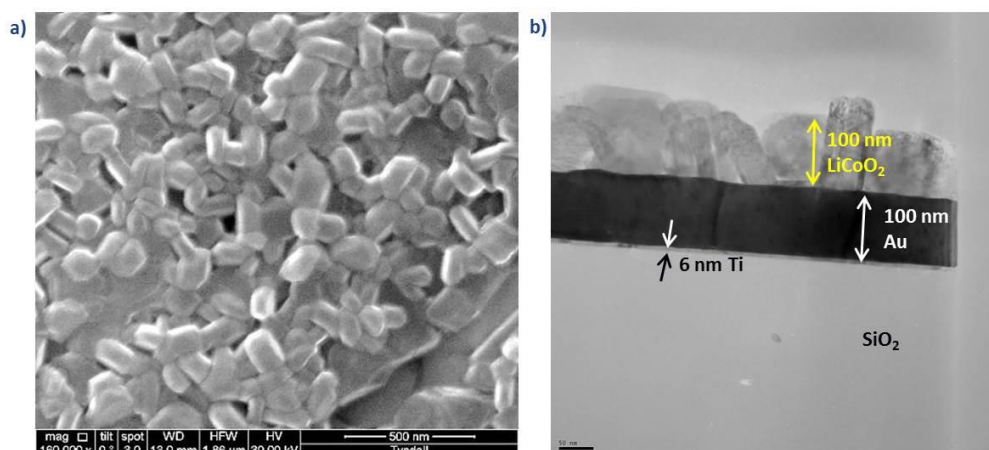
Figure 6.6: SEM plan view and TEM cross-section of nanoscale-film LiCoO$_2$ on a 100 nm Au current collector that contained a 6 nm Ti base layer to adhere to the 1µm thermal annealed SiO$_2$ layer on the Si wafer substrate.

The CV analysis in Figure 6.7 shows a well-defined redox couple for the anodic and cathodic reactions. A change in the crystalline structure can also result in a potential peak however the peak potentials observed is characteristic lithiation/delithiation of LiCoO$_2$. The peak separations at 1, 20 and 100 mV/s are 4, 36 and 98 mV, respectively, and are well defined indicating a small overpotential meaning the electrolyte charge transfer and electrode/electrolyte interfacial resistances are small. This is in contrast to a composite nanoparticle LiCoO$_2$ electrode that contained an electrically conductive additive in an Li-ion aqueous electrolyte where there is a large increase in overpotential resulting in the distortion of the CV shape with the potential shift of the anodic peak to outside the potential cut-off, after the potential window was already extended, at increasing scan rates[14d, 24]. The nanoscale thin film (100 nm) cathodes can achieve extremely high currents of up to 10 mA/cm^2 appropriate for a wireless sensor during active operation or data transmission. The potential distortion when analysing the characteristics of electrode materials in organic and solid-state electrolytes is minimised in the high conductivity aqueous electrolytes.
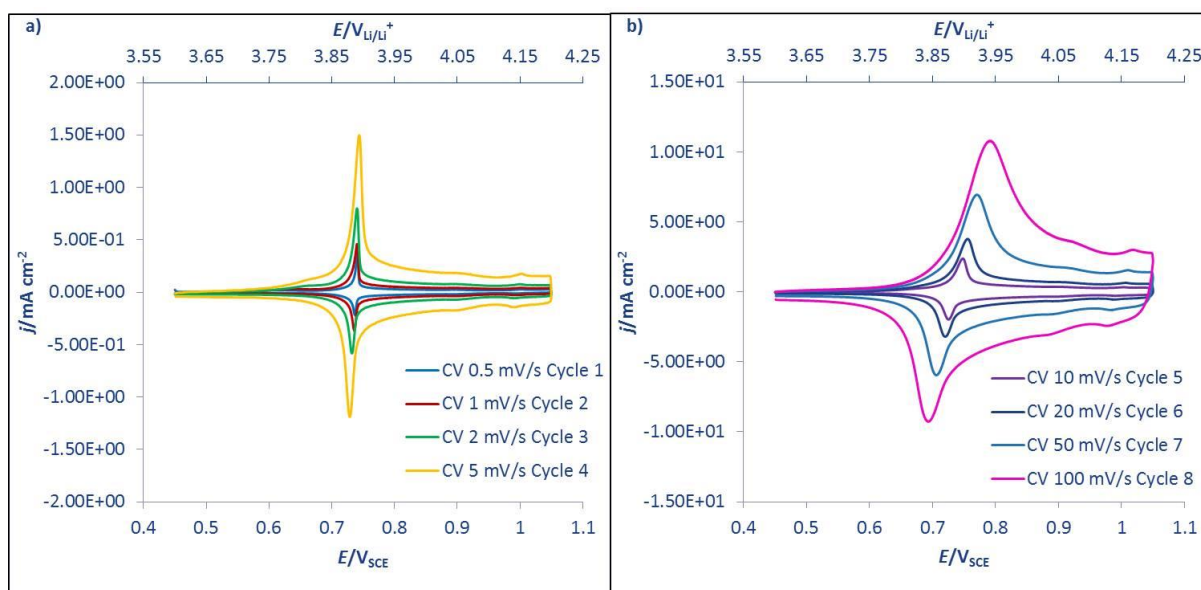
Figure 6.7: CV of 100 nm LiCoO$_2$ film at 0.5, 1, 2, 5 (a) 10, 20, 50 and 100 mV/s (b) in 5 M LiNO$_3$ aqueous electrolyte.

The peak current associated with lithium intercalation/deintercalation at layered oxide cathode materials is proportional to the square root of the scan rate. This is known as a diffusion controlled faradaic reaction within the crystalline structure. Alternatively, non-diffusion controlled faradaic reactions which depend on the outer surface area typically seen in supercapacitor materials exhibit a linear dependence on the scan rate. The equation for the peak current dependence on scan rate, Equation 6.1, is in the form of the power law relationship and can be used to determine the dominating kinetics, Equation 6.2.

$$i = av^b \qquad\qquad 6.1$$

$$\log(i) = \log(a) + (b)\log(v) \qquad\qquad 6.2$$

A slope of 0.5 demonstrates diffusion control while a slope of 1 implies non-diffusion controlled lithium storage. In Figure 6.8a the average slope for the logarithm of cathodic and anodic peak currents as a function of logarithm of scan rate (1 – 100 mV/s) is 0.69. This means that the lithium storage is dominated by diffusion controlled kinetics but has a significant non-diffusion controlled contribution[25]. This is in strong agreement with the well-defined CV profiles, seen in Figure 6.7, at fast scan rates (≥ 20 mV/s), which suggested that the lithium reaction was not solely diffusion controlled and that the contribution is from a faradaic redox process. Typically non-diffusion controlled contributions in an aqueous

systems are from double-layer capacitance (non-faradaic) and/or near surface confined pseudocapacitance (faradaic). As the reaction is clearly faradaic and the lithium ions are intercalated into the layer $LiCoO_2$ the non-diffusion controlled contribution is intercalation pseudocapacitance[25a]. The contribution of both diffusion and non-diffusion controlled lithium reactions are represented by Equation 6.3. That can be rearranged to Equation 6.4 so that the $i/v^{0.5}$ is plotted against $v^{0.5}$ with the slope equal to k_1 and the intercept equal to k_2. The contribution of the diffusion and non-diffusion controlled kinetics are quantified using Equations 6.5 and 6.6, respectively.

$$i = k_1 v + k_2 v^{0.5} \tag{6.3}$$

$$\frac{i}{v^{0.5}} = k_1 v^{0.5} + k_2 \tag{6.4}$$

$$\text{Fraction of Diffusion Controlled Current} = \frac{k_2 v^{0.5}}{k_1 v + k_2 v^{0.5}} \tag{6.5}$$

$$\text{Fraction of Non-Diffusion Controlled Current} = \frac{k_1 v}{k_1 v + k_2 v^{0.5}} \tag{6.6}$$

As seen in Figure 6.8b at slow scan rates, diffusion controlled Li-bulk insertion contribution is the dominant mechanism for energy storage. The contribution of the fast intercalation pseudocapacitance kinetics is $\leq 20\%$ at scan rates lower than 2 mV/s. However the intercalation pseudocapacitance kinetics become more dominant at increased scan rates and are responsible for $> 50\%$ of the energy storage at scan rates ≥ 50 mV/s which corresponds to accessing most of the cathode material in under 10 s. The pivotal input of the non-diffusion controlled kinetics, which is considered negligible in commercial Li-ion batteries, allows for lithium energy accessibility at high rates. This indicates that nanoscale thin-films of $LiCoO_2$ have the ability to achieve high energy and power densities for devices in an appropriate electrolyte.

The diffusion coefficient was estimated using the Randles-Sevcik equation (Equation 6.7).

$$I_p = (2.69 \times 10^5) n^{3/2} A C_{Li} D_{Li}^{1/2} v^{1/2} \tag{6.7}$$

where I_p is a peak current, n is the number of electrons transferred, A is the geometric area of the electrode, C_{Li} is the bulk concentration of Li in $LiCoO_2$, D_{Li} is the diffusion coefficient of Li in the thin film electrode, v is the scan rate.
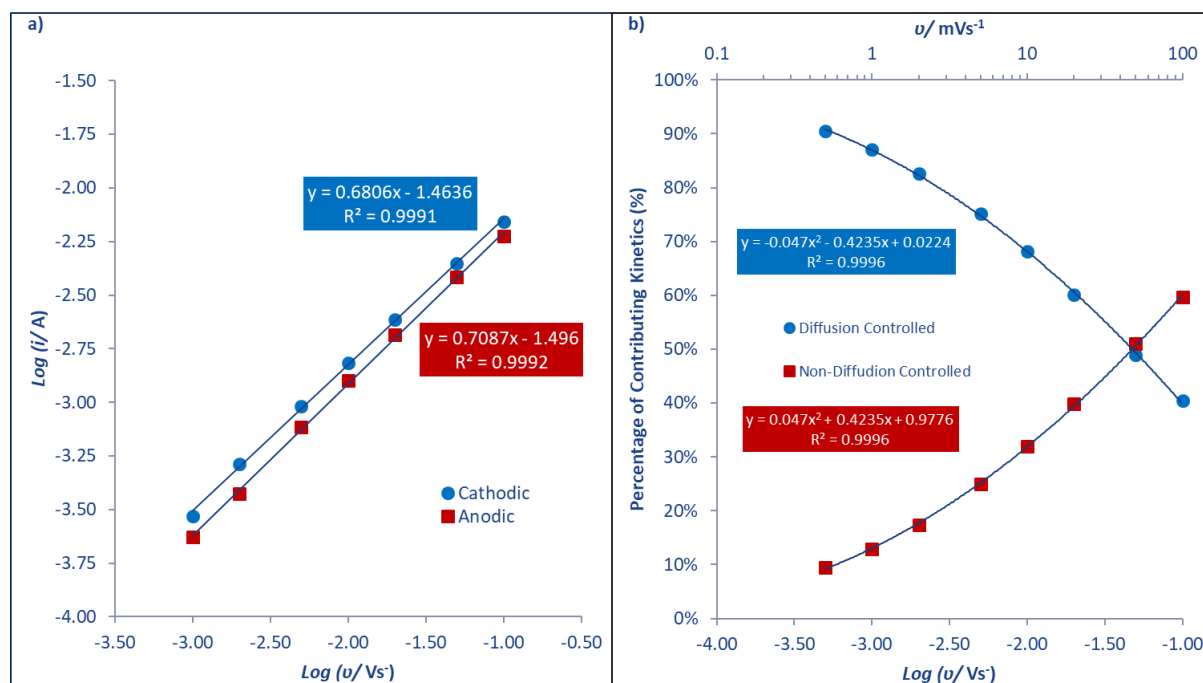
Figure 6.8: Log[Peak Current] vs. Log[Scan Rate] to determine b-value (a) and percentage of contributing kinetics at various scan rates (b).

There is a Li concentration gradient across the thin-film electrode during intercalation and for this analysis it is assumed that the diffusion is one dimensional in the thin-film electrode. This assumption is regularly utilised in the determination of the Li ion diffusion coefficient using electrochemical impedance spectroscopy (EIS), potentiostatic intermittent titration technique (PITT) and galvanostatic intermittent titration technique (GITT)[26]. The diffusion coefficient for lithiation and delithiation was found to be 5.31×10^{-12} and 7.07×10^{-12} cm^2 s^{-1}, respectively, which is in line with the literature for thin-film $LiCoO_2$[27].

Galvanostatic cycling was performed at current densities equivalent to C-rates of 3, 5, 10, 20, 50, 100 and 200 C. Figure 6.9a shows the galvanostatic charge and discharge curves of the fifth cycles in the sequence, while Figure 6.9b shows the specific capacity of the galvanostatic cycling. The main redox plateau is observed even at 200 C which is in agreement with the well-defined peak seen in the CV of Figure 6.7. Generally the redox plateau duration decreases and drops in potential at increased C-rates which implies an interference in lithiation/delithiation. The reverse is seen in this study when an increment in C-rate is applied, indicating superior lithiation/delithiation kinetics, in which a well-defined

plateau is still present with no drop in potential at a 200 C rate. At a 10 C rate, (full charge/discharge in 6 minutes), a reversible discharge capacity of 108 mAh/g (5.4 µAh/cm^2, 53.9 µAh/cm^{2}µm), is achieved assuming a film density of 4.98 g/cm^3 (data sheet density of sputter target) which is equivalent to 79% of the theoretical capacity (137 mAh/g)[28]. A 20 times increase in current density from 10 C to 200 C, (full charge/discharge in 18 s) exhibit excellent capacity retention with losses of only 12.5% and a capacity of 96.45 mAh/g. To the best of our knowledge the maintenance of such high capacities for LiCoO$_2$ thin-films has not been reported previously[29]. Typically such high C-rates would lead to a significant capacity drop for film electrodes. CV profiles tend to become distorted with peak separation increasing significantly at higher scan rates. Galvanostatic profiles lead to a drop in potential without a significant current plateau and would complicate the use of such a material in a wireless sensor system.
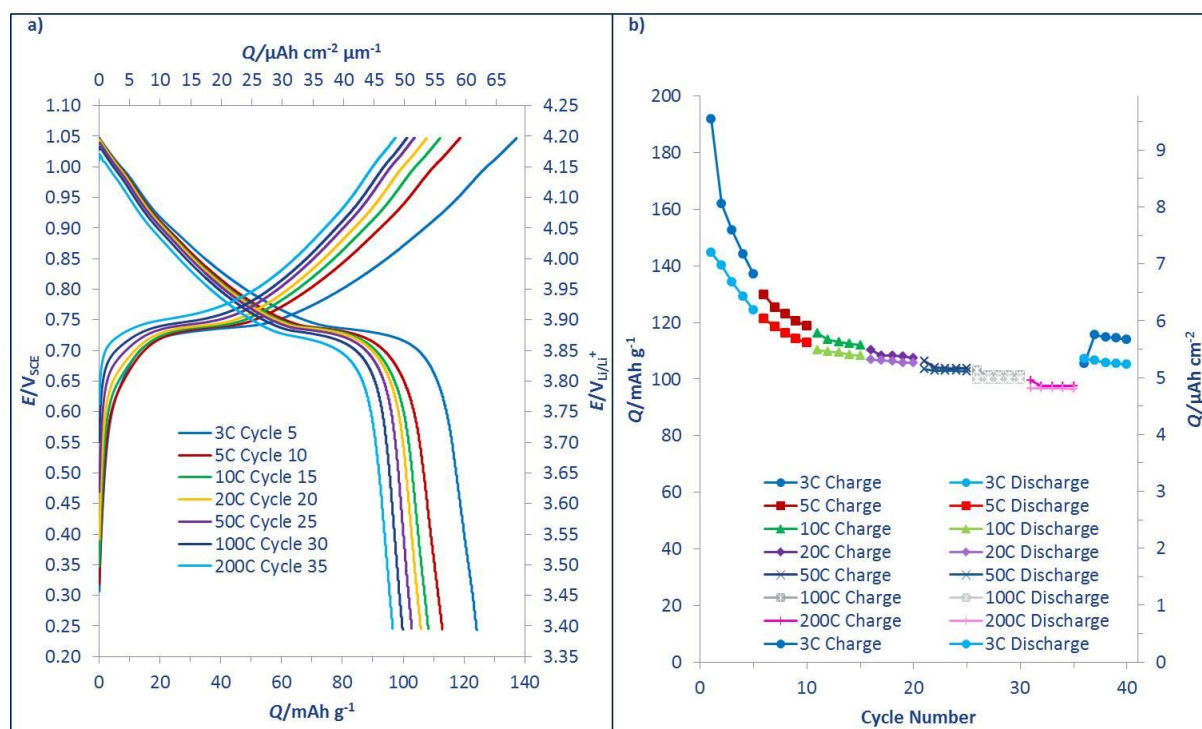
Figure 6.9: Galvanostatic profiles of a 100 nm LiCoO$_2$ film at various C-rates (a) and summary of galvanostatic cycling capacities (b) in a 5 M LiNO$_3$ aqueous electrolyte.

Longer-term cycling at a 200 C rate performed for over 500 cycles is shown in Figure 6.10. The capacity decreased in the initial cycles (134 cycles) as the system reached equilibrium and the capacity value was equivalent to the 200 C value obtained from the LiCoO$_2$ sample used in Figure 6.9, where the cycling was more intensive. The capacity after 533 cycles was

70 mAh/g which represents a capacity drop of 0.08 % per cycle over 400 cycles (after stabilisation) as shown in Figure 6.10. The galvanostatic profiles retain the characteristic plateau during cycling which indicates little interference from side reactions at the electrode/electrolyte interface generally seen in organic electrolytes which inhibit the Li^+ ion transport.
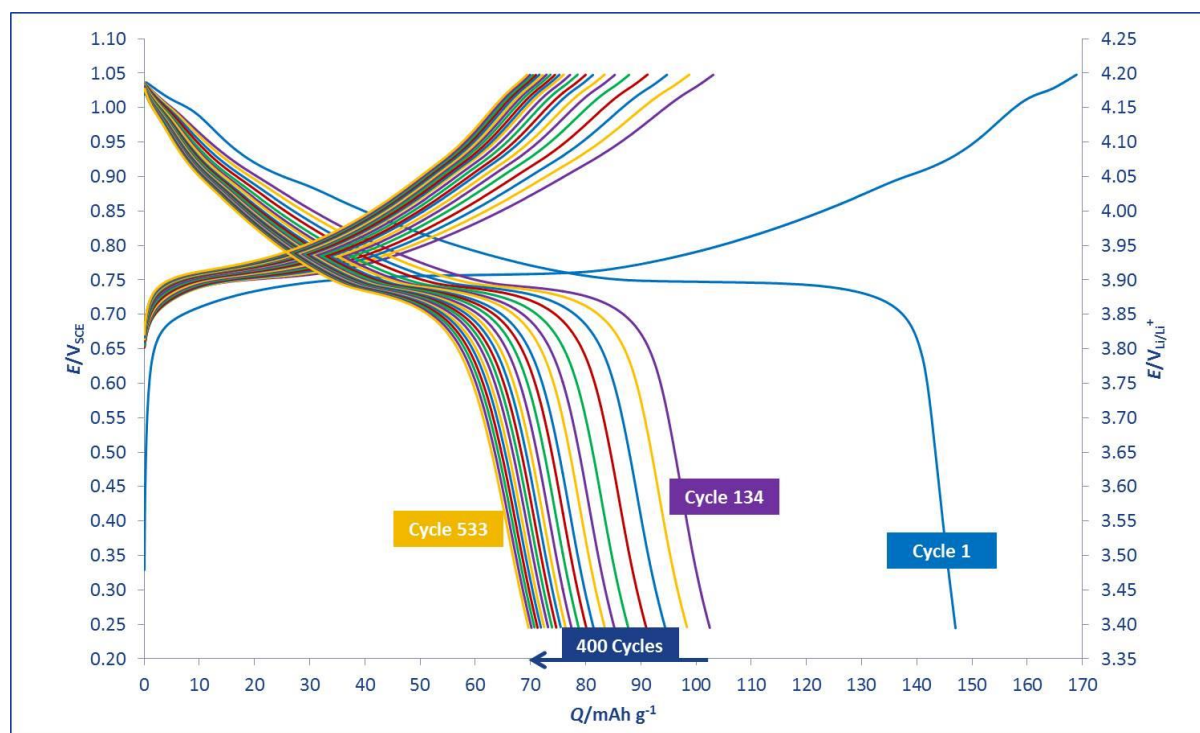
Figure 6.10: Galvanostatic Cycling of a 100 nm $LiCoO_2$ film at 200 C for 533 cycles in a 5 M $LiNO_3$ aqueous electrolyte.

Ni is an attractive current collector metal as it is unreactive in the electrochemical potential window for Li^+ ions. It has a high electrical conductivity and can be easily electrodeposited for 3D architectures. However, Ni is prone to diffusion and oxidation at elevated temperatures in the presence of O_2 making it unsuitable as a current collector when annealing is required to convert an amorphous structure to an Li^+ ion active crystalline structure as shown from the XRD and Raman analysis in Figure 6.2. Diffusion barriers have been used to minimize interlayer diffusion that has a negative effect on the application of the respective metal stack. TiO_2 was used as a diffusion barrier and was deposited by DC sputtering 200 nm of Ti followed by an RTA in an O_2 environment at 450^oC. The Ni substrate was also converted to NiO by RTA Ni in an O_2 environment at 600^oC in order to restrict the diffusion of Ni atoms while also ensuring that no more oxidation would occur during the processing of the $LiCoO_2$ that could cause stresses in the film during the transformation of Ni to NiO. Au and $LiCoO_2$ were deposited onto either Ni/TiO_2, NiO or NiO/TiO_2. Electrochemical analysis

was used to compare the performance of $LiCoO_2$ on the 3 different stacks. The CV results in Figure 6.11 show that TiO_2 does restrict Ni diffusion. The $LiCoO_2$ remains active but not at its full theoretical capacity which indicates that some Ni did diffuse through the barrier and interact with the Au or $LiCoO_2$ or both. Converting Ni to NiO results in a reduced amount of Ni diffusion compared to a Ni/TiO_2 layer and more $LiCoO_2$ capacity is available. A combination of both techniques results in the full utilisation of $LiCoO_2$ and the results are directly comparable to the $Si/Ti/Au/LiCoO_2$ stack in Figure 6.7a.
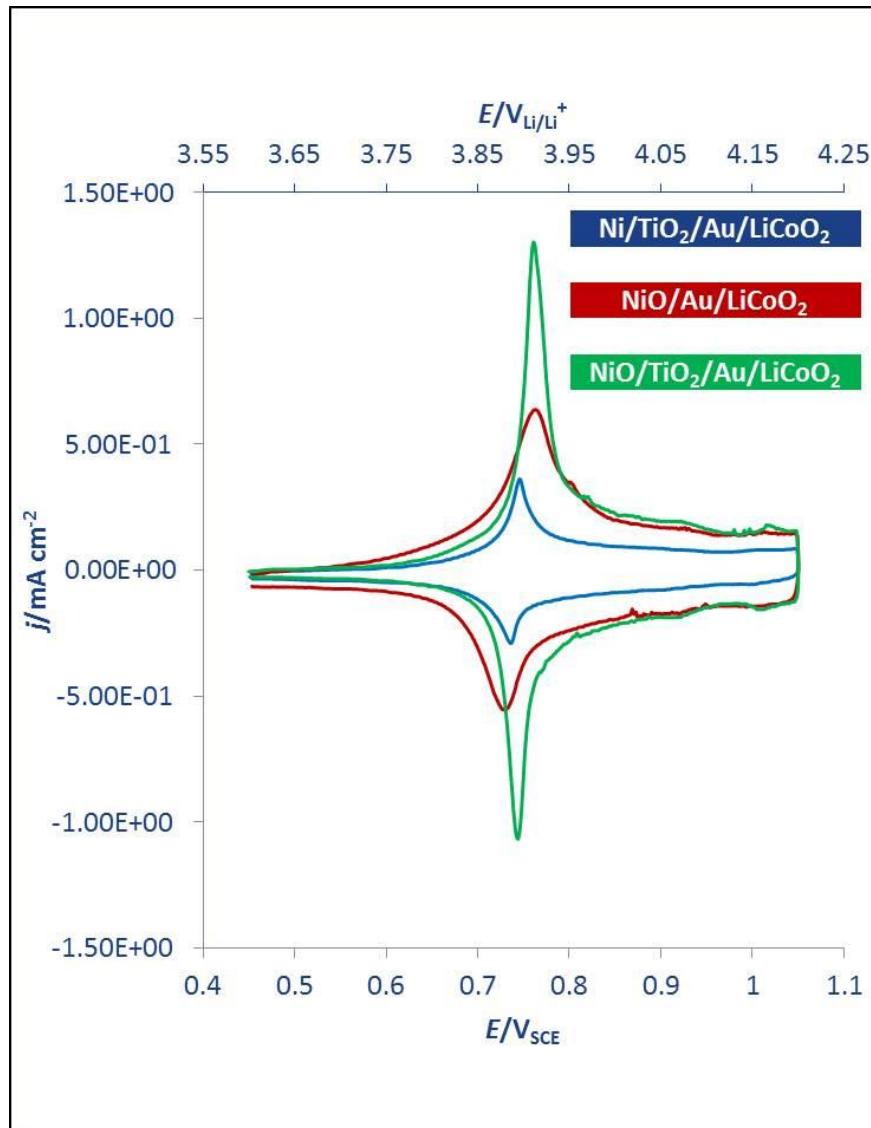
Figure 6.11: CV comparison at 5 mV/s scan rate in 5 M $LiNO_3$ of 100 nm $LiCoO_2$ on $Ni/TiO_2/Au$, NiO/Au and $NiO/TiO_2/Au$.

Conclusion

Nanoscale $LiCoO_2$ films fabricated by DC sputtering show exceptional electrochemical rate capabilities for Li-ion battery applications. At higher cycling rates, intercalation pseudocapacitive storage dominates the electrochemical kinetics. The charge storage is not limited by the crystalline structure for this nanoscale-film as a result of the decreased diffusion pathway and an increased surface reactivity. The improved wettability of the electrode surface may also play a role in the resultant electrochemical kinetics. At extremely high scan rates and galvanostatic current densities of up to 100 mV/s and 200 C, respectively, a capacity retention equivalent to 97 mAh/g (4.8 µAh/cm^2, 48.3 µAh/cm^{2}µm)) is obtained. Even at only 100 nm thickness the cathodes can achieve desirable high current densities of up to 10 mA/cm^2. Nanoscale-film $LiCoO_2$ is a potential electrode for an aqueous electrolyte based battery that can achieve the high current rates during device interrogation for the "Internet of Things" scenario. Aqueous Li-ion batteries can potentially decrease the cell area and increase the energy density to more closely match the power requirements of the sensors and electronic micropower management system.

References

[1]   D. S. Gardner, C. W. Holzwarth Iii, Y. Liu, S. B. Clendenning, W. Jin, B.-K. Moon, C. Pint, Z. Chen, E. C. Hannah, C. Chen, C. Wang, E. Mäkilä, R. Chen, T. Aldridge, J. L. Gustafson, *Nano Energy* **2016**, *25*, 68-79.

[2]   J. Janek, W. G. Zeier, *Nature Energy* **2016**, *1*, 16141.

[3]   C. Ó. Mathúna, T. O'Donnell, R. V. Martinez-Catala, J. Rohan, B. O'Flynn, *Talanta* **2008**, *75*, 613-623.

[4]   Y. Wang, B. Liu, Q. Li, S. Cartmell, S. Ferrara, Z. D. Deng, J. Xiao, *J. Power Sources* **2015**, *286*, 330-345.

[5]   B. J. Neudecker, N. J. Dudney, J. B. Bates, *J. Electrochem. Soc.* **2000**, *147*, 517-523.

[6]   W. Wang, J. F. Rohan, N. Wang, M. Hayes, A. Romani, E. Macrelli, M. Dini, M. Filippi, M. Tartagni, D. Flandre, in *Beyond-CMOS Nanodevices 1* (Ed.: F. Balestra), John Wiley & Sons, Inc, Hoboken, NJ, USA, **2014**, pp. 249-275.

[7]   S. Ferrari, M. Loveridge, S. D. Beattie, M. Jahn, R. J. Dashwood, R. Bhagat, *J. Power Sources* **2015**, *286*, 25-46.

[8]   K. M. Abraham, D. M. Pasquariello, E. M. Willstaedt, *J. Electrochem. Soc.* **1998**, *145*, 482-486.

[9]   a) M. Zukalová, M. Kalbáč, L. Kavan, I. Exnar, M. Graetzel, *Chem. Mater.* **2005**, *17*, 1248-1255; b) M. Fehse, E. Ventosa, *ChemPlusChem* **2015**, *80*, 785-795; c) C. Rong, S. Chen, J. Han, K. Zhang, D. Wang, X. Mi, X. Wei, *J. Renewable Sustainable Energy* **2015**, *7*, 023104; d) X. Yang, F. Qu, H. Niu, Q. Wang, J. Yan, Z. Fan, *Electrochim. Acta* **2015**, *180*, 287-294; e) K. Naoi, K. Kisu, E. Iwama, S. Nakashima, Y. Sakai, Y. Orikasa, P. Leone, N. Dupre, T. Brousse, P. Rozier, W. Naoi, P. Simon,

Energy Environ. Sci. **2016**, *9*, 2143-2151; f) M. Fehse, R. Trócoli, E. Ventosa, E. Hernández, A. Sepúlveda, A. Morata, A. Tarancón, *ACS Appl. Mater. Interfaces* **2017**, *9*, 5295-5301.

[10]   W. Li, J. R. Dahn, D. S. Wainwright, *Science* **1994**, *264*, 1115-1118.

[11]   a) H. Kim, J. Hong, K.-Y. Park, H. Kim, S.-W. Kim, K. Kang, *Chem. Rev.* **2014**, *114*, 11788-11827; b) G. Wang, L. Fu, N. Zhao, L. Yang, Y. Wu, H. Wu, *Angew. Chem. Int. Ed.* **2007**, *46*, 295-297; c) H. Yadegari, A. Jabbari, H. Heli, *J. Solid State Electrochem.* **2012**, *16*, 227-234.

[12]   a) H. Manjunatha, G. S. Suresh, T. V. Venkatesha, *J. Solid State Electrochem.* **2011**, *15*, 431-445; b) W. Li, W. R. McKinnon, J. R. Dahn, *J. Electrochem. Soc.* **1994**, *141*, 2310-2316; c) J. Y. Luo, Y. Y. Xia, *Adv. Funct. Mater.* **2007**, *17*, 3877-3884.

[13]   N. Alias, A. A. Mohamad, *J. Power Sources* **2015**, *274*, 237-251.

[14]   a) G. J. Wang, N. H. Zhao, L. C. Yang, Y. P. Wu, H. Q. Wu, R. Holze, *Electrochim. Acta* **2007**, *52*, 4911-4915; b) R. Ruffo, C. Wessells, R. A. Huggins, Y. Cui, *Electrochem. Commun.* **2009**, *11*, 247-249; c) G. J. Wang, Q. T. Qu, B. Wang, Y. Shi, S. Tian, Y. P. Wu, R. Holze, *Electrochim. Acta* **2009**, *54*, 1199-1203; d) W. Tang, L. L. Liu, S. Tian, L. Li, Y. B. Yue, Y. P. Wu, S. Y. Guan, K. Zhu, *Electrochem. Commun.* **2010**, *12*, 1524-1526; e) R. Ruffo, F. La Mantia, C. Wessells, R. A. Huggins, Y. Cui, *Solid State Ionics* **2011**, *192*, 289-292.

[15]   N. Alias, A. A. Mohamad, *Ceram. Int.* **2014**, *40*, 13089-13096.

[16]   S. Tintignac, R. Baddour-Hadjean, J.-P. Pereira-Ramos, R. Salot, *Electrochim. Acta* **2012**, *60*, 121-129.

[17]   M. Sathiya, A. S. Prakash, K. Ramesha, A. K. Shukla, *Materials* **2009**, *2*, 857-868.

[18]   a) J. B. Bates, N. J. Dudney, B. J. Neudecker, F. X. Hart, H. P. Jun, S. A. Hackney, *J. Electrochem. Soc.* **2000**, *147*, 59-70; b) Y. Yoon, C. Park, J. Kim, D. Shin, *J. Power Sources* **2013**, *226*, 186-190.

[19]   P. J. Bouwman, B. A. Boukamp, H. J. M. Bouwmeester, P. H. L. Notten, *J. Electrochem. Soc.* **2002**, *149*, A699-A709.

[20]   a) L. Bohne, T. Pirk, W. Jaegermann, *ECS Transactions* **2011**, *32*, 17-21; b) H. Y. Park, S. C. Nam, Y. C. Lim, K. G. Choi, K. C. Lee, G. B. Park, H. P. Kim, S. B. Cho, *Korean J. Chem. Eng.* **2006**, *23*, 832-837; c) H. Xia, L. Lu, G. Ceder, *J. Alloys Compd.* **2006**, *417*, 304-310; d) H. Y. Park, S. C. Nam, Y. C. Lim, K. G. Choi, K. C. Lee, G. B. Park, J. B. Kim, H. P. Kim, S. B. Cho, *Electrochim. Acta* **2007**, *52*, 2062-2067; e) K.-T. Jung, G.-B. Cho, K.-W. Kim, T.-H. Nam, H.-M. Jeong, S.-C. Huh, H.-S. Chung, J.-P. Noh, *Thin Solid Films* **2013**, *546*, 414-417; f) J. Xie, N. Imanishi, A. Hirano, M. Matsumura, Y. Takeda, O. Yamamoto, *Solid State Ionics* **2007**, *178*, 1218-1224.

[21]   Y. Iriyama, M. Inaba, T. Abe, Z. Ogumi, *J. Power Sources* **2001**, *94*, 175-182.

[22]   S.-W. Song, H. Choi, H. Y. Park, G. B. Park, K. C. Lee, H.-J. Lee, *J. Power Sources* **2010**, *195*, 8275-8279.

[23]   D. Song, C. Jiang, B.-S. L. Kwak, D. Severin, Electrochemical device fabrication process with low temperature anneal, **2014**,

[24]   Q. Liu, M. S. Javed, C. Zhang, Y. Li, C. Hu, C. Zhang, M. Lai, Q. Yang, *Nanoscale* **2017**, *9*, 5509-5516.

[25]   a) Y. Wang, Y. Song, Y. Xia, *Chem. Soc. Rev.* **2016**, *45*, 5925-5950; b) K. Brezesinski, J. Wang, J. Haetge, C. Reitz, S. O. Steinmueller, S. H. Tolbert, B. M. Smarsly, B. Dunn, T. Brezesinski, *J. Am. Chem. Soc.* **2010**, *132*, 6982-6990.

[26]   a) B. E. Conway, *Electrochim. Acta* **1993**, *38*, 1249-1258; b) M. D. Levi, D. Aurbach, *J. Electroanal. Chem.* **1997**, *421*, 79-88; c) M. D. Levi, D. Aurbach, *Electrochim. Acta* **1999**, *45*, 167-185; d) M. D. Levi, G. Salitra, B. Markovsky, H. Teller, D.

Aurbach, U. Heider, L. Heider, *J. Electrochem. Soc.* **1999**, *146*, 1279-1289; e) H. Xia, L. Lu, M. O. Lai, *Electrochim. Acta* **2009**, *54*, 5986-5991.

[27]   H. Xia, L. Lu, G. Ceder, *J. Power Sources* **2006**, *159*, 1422-1427.

[28]   B. Scrosati, K. Abraham, W. A. van Schalkwijk, J. Hassoun, *Lithium batteries: advanced technologies and applications, Vol. 58*, John Wiley & Sons, Hoboken, NJ, USA, **2013**.

[29]   Y. Matsuda, N. Kuwata, J. Kawamura, *Solid State Ionics* **2018**, *320*, 38-44.

Chapter 7 Electrochemical Analysis of Nanoscale Thin-Film V_2O_5 with a TiO_2 Coating and VC Electrolyte Additive in an Aqueous Electrolyte

Abstract

Electrodeposited thin-film V_2O_5 exhibited high power capabilities due to intercalation pseudocapacitance electrochemical kinetics when used in an aqueous rechargeable lithium batteries (ARLB) electrode in a 5 M $LiNO_3$ electrolyte. However, V_2O_5 suffers from dissolution in aqueous electrolytes which results in severe capacity fade and ultimately no capacity retention after 100 cycles. A TiO_2 coating and a VC electrolyte additive were used to enhance cycle stability and improve electrochemical kinetics. Capacity retention was increased to 59 % after 200 cycles for V_2O_5 in aqueous electrolyte with 10 wt. % VC additive and a 100 nm TiO_2 coated V_2O_5 in aqueous electrolyte with 5 wt. % VC additive.

Introduction

V_2O_5 has been extensively studied as an electrode material for Li-ion batteries due to its mixed valence state that allows it to hold up to 3 Li^+ ions in multiple phase transformations, α, ε, δ, γ and ω[1].

$$V_2O_5 + xLi^+ + xe^- \leftrightarrow Li_xV_2O_5 \qquad (0 \leq x \leq 3) \qquad 7.1$$

$$V_2O_5 + xLi^+ + xe^- \leftrightarrow \alpha Li_xV_2O_5 \qquad (x < 0.13) \qquad 7.2$$

$$V_2O_5 + xLi^+ + xe^- \leftrightarrow \varepsilon Li_xV_2O_5 \qquad (0.35 < x < 0.7) \qquad 7.3$$

$$V_2O_5 + xLi^+ + xe^- \leftrightarrow \delta Li_xV_2O_5 \qquad (0.8 < x < 1.8) \qquad 7.4$$

$$V_2O_5 + xLi^+ + xe^- \leftrightarrow \gamma Li_xV_2O_5 \qquad (1.9 < x < 2.8) \qquad 7.5$$

$$V_2O_5 + xLi^+ + xe^- \leftrightarrow \omega Li_xV_2O_5 \qquad (x = 3) \qquad\qquad 7.6$$
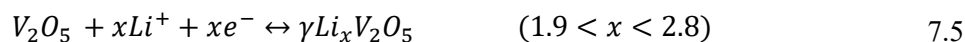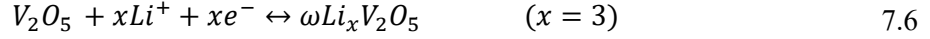
Every Li^+ ion held in the V_2O_5 structure is equivalent to a capacity of 147 mAh/g. During lithiation there is a coexistence of phases as some particles begin different stages of the lithiation process depending on particle distribution on the current collector and particle size[2]. In CV profiles reduction peaks at 3.4, 3.2, 2.35 and 1.95 V indicate phase transitions α/ε, ε/δ, δ/γ and γ/ω, respectively[3]. The α, ε, δ and γ are reversible phases while the ω-phase is an irreversible cubic rock salt structure that traps 0.4 Li^+ ions during formation. The mixed valence of V_2O_5 means that it can undergo volume expansion during lithiation which allows for more lithium to be held in its structure while also increasing the amount of electrolyte in contact with the increased surface area. V_2O_5 has lower lithium reaction potential in comparison to other intercalation metal oxides for Li-ion batteries however its higher capacity results in a higher energy density. Assuming the average voltage for the first Li^+ ion is 3.2 V with the capacity for the second Li^+ ion split between reactions at 2.6 and 2.1 V, the energy density of $Li_2V_2O_5$ is 816 Wh/kg.

V_2O_5 can be formed by a variety of methods such as sol-gel, hydrothermal synthesis, drop cast and electrodeposition[4]. Electrodeposition of V_2O_5 is a well-established controlled method that can produce dense crystalline deposits at relatively low cost and in a scalable manner. Electrodeposition can be performed on a variety of conductive substrates and shapes with uniform deposits. A range of 3D structuring methods such as nanowire formation of V_2O_5 using a polycarbonate template, the use of inverse opals or uniform coating of V_2O_5 on 3D current collectors (nanosized, micro, porous) can result in improved electrochemical performance[5]. The decreased path lengths for Li^+ intercalation results in enhanced rate capabilities while the increase in volumetric energy density is due to the larger mass loading per area.

The lower lithium reaction potential of V_2O_5 makes it an attractive anode in ARLB. $VO_2(B)$ was the anode used by Dahn et al. when they first proposed the ARLB[6]. Besides the improvements associated with safety and cost for aqueous based electrolytes, the other main advantages are an increase in ionic conductivity of the electrolyte which is usually two orders of magnitude higher and improved electrochemical kinetics in the electrode during the lithiation process[7]. Hollow spherical V_2O_5 has shown intercalation pseudocapacitance

kinetics in 5 M $LiNO_3$ in a supercapacitor study[8]. This electrode could also be used in ARLB with a high power density due to the improved kinetics but also the high energy density that is typical of Li-ion battery electrodes relative to supercapacitors.

One of the major problems associated with V_2O_5 in aqueous environments is the slight solubility of the V ion. Wang et al. showed that the dissolved content of the V ion in the electrolyte increased with cycle life and was larger than Mn ion in an ARLB that contained $LiMn_2O_4$ cathode, V_2O_5 anode and 5 M $LiNO_3$ electrolyte during cycling[9]. One of the main approaches used to date to improve the cycle stability in an aqueous electrolyte is to protect the electrode with a water insoluble electrically conducting polymer such as polypyrrole (PPy) and polyaniline (PAN)[10]. The capacity retention for a PPy coated V_2O_5 was 70% after 100 cycles in comparison to 43 % for an uncoated V_2O_5 electrode in a 5 M solution of $LiNO_3$[8].

The use of electrolyte additives to enhance electrochemical performance and cycle stability is a common approach used in organic electrolytes. The use of vinylene carbonate (VC) as an additive in aqueous electrolyte has been shown to improve cycle life of a $Li_{1.05}Cr_{0.10}Mn_{1.85}O_4$ electrode and maintain the high-voltage plateau after 50 cycles unlike the additive-free electrolyte[11]. The main advantage of VC is its higher reduction potential in comparison to the solvents typically used in organic electrolytes. Ouatani et al. investigated the effect of a VC additive in organic based cells of $LiCoO_2$/C, $LiFePO_4$/C and $LiCoO_2$/$Li_4Ti_5O_{12}$[12]. They showed that VC underwent reduction at 1.25 V vs. Li/Li^+ and the polymerisation product was present on the surface of the graphite anode but not on the $Li_4Ti_5O_{12}$ anode as its potential, 1.55 V, is higher than the VC reduction potential. Using X-ray photoelectric spectroscopy (XPS) the surface of the $LiCoO_2$ cathode in both the graphite and $Li_4Ti_5O_{12}$ cells had a VC polymer present on its surface after cycling which indicated that VC oxidation happened independently of the reduction mechanism and at potentials greater than ~ 3.7 V. The surface of the $LiFePO_4$, which had a final potential of 4.5 V showed no VC polymer present, which suggest the $LiCoO_2$ surface acted as a possible catalyst for VC oxidation. Further analysis of the VC reduction and oxidation mechanism shows that it undergoes reduction at 1.5 V and oxidation at 4.55 and 4.7 V in a carbon black/Li cell. The comprehensive research done on the reduction and oxidation decomposition of VC suggest that these potentials are outside the potential window of aqueous electrolytes. The reduction/oxidation mechanism of VC in an aqueous electrolyte must be catalysed either by the electrodes or by reacting with the electrolyte solution.

Experimental

A stack of Ti (10 nm) and Au (100 nm) was deposited on a 1 µm thermal annealed SiO_2 layer on a 4" diameter silicon wafer using metal sputter targets (Kurt J. Lesker) in a DC magnetron (Quorum Q300T D) Dual sputter coating system. The Ti layer acted as an adhesion layer between the SiO_2 substrate and Au current collector. V_2O_5 was electrodeposited at room temperature using a CH Instruments 660B potentiostat. A constant potential of 2 V was applied to the Ti/Au working electrode in a three electrode setup with a saturated calomel electrode (SCE) and platinum (Pt) mesh as the reference and counter electrode, respectively. The electrochemical bath was made up of a 0.25 M solution of $VOSO_4.xH_2O$, (assumed degree of hydration is 5) purchased from Sigma Aldrich, in a 1:1 (v/v) mixture of deionized water and ethanol. After deposition the samples were heated to 325 °C for 7 hrs. to crystallise the V_2O_5 deposit. Deposit thickness was confirmed using a surface profilometer (Tencor alpha-step 200). TiO_2 was coated onto the V_2O_5 by sputter depositing 50 or 100 nm of Ti and then rapid thermal annealed (RTA) in an O_2 environment at 450 °C for 10 min.

The structure and the morphology of the samples were analysed with a scanning electron microscope (FEI Nova 630 Nano-SEM) coupled with an energy dispersive X-ray (EDX) (Hitachi S4000) and for Raman spectroscopy a Renishaw Invia, 514 nm laser.

Electrochemical measurements were controlled using a CH Instruments 660B potentiostat and a three electrode setup. Cyclic voltammetry (CV) was performed on the V_2O_5 cathode over the potential window of 0.75 to -0.20 V against SCE. Delithiated $LiMn_2O_4$ was utilised as the counter electrode. The electrolyte used was 5 M $LiNO_3$ aqueous solution at a pH of 7 purged with N_2 gas prior to cycling to reduce the amount of dissolved oxygen. A high concentration of $LiNO_3$, neutral pH and little or no dissolved O_2 is critical to remove/suppress the side reactions that are associated with aqueous electrolytes[13]. The pH of the aqueous solution was checked after the addition of various amounts of Li salt and VC. The use of delithiated $LiMn_2O_4$ as a counter electrode rather than a metal counter, (e.g. Pt), is required to achieve stable electrochemical behaviour for extended cycling[14]. A metal counter electrode would have no storage capacity for the Li^+ extracted from the working electrode and would most likely evolve gas as the counter electrode reaction perturbing the electrolyte composition. The delithiated $LiMn_2O_4$ allows for Li^+ to cycle between the electrodes and operates without any significant changes to the chemical or physical properties of the electrolyte[15]. The measurements were carried out under ambient air and at 21 °C.

214

Results and discussion

SEM and EDX analysis confirmed that V_2O_5 was deposited with weight percentages of 59.89 and 40.11 % for vanadium and oxygen, respectively, which are in agreement with the theoretical weight percentages.
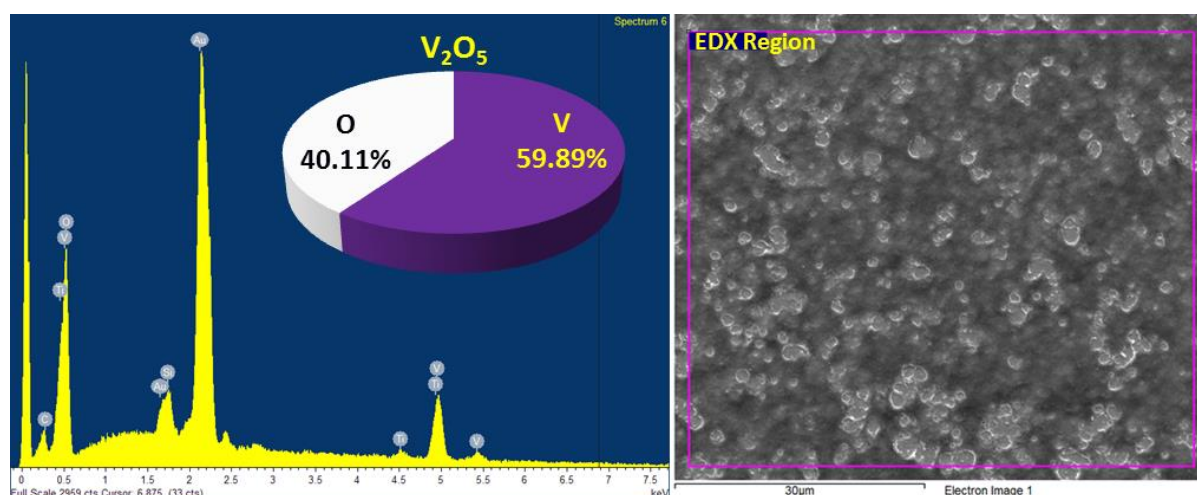
Figure 7.1: EDX and SEM analysis of V_2O_5 thin-film.

The orthorhombic phase of V_2O_5 has a well-established Raman spectra with a space group *Pmmn* and D_{2h} point symmetry[16]. There are 4 symmetry equivalent atomic positions per unit cell and 12 symmetrical combinations can be built from the Cartesian displacement of the equivalent atoms. Six of the combinations are IR-active and six are Raman active. A_g and B_{2g} Raman modes are from the displacements of the x and z-axis while the B_{1g} and B_{3g} Raman modes come from displacement of the y-axis. Raman peaks are determined by the derivative of the bond polarizability with respect to the bond lengths. In some symmetry, half the bond length is shortening and the other half is stretching so the bond stretching and shortening cancel each other out. Therefore even though some symmetries predict Raman active peaks the microscopic pattern determines them inactive and not present experimentally. Figure 7.2 2 shows a labelled molecular structure of a VO_5 pyramid that makes up V_2O_5. The Raman spectra of V_2O_5 in Figure 7.3 matches the literature data with peaks at 994.60 cm^{-1} for in-phase stretching vibration of V=O1 bonds, 700.90 cm^{-1} for anti-phase stretching of V-O2 bonds, 527.35 cm^{-1} x-axis displacements of stretching O2 atoms, 480.09 cm^{-1} bending of V-O3-V bridge angle, 403.88 cm^{-1} x-axis displacement of O1 atoms, 303.94 cm^{-1} z-axis displacements of $O2_1$ and $O2_2$ atoms, 283.31 cm^{-1} y-axis displacement of O1 atoms, 196.59 cm^{-1} x-axis displacement of V atoms, 144.84 cm^{-1} V atoms mixed signal of shear motion and

rotation of the ladders, O3-V-O2, in the y-axis and 103.94 cm^{-1} V atom vibration in the O3-V-O2 bridge in the z-axis.
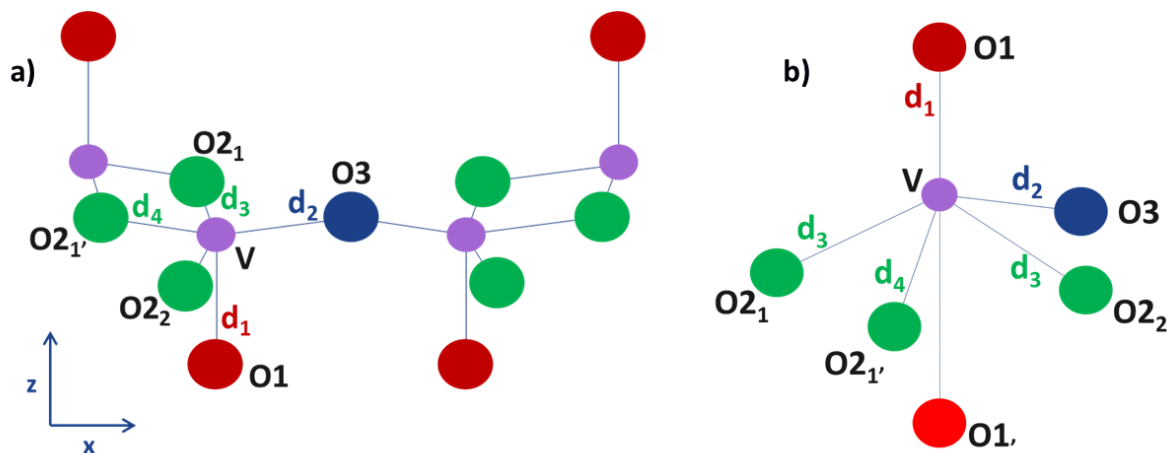
Figure 7.2: Crystal structure of V_2O_5 in the **a)**, xz-projection and **b)**, local vanadium environment.
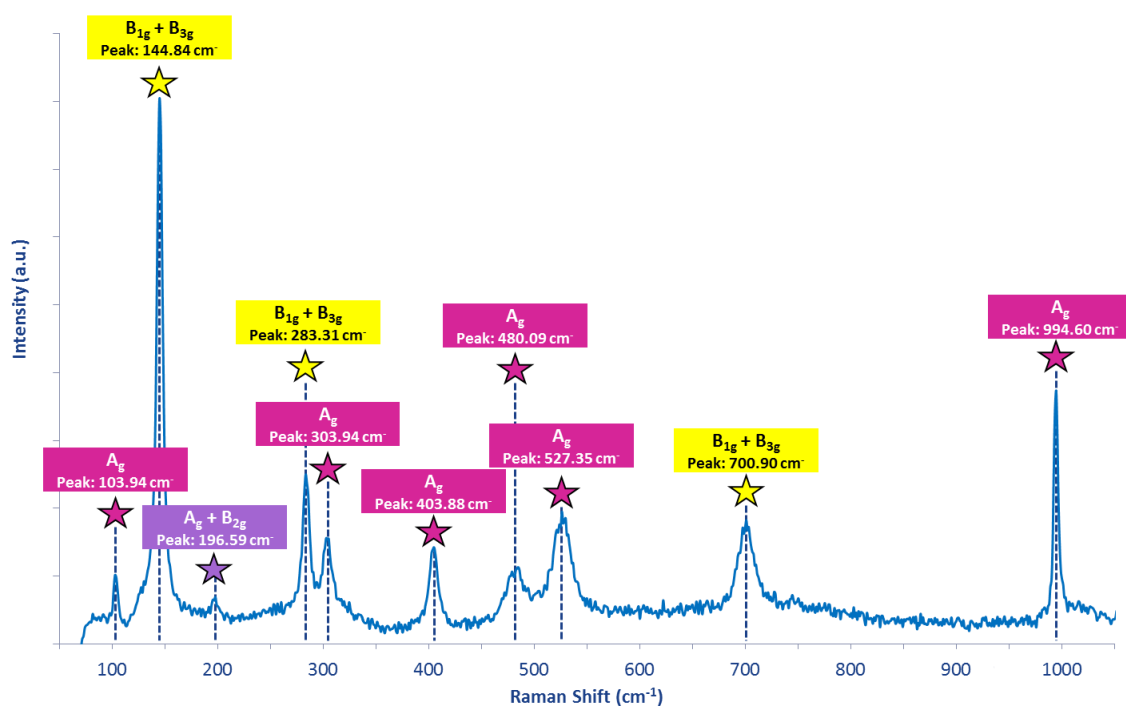
Figure 7.3: Raman spectrum of the V_2O_5 thin film.

The CV analysis in Figure 7.4 shows two well-defined redox peaks with little separation at 0.23 and 0.03 V (vs. SCE) which indicate changes in the crystal phases α/ε and ε/δ, respectively, to accommodate the lithium into the V_2O_5 structure. The redox peaks of the mixed phases α/ε and ε/δ are in accordance with the literature and are equivalent to 3.38 and 3.18 V, respectively, vs. Li/Li$^+$. The peak separation remains small at increasing scan rates with peak separations of 22, 52, 92 mV for α/ε and 12, 53, 110 mV for ε/δ at scan rates of 1,

10 and 50 mV/s, respectively, suggesting a low resistance for the electrolyte charge transport and transfer at the electrode/electrolyte interface. The redox peaks are still visible at 100 mV/s and have small peak separations in comparison to typical electrode materials at this scan rate which indicates a high rate capability. According to Equation 7.7 there is a power law relationship between the peak currents (i) and the scan rate (v) with (a) being a constant. Equation 7.8 shows that the slope for the plot of $\log(i)$ versus $\log(v)$ is the b-exponent which is representative of the electrochemical kinetics of the electrode.
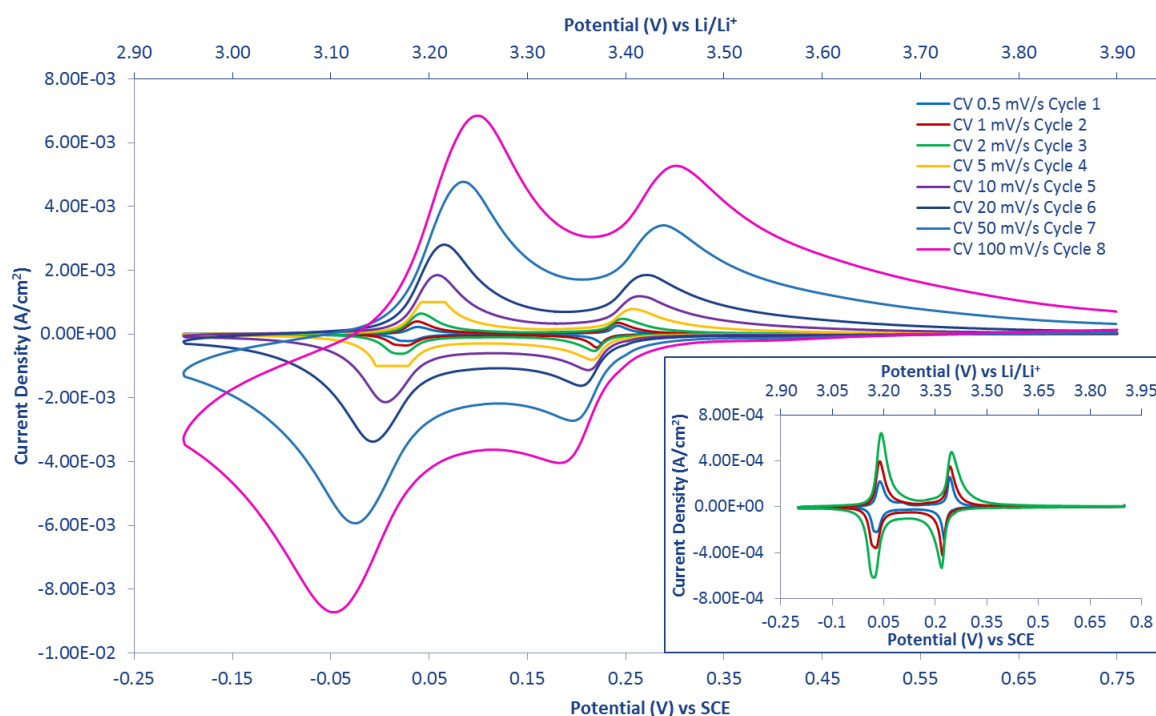
Figure 7.4: CV of V_2O_5 at 0.5, 1, 2, 5, 10, 20, 50 and 100 mV/s in 5 M $LiNO_3$ aqueous electrolyte. Insert lower current data of slower CV scan rates of 0.5, 1 and 2 mV/s.

$$i = av^b \qquad\qquad 7.7$$

$$\log(i) = \log(a) + (b)\log(v) \qquad\qquad 7.8$$

Two response conditions can be identified; where b = 0.5 the reaction is primarily a diffusion controlled faradic process (intercalation, alloying) and b = 1.0 is due to a non-diffusion controlled faradic reaction (pseudocapacitance, double layer capacitance). The contribution from the diffusion and non-diffusion controlled kinetics can be quantified as the measured current at a fixed potential where the current is a combination of the two kinetic regimes,

Equation 7.9. The equation is rearranged to a line equation (Equation 7.10) where k_1 is equal to the slope and k_2 is equal to the intercept when $\frac{i}{\sqrt{v}}$ is plotted against $\sqrt{v}$. The percentage contribution of diffusion and non-diffusion controlled kinetics is calculated using Equations 7.11 and 7.12, respectively.

$$i = k_1 v + k_2 v^{0.5} \tag{7.9}$$

$$\frac{i}{v^{0.5}} = k_1 v^{0.5} + k_2 \tag{7.10}$$

$$Fraction\ of\ Diffusion\ Controlled\ Current = \frac{k_2 v^{0.5}}{k_1 v + k_2 v^{0.5}} \tag{7.11}$$

$$Fraction\ of\ Non - Diffusion\ Controlled\ Current = \frac{k_1 v}{k_1 v + k_2 v^{0.5}} \tag{7.12}$$

The b-value for α/ε phase is 0.55 indicating that diffusion controlled kinetics is the primary reaction taking place. An increase in the b-value for the ε/δ phase to 0.66 suggests that non-diffusion controlled kinetics are having more of an influence in the reaction and is seen at the higher scan rate of 100 mV/s with almost a 50% contribution, Figure 7.5. The increase in non-diffusion controlled kinetics is expected with phase changes as this can expose metal ions within the bulk to the outer surface and promote intercalation that is not diffusion controlled[17].
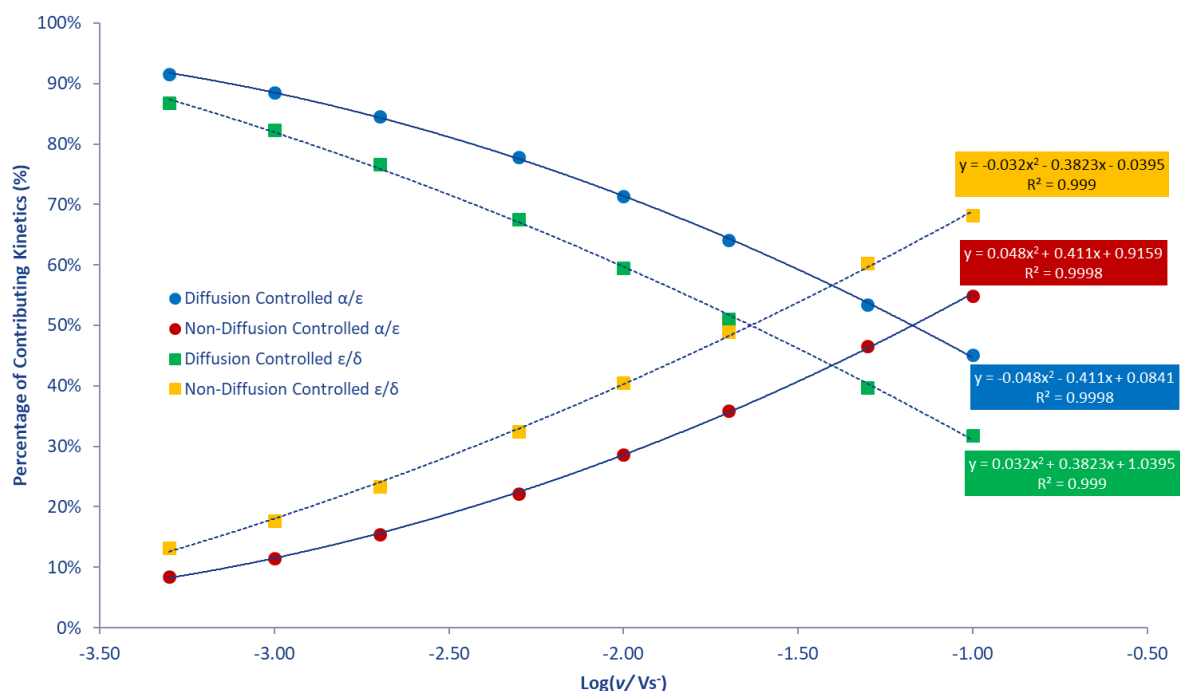
Figure 7.5: Percentage of contributing electrochemical kinetics at various scan rates for α/ε and ε/δ phases.

The diffusion coefficient was obtained using the Randles-Sevcik equation, (Equation 7.13).

$$i = (2.69 \times 10^5)n^{3/2}AC_{Li}D_{Li}^{1/2}\,v^{1/2} \qquad\qquad 7.13$$

where *n* is the number of electrons transferred, *A* is the geometric area of the electrode, C_{Li} is the bulk concentration of Li in the electrode and D_{Li} is the diffusion coefficient of Li in the thin film electrode. The diffusion is assumed to be one dimensional across the Li$^+$ ion concentration gradient for the thin film electrode. In techniques such as electrochemical impedance spectroscopy (EIS), potentiostatic intermittent titration technique (PITT) and galvanostatic intermittent titration technique (GITT) this assumption is used when measuring the diffusion coefficient for Li$^+$ ions in electrode materials[18]. The diffusion coefficients for the α/ε and ε/δ phases are determined using the Randles-Sevcik equation, where the peak current of the corresponding phases is plotted against the square root of the CV scan rate. The diffusion coefficients for the α/ε and ε/δ phases is 9.44×10^{-12} and 2.84×10^{-11} cm^2/s, respectively, with the average diffusion coefficient being 1.89×10^{-11} cm^2/s which is one order of magnitude greater than the literature [19].

The cycle performance was analysed by CV at a scan rate of 10 mV/s and it was found that the capacity faded rapidly with no capacity remaining at 100 cycles, Figure 7.6. The

dissolution of V_2O_5 is the main reason for the capacity drop and no V_2O_5 remained on the Au current collector at the end of the experiment.
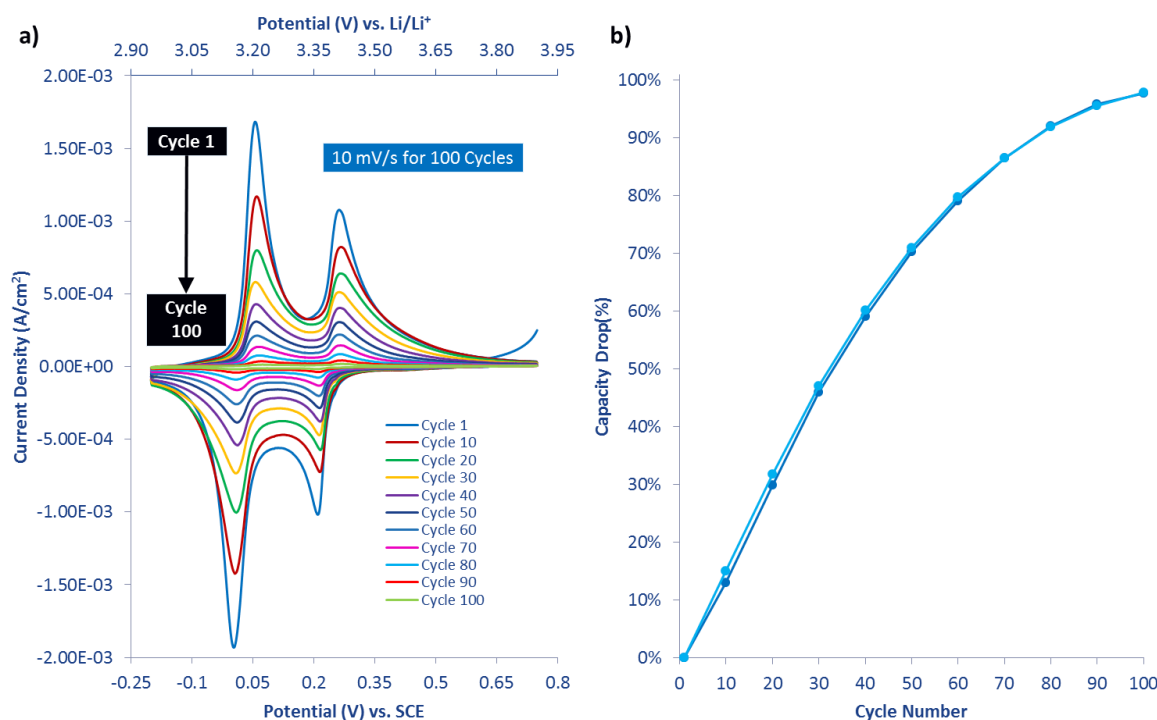
Figure 7.6: a, CV of V_2O_5 for 100 cycles at a scan rate of 10 mV/s. **b,** Capacity drop percentage per cycle.

This is expected since V_2O_5 is soluble in water (4 mM) and assuming all the V_2O_5 is dissolved into the electrolyte this would give a concentration of 0.007 mM which is almost 550 times lower than the solubility limit. The severity of dissolution of V_2O_5 suggests that the results in Figure 7.5 are not completely representative of the material.

TiO_2 is a common coating used on cathodes in organic electrolytes to protect the transition metal ions dissolution by HF generated during electrolyte degradation during cycling. HF is not generated in aqueous electrolytes but the principle of the TiO_2 coating to protect the cathode is applicable to ARLB as the coating can reduce the contact between the V_2O_5 and the H_2O molecules and subsequently reduce electrode dissolution. TiO_2 coatings of 50 and 100 nm were applied to the V_2O_5 electrode and the electrochemical kinetics and cycle stability were investigated.

The b-value obtained from the α/ε and ε/δ peaks were 0.52 and 0.53, respectively, for a 50 nm TiO_2 coated sample and 0.47 and 0.51, respectively, for a 100 nm TiO_2 coated sample which indicates that lithiation is solely diffusion controlled, Figure 7.7.

The Randles-Sevcik equation was again used to determine the diffusion coefficient for the α/ε and ε/δ phases and are 3.50×10^{-12} and 7.50×10^{-12} cm^2/s, respectively, with an average diffusion coefficient of 5.50×10^{-12} cm^2/s for a 50 nm TiO$_2$ coating. The 100 nm TiO$_2$ coated V$_2$O$_5$ has a lower diffusion coefficient of 2.85×10^{-12} and 6.45×10^{-12} cm^2/s for the α/ε and ε/δ phases, respectively, with an average of 4.65×10^{-12} cm^2/s due to an increase in distance between the V$_2$O$_5$ and the electrolyte. The slower diffusion coefficients and negligible contribution from non-diffusion kinetics for the TiO$_2$ samples can be explained as the coating protects and minimises the exposure of the V-ion in the bulk to the outer surface and pseudocapacitive processes.
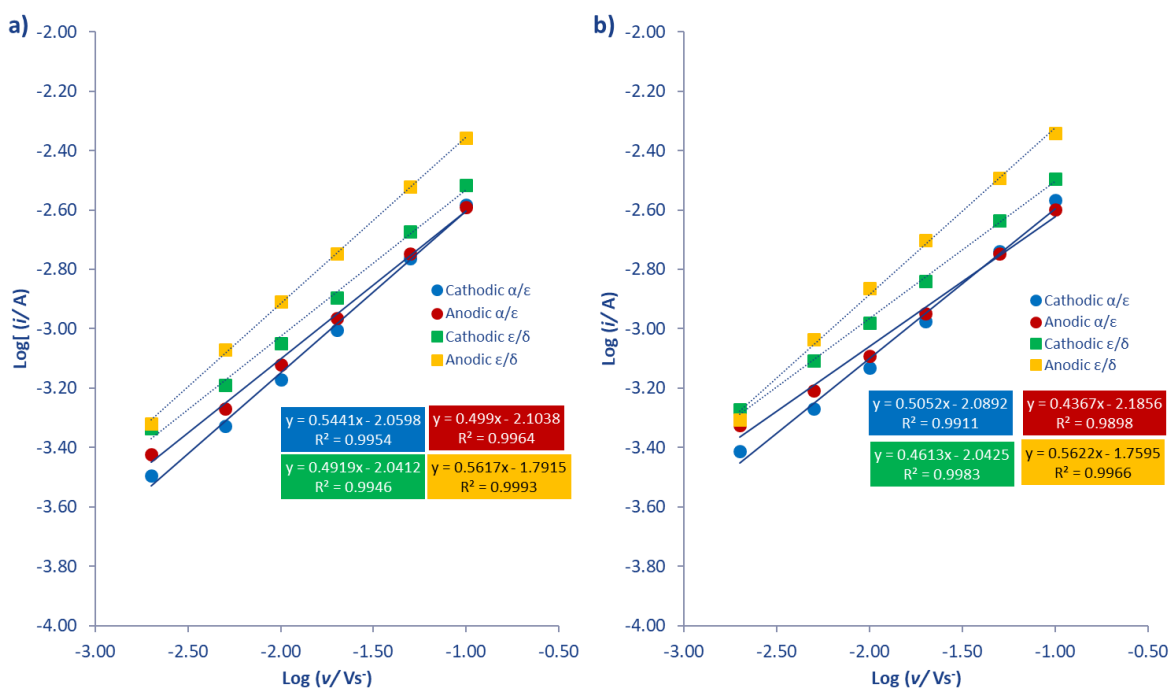
Figure 7.7: log(i) versus log(v) to determine of the b-exponent which is related to the electrochemical kinetics for **a,** 50 nm TiO$_2$ coated V$_2$O$_5$ and **b,** 100 nm TiO$_2$ coated V$_2$O$_5$.

The characteristic redox V$_2$O$_5$ peaks, α/ε and ε/δ, are present for both coating thickness values from 0.5 to 100 mV/s which indicates that lithiation is not prevented by the TiO$_2$ coatings on the V$_2$O$_5$ electrode, Figure 7.8. There was little or no change in the peak separation for the 50 nm TiO$_2$ sample in comparison to an uncoated sample however there was an increase for the 100 nm TiO$_2$ which is expected due to a thicker and more resistive electrode/electrolyte interface as seen in Table 7.1. The cycle performance was similar to uncoated V$_2$O$_5$ with capacity fading rapidly over 100 cycles. The TiO$_2$ coatings do not prevent the dissolution of V$_2$O$_5$ and capacity fading.
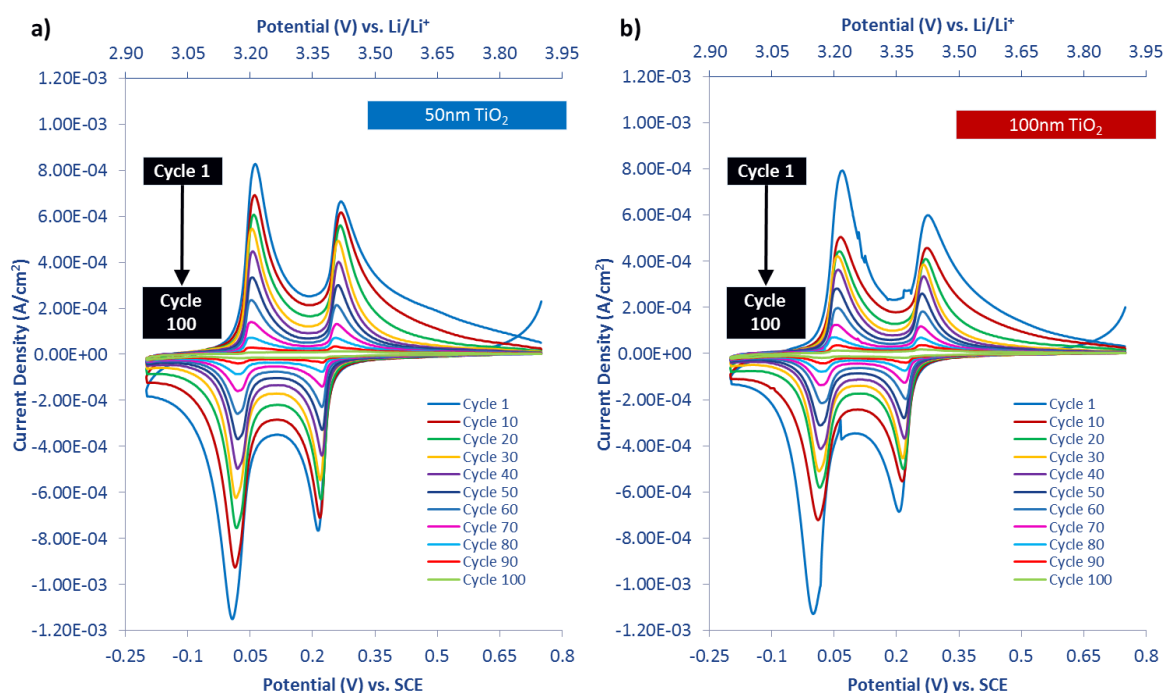
Figure 7.8: CV for 100 cycles at a scan rate of 10 mV/s for **a,** 50 nm TiO$_2$ coated V$_2$O$_5$ and **b,** 100 nm TiO$_2$ coated V$_2$O$_5$ in 5 M LiNO$_3$

Table 7.1: CV peak separation of the α/ε and ε/δ phases at 1, 10 and 50 mV/s for the V$_2$O$_5$, 50 nm TiO$_2$/V$_2$O$_5$ and 100 nm TiO$_2$/V$_2$O$_5$ samples.

Sample	1 mV/s		10 mV/s		50 mV/s	
	α/ε	ε/δ	α/ε	ε/δ	α/ε	ε/δ
	mV		mV		mV	
V$_2$O$_5$	22	12	52	53	92	110
50 nm TiO$_2$ + V$_2$O$_5$	24	22	53	59	103	115
100 nm TiO$_2$ + V$_2$O$_5$	28	25	69	74	134	151

An alternative approach was to use VC additive in the 5 M LiNO$_3$ aqueous solution as 5 and 10 wt. % of the lithium salt. An electrolyte additive is classed as ≤ 10 wt. % or vol. % with anything greater classed as a co-solvent. The pH of the electrolyte was monitored for 24 hours and exhibited a drop from 7 to 4.78 and 3.04 for 5 and 10 wt. % VC, respectively. The polymerisation of VC results in CO$_2$ as a by-product which would form carbonic acid (H$_2$CO$_3$) in an aqueous environment and result in a drop in pH. The pH decrease indicates that the VC is reacting with the electrolyte solution as it is either being oxidised or reduced to produce polymerised VC and CO$_2$, Figure 7.9. LiNO$_3$ is a well-known oxidizing agent and would explain the drop in pH as it would oxidise the VC additive to produce CO$_2$.
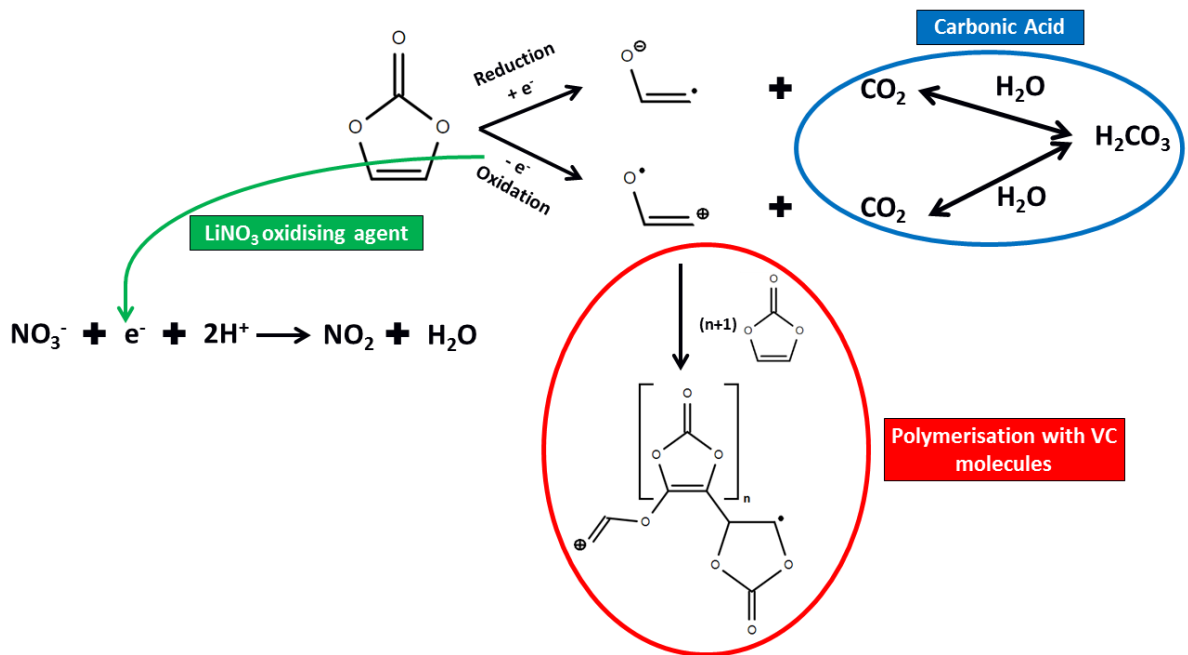
Figure 7.9: Schematic of VC reaction in 5 M LiNO$_3$ aqueous electrolyte.

The LiNO$_3$ is in excess in the electrolyte meaning the pH is directly related to the quantity of CO$_2$ produced, which is equal to the amount of VC in solution. Equation 7.14 shows the first acid equilibrium of CO$_2$ and H$_2$CO$_3$. At equilibrium the dissociation constant (K$_a$) of CO$_2$ in water at room temperature is 4.5×10^{-7}.

$$CO_2 + H_2O \leftrightarrow H^+ + HCO_3^-$$
(7.14)

The proton and bicarbonate concentrations are equal so the equation can be simplified according to Equation 7.15. The proton concentration is solved for and used in Equation 7.16 to calculate the expected pH of the electrolyte when 5 and 10 wt. % VC additive is used.

$$K_a = 4.5 \times 10^{-7} = \frac{[H^+][HCO_3^-]}{[CO_2]} = \frac{[H^+]^2}{[CO_2]}$$
(7.15)

$$pH = -\log[H^+]$$
(7.16)

The calculated pH for 5 and 10 wt. % VC is 3.52 and 3.37, respectively, which are in line with the pH recorded for the electrolyte. The cycle stability and electrochemical kinetics were investigated on the V$_2$O$_5$ electrode in the VC additive based electrolytes.

The cycle stability was enhanced with a capacity drop of 54 % and 21 % for the 5 and 10 wt. % VC electrolyte, respectively, over 100 cycles, Figure 7.10. V_2O_5 is more soluble in acidic solutions, however, even though the addition of VC to the electrolyte drops the pH the cycle performance is enhanced by a protective polymerised coating on the electrode which minimises V_2O_5 dissolution in the more acidic solution and V_2O_5 is clearly present and active on the current collector even after 200 cycles[20]. The α/ε and ε/δ redox peaks are well defined for scan rates as high as 100 mV/s for both electrolytes. There is a small increase, but not as large as the 100 nm TiO_2 coated sample. The peak separation of the redox peaks for the 10 wt. % VC electrolyte which is expected since the VC derived polymer coatings cause an increase in resistance.

Table 7.2: CV peak separation of the α/ε and ε/δ phases at 1, 10 and 50 mV/s for the V_2O_5, V_2O_5 in 5 wt. % VC and V_2O_5 in 10 wt. % VC samples.

Sample	1 mV/s		10 mV/s		50 mV/s	
	α/ε	ε/δ	α/ε	ε/δ	α/ε	ε/δ
	mV		mV		mV	
V_2O_5	22	12	52	53	92	110
V_2O_5 in 5 wt. % VC	23	13	50	42	92	94
V_2O_5 in 10 wt. % VC	24	32	60	55	117	121
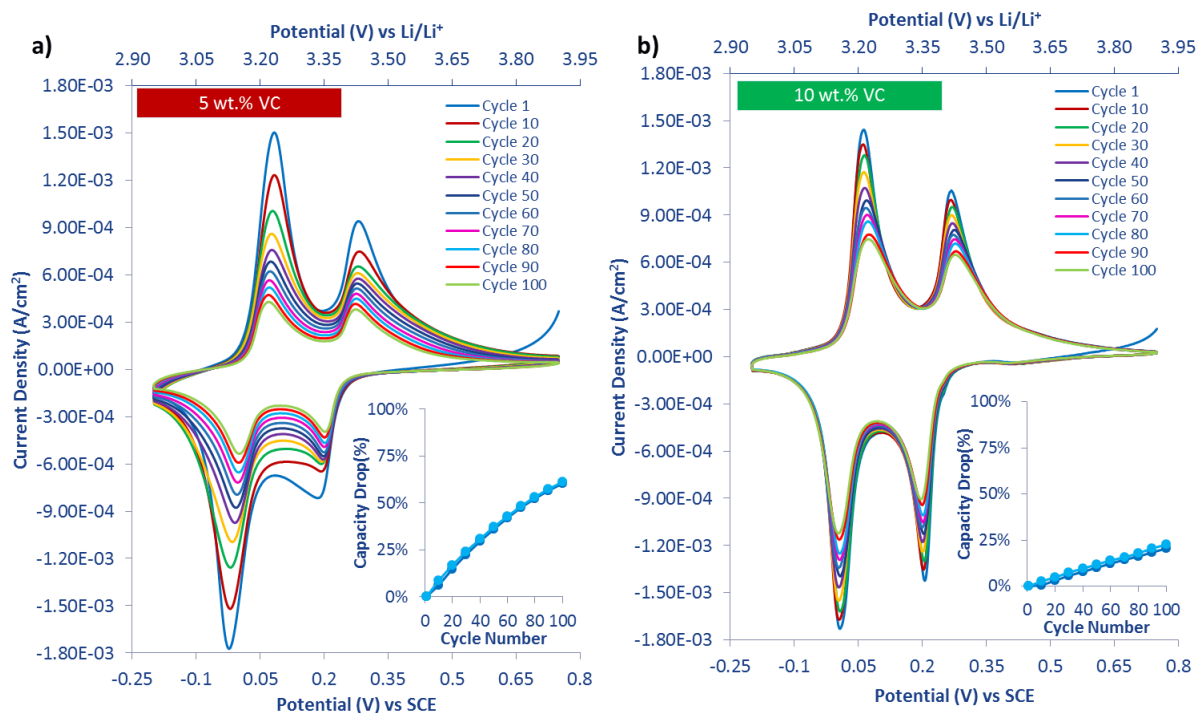
Figure 7.10: CV of V_2O_5 for 100 cycles at a scan rate of 10 mV/s in **a,** 5 wt. % VC and **b,** 10 wt.% VC additive in 5 M $LiNO_3$. Insert: graph of capacity drop per cycle.

The b-value for the ratio of for the α/ε and ε/δ peaks obtained for the V_2O_5 electrode in 5 wt. % VC additive is 0.67 and 0.75, respectively, and 0.66 and 0.83, respectively, for the 10 wt. % VC additive. This suggests that non-diffusion controlled kinetics have a significant contribution to the lithiation process. In Figure 7.11 the electrochemical contributions are quantified and it shows the non-diffusion controlled kinetics become the dominant kinetics at scan rates over 20 mV/s and 5 mV/s for 5 and 10 wt. % VC, respectively. The diffusion coefficient for the V_2O_5 in 5 wt.% VC is similar to the additive-free electrolyte with values of $1.17x10^{-11}$ and $2.61x10^{-11}$ cm^2/s for α/ε and ε/δ phases, respectively and an average value of $1.89x10^{-11}$ cm^2/s. The average diffusion coefficient for V_2O_5 in 10 wt. % VC is doubled to $2.60x10^{-11}$ cm^2/s, with α/ε and ε/δ phases having coefficients of $1.52x10^{-11}$ and $3.68x10^{-11}$ cm^2/s, respectively. The increase in b-value and decrease of the diffusion coefficient with increasing VC concentration confirm that the dissolution of V_2O_5 has significantly reduced, essentially the amount of V_2O_5 is considered fixed. Therefore the experimental results give a more accurate description of the electrode capabilities unlike the case discussed earlier which most likely had the complication of electrode dissolution also occurring during kinetic data analysis.
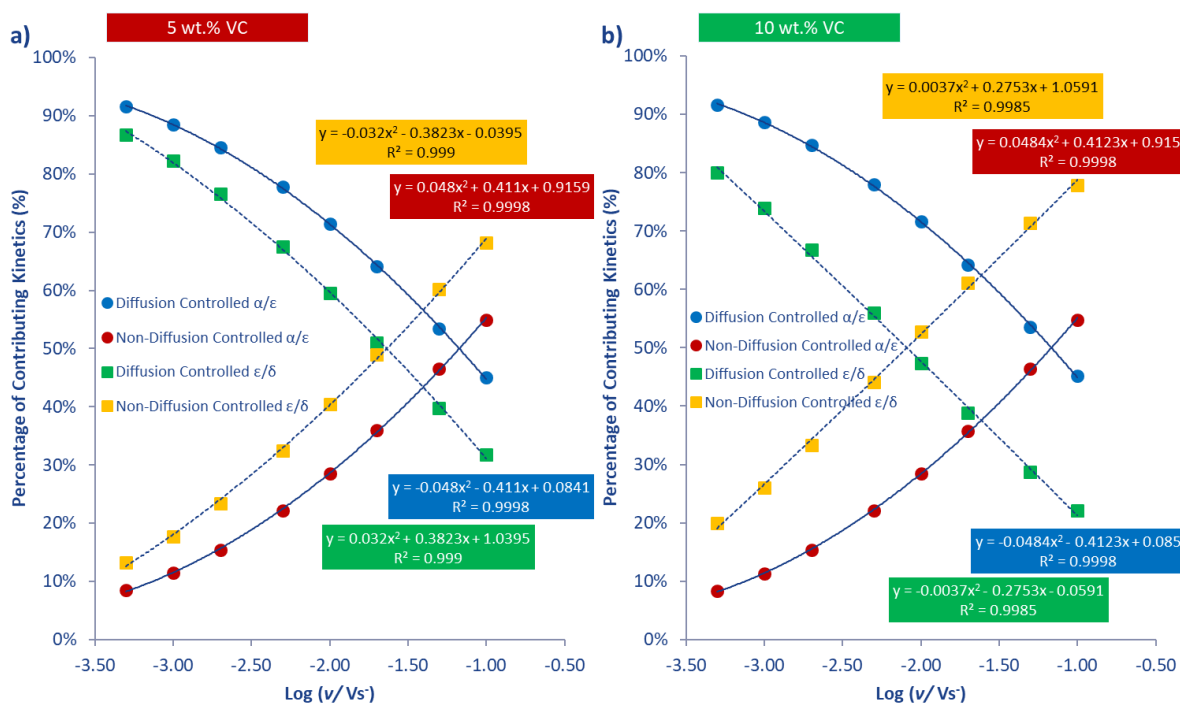
Figure 7.11: Percentage of contributing electrochemical kinetics at various scan rates for α/ε and ε/δ phases of V_2O_5 in **a,** 5 wt. % VC and **b,** 10 wt. % VC additive in 5 M $LiNO_3$ aqueous electrolyte.

A combination of VC electrolyte additive and TiO_2 electrode coating was investigated as the VC was shown to minimise V_2O_5 dissolution and the TiO_2 coating reduced the interaction between V_2O_5 and the H_2O molecules. The TiO_2 coating was fixed at 100 nm and the VC additive concentrations of 5 and 10 wt. % were used. A comparison of the CV profiles for the initial 8 cycles at 0.5, 1, 2, 5, 10, 20, 50 and 100 mV/s scan rates are seen in Figure 7.12. The 100 nm TiO_2 sample in 5 wt. % VC additive electrolyte shows the characteristic redox peaks indicating the α/ε and ε/δ phases for all scan rates. The redox peaks for the α/ε phase are present for the 100 nm TiO_2 sample in 10 wt.% VC additive electrolyte however the cathodic peak is broader and less intense while the redox peaks for the ε/δ phase appear to be suppressed and only become prominent at 100 mV/s scan rate. The current densities for all the scan rates are significantly smaller in comparison to the 100 nm TiO_2 sample in 5 wt. % VC additive electrolyte. This coupled with the suppression of the ε/δ phase peaks indicates that interaction between the VC and TiO_2 is hindering Li^+ ions from intercalating into the V_2O_5 electrode.

Figure 7.12: CV of 100 nm TiO$_2$ on V$_2$O$_5$ at 0.5, 1, 2, 5, 10, 20, 50 and 100 mV/s in **a,** 5 wt. % VC and **b,** 10 wt.% VC in 5 M LiNO$_3$ aqueous electrolyte. Insert lower current data of slower CV scan rates of 0.5, 1, 2 and 5 mV/s.

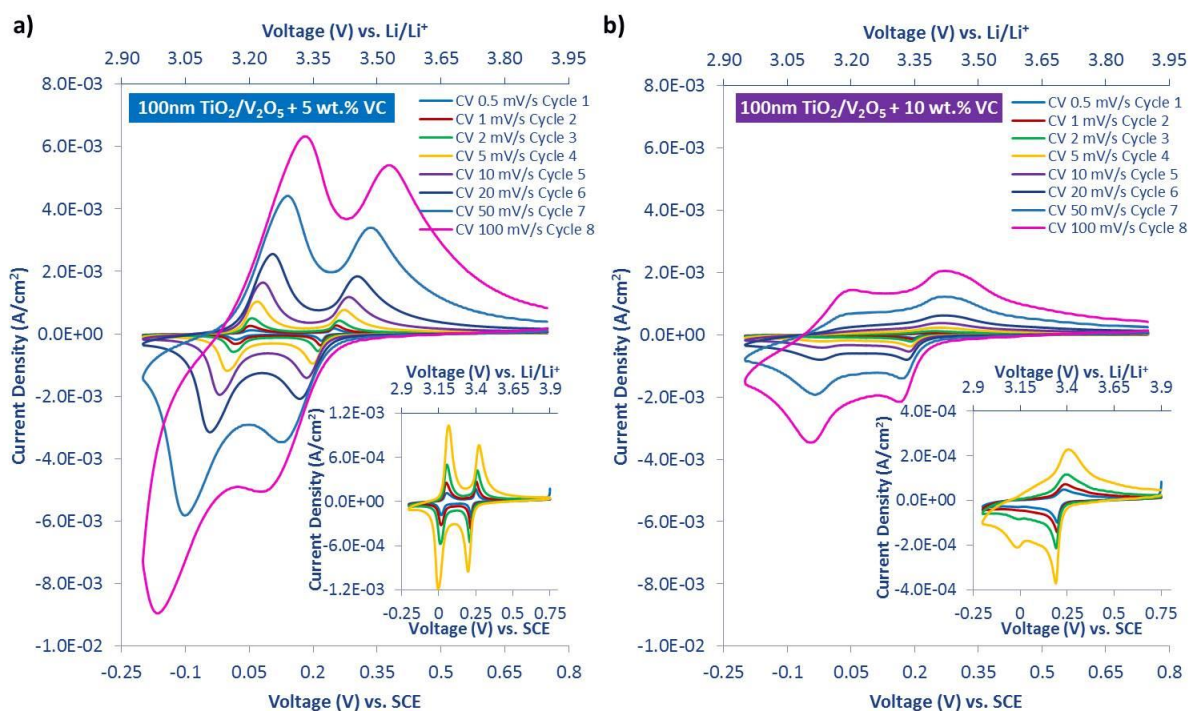The redox peaks for the α/ε and ε/δ phases showed a significant increase in peak separation, for the 100 nm TiO$_2$ coated sample in 5 wt. % VC additive electrolyte, with separations of 99 and 102 mV at 10 mV/s and 211 and 243 mV at 50 mV/s for the α/ε and ε/δ phase peaks, respectively, in comparison to an uncoated electrode and additive free electrolyte, Figure 7.13. At 10 mV/s the peak separations of an uncoated electrode in 5 wt. % VC is 50 and 42 mV for the α/ε and ε/δ phases, respectively, and 92 and 94 mV for the α/ε and ε/δ phases, respectively, at 50 mV/s. An additive-free electrolyte with a 100 nm TiO$_2$ coated V$_2$O$_5$ electrode has peak separations of 69 and 74 mV for the two characteristic redox pairs at 10 mV/s and at 50 mV/s the peak separations are 134 and 151 mV. The increase in peak separation is expected as the 100 nm TiO$_2$ coating increases the electrode/electrolyte interface resistance. However, the effect of the VC additive with TiO$_2$ coating was unexpected. There was little or no difference in peak separation for an uncoated sample in VC additive and additive-free electrolyte. This suggests that polymerised VC is interacting with TiO$_2$ at the interface resulting in larger peak separations and an increase in resistance.

A V$_2$O$_5$ electrode with a 100 nm coating of TiO$_2$ in an aqueous electrolyte with 5 wt.% VC additive has b-values of 0.61 and 0.70 for the α/ε and ε/δ peaks, respectively. The contribution from the non-diffusion controlled kinetics has increased significantly compared

to a 100 nm TiO_2 coated V_2O_5 electrode in additive-free electrolyte which was completely diffusion controlled and only slightly lower than that for the uncoated V_2O_5 in VC additive electrolyte. Again the contribution towards the non-diffusion controlled kinetics is greater for the ε/δ redox change compared to the α/ε redox which we have attributed to the phase change exposing metal ions which promote non-diffusion controlled lithiation. The diffusion coefficients for the α/ε and ε/δ phases is 1.21×10^{-11} and 2.83×10^{-11} cm^2/s with an average of 2.83×10^{-11} cm^2/s is slightly higher than the uncoated electrode in the electrolyte containing the VC additive and significantly higher than the 100 nm TiO_2 coated electrode in additive-free electrolyte.
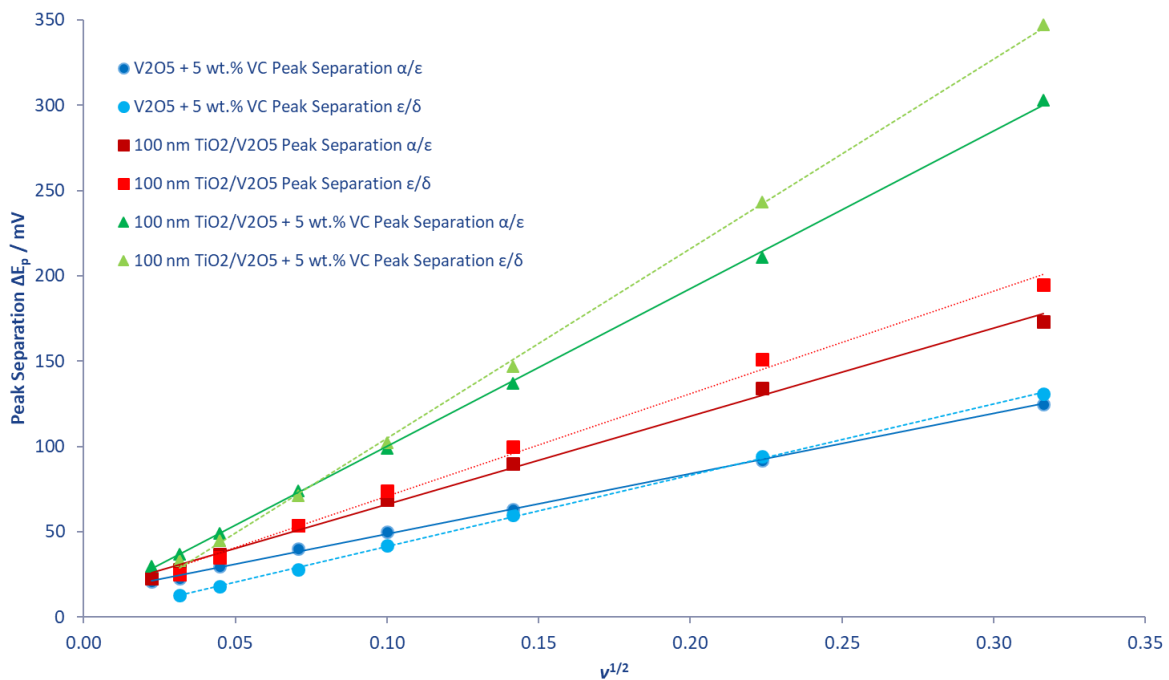
Figure 7.13: Peak separation comparison of uncoated V_2O_5 in 5 wt. % VC additive electrolyte, 100 nm TiO_2 coated V_2O_5 in additive free electrolyte and 100 nm TiO_2 coated V_2O_5 in 5 wt. % VC additive electrolyte at various scan rates.

The cycle stability was enhanced with a capacity drop of 28% and 41% after 100 and 200 cycles, respectively, when cycling at 10 mV/s scan rate. This is a considerably smaller capacity drop compared to 100% and 54% for a 100 nm TiO_2 coated V_2O_5 and an uncoated V_2O_5 in 5 wt. % VC electrolyte, respectively, after 100 cycles. The capacity drop is similar to that of an uncoated sample in 10 wt. % VC additive electrolyte, Figure 7.14. TiO_2 coating enhances the polymerisation of the VC additive in the electrolyte since an uncoated sample in 10 wt. % VC shows enhanced cycle performance without compromising the lithiation process of the V_2O_5 while a 100 nm TiO_2 coated sample in 10 wt. % VC results in excessive

polymerisation that suppresses the phase transformation from α/ε to ε/δ and the lithiation of the α/ε phase.
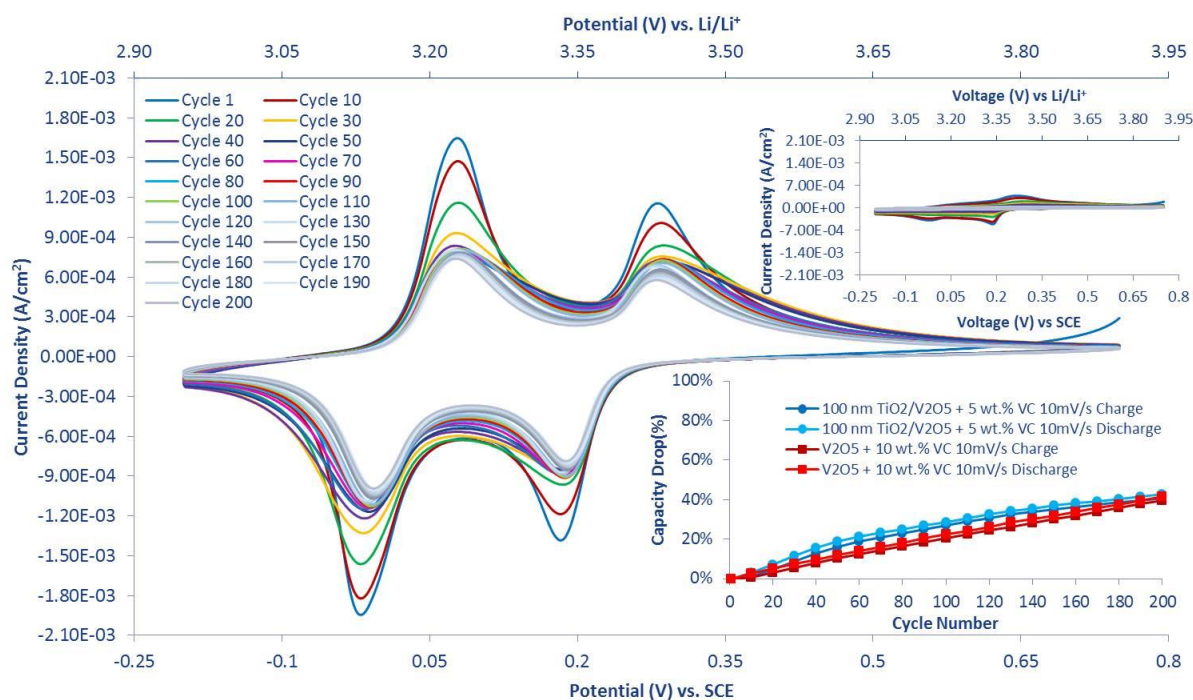
Figure 7.14: CV of 100 nm TiO$_2$ coated V$_2$O$_5$ for 200 cycles at a scan rate of 10 mV/s in 5 wt. % VC additive in 5 M LiNO$_3$. Inserted, CV of 100 nm coated V$_2$O$_5$ for 200 cycles with a 10 mV/s scan rate in 10 wt. % VC additive. Capacity drop per cycle comparison between 100 nm TiO$_2$ coated V$_2$O$_5$ in 5 wt. % VC additive and uncoated V$_2$O$_5$ in 10 wt. % VC additive.

Conclusion

Electrodeposited V$_2$O$_5$ was tested in a 5 M LiNO$_3$ aqueous electrolyte and showed high rate capabilities due to a significant contribution from non-diffusion controlled kinetics, pseudocapacitive processes at high CV scan rates. Severe capacity fade was observed which was attributed to the dissolution of the V$_2$O$_5$. 50 and 100 nm TiO$_2$ coatings were applied to minimise the direct exposure of the active V$_2$O$_5$ to the H$_2$O molecules. The coating did impact the exposure of the V$_2$O$_5$ and contributed to a slower diffusion coefficient. However, capacity fade for the V$_2$O$_5$ was not decreased. Utilising VC additive in the aqueous electrolyte resulted in a drop in pH which suggests polymerisation of VC. A decrease in capacity fade and improvement in electrochemical kinetics occurs with an increase in the wt. % of VC added to the aqueous electrolyte. The combination of a TiO$_2$ coating and VC

additive to the electrolyte results in a similar capacity fade however a lower wt. % of VC is required and slightly lower rate capabilities are seen with the TiO_2 coated V_2O_5. This study demonstrates that VC is an effective additive for ARLB with a V_2O_5 electrode that can improve the cycle stability. TiO_2 coated V_2O_5 in combination with small wt. % of VC additive shows similar performance. Further study is required to understand the mechanism that VC undergoes in the electrolyte and whether the VC polymerises and protects the V_2O_5. Future recommended work would include quantitative material analysis (TEM) at the V_2O_5 and V_2O_5/TiO_2 interface after lithium cycling in the VC additive electrolyte. UV-visible spectrophotometry of the electrolyte to determine the concentration of the V-ions that dissolves in the electrolyte over time.

References

[1]   C. Delmas, H. Cognac-Auradou, J. M. Cocciantelli, M. Ménétrier, J. P. Doumerc, *Solid State Ionics* **1994**, *69*, 257-264.
[2]   J. M. Cocciantelli, M. Ménétrier, C. Delmas, J. P. Doumerc, M. Pouchard, M. Broussely, J. Labat, *Solid State Ionics* **1995**, *78*, 143-150.
[3]   C. Leger, S. Bach, P. Soudan, J.-P. Pereira-Ramos, *J. Electrochem. Soc.* **2005**, *152*, A236-A241.
[4]   a) E. Armstrong, M. Osiak, H. Geaney, C. Glynn, C. O'Dwyer, *CrystEngComm* **2014**, *16*, 10804-10815; b) H. Y. Lee, J. B. Goodenough, *J. Solid State Chem.* **1999**, *148*, 81-84; c) R. N. Reddy, R. G. Reddy, *J. Power Sources* **2006**, *156*, 700-704.
[5]   a) T. Katsunori, J. L. Steven, W. Ying, C. Guozhong, *Jpn. J. Appl. Phys.* **2005**, *44*, 662; b) D. Chao, X. Xia, J. Liu, Z. Fan, C. F. Ng, J. Lin, H. Zhang, Z. X. Shen, H. J. Fan, *Adv. Mater.* **2014**, *26*, 5794-5800.
[6]   W. Li, J. R. Dahn, *J. Electrochem. Soc.* **1995**, *142*, 1742-1746.
[7]   a) R. Ruffo, F. La Mantia, C. Wessells, R. A. Huggins, Y. Cui, *Solid State Ionics* **2011**, *192*, 289-292; b) F. Sauvage, L. Laffont, J. M. Tarascon, E. Baudrin, *J. Power Sources* **2008**, *175*, 495-501.
[8]   J. Yang, T. B. Lan, J. D. Liu, Y. F. Song, M. D. Wei, *Electrochim. Acta* **2013**, *105*, 489-495.
[9]   H. Wang, Y. Zeng, K. Huang, S. Liu, L. Chen, *Electrochim. Acta* **2007**, *52*, 5102-5107.
[10]   a) A. D. Pasquier, F. Orsini, A. S. Gozdz, J. M. Tarascon, *J. Power Sources* **1999**, *81-82*, 607-611; b) S. Kuwabata, S. Masui, H. Yoneyama, *Electrochim. Acta* **1999**, *44*, 4593-4600; c) S. Kuwabata, T. Idzu, C. R. Martin, H. Yoneyama, *J. Electrochem. Soc.* **1998**, *145*, 2707-2710.
[11]   I. B. Stojković, N. D. Cvjetićanin, S. V. Mentus, *Electrochem. Commun.* **2010**, *12*, 371-373.
[12]   L. El Ouatani, R. Dedryvère, C. Siret, P. Biensan, D. Gonbeau, *J. Electrochem. Soc.* **2009**, *156*, A468-A477.
[13]   N. Alias, A. A. Mohamad, *J. Power Sources* **2015**, *274*, 237-251.
[14]   N. Alias, A. A. Mohamad, *Ceram. Int.* **2014**, *40*, 13089-13096.

[15]   R. Ruffo, C. Wessells, R. A. Huggins, Y. Cui, *Electrochem. Commun.* **2009**, *11*, 247-249.

[16]   a) R. Baddour-Hadjean, J. P. Pereira-Ramos, C. Navone, M. Smirnov, *Chem. Mater.* **2008**, *20*, 1916-1923; b) R. Baddour-Hadjean, A. Marzouk, J. P. Pereira-Ramos, *J. Raman Spectrosc.* **2012**, *43*, 153-160.

[17]   Y. Wang, Y. Song, Y. Xia, *Chem. Soc. Rev.* **2016**, *45*, 5925-5950.

[18]   a) B. E. Conway, *Electrochim. Acta* **1993**, *38*, 1249-1258; b) M. D. Levi, D. Aurbach, *J. Electroanal. Chem.* **1997**, *421*, 79-88; c) M. D. Levi, G. Salitra, B. Markovsky, H. Teller, D. Aurbach, U. Heider, L. Heider, *J. Electrochem. Soc.* **1999**, *146*, 1279-1289; d) H. Xia, L. Lu, M. O. Lai, *Electrochim. Acta* **2009**, *54*, 5986-5991.

[19]   a) J. M. McGraw, C. S. Bahn, P. A. Parilla, J. D. Perkins, D. W. Readey, D. S. Ginley, *Electrochim. Acta* **1999**, *45*, 187-196; b) D.-Y. Yoo, I.-H. Yeo, W. I. Cho, Y. Kang, S.-i. Mho, *Anal. Sci.* **2013**, *29*, 1083-1088; c) X. Huang, X. Rui, H. H. Hng, Q. Yan, *Part. Part. Syst. Charact.* **2015**, *32*, 276-294.

[20]   M. Skyllas-Kazacos, L. Cao, M. Kazacos, N. Kausar, A. Mousa, *ChemSusChem* **2016**, *9*, 1521-1543.

Chapter 8 Summary, Conclusion and Future Work

Summary

General Introduction

Fabrication techniques continue to evolve and have resulted in improved electrode structures and consequently battery performance. Research studies of the "form and function" of battery components for their intended application have increased slowly over the years. The need for further investigations into the connection between material morphologies tailored for specific application and performance characteristics required in these applications has become more apparent.

In this work, we have considered new geometries, materials and substrates for the development of high performance rechargeable 3D Li-ion microbatteries for application in wireless sensors in the "Internet of Things" scenario. To increase cycle life thin-film additive-free electrodes and solid-state electrolytes have been investigated. The thickness of the cathode electrode in thin-film microbatteries have a quadratic relationship with the time it takes for Li^+ ions to diffuse into the electrode and the solid-state electrolyte has an ionic conductivity that is almost 3 orders of magnitude smaller than typical organic electrolytes. This has resulted in thin-film solid-state microbatteries that have a limited energy (electrode thickness) and power (ionic conductivity of electrolyte) capabilities to power wireless sensors that are energy and power demanding. Area is also at a premium in such devices and thin film microbatteries occupy a large footprint per unit energy stored. The wireless sensor at peak operational time requires a large current which results in a significant voltage drop in typical thin-film microbatteries which results in a smaller energy density and an increase in the degradation of the microbattery leading to shortened cycle life.

The goal of the project was to design and fabricate nanosized electrodes that would enable increased life time and functionality of portable systems with specific Li-ion microbattery capacities. The main objective of this work was to use COMSOL Multiphysics to design and simulate nanosized electrodes in lithium batteries with high energy and power densities and then implement these designs using state-of-the-art fabrication techniques to fabricate 3D Li-

ion electrodes to overcome the size and energy-density deficiency of the conventional 2D battery.

Literature Review

In chapter 1, is a brief discussion on the history and chemistry of the battery pre 20th century, from the first battery in 1799 called the Voltaic pile through to the Daniell Cell in 1836, that enabled the deployment of telegraphic technology, to the Pb-acid battery (rechargeable) in 1859 and Leclanché cell (primary) in 1866. The rechargeable battery development in the 20th century was described that led to alkaline batteries, such as Ni-Cd and Ni-MH, and Li-ion batteries being the key enablers in new technologies. The evolution of the lithium battery was discussed in detail as this is the most prominent battery used today and its chemistry is the focus of this thesis.

A rechargeable Li-ion battery is made up of a 2 electrodes separated by an electrolyte. The characteristics of these 3 materials are discussed and how these characteristics, such as standard potential, diffusion rate, conductivity and charge transfer, affect the battery performance and can be used to theoretically calculate the cell potential, half-cell and full-cell capacity etc. by using the appropriate mathematical equations.

A comprehensive discussion on suitable anode and cathode materials is given. A particular focus is on advanced anode materials that have large capacities, such as Si, Ge and Sn, and cathode materials that have a larger standard potential and capacity. We discuss the lithiation process and the limitations of such electrode in bulk form. We highlight the current research involving such materials as anodes and cathodes and how state-of-the-art fabrication techniques are being used to create different nanoarchitectures to enhance the cycle life, rate capability, energy density and power density. This work is focused on additive-free electrodes that have a large surface area as they offer short transport paths for Li^+ and e^- and higher energy density of the cell within the same areal footprint.

The chapter also described a range of lithium salts that have been used in organic electrolytes and how they can influence the cell performance. We examined the properties of such salts and how derivatives have been developed to either improve certain characteristics or remove them or a combination of both. We also review additives that have been used to help form a stable SEI layer on the anode, prevent overcharging, act as a flame-retardant or scavenge detrimental intermediate products, anions or water molecules in the solvent.

A review of lithium cycling in aqueous electrolytes was also reported including recent advances. We highlight that switching to aqueous electrolytes would result in the costs being reduced, the system being inherently safer, high ionic conductivity, high lithium salt solubility and no SEI layer formation. This all adds up to a cheap battery system that is safer and has faster kinetics resulting in the electrolyte having minimum effect on the performance of the battery cell. The major disadvantage of such electrolytes is smaller electrochemical window of 1.23 V in comparison to an organic system, 4.2 V. Cathode materials such as $LiCoO_2$, $LiMn_2O_4$ and $LiFePO_4$ undergo lithiation within the electrochemical window of an aqueous electrolyte. We discuss the performance of such electrodes in an aqueous electrolyte and the side reactions between the electrode and electrolyte that can potentially influence performance. We discuss in detail the strategies that have been implemented to reduce negative side reactions which result in enhanced cycle life. Other strategies that extend the electrochemical window by reducing interaction between the water molecules and the electrode are also discussed in great detail.

Electrochemical & Physical Techniques

We discussed the fundamental principles of the electrochemical, physical characterisation and physical vapour deposition techniques in this chapter. Cyclic voltammetry, chronopotentiometry and chronoamperometry are typical techniques used in electrodeposition and battery studies. The scanning electron microscopy (SEM) coupled with the energy dispersive x-ray spectrometry (EDS) is an efficient instrument to study the surface morphology, microstructure changes during Li^+ intercalation and de-intercalation and give quantitative material analysis. The X-ray diffraction (XRD) and Raman spectroscopy are common non-destructive analytical techniques that give information on the crystalline structure and chemical structure, respectively. A profilometer was mostly used to measure the microstructured materials and thin film dimensions. DC magnetron sputtering was the physical vapour deposition technique used to deposit substrates, current collectors and electrode materials.

COMSOL Multiphysics Simulations of Thin-Film, 3D and 3D Core-Shell Nanoarchitectures

COMSOL Multiphysics was used to compare a planar thin-film microbattery to a 3D nanoarchitectured and 3D core-shell nanoarchitectured battery in solid-state, polymer, polymer-gel and organic solvent electrolyte characteristics. The electrodes simulated using

finite element analyses were non-porous electrodes and free of conductive additives. We show there is no increase in capacity with improving electrolyte characteristic for a planar thin-film microbattery at specific discharge rates just a decrease in the potential drop or loss of power at higher current rates.

In order to compare the performances of the geometries the areal capacity of the planar thin-film microbattery at 0.5 C a rate was used as the standard and the 3D and 3D core-shell nanoarchitectures were adjusted to match the areal capacity. The heights of the 3D and 3D core-shell nanoarchitectures were increased as required to ensure the same areal capacity as the planar thin-film microbattery as these geometries required more area in order to accommodate the additional electrolyte area in contact with the sidewall and the core current collector in these geometries.

A comparison of the 3 geometries with solid-state electrolyte characteristics results in the planar thin-film microbattery having the best performance. The low ionic conductivity and diffusion coefficient of the electrolyte result in lithium transport being faster through the electrode rather than the electrolyte. This means the additional area need for the electrolyte to be in contact with the electrode side walls in the 3D nanoarchitecture and the additional area need for the core current collector in the 3D core-shell nanoarchitecture has a negative impact on performance. The heights of the electrodes needed to be increased to accommodate the additional area. The additional electrode surface area in contact with the electrolyte is not fully utilised. This means that since the electrodes are taller for the 3D and 3D core-shell nanoarchitectures and lithiation of the cathode still takes place at the top of the electrode that effect of the 3D and 3D core-shell nanoarchitectures is to increase the diffusion length of the Li^+ ions within the electrode resulting in inferior performance.

With improving electrolyte characteristics the additional lithiation sites of the 3D and 3D core-shell nanoarchitectures are utilised. With polymer electrolyte characteristics we see a smaller potential drop and increased capacities at increasing discharge rates for the nanoarchitectures in comparison to the planar thin-film microbattery. The 3D nanoarchitectures show the best performance with the lithiation sites at the base and top of the electrode being dominant.

The polymer-gel and liquid electrolyte characteristics highlight the importance of the core current collector in 3D core-shell nanoarchitecture as this ensures uniform lithiation when Li^+ ion transport is favoured through the electrolyte rather than the electrode. This results in

significantly higher capacities at extremely high discharge rates with a small drop in potential and a battery with a high energy per unit area when operating at a high power.

Fabrication & Electrochemical Evaluation of Ge Core-Shell Anode Nanostructure

Following on from the COMSOL Multiphysics simulations which highlight the performance advantages associated with 3D core-shell nanoarchitectures, an experimental assessment of these advantages was undertaken. DC sputter deposited Ge on Cu nanotubes fabricated by electrodeposition through anodised alumina oxide (AAO) membranes is reported. The electrochemical performance of nanoscale Ge on a planar Cu substrate and the Ge film on Cu nanotubes was studied both in terms of improved electrochemical performance, suggested from the COMSOL simulations, and enhanced cycle life in order to reduce the mechanical stress the Ge films undergo due to volume expansion during lithium cycling.

Cycling of planar nanoscale Ge resulted in the formation of porous islands which result in a drop in capacity during the initial cycles as the porous islands are formed. A similar drop in capacity during the initial cycling occurred for the core-shell Cu nanotubes-Ge samples. The CV of planar nanoscale Ge was in agreement with the literature however a new redox peak was observed for the core-shell Cu nanotubes-Ge with the same Ge film presumably due to the over-lithiation of the crystalline $Li_{15}Ge_4$ phase. At low currents (20 and 30 μA) during galvanostatic cycling a voltage loop and plateau correspond to the new redox peak in the CV further supporting that the crystalline $Li_{15}Ge_4$ phase is over-lithiated.

The areal capacity increased by 150 % for the thin Ge deposit on Cu nanotubes in comparison to the Ge deposit on planar Cu. We show that at a low scan rate of 0.05 mV/s that doubling (12 min.) and quadrupling (24 min.) the deposition time of Ge on the Cu nanotubes increases areal capacity by 163 % and 260 %, respectively. Galvanostatic cycling at a discharge current of 750 μA gave capacities of 81, 121 and 144 $\mu Ah/cm^2$ for the 6 min., 12 min. and 24 min. Ge deposition on Cu nanotubes, respectively.

Galvanostatic intermittent titration technique (GITT) was used to determine the diffusion coefficient of 2×10^{-10} cm^2/s and 8×10^{-12} cm^2/s for when there is low and high concentration of Li in Ge, respectively. Ge conductivity of 1×10^{-2} S/cm was measured using a four point probe measurement.

Rapid thermal annealing (RTA) of planar Ge was shown to allow for the formation of a nanoporous network which resulted in a significant increase in capacity. Such a nanoporous

network is not typically seen for a planar sample as delamination generally occurs which reduces cycle life. However, we propose that the RTA helps to improve adhesion between the Ge and Cu current collector which prevents delamination and permits the nanoporous network to form.

Ultra-Fast Cycling of Nanoscale Thin-Film LiCoO$_2$ Cathode

We investigated the effect that the substrate has on the crystallisation of LiCoO$_2$ when the as-deposited amorphous LiCoO$_2$ nanoscale film is annealed with a RTA. We show that the RTA of LiCoO$_2$ on a borosilicate glass slide to 600 ^{o}C in both an O$_2$ and Ar environment results in the formation of inactive Co$_3$O$_4$. Ni is also an unsuitable current collector for LiCoO$_2$ that needs to be annealed to get the lithium active crystalline structure as RTA in an O$_2$ environment results in the Ni current collector being converted to NiO and the amorphous LiCoO$_2$ being converted to inactive Li$_2$O and Co$_3$O$_4$ by-products. RTA of a Ni/LiCoO$_2$ stack in an Ar environment results in crystallisation of the Ni current collector rather than being converted to NiO, however, there is little or no change in the Raman spectra which only indicates the presence of the inactive Li$_2$O and Co$_3$O$_4$ by-products.

Al is the most common current collector for composite electrodes where the cathode is already in the correct crystalline structure. We investigated its compatibility as a current collector in a fabrication processes that involved RTA. We show that the stepwise ramp up of the Al/LiCoO$_2$ to 550 ^{o}C results in the formation of the Li$^+$ ion active crystalline structure while a RTA recipe with no stabilising steps results in the formation of Li$_2$O. Both Pt and Au current collectors do not require any stabilising steps in the RTA recipe in either an O$_2$ or Au environment to be converted to the correct crystalline structure. We used SEM and TEM to show the morphology of a rough LiCoO$_2$ surface and confirm the thickness of the nanoscale thin-film on an Au current collector after being RTA to 600 ^{o}C in an Ar environment.

We report the electrochemical analysis of nanoscale thin-film LiCoO$_2$ as the COMSOL Multiphysics simulations in Chapter 4 indicate that 3D core-shell nanoarchitectures, essentially a nanoscale film of cathode material, can operate at large discharge currents with only a small drop in capacity and potential in liquid electrolyte. An aqueous electrolyte was used to investigate the electrochemical properties of a nanoscale LiCoO$_2$ thin-film in order to ensure that the performance of the electrochemical cell is solely dependent on the electrode and not influenced by the resistive electrolytes typically used in the investigation of Li-ion electrodes.

CV analysis demonstrated well defined peaks at scan rates as high as 100 mV/s. The dependence of the peak current on the scan rate shows that diffusion controlled faradaic reaction (intercalation) is not the sole transport mechanism and that there is a significant contribution from a non-diffusion controlled faradic reaction (pseudocapacitance) . We reported the percentage contribution of the storage kinetics at the various scan rates and show that pseudocapacitance becomes the dominant contribution at scan rates $\geq$ 50 mV/s.

Galvanostatic cycling at current densities equivalent to C-rates of 3, 5, 10, 20, 50, 100 and 200 C were reported where all charge and discharge curves had the characteristic plateau for $LiCoO_2$ and a minimal potential drop. Capacity values obtained for a cycle (charging and discharging) at 10 C (6 min.) and 200 C (18 s) rates were 108 and 96 mAh/g, respectively. Long-term cycling at a 200 C rate for over 500 cycles was recorded and showed that after the stabilising cycles (134 cycles) the capacity only dropped by 0.08 % per cycle for 400 cycles to 70 mAh/g. The galvanostatic profiles retained the characteristic plateau during all the cycles indicating little interference from side reactions at the electrode/electrolyte interface generally seen in organic electrolytes.

We described how a nickel substrate can be used in a fabrication process that takes place at elevated temperatures. TiO_2 was deposited onto the Ni substrate to act as a diffusion barrier that blocked Ni diffusion into the $Au/LiCoO_2$ stack which resulted in the formation of some activated $LiCoO_2$ however it was still substantially less than the theoretical capacity. The Ni substrate was converted to NiO and it restricts Ni diffusion into the $Au/LiCoO_2$ stack that meant a larger capacity was utilised though still below the theoretical capacity. A combination of both strategies, NiO/TiO_2 stack, resulted in no interaction with the $Au/LiCoO_2$ stack and the $LiCoO_2$ crystalline structure being defect free due to the absence of the Ni ions.

Electrochemical Analysis of Nanoscale Thin-Film V_2O_5 with a TiO_2 Coating and VC Electrolyte Additive in an Aqueous Electrolyte

We report the electrochemical analysis of an electrodeposited nanoscale film of V_2O_5. To make the fabrication of 3D core-shell nanoarchitectures a reality, electrode materials need to be easily deposited uniformly. Current additive-free electrodes are typically deposited via physical vapour deposition which is a line-of-site technique that makes it difficult to achieve uniform deposition onto micron tall 3D nanoarchitectures. V_2O_5 is a cathode material that can be easily electrodeposited and can be used to fabricate 3D core-shell nanoarchitectures.

An aqueous electrolyte was used to investigate the electrochemical properties of a nanoscale V_2O_5 thin-film in order to ensure the performance of the electrochemical cell is solely dependent on the electrode and not influenced by the resistive electrolytes typically used in the investigation of Li-ion electrodes. V_2O_5 was only cycled through the α/ϵ and ϵ/δ phases in order to avoid the H_2 evolution caused by the electrolysis of the aqueous electrolyte. CV cycling revealed the well-defined characteristics peaks for the crystal α/ϵ and ϵ/δ phases at scan rates of 0.5, 1, 2, 5, 10, 20, 50 and 100 mV/s. The contributing kinetics were investigated and revealed that the α/ϵ phase is diffusion controlled and that there is a significant pseudocapacitance (non-diffusion controlled) contribution in the ϵ/δ phases.

Rapid capacity fade was seen during CV cycling at 10 mV/s and was attributed to the dissolution of the V_2O_5 electrode. TiO_2 coatings of 50 and 100 nm thickness were applied in order to reduce the interaction between the V_2O_5 electrode and water molecules and extend the cycle life however no suppression of degradation was observed. VC was used as an electrolyte additive in quantities of 5 and 10 wt. % of the 5 M $LiNO_3$. A drop in pH was observed after the addition of the VC additive and it was attributed to the $LiNO_3$ oxidising the VC additive which produced CO_2 in the aqueous solution that is readily converted to carbonic acid and promoted polymerisation of VC. The capacity drop after 100 cycles was decreased to 61 % and 22 % with the addition of 5 and 10 wt. %, respectively, most likely due to the VC polymerising on the V_2O_5 electrode. A combination of a TiO_2 coating and VC was also reported and reveals that a 100 nm TiO_2 coating interacts more readily with the VC additive than an uncoated V_2O_5 electrode. A 100 nm TiO_2 coated V_2O_5 in 5 wt. % VC decreased the capacity drop to 28 % and 41 % after 100 and 200 cycles respectively. A 100 nm TiO_2 coated V_2O_5 in 10 wt.% VC decreased the current density and distorted the CV profile of the V_2O_5 which suggests that there is a stronger interaction between the TiO_2 coating and polymerised VC that suppressed lithiation.

Conclusion

In this thesis, the importance of the relationship between the electrode architecture, the electrolyte, and the performance of the Li-ion battery was examined in detail. COMSOL Multiphysics is a powerful tool that can be used to optimise electrode architectures and provide guidance for experimental analysis as shown in chapter 4. Structural engineering of the current collector can lead to improvements in the electrode performance, indicated by the

simulations and experimental findings in chapter 4 and 5, respectively. Electrode nanoscale thin-films of $LiCoO_2$ and V_2O_5 have a hybrid energy storage capability of intercalation and pseudocapacitance when the cells performance is solely dependent on the energy storage kinetics of the electrode, as indicated in chapter 6 and 7, respectively. The fabrication process can influence the performance of an electrode as seen in chapter 5 and 6 with annealing of Ge and $LiCoO_2$ being dependent on the substrate, respectively. Understanding the materials their architectures and electrolyte properties and interactions is critical in maximising performance as seen in chapter 7 where the V_2O_5 dissolved in the aqueous electrolyte over time and the simple addition of VC would result in a pH drop due to the $LiNO_3$ oxidising the VC additive and polymerising the VC to reduce interaction between V_2O_5 and the aqueous electrolyte.

Future Work

The area of focus in lithium ion battery research has been silicon-based anodes, cathode materials, liquid electrolytes, and solid-state electrolytes. Silicon must first overcome its limited life cycle due to large volume expansions. New advanced cathode materials have large capacities and voltages however this brings its own problems since standard electrolytes break down at voltages above 4.4V. High energy density conversion cathodes such as sulfur and oxygen has also attracted attention but additional issues such as dissolution/shuttling of electrode and reacting with the electrolyte respectively. The area that has received the most attention as been the liquid and solid-state electrolyte as a breakthrough in this area will result in the unlocking of lithium metal as an anode material, new cathode materials (metal oxide, S and O2) and improved battery safety. The number of patents files in 2015 on liquid and solid state electrolytes was 2,020 and the news from companies, such as Samsung and Toyota, claim they will be able to produce solid-state batteries before 2020.

Future work based on these findings should focus on developing deeper understanding of the materials and architectures relationship and the development and optimisation of fabrication processes. Improving the understanding between the form and function of nanomaterials and their processing is a very important field, which undoubtedly will experience significant growth in the coming years. New high conductivity electrolytes are required. Ionic liquids that can be used to electrodeposit the structured electrode materials and could also be used as an electrolyte to expand the electrochemical window. Ionic liquids have many of the advantages of solid-state electrolytes but with have a higher conductivity.

Appendix: Publications and Presentations

Oral Presentations

T. Clancy and J.F. Rohan, "Sn-Based Micro and Nano Lithium Battery Materials", 225th ECS Annual Meeting, Orlando, FL, USA, May 14 - 15, (2014)

T. Clancy, M. Hasan, and J.F. Rohan, "Core-Shell Nanoarchitectures for Lithium-Ion Energy Storage Applications", MRS Fall Meeting & Exhibit Boston, November 29 - December 4, (2015).

T. Clancy, L.M. McGrath, J.F. Rohan, "Nanoarchitectures for hybrid micro-energy harvesting and storage solutions", European Materials Research Society Spring Meeting, Lille, France, May 2 – 6, (2016).

T. Clancy, L.M. McGrath, J.F. Rohan, "High power thin film $LiCoO_2$ for wireless sensor applications", The 68th Annual Meeting of the International Society of Electrochemistry, Providence, RI, USA, August 27 – September 1, (2017).

Publications

J. F. Rohan, M. Hasan, S. Patil, D. P. Casey, T. Clancy, "Energy Storage: Battery Materials and Architectures at the Nanoscale", in ICT - Energy - Concepts Towards Zero - Power Information and Communication Technology, 2014.

T. Clancy, M. Hasan, J. F. Rohan, "Sn-Based Micro and Nano Lithium Battery Materials", ECS Transactions 2014, 61, 21-28.

T. Clancy, J. F. Rohan, "Multiphysics simulations of nanoarchitectures and analysis of germanium core-shell anode nanostructure for lithium-ion energy storage applications", Journal of Physics: Conference Series 2015, 660, 012075.

T. M. Clancy, J. F. Rohan, "Core-shell Nanoarchitectures for Lithium-Ion Energy Storage Applications", MRS Advances 2016, 1, 1055-1060.

T. M. Clancy, J. F. Rohan, "Ultra-fast cycling of nanoscale thin film $LiCoO_2$ electrodes in aqueous electrolytes", ChemElectroChem 2018, 5, 3273-3278.

T. M. Clancy, J. F. Rohan, "Simulations of 3D nanoscale architectures and electrolyte characteristics for Li-ion microbatteries", Journal of Energy Storage 2019, 23, 1-8.